

# Characterisation of cementitious materials by $^1\text{H}$ NMR

by  
Andrea Valori

Submitted for the degree of Doctor of Philosophy from the  
University of Surrey

University of Surrey  
Faculty of Engineering and Physical Sciences  
Department of Physics

October 2009

## **Declaration of Originality**

This thesis and the work to which it refers are the results of my own efforts. Any ideas, data, images or text resulting from the work of others (whether published or unpublished) are fully identified as such within the work and attributed to their originator in the text, bibliography or in footnotes. This thesis has not been submitted in whole or in part for any other academic degree or professional qualification.

I agree that the University has the right to submit my work to the plagiarism detection service TurnitinUK for originality checks.

Whether or not drafts have been so-assessed, the University reserves the right to require an electronic version of the final document (as submitted) for assessment as above.

## **Acknowledgements**

I have to thank several people who have helped me in completing this work.

I would like to thank my fellow PhD students and staff at the University of Surrey who shared with me time and challenges in the lab and outside for useful exchange of advice, Dr Rodin for his very close collaboration, my supervisor Professor McDonald for guidance and Dr Aptaker for the always useful and pleasant discussions.

I would also like to thank all the several people of Nanocem I have been working with and whose company I have enjoyed during these three years and in particular the one involved in the Marie Curie projects. Thanks to Willmott-Dixon and Leadbitter that allowed the on-site experiments in their construction sites in Guildford.

Thanks also to the tax payers of the European Union for funding the Marie Curie Nanocem project thus allowing me to have this stimulating and growing experience that has enriched me both professionally and personally.

I would also like to thank my family who have always supported me, as well as all those who have helped me through several revisions and corrections of this work.

The last, but the most important thanks goes to my wife Anna who has always supported and motivated me and for this has considerable part in the merit of this work.

## Abstract

This thesis addresses the problem of better characterising pore-water interactions in cement at the nano-scale and of providing a macroscopic in-situ measurement of water distribution in concrete infrastructure.

With regard to pore water interactions in cement three topics are addressed. First it is shown that the exchange observed in  $^1\text{H}$  Nuclear Magnetic resonance (NMR) 2D  $T_2$ - $T_2$  exchange experiment by Monteilhet et al. [Physical Review E, 2006. 74(6)] is due to water exchanging between pores of different size and not alternate Fe impurities density as had been suggested by subsequent discussion [Nanocem Open Meeting, April 2007].

Second, it is shown that the amplitude of the single quantum  $^1\text{H}$  NMR signal as a function of drying can be interpreted in term of a pore size and geometry that is consistent with other estimates. Two pore reservoirs are identified corresponding to sheet and gel pores. The pore thicknesses are founded to be 1.5 and 4.1 nm respectively.

Third, Double Quantum Filtered  $^1\text{H}$  NMR is shown as a new method of study anisotropic water in cement. The theoretical spectrum of water in the proximity of a  $\text{Fe}^{3+}$  ion has been calculated. This has been used to provide an estimate of a characteristic distance that can be interpreted either as characteristic size of the nano particles constituting the C-S-H or the  $\text{Fe}^{3+}$ - $\text{Fe}^{3+}$  inter ion distance. The best estimate is 11 nm.

With regard to the in-situ measurements, the characteristic signal to noise ratio and the portability of the Surface GARField magnet [Journal of Magnetic Resonance, 2007. 185(1): p. 1-11] has been greatly improved. The first measurements outside the laboratory have been successfully performed and are presented in this thesis.

# Table of Contents

<b>Acknowledgements .....</b>	<b>i</b>
<b>Abstract.....</b>	<b>ii</b>
<b>Table of Contents .....</b>	<b>iii</b>
<b>1 Introduction .....</b>	<b>1</b>
1.1 Ancient history of cement and concrete and current use .....	1
1.1.1 History.....	1
1.1.2 Scale of current use and reasons .....	3
1.2 What is cement .....	6
1.2.1 Chemistry nomenclature .....	6
1.2.2 Production .....	7
1.2.3 Hydration chemistry.....	8
1.3 Structure from macro to nano.....	10
1.3.1 Models.....	11
1.3.1.1 Power-Brownyard for the cement paste.....	11
1.3.1.2 C-S-H models.....	12
1.3.2 Need of basic understanding .....	14
1.3.3 Need for in situ analysis.....	15
1.3.4 Porosity .....	15
1.3.4.1 Techniques .....	16
1.3.4.1.1 Gas sorption and BET analysis.....	17
1.3.4.1.2 Low Temperature calorimetry .....	18
1.3.4.1.3 Mercury intrusion porosimetry (MIP) .....	18
1.3.4.1.4 Scanning Electron Microscopy (SEM).....	19
1.3.4.1.5 Transmission Electron Microscopy (TEM and STEM).....	19
1.3.4.1.6 Nuclear Magnetic Resonance .....	20
1.4 NMR and porous media.....	20
1.4.1 Generic NMR basics .....	20
1.4.1.1 Quantum Mechanics .....	21
1.4.1.2 Solid Echo .....	22
1.4.1.3 Double Quantum Filtered (DQF) .....	23

1.4.2	Techniques and theory on porous media.....	23
1.4.2.1	$T_1$ and $T_2$ relaxometry and Volume to Surface ratio .....	23
1.4.2.2	$T_1$ - $T_2$ correlation and $T_2$ - $T_2$ exchange experiments.....	27
1.4.2.3	PFG measurements for flow and diffusion and q space.....	34
1.4.2.4	Restricted diffusometry .....	35
1.4.2.5	Diffusion in internal gradients .....	37
1.4.2.6	Imaging .....	38
1.4.2.7	NMR Cryoporometry .....	38
1.4.3	Mobile and single side NMR .....	38
1.4.4	Applications .....	40
1.4.5	Problems .....	41
1.4.5.1	Laplace inversion .....	41
1.4.5.2	Surface relaxivity and paramagnetic impurities.....	43
1.4.6	Works done on cement/review.....	43
1.5	What this thesis is going to say .....	47
<b>2</b>	<b>Portable magnet.....</b>	<b>48</b>
2.1	Introduction .....	48
2.2	Magnet specification materials and methods.....	49
2.2.1	Probe and electrical scheme .....	52
2.2.2	Pulse sequence and slice selection .....	56
2.2.3	Signal processing .....	57
2.2.4	Other equipment.....	57
2.3	Improvements to the system.....	58
2.3.1	Software and new spectrometer .....	58
2.3.2	Lumped element $\lambda/4$ .....	59
2.3.2.1	Scheme and theory and building .....	59
2.3.2.2	Tests .....	61
2.3.2.2.1	Impedance measurements.....	61
2.3.2.2.2	Pulse length .....	62
2.3.3	Resonant coil.....	65
2.3.3.1	Increased thickness of probe .....	65
2.3.3.2	Analysis of the original S/N.....	66
2.3.3.3	Potting .....	70
2.3.3.4	Analysis of the S/N following potting of the coil .....	71
2.3.4	Shielding .....	71
2.4	Test experiments.....	73

2.4.1	Rubber block for calibration .....	73
2.4.2	Rebars and phantom.....	73
2.4.3	On-site experiments .....	77
2.4.4	Calibration.....	80
2.5	Conclusions .....	83
<b>3</b>	<b>2-D relaxometry.....</b>	<b>84</b>
3.1	Introduction .....	84
3.2	Theory.....	84
3.3	Experimental materials and methods.....	89
3.3.1	Pulse sequence .....	89
3.3.2	Laplace inversion .....	90
3.3.3	ESR measurements .....	91
3.3.4	Materials and sample preparation .....	91
3.3.4.1	Characterisations of samples performed at CTG Laboratories .....	95
3.4	Results .....	99
3.4.1	$T_2$ - $T_2$ NMR .....	99
3.4.1.1	Typical example, the white cement.....	99
3.4.1.2	The grey cement.....	102
3.4.1.3	The doped cement samples .....	103
3.4.1.4	The $C_3S$ and doped $C_3S$ samples.....	105
3.4.1.5	Synthesised C-S-H .....	109
3.4.1.6	ESR results.....	114
3.5	Analysis and discussion.....	115
3.5.1	ESR measurements .....	115
3.5.2	White and grey cements.....	116
3.5.3	The doped cement samples .....	117
3.5.4	$C_3S$ and doped $C_3S$ .....	117
3.5.5	Synthesised C-S-H .....	118
3.6	Conclusions .....	119
<b>4</b>	<b>Solid echo and drying model .....</b>	<b>120</b>
4.1	Introduction .....	120
4.2	Materials and methods.....	122
4.2.1	NMR measurements.....	122
4.2.1.1	Solid Echo .....	122
4.3	Data analysis.....	123

4.4	Theory.....	124
4.5	Results .....	130
4.6	Discussion.....	136
4.7	Conclusion.....	141
<b>5</b>	<b>DQF .....</b>	<b>142</b>
5.1	Introduction .....	142
5.2	Experiment materials and methods.....	142
5.2.1	Sample preparation .....	142
5.2.2	NMR experiments .....	142
5.3	Model.....	143
5.3.1	General model .....	143
5.3.2	Sheet model.....	144
5.3.3	Powder average .....	147
5.3.4	Magnetic interactions.....	147
5.4	Results .....	155
5.5	Analysis and discussion.....	158
5.5.1	DQF signal integral amplitude.....	158
5.5.2	Analytic fitting .....	158
5.5.3	Analytic-simulated fitting .....	159
5.5.4	Average splitting.....	165
5.6	Conclusions .....	167
<b>6</b>	<b>Conclusions and future work .....</b>	<b>169</b>
6.1	Conclusions of relaxation analysis and DQF work .....	169
6.2	Conclusion of the work on the portable magnet.....	170
6.3	Future work on DQF .....	171
6.4	Future work on the portable magnet.....	171
<b>7</b>	<b>Appendix .....</b>	<b>173</b>
7.1	Quantum mechanics calculation.....	173
7.2	Matlab code .....	180
	<b>Bibliography .....</b>	<b>184</b>

# 1 Introduction

In this thesis the work done in the framework of the Nanocem Marie Curie European project number 4 will be presented.

Reporting the description on the Nanocem Website: “*Nanocem is a consortium of European academic and industrial partners, all interested in fundamental research in the nanoscale science of cement and concrete. Working together, the members of Nanocem can make technological breakthroughs in the field, providing added value for the industry around the world*” [1].

Nanocem was founded in 2004 and started funding the Core Projects, which are fundamental, long-term research projects carried out by two or more contractors, funded by the resources of the Nanocem Consortium. The work of one of these Core Projects (the number 2) has been done between the Laboratoire de Physique de la matière condensée at the Ecole Polytechnique of Palaiseau (near Paris) and the University of Surrey. Later on, in 2006, Nanocem successfully applied to the European Community for a large amount of money in the Framework Project 6 in the form of Marie Curie fellowships for funding 15 between PhD and post doc.

Each one of these projects has a secondary academic partner and an industrial partner. In the case of the specific project presented in this thesis it collaborated with the project 3 located at the Danish Technical University and the CTG Italcementi Group laboratories situated in Bergamo (Italy). A visit to Bergamo allowed collaboration and performance of some measurements that will be presented in the thesis.

The project presented in this thesis, entitled “State of water in cover concrete” is one of them and is an expression of the continuation of the commitment within Nanocem in dedicating interest to NMR application to study dynamics of water in cementitious materials. This project has closely collaborated in particular concerning chapters 4 and 5 of this thesis with a Nanocem partner project funded by EPSRC, both of which are based at the University of Surrey.

## **1.1 Ancient history of cement and concrete and current use**

### **1.1.1 History**

Cement and concrete are ubiquitous materials found and used in huge quantities across the world. Cement and concrete may sound and are frequently treated as synonymous in the

everyday language, however, technically they are different. Cement is a finely powdered material that when mixed with water, creates a paste (the cement paste) that hardens via hydration and curing. During this process it is capable of binding rocks and sand (also called aggregates) together in a matrix. All these constituents bound together make concrete. Cement is the key ingredient of concrete. There is an additional distinction between mortar and concrete that is based on the size of the aggregates; if only sand is used, it is called mortar while if bigger stones are also used, it is called concrete.

Incredibly complex constructions have been built by humanity using just dry stone techniques without the use of any binder but rather with extremely careful and time consuming shaping of the rock construction blocks. However, the support that a binder phase can bring to any construction means that man has been seeking cement since the earliest ages of civilisation. Assyrians and Babylonians used clay to build their constructions; the Egyptians advanced with the discovery of lime and used it to build the pyramids. However, it was not until the Romans, that a cement similar in composition and durability to the one we use today was discovered. The secret of Roman success can be traced to their mixing slaked lime (calcium hydroxide) as a source of calcium, and pozzolana, a volcanic ash of Mount Vesuvio, as a source of silica with water. This calcium, silica and water mixture is the basis of all cement chemistry. The calcium silicate hydrate gels (usually abbreviated as C-S-H in cement literature) are the main glue of cement paste.

The main advantage of this new kind of binder is that water is part of the hardening reaction; it is, in fact, itself bound into the structure, and it is not only a way of keeping the material in suspension that allows putting it in place. This creates a much more compact material after hardening and for the reason previously mentioned it is called a hydraulic binder.

The Romans relied on the geology of their environment to make cement. Artificial production was not possible as this requires high temperature processes that were not achievable before the industrial period. Knowledge of hydraulic cement was then lost during the Middle Ages, only to be then rediscovered during the 18<sup>th</sup> century by the British engineer John Smeaton seeking a durable material with which to rebuild the Eddystone Lighthouse on the coast of Cornwall after frequent failures due to the harshness of the location. For some years natural cement was produced by burning a naturally occurring mixture of lime and clay. The discovery of synthesising cement by heating was fundamental in enabling the start of production on an industrial and later global scale. Because the raw materials are naturally mixed, their proportions varied widely and therefore so did the actual chemical composition and moreover, the performance of the final material as well. In 1824 Joseph Aspdin patented a cement that he called Portland due to the similarity in colour with the stone quarried on the

Isle of Portland [2]. The Aspdin method of producing cement was based on a careful proportioning of limestone and clay, their pulverisation and mixing, cooking in a kiln to obtain a clinker and grinding again. This basic process is, with some optimisation, the one used to the present.

### 1.1.2 Scale of current use and reasons

The world growth of population and the construction of housing and infrastructure cause a huge demand for building materials. The material that is the most suitable to respond to this demand is clearly concrete, now being produced in the order of  $10^{10}$  tonnes per year [3,4]. The first clear reason for this popularity is its price. As Figure 1.1 clearly shows, the amount of a material used is strongly correlated to its price. Concrete is cheap!

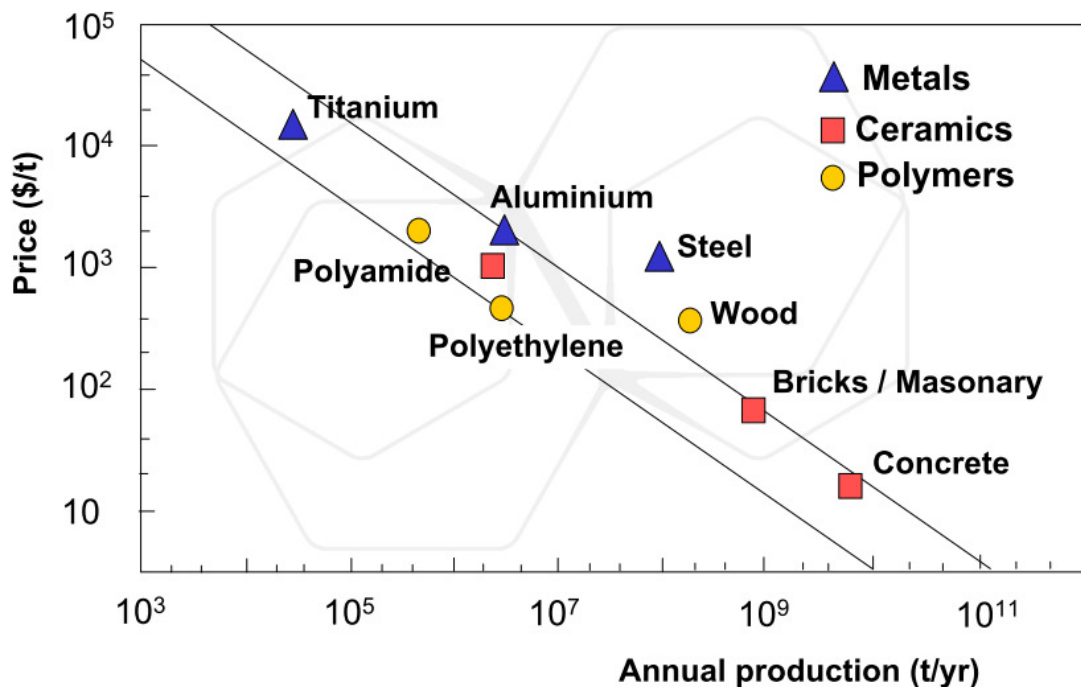


Figure 1.1 Price of materials versus annual production, from [4]

The reasons for the low price of concrete are several: first of all the availability of the raw materials. Since, apart from Ca that is easily available from limestone, the composition of cement is very similar to the mean one of the earth's crust (Figure 1.2), this means that cement can be produced virtually everywhere in the world using materials quarried locally saving huge amounts in transport.

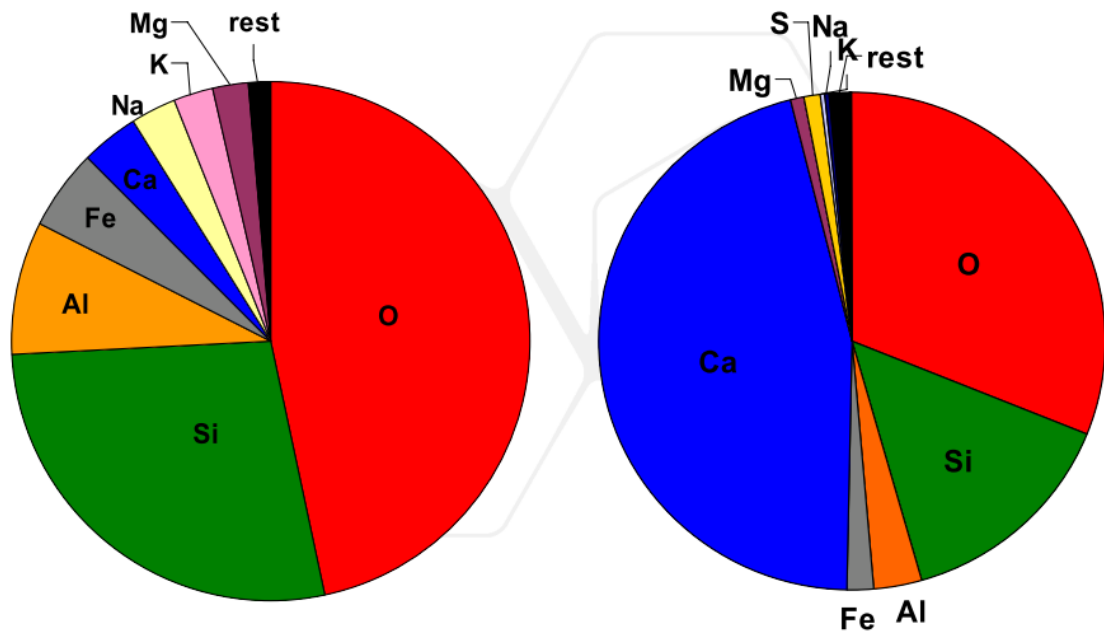


Figure 1.2 Composition of the earth's crust (left) and cement (right); Apart from the different amount of Ca, the high similarity in composition is clear. (From [4]).

Other factors that make cement and concrete easy to use (and that translate into a low final price) are the ease of transport (cement can be transported in hand movable sacks or, for big quantities, in bulk and pumped through pipes onto lorries, trains and ships), the ease of constructability (it does not require complex equipment on the construction site, just the adding of water and stirring, although it requires some care) and its flexibility in use (it fills volumes of almost any shape, sets and hardens at different room temperatures and with little volume change). Cement is also water tight, another greatly appreciated characteristic.

Concrete performs very well when compared with other materials if we consider its compressive strength. It is, however, pretty poor in tensile strength. To overcome this lack, steel reinforcements are commonly introduced into concrete structures. This composite material is the one called reinforced concrete; the combination of the concrete high compressive strength and the steel high tensile strength create a great material that is suitable for the most varied applications.

Cement, despite what is commonly believed, is also a low energy production process per unit mass (or volume) of material; it is the huge total amount of cement produced yearly worldwide that creates the myth of high energy consumption of its production process. In Figure 1.3 the production energy of cement and concrete is compared with other construction materials. All these characteristics put together make cement a unique material and are the reasons why cement is (and will remain for a long time more) the most used material in the world.

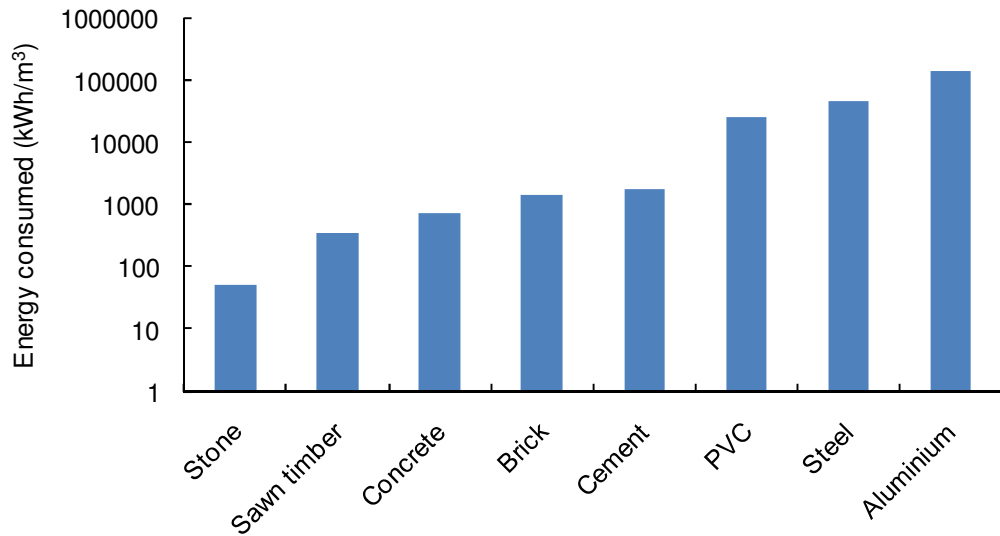


Figure 1.3 Energy production cost of various construction materials (after [5])

CO<sub>2</sub> emissions for cement production cannot be directly evaluated from the energy cost. In fact, despite the low emissions for fuel consumption cement production possesses another huge source of carbon dioxide. One of the main reactions occurring during calcinations is the decarbonation of the calcium carbonate (CaCO<sub>3</sub>) following the chemical reaction (1.1); almost 50% of the total CO<sub>2</sub> emissions of cement production have this origin.



The huge amount of cement produced worldwide causes this industry to be responsible for 5% of the total anthropogenic CO<sub>2</sub> emissions [1], making it an important target for CO<sub>2</sub> emission mitigation strategies, therefore emission reduction is one of the main tasks that the cement industry is facing at the moment. The difficulty in reducing the emissions comes from the fact that only small improvements can be made with better combustion or using alternative fuels. The cement manufacture is already close to the 80 % efficiency in terms of heat recovery and fuel optimisation [4]; to drastically reduce the emission a different chemistry must be adopted. Although a change in the basic chemistry is not foreseeable in the near future, a present useful trend is the one of using Supplementary Cementitious Materials (SCM); these materials are usually by-products of other industries (slag from metallurgy industry, fly ashes from power plants) and contain Ca or Si that is already decarbonated and in the oxidised state necessary for cement production. The substitution of cement with SCM lowers the nominal emissions by the simple fact that the CO<sub>2</sub> has already been emitted by the previous industrial process. The fact that the “useful by-product” are

themselves in limited quantity and that also the by-product producers are pushed towards limiting the emissions causes the SCM solution to be a good but only temporary solution. Improvements in the long term aim of lowering the CO<sub>2</sub> emissions in the cement industry can only come from the use of different materials.

Concrete structures are durable. There are buildings such as the pantheon, that were built in the 120 AC and are still in good condition, however, 50 % of the budget spent on structures is spent on maintenance and repairing [6]. This number gives an idea of the fact that concrete *can* be durable but that there are still huge durability issues. On this subject one fact that must be kept in mind is that concrete can be, in the first instance, divided into high quality and low quality and, as usual, with inverse proportionality between quality and price. This means that there are very few constructions that cost a huge amount of money but will last for a long time, while the vast majority of the constructions are built in a relatively cheap and not long-lasting material. Durability issues arise also because often (if not always), due to the inevitable fact that the evolution of admixtures and new cement mixes is much faster than the expected lifetime of the structures built, there is not full knowledge of the behaviour of the materials employed especially at long term.

Simulations are helping in foreseeing the long term properties of cement and concrete. However, the lack of basic knowledge on the microstructure greatly limits the possibilities. Industry needs predictors of performance and durability and both these are, in one way or another, related to water content, dynamic interactions with the pore surfaces and macroscopic transport. All these necessities are the motivations for this work.

## ***1.2 What is cement***

### **1.2.1 Chemistry nomenclature**

Cement is such a particular material that has its own chemistry nomenclature (although, of course, obeying the same fundamental physical and chemical rules). In practice all the elements are described in term of oxides (Table 1.1).

Cement notation formula	Traditional formula	Name
C	CaO	Calcium oxide
S	SiO <sub>2</sub>	Silica
A	Al <sub>2</sub> O <sub>3</sub>	Aluminium oxide
F	Fe <sub>2</sub> O <sub>3</sub>	Iron oxide
H	H <sub>2</sub> O	Water
\$	SO <sub>3</sub>	Sulphur trioxide
Č	CO <sub>2</sub>	Carbon dioxide

Table 1.1 Cement nomenclature and chemical notation

In fact, cement powder is “nothing else” other than a combination of oxides of calcium, silicon, aluminium and iron.

Using the nomenclature in Table 1.1, the main components of Portland cement are C<sub>3</sub>S and C<sub>2</sub>S (tri-calcium and di-calcium silicate, also called Alite and Belite); the European standard required for a Portland cement is a C<sub>3</sub>S+C<sub>2</sub>S content of 67% [7]. These are the two phases that develop the main strength during hydration forming a gel like calcium silicate hydrates (C-S-H) and calcium hydroxide (Ca(OH)<sub>2</sub> or “Portlandite” or CH):

Two other fundamental phases in cement are the C<sub>3</sub>A and C<sub>4</sub>AF (calcium aluminates phases and calcium ferrous aluminates phase, also called aluminate and ferrite phases). These react with the calcium sulphate (gypsum, which is added to the ground clinker) to form another two important groups of products: AFm (Al<sub>2</sub>O<sub>3</sub>-Fe<sub>2</sub>O<sub>3</sub>-mono) and AFt (Al<sub>2</sub>O<sub>3</sub>-Fe<sub>2</sub>O<sub>3</sub>-tri), also called monosulfate and ettringite.

### 1.2.2 Production

Cement production is nowadays an industrial process on a huge scale; cement plants work 24 hours a day 7 days a week with a continuous flow of material.

The main raw materials for cement production are limestone and clay that are finely ground to have a good intermixture. Usually, because the limestone and the clay have different grindability the two materials are ground separately and then carefully mixed to achieve the right chemical composition. The addition of other materials is often required to obtain the right raw material composition.

The “raw feed”, the mixture of raw materials, is cooked up to 1500°C in a rotary cylindrical kiln. At this high temperature the full decarbonation of the  $\text{Ca}(\text{CO}_3)$  is achieved and the material partially melts. The kiln has a slope so the materials are fed into the highest part and they slowly move towards the lower part. The last stage is a quick cooling of the final product of the cooking phase that is the clinker nodules. These are finely ground and gypsum is added to obtain the final cement powder.

The biggest kilns are 150 m long and have a diameter of 3 to 5 m. This leads to the fact that a kiln cannot be switched on and off easily. It requires a long time to cool down in case of servicing and another long time to reach the working temperature again. In addition, due to the fact that the temperature must be reached in working condition, a considerable amount of material is wasted at each switching off and on of the kiln.

### 1.2.3 Hydration chemistry

After mixing cement powder with water, there are two phenomena that happen together but are conceptually different.

One is hydration, that is a chemical process that takes the system constituted by a liquid and a solid phase to a single solid phase (that anyway can be constituted by different chemically distinguished solid phases) the other is the setting, which is referred to as a “collective” physical evolution that makes the paste a solid.

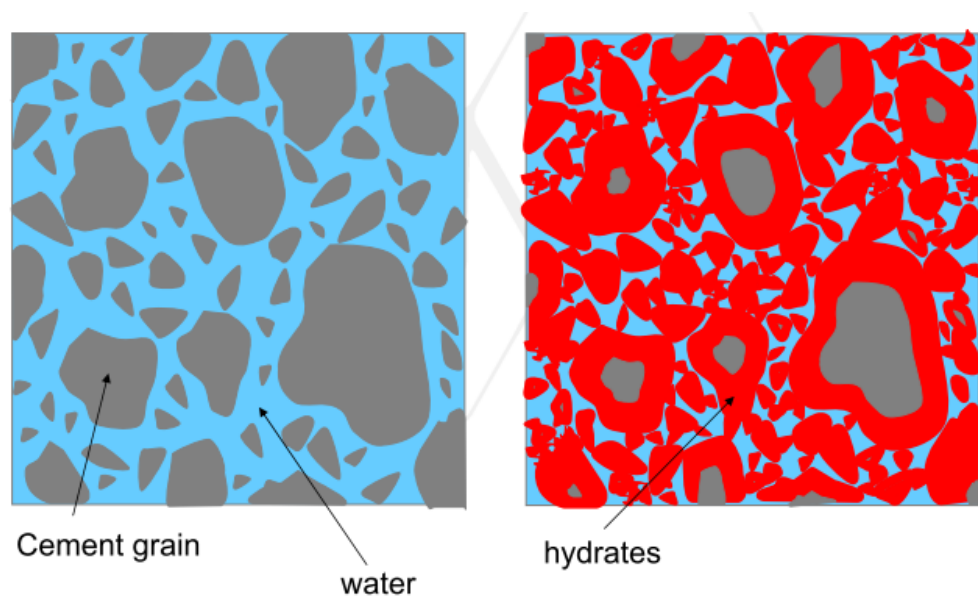


Figure 1.4 Schematic of the hydration of cement grains. The outer portion of the grains dissolves and re precipitates around the grain increasing its size, eventually bringing all the grains into contact. (From [4])

The hardening of cement is a hydration phenomenon, via a dissolution precipitation process; the water can then be seen as the “trigger” of the hardening process. The highly soluble components present in the cement powder, when in contact with water, dissolve quickly creating a supersaturated solution respect the hydrates components causing precipitation. The hydrates grow on the surface of the cement grain as long fibrillous structures that eventually connect the grains to each other.

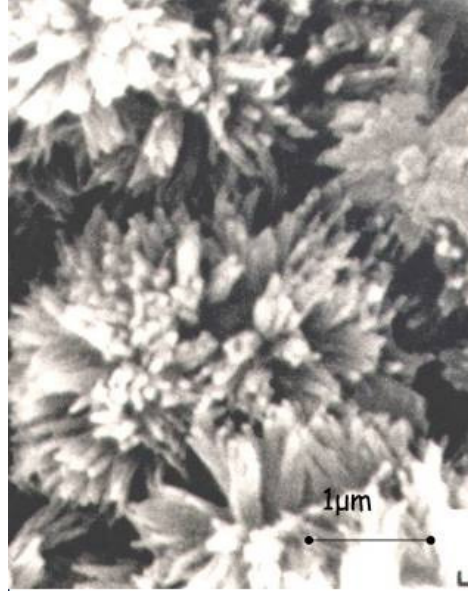
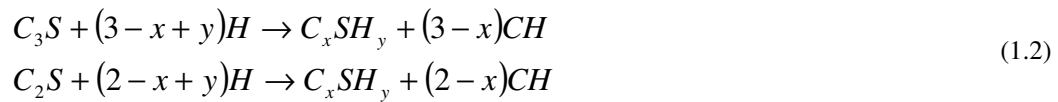


Figure 1.5 Appearance of the hydrates after 24 hour of hydration (from [8])

The fact that the specific volume of water is lower when in the hydrates than when in the free state causes the cement to be subject to chemical shrinkage during hydration, and therefore to be intrinsically and inevitably porous.

As already mentioned the main reaction in the hydration of cement is the hydration of the  $C_3S$  and  $C_2S$  following the reactions



The main role of the aluminates and ferrite phases and gypsum is to slow down the reaction at the early ages creating a protective and relatively impermeable layer on the surface of the cement grain. This slowing of the reaction is necessary to keep the workability of cement paste (or concrete) for a time that allows casting.

Hydration of cement is a long process. As well as the primary processes above, it also involves other much slower secondary chemical reactions that consume primary products (as

for example the CH) to form secondary products; in fact cement hydration slows down with time but keeps occurring for years.

Other fundamental chemical reactions are responsible for the ageing and loss of the characteristics of cement and concrete properties. One of the most evident phenomena is the corrosion of the reinforcement rebars embedded in concrete; the expansion produced by rust formation causes the surrounding concrete to crack destroying the cement matrix. In the “normal” situation rust is prevented by the high pH of concrete, which stabilise an oxide layer on the steel that inhibits further attack. This layer is unstable at lower pH values, which can result from carbonation or presence of  $\text{Cl}^-$ . Both carbonation and  $\text{Cl}^-$  ingress require the presence of water as a transport medium; in fact virtually all the degradation processes of cement involve, to some extent, water and its mobility, making the study of the state of water and dynamics a very relevant subject.

### ***1.3 Structure from macro to nano***

At some level the behaviour of every material is related to its microstructure [9]. The lack in developing microstructures/properties relationships for concrete is due mainly to the lack of good microstructural characterisation.

In microstructural terms, concrete is a very complex system of solid phases, pores and water, with a high degree of heterogeneity on several levels and order of magnitude in length scale.

At the first level, concrete consists of aggregates embedded in a cement paste matrix. At a finer level hydrated cement paste can be divided into unreacted cement (the inner part of the original cement grain), reaction products and porosity. At an even lower level the reaction products can be subdivided into different phases each one having its own structure, and the pores can be divided into capillary and gel pores on the basis of size formation and location, than can be empty or filled with water. Water must always be considered as part of the cement structure since it plays a key role in most (if not all) the processes, from hardening to degradation.

CH is the only hydration product in cement with a well defined stoichiometry and crystal structure. The calcium silicate hydrate, instead, although can form well defined structures as tobermorite, or jennite in other systems, in cement forms a gel with limited local crystalline order but no long range order and that can be related to the crystalline structures only at the short range.

### 1.3.1 Models

#### 1.3.1.1 Power-Brownyard for the cement paste

This model has been developed by Power and Brownyard [10-12] in 12 years of systematic experimental work in the 40's and was later modified by Power alone. It is surely one of the most complete empirical models for cement paste developed. This model does not distinguish between different solid phases whether in the unreacted cement or in the hydration products which are collectively called "cement gel", although for some materials (e.g. CH) the term gel is not completely appropriated.

This model can be described as a "Volumetric phase distribution in a hardening cement paste" [13]. In this model water is divided into 3 kinds: chemically bound, that is held in the hydration products (non evaporable below 105 °C); physically adsorbed (or chemisorbed water), that is adsorbed on the surfaces of the hydration products and occupying the gel pores and free water (or capillary water)

To determine the amount of chemically combined water, Power measured the difference in mass loss during burning, for 20 minutes at 1000 °C, unhydrated cement and the hydrated cement dried with a well defined solution of magnesium perchlorate dihydrate [12]. Power himself remarked that different drying processes may be equally valid and lead to different conclusions. The fact that Power's work is completely empiric does not lower its value but makes it strongly procedures dependent.

The physically adsorbed water is the one retained at a vapour pressure value of  $\sim 0.4$  respect the saturation level for the cement paste. This definition comes from the fact that below this level all the adsorption isotherms (water retained vs. water pressure) for any paste of Ordinary Portland Cement lay on each other. This observation led Power to believe that "the physical structure and the physical properties of room temperature cured cement gel such as strength, elasticity, creep, shrinkage, permeability and chemical properties are nearly the same in all pastes. The characteristics of the paste structure, however, depend on the extent and manner in which the cement gel occupies the available space." [14]

Power also observed that there is a minimum water to cement ratio (w/c) that allows full hydration and is 0.38. Also the minimum achievable porosity is measured and estimated as  $\sim 8\% \text{ v/v}$ .

### 1.3.1.2 C-S-H models

As mentioned in paragraph 1.3, some of the phases in cement are crystalline and therefore have also a fixed composition, allowing the application of techniques based on diffraction or chemical analysis that give good and reliable results. The main binding phase (the C-S-H), is instead nearly amorphous, highly variable in chemical composition, nanostructure and morphology, and it is mixed on a very fine scale with microcrystals of other phases; establishing its exact nature has consequently proved somewhat difficult. For this reason long debates are still ongoing and several models have been proposed.

Some models focus on the globular structure of the C-S-H, proposing two kinds of this material with different porosity and density [15,16]. Others are focused more on the internal structure of this globule proposing a layered structure [7,17]. The differences are based on the considered length scale, in fact both are fully compatible considering that the layered structure is at the nanometric scale, while the aggregation of layered particles (by some author called globules) are at least one order of magnitude bigger.

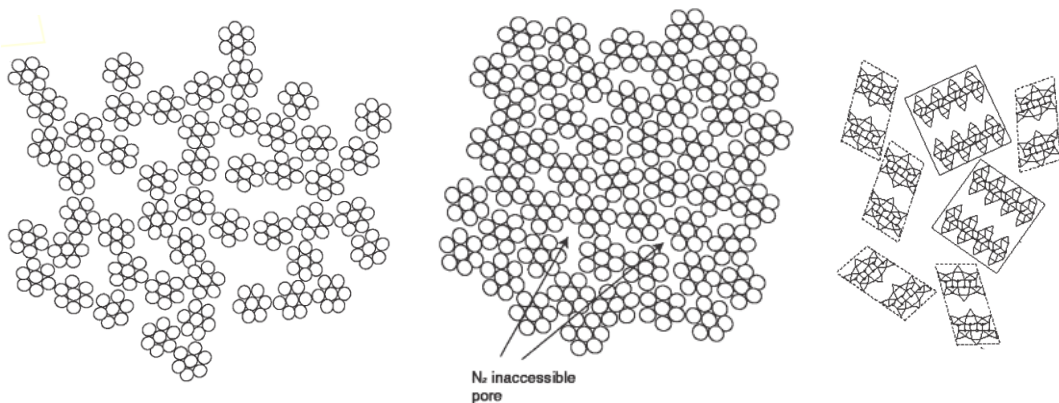


Figure 1.6 Low density and high density C-S-H, different packing and layered structure of the basic unit as proposed by Jennings (adapted from [15])

Similar to the Jennings model [15] also the Feldman Sereda model [7] takes into account for two types of porosity in the C-S-H: an interlayer water and a gel one.

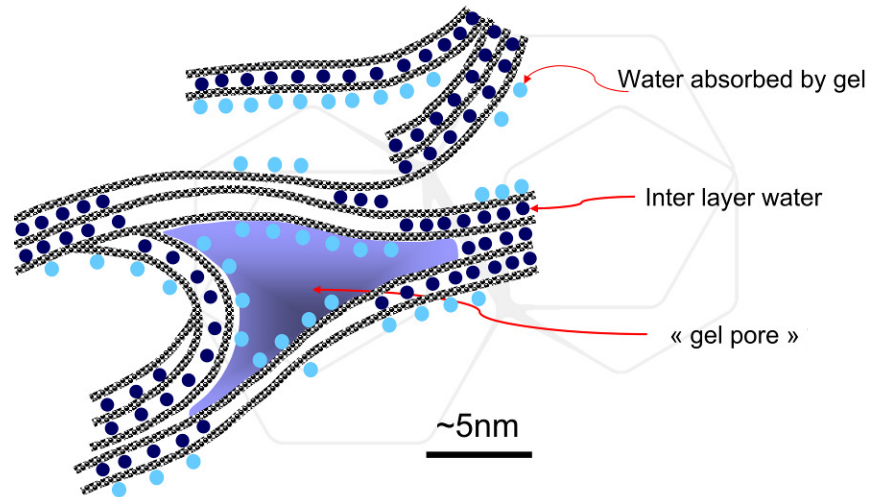


Figure 1.7 Feldman Sereda model for the C-S-H (from[8])

In practice all the models include a layered nanometric structure and slightly coarser porosity due to the non-crystalline structure of the packing.

The crystalline calcium silicate hydrate that is most similar to the C-S-H in cement is believed to be the 1.4 nm tobermorite, where the prefix 1.4 nm stays for the interlayer spacing.

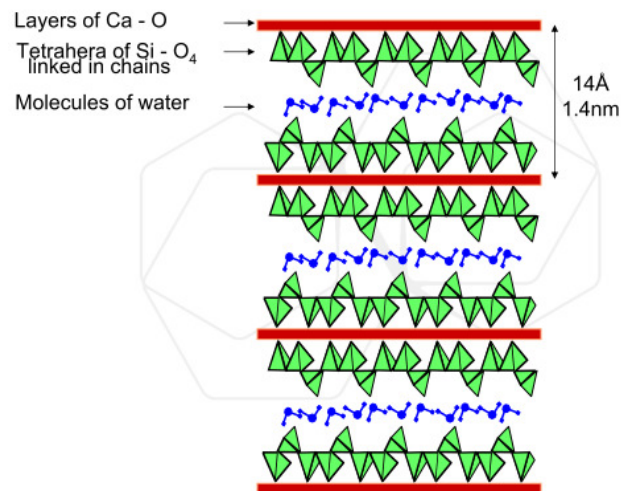


Figure 1.8 Schematic representation of the layered nanostructure of tobermorite, (from [8])

Transmission Electron Microscopy is an extremely valuable tool to examine the structure of the C-S-H at the nanoscale. Richardson in several papers [18-20] presented very explanatory images acquired with this technique on both tobermorite and C-S-H.

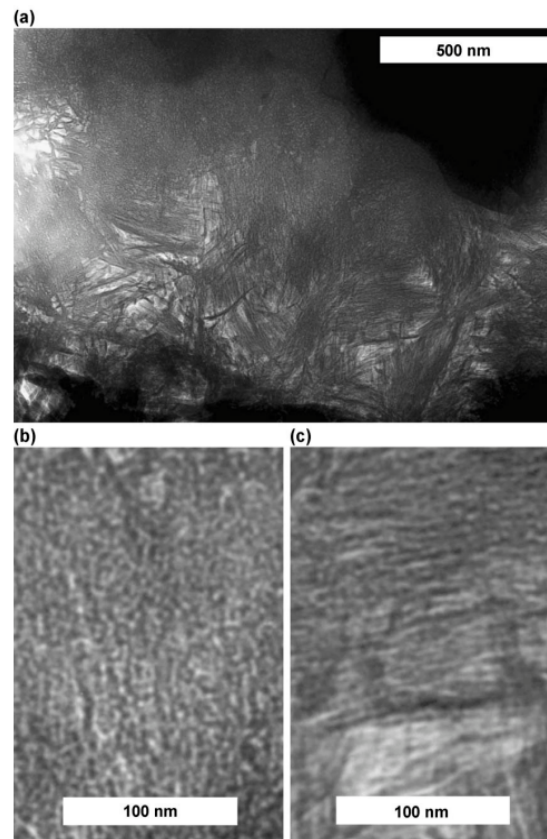


Figure 1.9 Examples of inner and outer product C-S-H as seen with TEM (from Richardson [19]).

### 1.3.2 Need of basic understanding

Although cement and concrete, as we said in paragraph 1.1.2, is incredibly widely used, there are still several open questions, and the basic knowledge of the material is still (relatively) poor. The demonstration is in the fact that 50 % of the budget spent in infrastructures is spent on maintenance and reparation [6]. New cement types and additives are developed and used virtually every day to meet the requirements of new challenging projects. Examples of this requirement include the decrease in the cost of the structures (and therefore the facility of application), the increase in the construction speed, the environmental exposure during or after casting (for example required long time workability). Also the interest in new SCM, to lower the energy consumption or CO<sub>2</sub> emissions, is high. The materials are evolving faster and faster, and the required lifetime of the structure is also becoming longer and longer, approaching (or exceeding for several major infrastructures) 100 years. This means that there is absolutely no time to test the materials in the real conditions that they will encounter when put in place. Accelerated tests for the durability have been developed, but the results have often been demonstrated as not very reliable. More

interest is probably placed in simulation, both for simplicity of execution and for the lower cost; however this technique relies heavily on the fundamental phenomena and parameters governing the system studied. For this reason there is great interest in basic understanding of the science undergoing the phenomena in cement and concrete. One of the most important of these phenomena is the water content and mobility. The water is both part of the structure and also carrier of virtually all the harmful substances for cement.

NMR can be a very valuable tool in helping to move forward on this subject, in fact in this technique, water, or more precisely its protons, are the direct probe used. The NMR parameters are very sensitive to the mobility and dynamics of protons, also on the length scale of only a few nm. As an example, spin-spin relaxation time can span from a few  $\mu\text{s}$  to seconds when we move from considering bound protons to protons of bulk water. For this reason, NMR is the probe used in this work, especially because the interest is in probing the pore water interactions, but first a review on the other (complementary) techniques will be presented.

### **1.3.3 Need for in situ analysis**

Half of the money spent on structures is on maintenance. This often requires assessment of the building and of the reasons for the damage. Water, as we said plays a key role, and therefore in-situ detection of the water content in built infrastructure is very important. Additionally this parameter can be of interest when thinking to quality control procedures on either new or old constructions. This in-situ analysis can be performed using NMR, however, this is not a well established and diffuse technique with well tested instrumentation, and instead it is performed with specifically designed, most of the time, one-off magnets.

### **1.3.4 Porosity**

Porosity is one of the most (if not *the* most) important characteristic of cement. It is the main parameter that determines strength and, influencing transport properties and permeability, is also a major parameter determining durability.

The reason of the strong influence on mechanical properties is simply because air (or water) in the pores do not contribute to the strength.

During hydration the fraction of the larger porosity (capillary pores) decreases onto the expense of solids and finer porosity (gel pores). This evolution can be modelled, in some extent, by Power's model [10-12], which is a very powerful tool to describe the effects of different w/c ratios, age and degree of saturation. However, this model divides the paste in just three components from the volumetric standpoint: unreacted cement, hydration products



vary between nm sizes to  $\mu\text{m}$  or even more) and which the effects of the sample preparation are.

There are some important concepts that must be kept in mind when talking about porosity and its measurement. The tortuosity is defined as the “twistiness” of a path, it is quantified by the tortuosity factor, calculated as the length of the path that a molecule must travel to traverse a film of unitary thickness. Two pores are defined as connected if there is a continuous path that connects them. The experimental connectivity, of course, depends on the minimum size of the pore measured, if the connection is smaller than the detection threshold, the pores will appear as not connected. The threshold pore is the minimum diameter of a channel that is continuous (“percolated”) through the sample.

#### 1.3.4.1.1 Gas sorption and BET analysis

Physical gas sorption is a volumetric method to measure the amount of gas adsorbed on the porous material surface. What is measured in practice with this technique is the mass of gas adsorbed as a function of the gas pressure. The analysis is based on the theory developed by Brunauer, Emmett, and Teller (BET) [29] using two equations; from the mass of gas adsorbed the specific surface can be calculated using:

$$S_{BET} = \frac{X_m}{M} \cdot N \cdot A_m \quad (1.3)$$

Where  $S_{BET}$  is the specific surface area ( $\text{m}^2/\text{g}$ ),  $X_m$  the mass of adsorbate gas (g),  $M$  the molecular weight of adsorbate (g/mol),  $A_m$  the area occupied by one adsorbed molecule ( $\text{m}^2/\text{molecule}$ ), and  $N$  the Avogadro number (molecule/mole).

From the pressure, instead, the Kelvin equation leads to an estimation of the radius,

$$r_k = \frac{-2 \cdot V_{mol} \cdot \gamma_{s-v}}{R \cdot T \cdot \ln\left(\frac{p}{p_0}\right)} \quad (1.4)$$

Where  $r_k$  is pore radius (m),  $\gamma_{s-v}$  the surface tension, vapour-solid interface, (N/m), for nitrogen  $V_{mol}$  the molar volume adsorbed ( $\text{m}^3/\text{mol}$ ),  $p$  the pressure ( $\text{N}/\text{m}^2$ ),  $p_0$  the saturated vapour pressure ( $\text{N}/\text{m}^2$ ),  $T$  is the temperature (K) and  $R$  is the universal gas constant ( $\text{J}/\text{mol}$ ).

This technique can be used with different gases, the most common nitrogen, water or helium. One great advantage of this technique is that it is widely used and is defined with international standards. One of the disadvantages for the applicability to cementitious

materials is that, if a gas different from water is used, it requires drying and evacuation of the sample; this affects the delicate gel structure of cement [30]. Another limitation is the assumption of cylindrical pores embedded in the Kelvin equation and the relatively big size (16.4 Å) of the nitrogen molecule compared to the water one (10.6 Å), that excludes the smaller porosity if this gas is used. This is a slow test especially in the range of relative humidity 0.3 to 0.8 and may require weeks to reach the equilibrium [31], if water is used as gas, the hydration carries on considerably in that period, unless very old samples are used.

#### **1.3.4.1.2 Low Temperature calorimetry**

Low temperature calorimetry is based on the fact that the water restricted in pores freezes at lower a temperature than in bulk. The solidification heat is measured as a function of temperatures ranging typically between 20 and -50 °C. Ice forms through the advance of a freezing front analogously to the desorption of water. Hysteresis effects show “bottle neck” effects, for this reason the experiment has to be performed in both freezing and thawing mode. The first gives the size of the pore entrance, while the second the pore size distribution.

The sample preparation consists of saturation at high (150 atm) pressure for 24 hours [32], and the drawbacks are mainly due to the fact that the water freezing may break the cement structures [33].

Applications on cement show the occurrence of three distinct peaks on curves of apparent heat capacity against temperature. These were interpreted as maxima in the pores size distribution and therefore confirmation of the intrinsic discreteness of porosity in cement [7]. The range of applicability is not well defined, 2 to 40 nm according to [34], up to 200 nm according to [35].

#### **1.3.4.1.3 Mercury intrusion porosimetry (MIP)**

This technique is based on the fact that a non wetting liquid can enter the pores of a solid only under pressure. The volume of liquid intruded is measured as a function of the pressure applied. Assuming cylindrical pores the pressure required is given by the Washburn equation

$$p = -4\gamma \cos\left(\frac{\theta}{d}\right) \quad (1.5)$$

Where  $\gamma$  is the surface energy of the liquid,  $\theta$  is the contact angle and  $d$  is the pore diameter. For Hg  $\gamma = 0.483$  N/m and the common values for  $\theta$  are between 117° and 140°, however

values up to  $180^\circ$  have been proposed [36]. The values of pressure used typically go up to 400 MPa that allow pores down to 3.5 nm to be monitored.

The extensive amount of data acquired in the last years make this technique very valuable for comparison tests and for the reproducibility that gives, however pretty strong limitations apply.

There are a few drawbacks of this technique: the method does not measure the pore size itself but pore entry size, and therefore the size of the big pores with small entries is underestimated; the sample preparation (strong drying) and the high pressures applied are very likely to damage the structures of the sample; the technique is not very sensitive to the coarser porosity [7] and last but not least, there are considerable environmental issues related to the large amounts of liquid mercury employed for these measurements and its toxicity.

#### ***1.3.4.1.4 Scanning Electron Microscopy (SEM)***

This methodology, as opposed to the previous one, is a direct technique. The sample is scanned with a high energy beam of electrons and different signals are created: secondary electron (SE) from the surface of the sample and backscattered electrons (BSE) and characteristic x-rays from the bulk.

One of the main advantages of this technique is that it does not limit the analysis to the porosity. In fact it can give spatially resolved chemical composition via the backscattered electrons but also morphological surface information using the secondary electrons.

The pores (and the other phases) are determined via image analysis segmenting the greyscale image introducing some empirical threshold [37]. Other advantages are the fact that the pore shape can be detected and give information on pore distribution within the sample. The disadvantages are again the damage caused by the sample preparation and the fact that it requires skill and is time consuming. The sample must be dried, vacuumed and impregnated with a resin that fills the pores. After impregnation a careful polishing procedure is required to have good resolution. Additional limitations of SEM are the fact that giving a 2D section it does not allow determination of the connectivity of the pores and it has relatively limited a range of applicability (greater than  $\sim 500$  nm) [7,37].

#### ***1.3.4.1.5 Transmission Electron Microscopy (TEM and STEM)***

These techniques are again imaging techniques and are based on the transmission of electrons through a thin section of material. The difference between TEM and STEM is that in the first the electron beam is wider and fixed, in the second is narrower and scans the

surface of the sample achieving a much higher resolution. Due to the very short wavelength of the electrons (0.0025 to 0.002 nm) at the typical operating voltages of 200-300 kV[37] the diffraction is not a problem and the achievable resolution, according [37] goes down to  $0.5 \text{ \AA} = 0.05 \text{ nm}$ . This allows, for example, one to see the layered structure of the C-S-H.



Figure 1.11 Coherence domain in C-S-H, (from [38])

At the very high resolutions of these techniques the sample preparation is crucial and the thickness needs to be only a few nm. Although the strong conditioning may again affect the sample structure especially on the length scale due to drying shrinkage, the power of these techniques in giving information on the structure at the nanoscale is huge.

#### **1.3.4.1.6 Nuclear Magnetic Resonance**

Due to the great relevance for the work presented in this thesis, all the techniques that are based on NMR will be presented in a separate main section.

### **1.4 NMR and porous media**

#### **1.4.1 Generic NMR basics**

This thesis will not deal with the basic theory of NMR as well as the main experimental techniques for which extensive literature is available. As suggested literature, Farrar and Becker *Pulse and Fourier Transform NMR* [39] is a really good basic “1<sup>st</sup> approach” textbook; on a higher profile but starting from the basics as well Callaghan book *Principles*

of *Nuclear Magnetic Resonance Microscopy* [40] is highly recommended. With more than 100 figures a good visual aid introduction is found in Blümich *Essential NMR for scientist and engineers* [41]. A good “working aid” on the theory, with numerous full representation of Quantum Mechanics matrix operator is Kimmich’s book *NMR Tomography Diffusometry Relaxometry* [42]. More “imaging focused” but with good general theory is also Blümich *NMR imaging of Materials* [43]. Other two strongly “quantum mechanics style” books are Abragam and Goldman *Nuclear magnetism: order and disorder* [44] and Slichter *Principles of Magnetic Resonance* [45]. A very practice focused book, discussing several, if not all, the experimental and hardware issues and how to practically perform experiments is the Fukushima Roeder *Experimental Pulse NMR: A Nuts and Bolts Approach* [46]. Also the *Principles of Nuclear Magnetic Resonance in One and Two Dimensions* [47] is a suggested high profile book.

The author assumes that the reader has followed a course at undergraduate level on NMR or is anyway already familiar with the fundamental principles of pulsed magnetic resonance and its basic parameters and measurements techniques such as  $P_{90x}$  (a 90 degree excitation pulse of phase x) and  $P_{180x}$ , (a 180 degree excitation pulse of phase x) FID (Free Induction Decay), CPMG (Carr Purcell Meiboom Gill pulse sequence), inversion recovery (pulse sequence to measure  $T_1$  relaxation time),  $T_1$  and  $T_2$  (spin-lattice and spin-spin relaxation times) vector model and Bloch equations (classical approximation approach to describe the evolution of the macroscopic magnetisation), BPP (Bloembergen Purcell and Pound) theory for the  $T_1$  and  $T_2$  origin from molecular motion, the dead time of the instrumentation (time during which is not possible to detect signal after an excitation pulse), recycle delay (time between successive scans), signal to noise ratio, number of scans, magnetic field gradients, pulse sequence, phase cycling. Applications of two pulse sequences less widely used will be presented later on in this thesis and therefore will be briefly presented in the next paragraphs.

What follows is a “pot-pourri” of more advanced/significant concepts, methods & theory that is directly applicable to the experimental work of this thesis.

#### 1.4.1.1 Quantum Mechanics

The spin dynamics cannot be described with the ordinary classic equation of motion, but some other tools are needed. The purpose of this paragraph is not to give a full description of the QM, but rather to introduce the strictly necessary tools to calculate an experimental NMR signal.

The main one to describe the state of the particle is the density matrix  $\rho$ , its representation is basis dependent and gives the population of each possible state.

The Hamiltonian is another fundamental tool that, as well, can be represented by a matrix  $H$  that fully describes the evolution of the density matrix. In practice, in the assumption of time independent interactions, the value of  $\rho(t)$  can be calculated from  $\rho(0)$  calculating the matrix

$$\rho(t) = e^{\frac{i}{\hbar} H t} \cdot \rho(0) \cdot e^{-\frac{i}{\hbar} H t}. \quad (1.6)$$

The mean value of the magnetisation  $M$  along  $x$  or  $y$  can be calculated using the angular momentum operators  $I_x$  and  $I_y$  respectively (that are represented by matrices as well) using the equation

$$M_{x,y} = \text{tr}(I_{x,y} \cdot \rho). \quad (1.7)$$

The effect of the rotation pulses during the NMR experiment on the density matrix (shown for a  $P_{90x}$ ) is:

$$\rho(P_{90}) = e^{\frac{i\pi}{2} I_x} \cdot \rho(0) \cdot e^{-\frac{i\pi}{2} I_x}. \quad (1.8)$$

### 1.4.1.2 Solid Echo

The Solid Echo (SE) pulse sequence is constituted by two 90 degree pulses at 90 degree out of phase:

$$P_{90x} - \tau - P_{90y} - t_{acq} \quad (1.9)$$

Where  $\tau$  the pulse-pulse spacing and  $t_{acq}$  the acquisition time variable. This pulse sequence allows the discrimination between the solid bound protons fraction (that refocus creating an echo at  $t = \tau$  after the second pulse) and the liquid fraction (that decays exponentially with characteristic relaxation time  $T_2^*$  from the first pulse).

It has been shown by Powles and Strange [48] that rigid spin 1/2 coupled by dipole-dipole interactions refocuses at the echo peak (for  $t = \tau$ ) within an estimated error that is proportional to the fourth power of  $\tau$ . This error can be regarded as a measure of the deviation of the echo decay from the true Bloch decay for the spins occurred just after the first pulse. This is the decay that occurs after the first pulse but is not detectable because it is obscured by the dead time of the spectrometer. This explains the  $\tau$  dependence of the echo amplitude and is expression of the incoherent part of the spin-spin interactions. Extrapolation

can be used to estimate the initial signal, of course introducing additional errors. A more detailed explanation of this process will be given when applied on experimental data later on.

### 1.4.1.3 Double Quantum Filtered (DQF)

DQF is a pulse sequence that allows filtering out of signals due to single quantum coherences (that represents the total magnetisation precession) and detects higher coherences not readily detectable.

In general, multiple quantum coherences cannot be excited in the limit of fast isotopic motion [43]. This can be useful to detect molecular order in materials by probing residual anisotropic interactions that are not completely averaged to zero by molecular motion. Furthermore, due to the strong dependence of the couplings with the distance, DQF NMR is used to probe internuclear distances. It has been employed to detect water in biological tissues such as tendons [49], but also to detect anisotropies in polymers and other materials [43].

It is constituted basically by three 90 degree pulses. A 180 degree pulse between the first and the second 90 degree pulses is introduced to refocus the chemical shifts without affecting the couplings.

$$P_{90} - \frac{\tau_c}{2} - P_{180} - \frac{\tau_c}{2} - P_{90} - \tau_E - P_{90} - t_{acq} \quad (1.10)$$

In equation (1.10)  $\tau_c$  is the creation time for higher coherences; the following 90 degree pulses are used to transform these coherences to single quantum (and therefore detectable). The  $P_{180}$  refocuses the chemical shift and the phase cycling is fundamental to suppress ordinary single quantum coherences.  $\tau_e$  is the evolution time and will be kept as short as practically possible.

## 1.4.2 Techniques and theory on porous media

Several NMR techniques have been applied on porous media to measure different physical parameters, in the next paragraphs there is an overview of the more relevant ones.

### 1.4.2.1 $T_1$ and $T_2$ relaxometry and Volume to Surface ratio

$T_1$  and  $T_2$  relaxation times are strongly related to the proton dynamics. BPP theory [50] is probably the first and the more basic to be developed. It derives the relaxation times from the

spectral density functions of the motion of the spins in the neighbours of paramagnetic impurities and therefore in a strong internal magnetic field.

The suitability of NMR to study porous media is based on the fact that there is an increase of the relaxation rate of the liquid when introduced in the empty spaces of the material compared to when the liquid is in bulk. This must be then related to interaction at the solid liquid interface.

Although the specific origin of the enhanced relaxation can have a different nature, for many applications specific knowledge is not required, provided that some assumptions hold. These assumptions are that a short range surface interaction is present and that there is a fast exchange of molecules between the surface region and the bulk fraction of the liquid that allow averaging between the two environments.

In these limits the magnetization decays exponentially with a relaxation rate that is a weighted average between the surface and the bulk rates [51].

$$\frac{1}{T_{obs}} = \left(1 - \frac{\lambda s}{v}\right) \frac{1}{T_b} + \frac{\lambda s}{v} \frac{1}{T_s} \quad (1.11)$$

Where  $T_b$  and  $T_s$  refer are the bulk and surface relaxation times;  $s$  and  $v$  the surface and volume of the pore respectively and  $\lambda$  the thickness of the layer involved by the enhancement of relaxation rate. Equation (1.11) is valid for both  $T_1$  and  $T_2$  relaxations, although  $T_1$  and  $T_2$  may be different.

Equation (1.11) can be conveniently rewritten as [51]

$$T = \frac{v}{s\rho} \quad (1.12)$$

Where the relevant relaxation time  $T$  is related to the measured  $T_{obs}$  by the formula [51]

$$\frac{1}{T} = \frac{1}{T_{obs}} - \frac{1}{T_b} \quad (1.13)$$

(that can be also conveniently thought as a difference in relaxation rates) and the physical constant  $\rho$  called surface relaxation strength and defined as [51]

$$\rho = \lambda \left( \frac{1}{T_s} - \frac{1}{T_b} \right) \quad (1.14)$$

The great convenience in this representation is the fact that  $\rho$  is a constant of the liquid-volume system and does not depend on the pore size. In addition, because in most cases  $Tb \gg Ts$ , (and therefore  $T \approx T_{obs}$ ) the measured relaxation time is directly proportional to the surface over volume ratio of the pore.

$$T_{obs} \approx \frac{v}{s\rho} \quad (1.15)$$

If we are in the case of a distribution of non communicating pores of different sizes in the sample, a superposition principle held, and the observed magnetisation is the sum of the magnetisation decay of all the pores. Theoretically the total magnetisation could be separated in components and the amplitude of each component is an expression of the volume of porosity of that diameter. We will see that, although this approach is feasible, the resolution is strongly limited by the noise present in the experimental data.

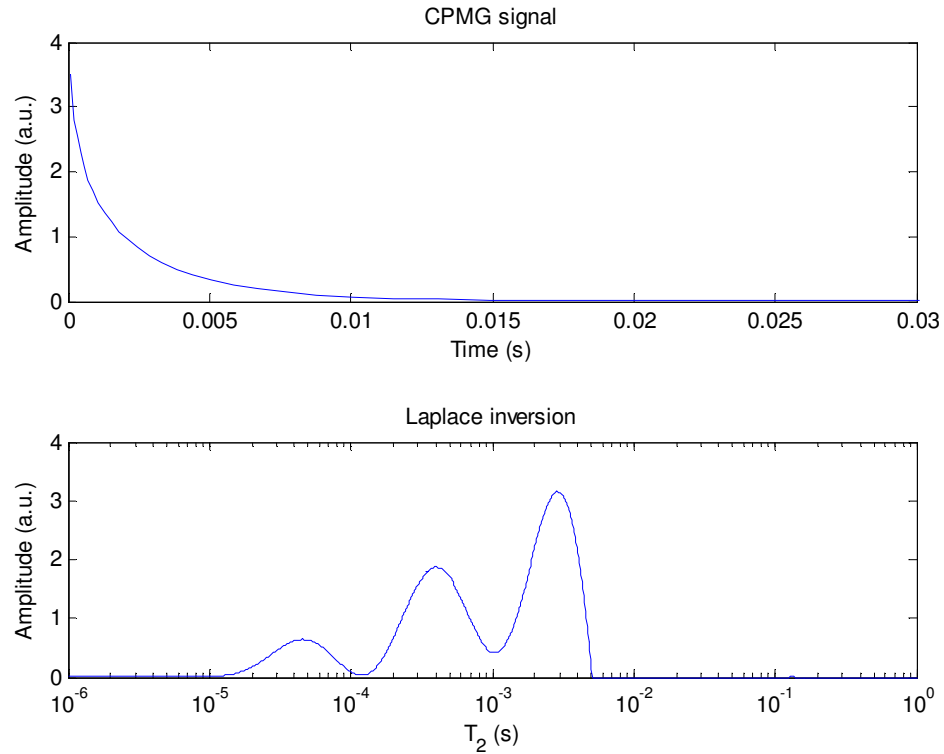


Figure 1.12 Theoretical procedure to determine the pore size distribution from  $T_2$  measurements. Top: the acquired signal from the CPMG pulse sequence Bottom: the  $T_2$  distribution following the Laplace inversion. Application of the (1.15) leads to the pore size distribution that has the same shape of the  $T_2$  distribution due to its linearity.

There are two main limitations in being able to successfully and reliably apply the equation (1.15) following the step shown in Figure 1.12 to determine the absolute pore size. The first is the lack in knowledge of the  $T_1$  and  $T_2$  relaxation times for the surface layer ( $T_s$  in the notation of the previous equations), because these parameters are not readily measurable. The second is that the Laplace inversion on noisy and/or incomplete data is very difficult. The name of this procedure is often a source of misunderstandings or sometime even misleading, especially when the Laplace Transform is compared to the more “popular” Fourier transform. The most widely used term in literature is probably Laplace Inversion. For consistency this name will be adopted also in this thesis, although is probably not the most adequate. However in paragraph 1.4.5.1 a more detailed discussion on the terminology will be presented.

One approach widely used by the oil industry to overcome the absolute pore size uncertainty is the one of calibrating the results via measurements of pore size distribution obtained with other technique on standard or synthetic samples [52].

Another approach is the one of drying the sample down to a monolayer of water keep measuring  $T_2$ . This has been attempted [53], but the difficulty of discriminating between the characteristics of the adsorbed or bound water left major doubts on the approach.

Another much more successful approach is the use of field cycling measurements. With this technique the spin-lattice relaxation time are measured as a function of the magnetic field strength (and therefore Larmor frequency), giving a much broader information compared to measurement at a single or even only few fixed frequencies [54]. The analysis of the Nuclear Magnetic Relaxation Dispersion (NMRD) is done in term of paramagnetic impurities on the surface of the pore and analysing in the details the motion of the protons in their neighbours [55,56]. However this approach is dependent on the model of relaxation and is dependent on a large set of parameters that is difficult to know entirely.

The main characteristic of these models is the presence of a 2D surface walk (or translational motion). The water molecules come from the bulk, where they undergo a 3D diffusion, approach the surface and “stick” on the surface for a certain length of time during which they undergo a 2D motion, and eventually go back to the bulk of the pore.

This motion is much more complex than the simple magnetisation sink model (where if a molecule touch the surface it always “dies” instantaneously) and it is the main strength in describing the low frequency NMRD dependence and its linearity in two parts.

Statistically the strong frequency dependence arises from the very different probability of returning to the origin for a 2D or 3D random walk.

Application on cement [55] and development of a model with 3 reservoirs (liquid solid and lattice) has been developed[54]. The main feature of this is the description of the dynamic of the water as characterised by two fundamental time parameters:  $\tau_m$  (surface diffusion correlation time) that represents the characteristic “hopping time” of the water molecule during its 2D random walk on the surface and  $\tau_s$  (surface residence time) that represents the average mean time that the water molecule walk on the surface before going back in the bulk reservoir.

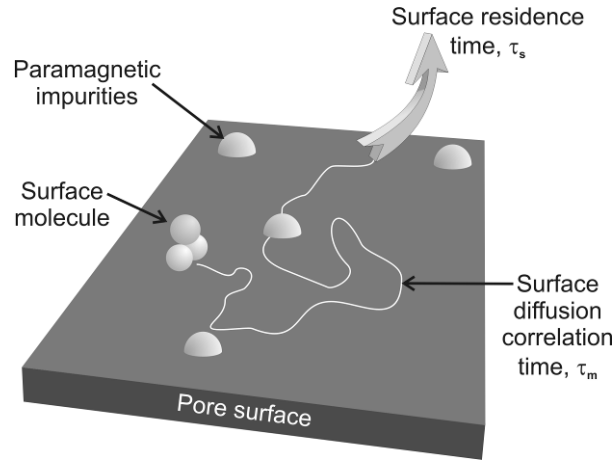


Figure 1.13 Schematic representation of the 2D diffusion of water molecules in the vicinity of paramagnetic impurities and relative characteristic times (From [57]).

NMRD results and the theoretical derived parameters for diffusion coefficients in the bulk and on the surface have been compared with MD simulation results for the same kind of environments showing good agreement, providing mutual support to the validity of both approaches [58].

Additional support to the validity of the theory described comes from the fact that the spectral density function of the motion can also be used to calculate the spin-spin relaxation rate  $T_2$  and predict that the ratio  $T_2/T_1 \neq 1$  (as observed experimentally) and that is a function of the Larmor frequency only [57]. This relationship has been verified over 3 orders of magnitude (2, 20 and 400 MHz) [59].

#### 1.4.2.2 $T_1$ - $T_2$ correlation and $T_2$ - $T_2$ exchange experiments

We have described how one dimensional relaxation measurements as the CPMG [60,61] can be useful in determining the  $T_2$  distribution function of liquids filling empty spaces in porous media and from this extract information about the pore size distribution. However this technique gives a snapshot of the porosity without giving any information on the

connectivity or less of the pores, we will see that 2D NMR relaxation analysis can help in determining also the connectivity of the pores.

The first evident advantage of the 2D NMR is an enhancement in resolution compared to the corresponding 1D experiments. For example, for a sample with broad distribution of  $T_1$  and  $T_2$ , a  $T_1$ - $T_2$  correlation spectra can better determine the  $T_1/T_2$  ratio of each specie compared to the separate  $T_1$  and  $T_2$  experiments [62]. Also, there may be cases where there are spin population that have the same  $T_1$  but different  $T_2$  (or the other way round), this may be easily detected with a 2D experiment but not with two 1D experiments.

2D relaxation NMR experiments have been proposed since the early 80s [63], however, the lack of a fast and reliable algorithm for the 2D Laplace inversion strongly limited the applications. Recently a Fast Laplace Inversion (FLI) software has become available [64-66] and the 2D relaxometry has become very popular.

Any two-dimensional experiment and its pulse sequence can, in general, be separated into two parts, each one of which described by a different Hamiltonian or process and parameterised with a time parameter.

The  $T_1$ - $T_2$  correlation experiment can be performed using an inversion recovery followed by a CPMG; following the notation in [57]

$$\left[ P_{180} - \alpha^i \tau_1 - P_{90} - \beta^0 \tau_2 - (P_{180} - \beta^j \tau_2 - (echo) - \beta^{j+1} \tau_2)_m - \tau_{RD} \right]_n \quad (1.16)$$

$\alpha^i \tau_1$  and  $(\beta^j + \beta^{j+1}) \tau_2$  are the inversion recovery and echo sequence  $180^\circ$ - $180^\circ$  pulse gap intervals, respectively. The index  $i$ , the power to which the constant is raised, is increased from 0 to  $n-1$  over the  $n$  repeats of the primary sequence enclosed in square brackets. Similarly, the index  $j$  is increased from 0 to  $m-1$  over the  $m$  repeats of the echo sequence part of the sequence in round brackets. The inversion recovery interval and the echo pulse gap are therefore both increased logarithmically so as to span a very wide range of time intervals. The advantages in using a logarithmically spaced time domain versus a linear one is the ability to sample a very wide range of relaxation times with a relative moderate number of echoes. This will be better explained later on in the section.

In this way the experiment yields a two-dimensional  $n$  by  $m$  data set encoding  $T_1$  in the first dimension and  $T_2$  in the second.

One scan has to be performed for each value of the first parameter, while one scan allows acquiring all the points in the second dimension of the dataset (one for each echo). The magnetisation is inverted along the  $-z$  axis by the first  $P_{180}$  pulse, and then relaxes with

characteristic relaxation time  $T_1$  for the time  $\alpha^i \tau_1$ . The  $P_{90}$  pulse brings the residual magnetisation back in the transverse plane where the train of  $P_{180}$  pulses constituting the CPMG allows measure of the  $T_2$  relaxation time.

The signal equation, in absence of exchange during the length time of the experiment is [57]

$$M(\tau_1, \tau_2) = \iint P(T_1, T_2) \left[ 1 - 2e^{\left(-\tau_1/T_1\right)} \right] e^{\left(-\tau_2/T_2\right)} dT_1 dT_2 \quad (1.17)$$

Where  $M$  is the magnetisation deviation from equilibrium and  $P(T_1, T_2)$  is the probability density of molecules with specific relaxation times  $T_1$  and  $T_2$ . To obtain the function  $P$  from the measured data  $M$  a 2D Laplace inversion is needed (see Paragraph 1.4.5.1 for more discussion)

In analogy with the  $T_1$ - $T_2$  experiment also a  $T_2$ - $T_2$  experiment can be performed. The first to propose such an experiment was Lee in [67]. Using the notation in (1.16), the pulse sequence for this experiment is

$$\begin{aligned} &P_{90} - (\beta^i \tau_{echo} - P_{180} - \beta^i \tau_{echo} - echo -)_m - P_{90} - \tau_{delay} - \\ &P_{-90} - (\beta^j \tau_{echo} - P_{180} - \beta^j \tau_{echo} - echo -)_n - \tau_{RD} \end{aligned} \quad (1.18)$$

This experiment consists of three time intervals:  $t_1$ ,  $t_2$ , and  $t_3$ .

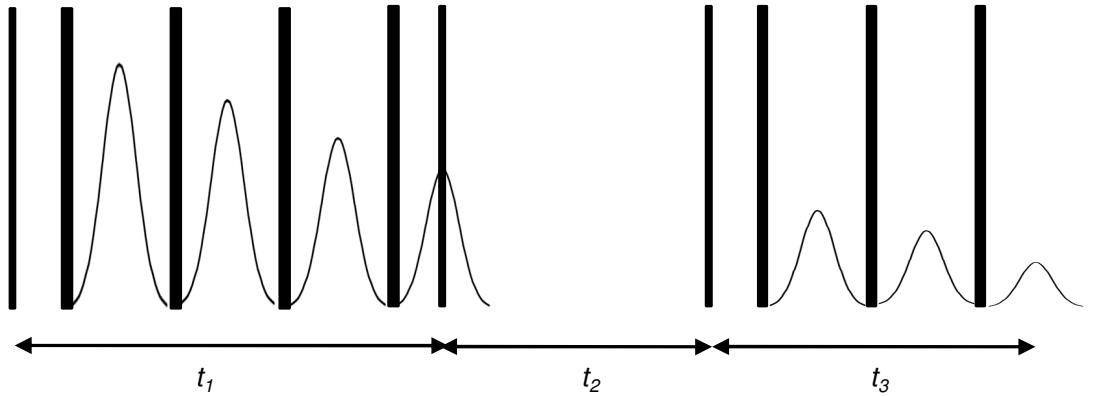


Figure 1.14 Timing of the  $T_2$ - $T_2$  pulse sequence. In this schematic case the echo spacing is linear.

During the first interval a CPMG pulse train consisting of  $m$  inversion pulses and echoes is applied. In the implementation presented in [68], the inversion pulse gap increases throughout the sequence according to a geometric sequence ( $2\beta^i \tau_{echo}, i = 0, 1, \dots, m-1$  and  $\beta = \text{constant}$ ). At the end of the sequence, at the time of the  $m_{th}$  echo, a  $90^\circ$  pulse is applied

so as to store the magnetization along the  $z$  axis. Phase cycling is used between averages so as to store along both  $+/-z$ . The magnetization is stored for the period  $\tau_{delay} = t_2$ . Thereafter, the magnetization is recovered with a further  $90^\circ$  pulse. During the third period  $t_3$ , a second CPMG sequence of  $n$  inversion pulses similarly spaced in geometric progression is applied and the series of echo intensities is recorded. The experiment is repeated for  $m = 1, 2, \dots, n$  with repetition delay  $\tau_{RD}$ . In this manner, a square two-dimensional relaxation data set is acquired.

Because during the exchange time the magnetisation relaxes with  $T_1$ , this time is limited to few units of  $T_1$ .

If the spins do not change their  $T_2$  relaxation time between the first and second CPMG the magnetisation as a function of  $\tau_1$  and  $\tau_2$  is described by the equation

$$M(\tau_1, \tau_2) = \iint P(T_1, T_2) e^{\left(-\tau_1/T_1\right)} e^{\left(-\tau_2/T_2\right)} dT_1 dT_2 \quad (1.19)$$

and the dataset is exactly symmetric. In this case the 2D experiment does not give any additional information compared with the 1D CPMG experiment described in paragraph 1.4.2.1.

If the two reservoirs are interconnected and exchange occurs during the lengthtime of the experiment, the signal observed in both  $T_1$ - $T_2$  and  $T_2$ - $T_2$  is much more complex (and interesting).

The basic equation governing the process of exchange during relaxation is [69]

$$\begin{bmatrix} dM_a/dt \\ dM_b/dt \end{bmatrix} = \begin{bmatrix} -R_{a1} - k_{a1} & k_{b1} \\ k_{a1} & -R_{b1} - k_{b1} \end{bmatrix} \begin{bmatrix} M_a - M_a^0 \\ M_b - M_b^0 \end{bmatrix} \quad (1.20)$$

where  $M_a^0$  and  $M_b^0$  are the two initial magnetization,  $R_{a1}$  and  $R_{b1}$  the two relaxation rates and  $k_{a1}$  and  $k_{b1}$  the exchange rates.

This is exactly the same phenomena occurring between the surface layer and the bulk of a pore described in paragraph 1.4.2.1 however, in that case, considering the diffusion within the pore, the exchange is almost always fast. If the exchange considered is between pores of different sizes in porous media, and therefore possibly different regions of the sample, the fast exchange approximation may not hold any more. Also in this intermediate exchange rate condition the signal will be the sum of the signal of the two magnetisation reservoirs, but they will influence each other.

The solutions of the system of equations (1.20) are derived from the work of McConnell [69] and given in full in [57] for  $T_1$ - $T_2$  and in [68] for  $T_2$ - $T_2$ . To describe the magnetisation of the  $T_1$ - $T_2$  experiment it must be noticed that there are two different stages in this experiment during which different phenomena occur. During the inversion time only  $T_1$  relaxation occurs due to the absence of transverse magnetisation. In the second part, during the CPMG, the magnetisation relaxes due to  $T_2$ . The experiment has to be then treated in step applying the (1.20) twice using the final magnetisation of the first step as the starting condition for the second one. This has been done and shown into details in [57], here the magnetisation following the  $T_1$ - $T_2$  experiment has been simulated for several values of relaxation and cross coupling parameters and Laplace inverted. The general result is a relaxation spectrum showing four peaks, two diagonal ones and two off diagonals; under condition of slow exchange just two peaks are observed, while in condition of very rapid exchange only a single peak is observed at a weighted average location; detailed discussion of all the three regimes can be found in [70]. This fact will be analysed in more detail with reference to the Figure 1.15 at Page 32.

The simulation for the  $T_1$ - $T_2$  experiment has been compared with experimental results showing a series of discrete features lying on the line  $T_1 = 4T_2$ , this is interpreted as water in different pore sizes and is consistent with the surface relaxation theory of Korb [71]. McDonald et al. [57] found also an off diagonal peak in a  $T_1$ - $T_2$  relaxation spectra, this could have been interpreted as protons in a solid like environment, because characterised by  $T_1 \gg T_2$ , but also due to chemical exchange. Although the value of  $T_2$  measured much longer than that reported for bound hydrogen it may suggest that the latter explanation is the more probable,  $T_1$ - $T_2$  experiment is not able to fully discriminate between the two. Moreover, the absence of one of the off diagonal peaks on the experimental results is explained by the fact that the Laplace inversion used assumes the positivity of the peaks. This is not true in the  $T_1$ - $T_2$  experiment, where one of the off diagonal peaks is actually negative.

Hence, there are advantages in using the  $T_2$ - $T_2$  instead the  $T_1$ - $T_2$ ; one is that in the  $T_2$ - $T_2$  the water exchange is unambiguous (the spin-spin exchange hypothesis is unlikely being a phenomenon much faster than the exchange measured), another is that having both peaks positive is not affected by the assumption embedded in the Laplace inversion algorithm.

For the purposes of calculating the result of the  $T_2$ - $T_2$  experiment (1.20) has to be applied three times instead, one for each interval of the experiment. This long calculation has been fully performed in a similar way to the one for  $T_1$ - $T_2$  in [57] in [68]. In that publication the data are simulated in the same way and the result after 2D Laplace inversion is a plot having again generally 4 peaks, two on the diagonal and two outside. Again, the simulated data for

two discrete magnetisation reservoirs with different relaxation times has a relaxation spectrum that collapses in a single peak on the diagonal at an average value. To be noticed that the theory in the event of  $T_1 = T_2$  predict off diagonal peaks intensity equal to zero whatever the exchange rate is, however, in cement, as in other porous media, has been observed values of  $T_1 \neq T_2$  and therefore the experiment is applicable.

Additional advantage of the  $T_2$ - $T_2$  experiment compared with the  $T_1$ - $T_2$  one is that it allows a quantitative estimation of the exchange rate via the third parameter of the experiment that is the exchange time  $\tau_{exch}$ .

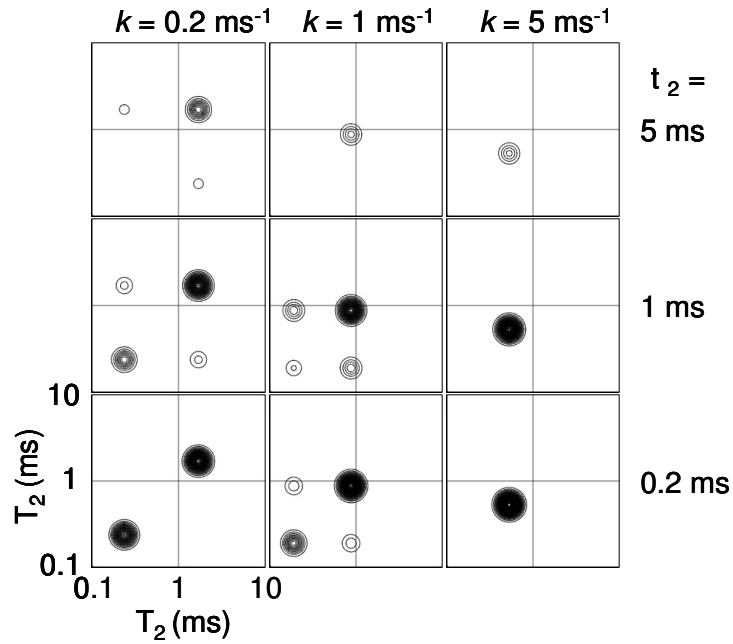


Figure 1.15 Calculated 2D  $T_2$ - $T_2$  spectra for (left to right) slow, medium, and fast exchange rates and (bottom to top) short, intermediate, and long storage times (from [68]).

In Figure 1.15 the effect of varying the exchange time  $\tau_{exch}$  is shown on simulated data. The cross peaks are visible only when the exchange time is comparable with the reciprocal of the exchange rate between the two pores. Another fact that must be taken into account is that the different population are affected by the increasing storage time (looking from bottom to top in Figure 1.15) in different ways, in particular, the peaks representing the populations with shorter  $T_2$  (and therefore shorter  $T_1$  due to the observed relationship in cement  $T_1 = 4T_2$  valid at the frequency of the work presented) become weaker quicker than the one representing populations with longer  $T_2$  and  $T_1$ . This causes the quantitative estimation of the population to be much more difficult. To have a quantitative estimation of the exchange time between different pores, the experiment has to be performed for many different exchange times and then the amplitude of the peaks fitted to an exponential function. This allows the extraction

of some effective exchange rates that are  $T_1$  weighted. This procedure is described and demonstrated on sandstone by Washburn and Callaghan [72]. Mitchell et al. [73] with experiments on synthetic samples examined and discussed also the reliability of this technique and the limitations/uncertainty involved that are dependent on the relaxation times present in the sample. The values of  $T_2$  considered in both papers are typically much longer than the one observed in cement, and therefore the application on this material is much more difficult as found by Monteilhet et al. [68].

The CPMG in general and therefore also the one included in the 2D experiments just described can have several versions and modifications. A fundamental difference is the echo spacing. The very broad distribution of  $T_2$  values in porous media require a detection over several orders of magnitude, typically from few  $\mu$ s to several ms or even up to the second. To achieve coverage over a such broad range of  $T_2$  values there are two different approaches; the first is to keep the echo time constantly short (to detect the short components) and have a huge number of echoes, the other approach is to logarithmically space the echoes, in this way there are many more echoes in the first quickly variable part of the decay and fewer in the last slowly varying part; both solutions, as always present advantages and disadvantages that are summarised in Table 1.2.

		ADVANTAGES	DISADVANTAGES
LOG SPACING		<ul style="list-style-type: none"> <li>Is able to cover a broad range of <math>T_2</math> values with low power required.</li> </ul>	<ul style="list-style-type: none"> <li>Diffusion affects different populations in different ways.</li> <li>Is more difficult to predict the coherences, therefore requires accurate phase cycling.</li> </ul>
		<ul style="list-style-type: none"> <li>Less affected by the influences of different diamagnetic susceptibility within the sample.</li> <li>Diffusion effects more defined and smaller.</li> </ul>	<ul style="list-style-type: none"> <li>Requires lots of pulses and therefore lot of power is driven in the sample, causing sample heating and possibly also instrumentation damage.</li> </ul>

Table 1.2 Advantages and disadvantages of the two alternatives to sample broad distributions of  $T_2$  values.

In addition, typically only the even echoes are used, because the phase evolution associated with the velocity (first moment of the internal gradients) compensates as well as the zero moment relating to the position. Also pulse imperfections are cancelled if alternate phases

are used ( $P_{90x}-P_{180y}-P_{180-y}-P_{180y}-\dots$ ). As a consequence every odd echo is attenuated by molecular diffusion and flow and every even echo is not [43].

### 1.4.2.3 PFG measurements for flow and diffusion and q space

Pulse Field Gradient experiments are particularly suitable to measure the effects of diffusion and flow.

Translational motion plays a key role in any NMR experiment. In spectroscopy it is detrimental for the resolution; this is because random molecular displacement in a magnetic field imparts a spread to the spin transverse magnetisation. While this effect, when unwanted, may degrade NMR images or introduce additional experimental difficulties, if carefully employed may be useful in measuring the motion itself. The main tool in this is the spin echo amplitude. The formation of an echo arises when the precessional phase shifts associated with the position of a molecule in a magnetic field are cancelled by reversing the phase evolution in some manner. Any movement of a molecule over this time-scale result in residual phase offset and the effect on the echo signal can be used to deduce the form of the motion [40].

The typical experiment for this kind of measurement is the Pulsed Gradient Spin Echo (PGSE). There are different pulse sequences to achieve this, however all are based on the same principle.

After a RF pulse used to create transverse magnetisation, a magnetic field gradient is applied to the spin ensemble. During the presence of the gradient, the phase of the spins will evolve at a rate proportional to the strength of the gradient field at the spin position. At the end of the gradient pulse, therefore, the total phase achieved will be proportional to the gradient field strength as well. After a time  $\tau$  another gradient pulse of opposite effective strength (this can be achieved either inverting the amplitude of the gradient or inserting a 180 pulse in between two gradient pulses of same amplitude) is applied. The spin that did not move in between the two gradient pulses will have achieved a total phase equal to 0, the one that did move a net phase different from 0 and proportional to the distance travelled. Flow is a coherent translation of all the particles of an ensemble, this would reflect on the NMR signal as a net, equal, phase shift on all the spins, while diffusion, being a random movement, will give a random phase shift to the different spins. The combined effect of diffusion and flow is therefore a phase shift due to the flow and an attenuation due to diffusion [40].

The equation for the relative amplitude of the echo, defined as the amplitude at gradient strength  $g$  compared to the one without gradient is:

$$E(\mathbf{g}) = \exp\left(i\gamma\delta\mathbf{g} \cdot \mathbf{v}\Delta - \gamma^2\delta^2 g^2 D\left(\Delta - \frac{\delta}{3}\right)\right) \quad (1.21)$$

where  $\gamma$  is the gyromagnetic ratio of the nucleus,  $\delta$  the gradient pulse duration,  $\Delta$  the gradient pulse separation measured from the beginning of the first pulse to the beginning of the second one,  $\mathbf{g}$  the gradient strength,  $D$  the diffusion coefficient and  $\mathbf{v}$  the flow velocity [40].

The pulse sequence just described can be modified with gradient pulses that fulfil the narrow pulse approximation, meaning that the molecular motion can be neglected during the length of the pulse. In this condition can be shown [40] that the net phase shift for each spin at the echo is proportional to the dynamic displacement.

In analogy with the  $\mathbf{k}$  space used in NMR imaging, is possible to define a  $\mathbf{q}$  space where

$$\mathbf{q} = \frac{1}{2\pi} \gamma\delta\mathbf{g} \quad (1.22)$$

In this new variable there is a simple Fourier relationship between the echo amplitude in the  $\mathbf{q}$  space and the average propagator in the  $\mathbf{R}, \Delta$  space, where the propagator is the displacement probability distribution. Acquisition of the signal in the  $\mathbf{q}$  space, then, allows imaging the average propagator.

In the case of unrestricted self diffusion the propagator is a Gaussian function, and, the echo amplitude is its Fourier transform.

#### 1.4.2.4 Restricted diffusometry

Because the PSGE image detects the average propagator care should be taken when the diffusion taken into account is restricted, in fact  $\overline{P(\mathbf{r}' - \mathbf{r})}$  will be equivalent to  $P(\mathbf{r}|\mathbf{r}')$  only when the displacement is independent of the starting position, that is of course not true in the case of molecules moving in the vicinity of boundaries.

When the diffusion occurs in a porous media (or in any other restricted environment), the water cannot move further away than the pore walls making the expression more complicated but also full of useful information. The calculation of the solution for  $P(\mathbf{r}|\mathbf{r}')$  is a very demanding task and has been solved exactly for only few geometries as the rectangular box of width  $a$ . Is not surprising that in the *short time scale limit* ( $\Delta \ll a^2/2D$ ) the behaviour is the same as the one for unrestricted diffusion simply because the water had no time to experience the surface of the pore, for the *long time scale limit* ( $\Delta \gg a^2/2D$ ) and with the

additional hypothesis of weak gradient ( $2\pi qa \ll 1$  or  $g \ll 1/\gamma\delta a$ ) the apparent diffusion coefficient decreases inversely to the inter gradient pulses spacing and the coefficient is directly related to the size of the restricting structure.

In case of communicating pores the expression become even more complex, however, the same principle can be applied.

A simple but quite instructive solution is the one of the connected pores in a regular lattice.

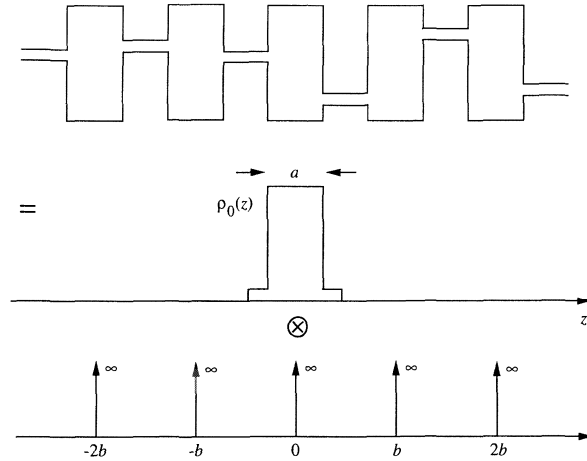


Figure 1.16 Schematic representation of communicating pores in a regular lattice (from [40])

When the echo amplitude is plotted against  $q$  (it should be noticed that it has the dimension of the reciprocal of a distance) the plot shows peaks at values multiples of the reciprocal of the boxes distance modulated by a form factor that is pore shape dependent. This clearly shows the analogy between diffraction and  $q$  space NMR.

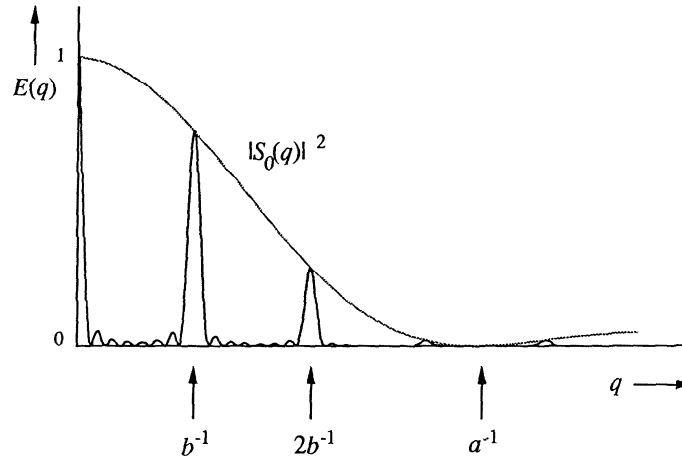


Figure 1.17 Echo amplitude versus  $q$  for the pore distribution in Figure 1.16 (from [40]) where the width  $a$  is approximately  $1/4$  the pore spacing  $b$  and  $N$  is taken as 8. The behaviour is identical to that of an  $N$ -slit diffraction grating where  $a$  is the slit width and  $b$  the slit spacing. Note the modulation of the diffraction peaks by the “form factor”,  $|S_0(q)|^2$ .

#### 1.4.2.5 Diffusion in internal gradients

When a heterogeneous saturated porous sample is placed in a magnetic field, a spatially variable field appears due to the different magnetic susceptibility of the material itself and the filling medium. These internal gradients of course affect the NMR signal and hence can give information on the pore structure. The internal gradients and their effect can be computed [74] and simulated to be later compared with the experimental result.

DDIF stands for Decay due to Diffusion in the Internal Field. It is the simplest technique of this kind and detects the diffusion of the fluid molecules in the internal field of the pore [62,75] and uses that information to derive the pore sizes.

The principle is based on the fact that, because the source of gradient is the interface on the pore surface, the internal gradient is generally very different (opposite in direction) on the opposite sides of the pore. In fact this has been demonstrated showing that the correlation function of the field is closely related to the pore size [76]. Experimentally, the magnetisation is rotated in the transverse plane, then left precessing due to the internal magnetic field for a period  $t_e$ , then it is rotated back to the longitudinal to allow diffusion to occur. After a diffusion time  $T_d$ , the magnetisation is again rotated in the transverse plane to detect an echo. If the time  $T_d$  is the characteristic time required for the spin to move from one side to the other of the pore, the two precessions in the first and the second  $t_e$  periods cancel out giving rise to a peak in the amplitude vs  $T_d$  plot. The characteristic pore size can be calculated from the decay rate  $\tau$  using  $d = \sqrt{D\tau}$  [62]. Because  $T_d$  can be varied from

microseconds to a few  $T_1$  (because during the  $T_d$  period the magnetisation is longitudinal decays with  $T_1$  and not  $T_2$ ) this technique can be applied (using water) to measure pores of submicrons to several hundreds of microns [62].

The results of this technique, especially in the study of rocks are very suitable to be overlaid to mercury porosimetry data to identify pore's bodies and throats.

#### 1.4.2.6 Imaging

NMR imaging itself is a technique with pretty limited resolution; as a “rule of thumb” it is usually compared to the human eye resolution [77]. This makes this technique absolutely unsuitable to detect water within the nanometric structure of hydrated phases, however it can be of great utility in measuring macroscopic water ingress or cracks in the material. Examples of such applications using STRAFI imaging are presented in [78]; in this thesis an application of such technique in its “*in-situ*” version on a construction site will be presented as well. Now this technique is often called “*one-sided*” NMR if a “portable system” is employed.

#### 1.4.2.7 NMR Cryoporometry

The NMR cryoporometry is partly based on the same principle of the LTC presented in paragraph 1.3.4.1.2, which is that the lower the temperature the water freezes at, the greater the confinement is. In this case, however, the way the freezing of the water is detected is different; instead of using the heat flux due to the change of state from liquid to solid (or vice versa) the detection of the amount of water in the liquid state is measured via NMR. The separation between the solid and liquid component is immediate due to the huge difference in relaxation time for protons in the two states [79]. A good detailed review on this technique can be also found in [80] and a comparison with relaxation analysis data in [81].

An interesting alternative of this technique is the one proposed by [82], which is based on a solution of salt containing Na that crystallise bounding crystallisation water, due to the NMR echo time used in the experiments, only the Na nuclei in the solution are measured; no signal is observed from the crystals. For the same reason, the H nuclei of crystal water are not observed. From the NMR intensity profiles the solution concentration can be determined. The relaxation measurements give information on the pore size.

#### 1.4.3 Mobile and single side NMR

As we have seen, NMR is a versatile, non invasive technique to measure water content and proton mobility. These kinds of measurements are of great interest in several fields including

material science and quality control in industrial applications; however, the size and weight of “traditional” magnets put a main limitation on the size and location of the sample. To overcome this limitation the completely new field of the mobile NMR magnet is being developed. This is a very interesting niche section of the much wider NMR techniques and application. The challenge (and interest) of this field is the fact there is never an easy and unique answer to the problem. The instrumentation is still developing quickly and most of the magnets are a “one-off”. All the designs of this kind of instrument are a fine balance between different aspects that have to be taken into account. In fact, most of the time the magnets are built taking into careful account the compromises that rule this field and each application.

There are closed magnets and open ones. This is the first choice to be made while developing a portable device; of course there are advantages and disadvantages of both. The closed magnets have higher strength, higher homogeneity and have been recently employed also for spectroscopy purposes [83]. Portable instruments that use a really homogeneous “free” field are the one using the Earth magnetic field; examples of this are the commercial Terranova made by Magritek [84] where the coil is around the sample, or the detection of ground water with a 100 m in diameter coil placed on the surface of the earth [85]; this is probably an extreme setup, where the polarising magnetic field is, of course, highly homogeneous but the RF is not.

The one-sided or open-access magnet, allows the measurement of samples that are much bigger than the magnet itself. Focusing more on this probably more advanced, versatile and diffused kind of portable magnets, the following is a short review of the most successful applications that are being developed.

The oil industry is probably the one that started in the evolution of the one side approach. Los Alamos NMR Well Logging Project, started in the late '70 in concomitance with the first test done by Schlumberger has been a really successful project that gave a impressive start at this subject [86-89]. Now Schlumberger regularly use NMR as a tool to characterise the rocks around the bore hole. This is a kind of “bulky” mobile NMR tools, in fact the Schlumberger one is 10 meters long, 544 kg in weight and 12 cm in diameter to be able to fit in the bore hole. It is designed to work at a maximum pressure of 137 MPa and at a maximum temperature of 150 °C [90]. With exactly the same idea but at the opposite extreme in sizes, a miniature self-contained intravascular magnetic resonance (IVMI) probe for clinical applications is being developed in Israel. It is designed to be used as an endoscope inside the blood vessel, for this reason it is miniaturised down to 1.73 mm in diameter [91].

These were the most interesting applications of inside-out magnets, the other, probably more varied, field is the one of unilateral magnets. These divide broadly speaking into two categories: the one that uses a high gradient to achieve spatial resolution in the depth directions and the one that tries instead to produce a volume where the magnetic field is as homogeneous as possible; this volume is commonly referred to as a “sweet spot”.

Example of the first category are the “first generation” NMR Mouse developed by Aachen group [92,93], the *constant gradient unilateral magnet for near-surface MRI profiling* developed at the University of New Brunswick, Fredericton, New Brunswick, Canada [94,95] and the Surface GARField made by Laplacian and under development at the University of Surrey, Guildford, UK whose improvements will be further discussed in this thesis [96].

Examples of instruments with more uniform fields are the “second generation” NMR Mouse (with added shimming) [97,98], the NMR MOLE [99] and the one developed in Albuquerque by Fukushima group [100-102]

#### **1.4.4 Applications**

NMR in its different forms has been widely applied to porous media, and the oil industry has definitely been the one that boosted the development of these techniques[62,86,87,90,103-105].

The power of NMR is its flexibility and all the different variants, spans from the spectroscopy that is capable of probing inter-atomic distances in molecules to the imaging that is capable of getting sub millimetric resolution information of structures of the order of the meter as in a whole body MRI medical scanner to the oil well logging that is able to map relaxation times down a bore hole kilometres deep in the ground.

One of the main limitations in exploiting the work done by the oil industry on reservoir rocks to cement is due to the fact that oil reservoirs are necessarily much more porous than cement. In fact, there would be not much interest in extracting oil from a field with rocks as compact as cement or concrete. This much lower porosity leads to a much smaller signal per unit of volume of sample and to a much shorter relaxation times; the signal therefore “dies” much quicker and the experimental and hardware issues become more and more relevant since there is less time to perform the experiment.

### 1.4.5 Problems

#### 1.4.5.1 Laplace inversion

The confusion on the nomenclature of this operation has been mentioned briefly before. Here an attempt to clarify the details of this confusion will be presented.

Mathematically, the Laplace transform is defined as:

$$F(s) = \int_0^{\infty} e^{-st} f(t) dt \quad (1.23)$$

where  $s$  is complex with real and imaginary parts. It transforms the function  $f$  into another one  $F$ . Because the experimental data are always finite in time and digitised, when the transform is applied in practice the integral becomes a summation.

If  $\text{Re}(s)$  is zero, the (1.23) becomes the Fourier transform. It maps time domain data into frequency domain data and gives the Fourier coefficients that can be interpreted as the amplitudes of the different frequency components contained in the original signal. Due to the orthogonality of sines and cosines harmonics over a finite interval the integral is possible also on experimental data and the result is stable also in the presence of noise. The inverse of the Fourier transform is a simple summation of the components and, due to the elegant symmetry of the problem, differs only by a sign.

If  $\text{Im}(s)$  is zero, the (1.23) is an expression of the problem of finding the exponential components contained in the original time domain signal. Because the exponentials are not orthogonal (and even not integrable over the limits) this is not properly speaking a transform with a single solution. Instead this is a problem with several solutions mathematically all equally valid and therefore is what is commonly called an inverse or ill-posed problem [106] and therefore Exponential, Distributed Exponential or Multi-Exponential inversion would be probably the most suitable name [107,108]. Additional constraints arising from the evaluation of the physical characteristics of the specific problem must be introduced to obtain a single solution. The inverse procedure of obtaining the time domain data from the exponential components is (as for the inverse Fourier transform) again a simple summation and therefore stable (and trivial).

The one that is sometime called Inverse Laplace Transform (ILT) in literature [65,67,72] is actually the solution of the exponential inversion problem. This name has been used as well

[107,109]. Anyway, due to very wide application of the term “Laplace” for this operation, for compatibility, the term Laplace Inversion (LI) will be adopted also in this thesis.

Mathematically, can be formalised writing:

$$M(\tau) = \int F(T) e^{-\frac{\tau}{T}} dT \quad (1.24)$$

The objective is to find the function  $F(T)$  knowing the  $M(\tau)$ .

The (1.24) can be expanded in 2 dimensions to describe the magnetisation of the  $T_1$ - $T_2$  and  $T_2$ - $T_2$  experiments previously described as:

$$M(\tau_1, \tau_2) = \iint \left( 1 - 2e^{-\frac{\tau_1}{T_1}} \right) e^{-\frac{\tau_2}{T_2}} F(T_1, T_2) dT_1 dT_2 \quad (1.25)$$

for the first and

$$M(\tau_1, \tau_2) = \iint e^{-\frac{\tau_1}{T_2}} e^{-\frac{\tau_2}{T_2}} F(T_2', T_2'') dT_2' dT_2'' \quad (1.26)$$

for the second. The (1.25) and (1.26) are two examples with the kernels for the two specific experiments mentioned, however, the solution is much more general and different kernels  $K$  for different experimental situation can be defined obtaining a generalised version of the two equation above as

$$M = KF \quad (1.27)$$

The typical workaround to the instability and not unique solution of the problem is to constrain the solution using some a priori information on the function itself. The simplest condition is the non negativity, dictated by the physical meaning of the required function  $F$  in equation (1.25) representing the probability density of molecules with relaxation times  $T_1$  and  $T_2$ .

Another approach (usually used in conjunction) is to insert in the treatment of the data a regularisation parameter  $\alpha$ ; this parameter is a measure of the desired smoothness of  $F$  and makes the inversion less ill conditioned [65,66]. The regularisation parameter allow in practice to move from a high resolution (but unstable) solution to a broad, low resolution solution but highly stable approximation. The issue can be thought of in terms of information

contained in the experimental dataset. If this amount of information is not enough to define the distribution function for a determined resolution, the result will be unstable and dependent on the noise more than on the actual data.

Detailed discussion on the stability of the inversion and on how to find the optimum  $\alpha$  value is found in [64-66]; has been found that in first approximation the resolution of the LI is approximately inverse proportional to the signal to noise ratio of the experimental dataset.

#### **1.4.5.2 Surface relaxivity and paramagnetic impurities**

As mentioned in paragraph 1.4.2.1, the power of the equation (1.12) is due to the fact that the parameter  $\rho$  depends only on the characteristic of the pore surface. This is of great help in determining the relative pore size under the assumption of having surfaces of the same characteristic for all the pores in terms of surface relaxation mechanism and strength. One of the most (if not *the* most) important parameter influencing the surface relaxation is the density of paramagnetic impurities on the surface of the pore. This can be easily understood because the higher the density, the higher the encounter probability will be and therefore the higher the relaxivity. This assumption can be totally justified in several materials. In cement it is a strong but necessary assumption. Due to the variability of the natural resources, the quantity of paramagnetic impurities (mainly but not only  $\text{Fe}^{3+}$ ) may vary widely from kind to kind of cement and where the fact that the material is constituted by different phases may cause the distribution to be not homogeneous within the same sample.

#### **1.4.6 Works done on cement/review**

Some of the work done with NMR applied to cement has been mentioned previously during the introduction of the different techniques. The scope of this section is to give an historic/logic overview of the work, in particular, of the one that preceded (and led to) the work that will be presented in this thesis.

Good literature [110] is available on the applications of chemically resolved NMR spectroscopy used to study cement chemistry, hydration kinetics, and C-S-H gel. However, in this thesis, this type of NMR will not be discussed. This section is a review on  $^1\text{H}$  relaxometry diffusometry, cryoporometry and imaging.

The fact that the relaxation times of fluids in confined spaces is an expression of the size of the confining structure has been known since 1979, with the work of Brownstein and Tarr [111].

Later experiments and theory developments [51] have found that the observed relaxation time was a weighted average between the fast relaxing layer of water on the surface of the pore and the slow relaxing bulk water that was experiencing unrestricted self diffusion. This behaviour is independent of the physical reasons of the surface enhancement of the relaxation rate. This allows the pore size distribution (or better the relative size distribution) to be derived from 1D relaxation time measurement and decomposition in multimodal exponential decays via Laplace inversion.

A 3 phases model for water in cement based on different relaxation times have been proposed in [112], other authors proposed 5 [113] or even 7 compartments [114]

Korb, using field cycling NMR, developed an elegant theory that addresses the reason of the surface enhancement, which is now widely accepted that in cement is due to a 2D random walk of the water molecules in the vicinity of paramagnetic impurities on the surface of the pore [54,58,71,115]. This theory is able to well reproduce the experimental NMRD curve and predict the behaviour of the ratio between  $T_1$  and  $T_2$  as a function of only the Larmor frequency [59]. However, the calculation of the actual relaxivity of the surface layer requires the knowledge of several parameters, each one having its experimental error causing the absolute result to be highly undetermined.

The implementation of a reliable, fast and stable algorithm to perform the 2D Laplace inversion [64-66] allow a huge advance in 2D relaxation experiments that were proposed since the 80's [63] but were limited in the analysis of the results by the lack of suitable tools.

McDonald et al [57] observed in  $T_1$ - $T_2$  experiments on cement two peaks on the diagonal and one off diagonal peak. The spectra simulated with the addition of exchange during the length of time of the experiment show the same basic features but with two off diagonal peaks, and therefore it has been suggested that one of the off diagonal peaks could have been due to chemical exchange between two different pore sizes. For the other, the reason of its invisibility in the spectra has been discussed. Although the peak could have originated also from a population with different characteristic  $T_1/T_2$  ratio the absolute values of the relaxation times strengthen the first hypothesis of exchange.

The following  $T_2$ - $T_2$  [68] moved the understanding forward considerably, allowing the confirmation of detection of exchange and estimate its characteristic time. The  $T_2$ - $T_2$  spectra obtained by [68] is reported in Figure 1.18.

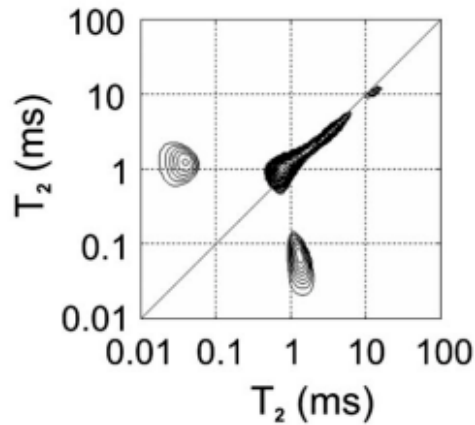


Figure 1.18 the  $T_2$ - $T_2$  relaxation plot as obtained by [68].

The best available calibration led to the estimation of the two pore sizes in circa  $1 \pm 0.3$  nm layered for the first and  $6 \pm 2$  nm layered or  $19 \pm 6$  nm spherical for the second; the exchange time is estimated in 5 ms. The hypothesis is that the two materials refer to inner and outer gel pores.

In the same work the meaning of this exchange time has been briefly discussed and interpreted. Because the particle size distribution of the original cement grain has been found to be strongly centred on a radius  $r = 7.5 \mu\text{m}$ , it has been considered that a typical length scale between inner and outer product was half the radius and therefore  $\sim 4 \mu\text{m}$  (Figure 1.19). From this length and time a diffusion coefficient can be calculated employing  $D = r^2/6t$  as a diffusion equation. The result found is  $5 \cdot 10^{-10} \text{ m}^2/\text{s}$  mentioning but not considering tortuosity issues.

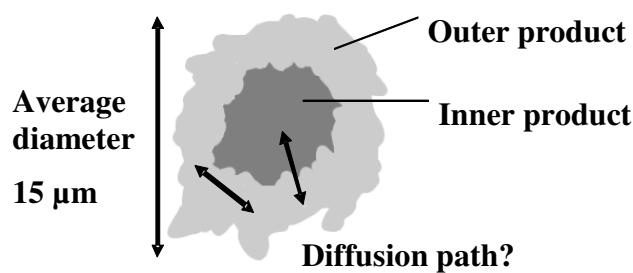


Figure 1.19 the exchange hypothesis presented in [68] between inner and outer C-S-H product.

This diffusion coefficient has been compared to the one obtained for water diffusing in the pore space above the internal pore surface of tobermorite by molecular dynamic simulations ( $6 \cdot 10^{-10} \text{ m}^2/\text{s}$ ) [116] and considered to be in good agreement. An additional observation

proposed it is the fact that the diffusion coefficient calculated from the hopping time in the 2D random walk on the surface (1 ns) and the water size molecule (0.3 nm) lead to a diffusion coefficient on the surface of  $2.3 \cdot 10^{-11} \text{ m}^2/\text{s}$ . This is again in good agreement with the value  $5.0 \cdot 10^{-11} \text{ m}^2/\text{s}$  obtained in the same simulations for water diffusing on the internal pore surfaces of tobermorite. This double coincidence, although not being a definitive confirmation, has been suggested to be promising and warranting further investigations.

Generic articles on cryoporometry have already been mentioned, applications on cement in particular can be found in [117,118].

The NMR imaging performed on cement is very challenging because of the very short relaxation times involved; for this reason the “traditional” medical imaging cannot be performed. However, several successful applications have been achieved with modified pulse sequences or setup. Examples of these are the STRAFI (STRAY Field Imaging) setup [119-121], where the gradient field is not generated by coils but from the fact that the experiment is performed into the fringe of the stray field of a magnet. Sometimes has also been proposed the embedding of coils in the concrete. The STRAFI setup restricts the measurements to 1 dimension only; however rotation of the sample and the subsequent reconstruction of the 3D image is hard but possible. Another technique for imaging, that uses electrically driven gradient in a clever way to be suitable for short relaxing material (and therefore cement) is SPI (Single Point Imaging) [122] that however is very time consuming due to the fact that only one point in the  $k$  domain is acquired at the time and its evolution SPRITE (Single Point Ramped Imaging with  $T_1$  enhancement) [123] where the gradients are ramped instead of switched on an off to speed up the acquisition.

Gradient echo imaging of deuterium was used to observe water transport in concrete [124] the use of deuterium is to separate the background signal from the hydration water within the cement matrix.

Capillary water uptake has also been monitored by different imaging technique on cement in [78] and an application on roof tiles is shown in [125]. Similar experiments using SPRITE are presented in [126], where sub millimetric resolution is achieved.

Two dimensional gradient echo imaging have been used to monitor non-uniform flow through hardened cement sample [127]. The same idea but performed with SPI is presented in [128].

Monitoring of microcrack is another application where MRI can be very useful, this task using SPRITE for imaging and gradient pulse to monitor the spatially resolved  $T_1$  can be found in [129] and [130].

The effect of admixtures, coatings and blended cements have also been successfully studied with bulk or spatially resolved NMR, some examples of the first are:[131] where the effect of clay is considered and [132] where an expansive additive is considered; an example of combination of both is presented in [133]. Work in monitoring coatings has been presented using STRAFI in [134] and using SPRITE [135].

The *in-situ* applications of NMR on cement and concrete and the evolution of dedicated magnets are getting more and more popular, with few examples of applications on historical buildings and heritage [136] or magnet development for concrete [137]. An “alternative” approach of “*in-situ*” presented in [138] is to build some low cost magnet-coil devices and fully embed them into the concrete.

## **1.5 What this thesis is going to say**

In this thesis some applications of NMR techniques to cement and concrete will be presented. Chapter 2 will deal with development and applications of a portable surface magnet (Surface GARField). This is the first time such a magnet is used on a real construction site.

Chapter 3 will present 2D relaxation analysis experiments on cement pastes, C3S pastes and synthesised C-S-H. The objective successfully achieved is to answer the question whether the  $T_2$ - $T_2$  experiments previously performed and reported in literature were really detecting exchange between pores of different sizes between inner and outer product or other “two sizes materials” or whether an alternative hypothesis of exchange between different paramagnetic impurities environments could have been possible; moreover, a puzzle raised from the  $T_2$ - $T_2$  experiment that apparently was detecting an exchange between nanometric structures over micrometric distances, has been solved proposing an alternative explanation. The exchange is probably between intra and inter C-S-H layers and not between inner and outer product. The apparent low diffusion coefficient is probably due to tortuosity or “barrier” effects.

Chapter 4 will present solid echo experiments. Careful examination of the amplitude of the signal as a function of the mass led to the formalisation of a simple drying model for the water restricted in the cement gel pores. The model is also capable of estimating the layers thicknesses and the results are comparable with the previous  $T_2$ - $T_2$  estimations.

Experiments using DQF NMR presented in chapter 5, will show that the anisotropy of water increases as the sample is dried. This increased the confidence that the protons detected can be referred to the one of inter and intra C-S-H layer water.

## 2 Portable magnet

### 2.1 Introduction

In this chapter, development and improvements on the Surface GARField will be presented, including applications to a real construction site. This is the first application of this magnet outside the laboratory.

The most immediate and clear difficulty in working at low frequency is the lower sensitivity, meaning the reduced signal to noise ratio due to the diminished Boltzmann factor compared to the higher fields. At low field (and therefore frequency) also dead time is generally longer, which is because the decay of a transient in a resonant circuit is proportional to its quality factor and the number of cycles from the transient and at lower frequency each RF cycle is longer.

Another difficulty that is not related to the low field itself but from the fact of having big coils is the acoustic (or mechanical) ringing. This is due to the fact that when the coil is energised, it behaves as a magnet and therefore is attracted and repulsed from the main magnetic field; this force may cause vibrations of the coil that give origin to induced currents detectable as coherent noise.

Another issue that can be a significant limitation in the use of the surface magnet on real constructions is the fact that most of the time, concrete is reinforced with steel rebars. These, when in the proximity of the magnet, will distort the magnetic fields of the device and may strongly affect the readings. This is due to the fact that the steel polarizes when in proximity of the magnet creating an additional magnetic field that superimposes on the magnet one and distorts it. To determine what the limits of the applicability of the magnet are and which minimum operative distance can be accepted, some experiments on phantom specimens have been performed and will be presented. These will show that in typical conditions the reinforcing rebars are not a problem.

The magnet has now, also helped by the purchase of a much more compact and light spectrometer, reached a real portability. However, the aim of always making it lighter and lighter is still in mind. The most bulky pieces at the moment are the transmitting amplifier and the quarter wavelength cable. The amplifier is not an issue that will be considered at the moment. The fact that it is heavy and bulky is mainly due to the fact that in this test system the flexibility has been preferred to the lightness; at a final stage, when the setup will be considered reliable and optimised, a narrow bandwidth amplifier in the place of the

broadband used at the moment will automatically decrease the weight of the system dramatically. For the  $\lambda/4$ , instead, there could be a more compact solution of a “simulated  $\lambda/4$ ” called lumped circuit. This solution has been tried and tested.

## 2.2 Magnet specification materials and methods

The magnet presented is the result of a long evolution and approximations starting from the idea of the Halbach [139] magnet array.

Halbach cleverly designed a magnet arranging small magnetic pieces oriented in different directions in such a manner as to have their magnetic field to sum on one side of the array and cancel out on the other. The design is better understood by looking at the Figure 2.1.

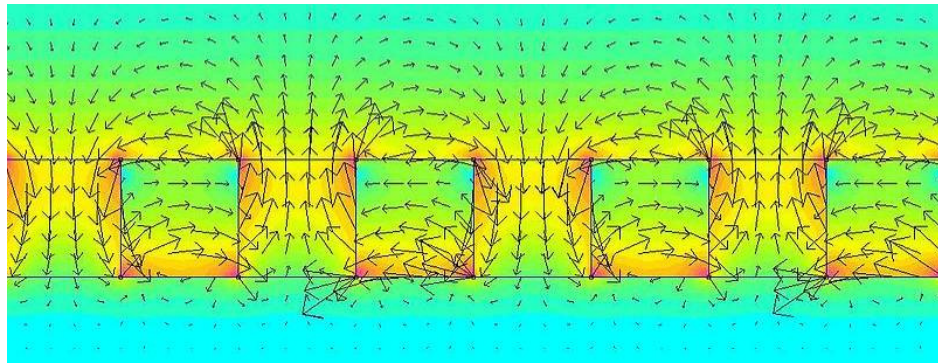


Figure 2.1 Magnetic field plot around an infinite Halbach array of cube magnets (modified from [140])

The resulting field at a distance longer than the inter distance between the magnetic pieces is constant in magnitude (but not in direction) in a plane parallel to the array. To be able to eliminate the requirement of “far field”, a continuous distribution of magnetisation in different direction within magnetic bar would be required; however, this is not practically achievable.

In addition to the “far field” approximation, the infinity of the array is also required to achieve the uniformity of the magnetic field strength on a plane. This requirement is even harder to achieve than the continuous distribution of magnetisation. In practice, therefore, approximations are always used.

The magnet discussed and used in the work of this thesis, is a variant of the original GARField; where the name stands for Gradient At Right angle with the Field. The original is manufactured using two curved shaped poles to provide between them a series of horizontal planes of constant magnetic field magnitude and a strong fixed gradient orthogonal to it to allow measurement with high resolved spatial information. The shape and magnetisation of

the poles is determined to satisfy the boundary conditions for the solution in the open space for the field required.

The single side (Surface) GARField is designed to achieve the same result but from just one side, to be able to measure samples that are much bigger than the magnet itself. To have a “true” one side GARField, the setup required would be to have an infinite series of equidistant curved shape poles. This is of course not feasible, and in fact the solution adopted is to have the very limited series of just 3 magnets oriented with alternate direction.

The setup is basically a very short Halbach array with only 3 magnets and 2 orientations. The distance between the magnets is chosen in such a way as to optimise the uniformity of the modulus of the magnetic field and minimise the truncation effects due to the non infinity of the array (Figure 2.2). The field is on one side of the magnets only because there is a steel plate underneath the magnets block that breaks the symmetry introducing a “mirror effect”.

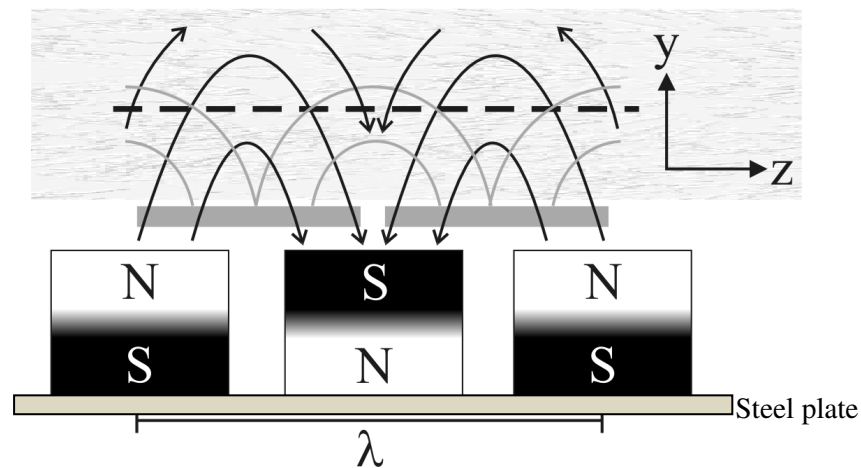


Figure 2.2 The relative positioning of the three magnetic blocks and the two winding coils sitting on the gaps between them (from [96]). The grey thick horizontal lines represent the coil windings, the thin black solid the main magnetic field and the grey thin the RF field. The broken black line shows the depth at which the orthogonality between the fields is optimised.  $\lambda$  represent the wavelength associated to the periodicity of the magnetisation of the truncated Halbach array.

This is achieved within portable size and weight, since the magnet is only ~15 Kg in weight and is of the size of a shoe box.



Figure 2.3 The Surface GARField magnet. On the top the double winding surface coil is visible.

The design of the RF coil patterns the one of the magnet itself, with the only difference that the origin of the magnetic field is current through coils instead of magnetic material. To achieve orthogonality between the fields the array of coils has to be shifted by a quarter of the period of the magnetisation and therefore  $1/2$  of the inter distance between the magnetic blocks. The fact that the magnet array is only 3 pieces long causes the maximum useful length of the coils array to be 2. Figure 2.2 shows the setup of the magnetic bars and the coil. The full description of the magnet development and construction is in [96].

The slice selection at different depths is achieved moving the magnet with a stepper motor controller in respect to the surface of the sample. In this way the plane at the resonance frequency (that is at fixed distance from the magnet) moves deeper or shallower in the sample. There are two modes of obtaining the slice selection, each one with advantages and disadvantages. The first is to keep the coil on the magnet and move both the components at the same time, the alternative is to leave the coil on the surface of the sample and move just the magnet. There are advantages and disadvantages in both setups. The first advantage in moving both components is that constant sensitivity is achieved; in fact the distance between the slice being measured and the coil is constant, therefore the signal is attenuated in a similar way whatever its operating depth. The second advantage is that a constant S/N is achieved: this is a direct consequence of the advantage already presented. Additionally, there is the advantage that the orthogonality between the fields is maintained: the relative position

of magnet and coil is kept constant as determined by the design, therefore the angle between the constant magnet field and the RF coil field is constant, keeping the optimisation of the pulses. The advantage of moving only the magnet, instead, is that the coil is closer to the sample for all the distances but the furthest; this means that the sensitivity is higher and this is evident especially for the first few millimetres from the surface, often the most interesting part of the sample.

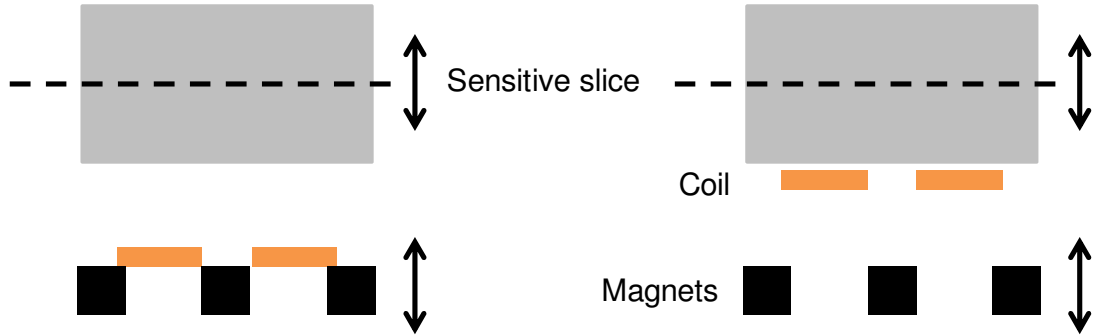


Figure 2.4 Scheme of the two different operating modes.

The first solution is preferable if the high resolution is required, but for our applications, because the lack of signal is the major limitation, the second approach is adopted. This will require, of course, some solution to the variable sensitivity to be discussed later. Also the differences affecting the pulses will be discussed in more detail.

The concept of “on resonance” on a strong gradient inhomogeneous magnet has a different meaning from the one applying while using uniform fields. In fact, there is always a part of the sample that is at the chosen frequency and therefore it is not really magnet dependent but operator (via the chosen spectrometer frequency) and circuit dependent.

### 2.2.1 Probe and electrical scheme

The probe is a surface one constituted by two coils printed on a PCB and winding in opposite directions. In this way it creates a field that is approximately the one of a dipole sitting on the surface. The distance between the centres of the two windings is calibrated with the inter-magnet spacing to keep the orthogonality condition between  $B_0$  and  $B_1$  satisfied.

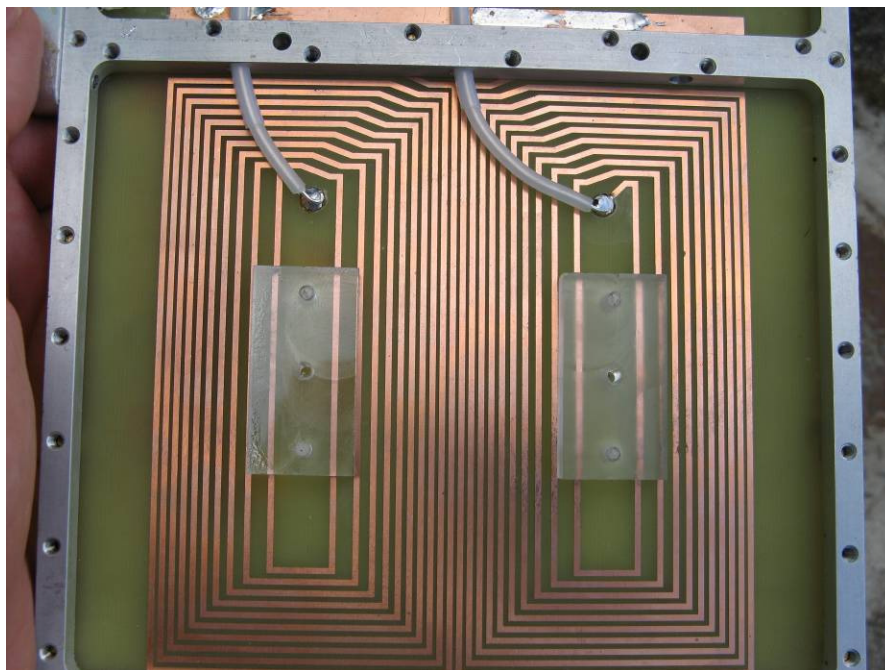


Figure 2.5 The surface probe seen from behind. The space within the frame has been subsequently potted to decrease the systematic noise.

The coil, as in any other NMR equipment is the core of the detection, however many other components play a fundamental role to bring in a successful way the RF power from the amplifier to the sample and the signal from the sample to the spectrometer. The complete electrical scheme for the entire instrument is drawn in Figure 2.6.

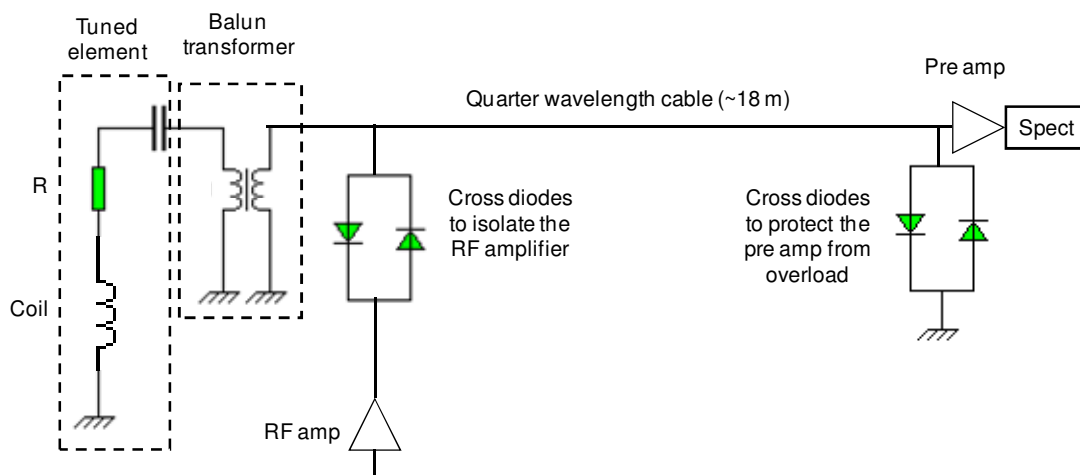


Figure 2.6 Complete electrical scheme of the Surface GARField.

The frequency at which the resonating circuit is tuned can be, within limits, varied changing the value of the capacitor included in the tuned element. Also in this case, everything is a matter of a conscious compromising and finding the right (relative to the application)

balance. A lower frequency allows to target a slice that is further away from the magnet and therefore deeper in the sample, however, the price to pay is a lower signal. In the other way, an improvement of the signal is paid for a lower “range”. When varying the frequency it must be taken into account that the geometry of the magnet-coil ensemble is dependent on the distance of the slice targeted; therefore, an excessive shift in the frequency may destroy the orthogonality of the fields; this is not true for an infinite Halbach array and originates from the truncation effects.

The capacitors employed to tune the coil are Panasonic high voltage ceramic capacitors (codes ECKD4A471MDV and ECKD4C101MDV) placed in series with the coil. Their total value is 670 pF. For the match, a particular and rarely used setup has been chosen; the coil-capacitor series has been placed further in series with a resistor to bring the total series L-C-R matched to  $12.5 \Omega$  at the resonant frequency; subsequently a 4:1 transformer has been used to raise the total impedance of the circuit to the necessary  $50 \Omega$  to match the amplifiers (both transmitting and receiving) and the cable.

This is a very unusual setup, in fact the “common belief” is that it is never a good idea to have additional impedance in the circuit. The reasons are mainly two, the first is because there is also some magnetic field “wasted” instead of having all of it flowing into the sample, the second is that the addition of other impedances distorts the resonant frequency of the circuits introducing resonances that may be different from the main one matching the main magnetic field and creating ringing and beating in the signal.

However, the main parameter and objective when talking about RF NMR coils, is the ability of producing the maximum magnetic field possible, and this directly translates into having the maximum current flowing in the coil.

Introducing a dummy resistor, there are two effects that reduce the current flow in the coil and therefore are unwanted: the  $Q$  of the circuit decreases, therefore the “ $Q$  amplification factor” is lost; the impedance of the circuit increases and therefore the current, at maximum amplifier voltage, is decreased. Another disadvantage is that the introduction of a resistor brings thermal noise.

Nevertheless, as mentioned, the aim is to maximise the current flowing through the coil matching the impedances to  $50 \Omega$  and real, does not really matter how, any way to reach the target is equally valid.

Further discussion on the effects of the  $Q$  of the circuit and its connection with the dead time is probably useful, in fact in low field magnets one significant problem is the ring down of the coil (that is a dead time for the acquisition). This time is roughly proportional to the

quality factor  $Q$  time the period of the signal, therefore, as the frequency decreases, the period increases and the dead time increases. This is a reason why, in a low frequency instrument, as well for an imaging one (although for different reasons) higher  $Q$  is not always better. The  $Q$ , however, is also an expression of the sensitivity of the coil, therefore a balance between a too high  $Q$  and a too low  $Q$  is always required. Sometimes, the value of  $Q$  is changed between the transmitting period and the detecting period to allow short dead time but high sensitivity, however, this requires the introduction of more electronics (usually transistors) and complexity.

The  $Q$  of a circuit is  $Q = \frac{\omega L}{R}$  but also  $Q = \frac{f}{\Delta f}$  where  $\Delta f$  is the bandwidth of the resonant circuit. This bandwidth has several repercussions. It must be wider than the bandwidth of the pulses that is a function of the length and roughly  $bw = \frac{2\pi}{t_p}$ . Additionally must be wider

than the line width of the signal that is roughly  $lw = \frac{1}{\pi T_2^*}$ . These, together with the dead

time issue already discussed are the reasons why higher  $Q$  is not always better. The typical times for both pulse length and signal decay on this device are circa 10  $\mu$ s, therefore a bandwidth lower than about 200 KHz is not advisable.

To protect the preamplifier during the transmitting period, a common simple solution is to place a  $\lambda/4$  cable between the coil and the grounding cross diodes. The quarter wavelength cable acts as an impedance transformer with the property that:

$$Z_i Z_o = |Z|^2 \quad (2.1)$$

Where  $Z_i$  and  $Z_o$  are the input and output impedance; and  $Z$  the characteristic impedance of the cable (50  $\Omega$ ). When the transmitter amplifier is pulsing, the grounding diodes placed near the preamplifier to protect it (Figure 2.6) experience a voltage greater than their threshold and therefore are closed causing  $Z_o$  to be almost zero. This is translated into a very high impedance by the quarter wavelength cable at the coil side. Because the cable has very high impedance, almost all the current flowing from the RF amplifier goes in the coil. During the detection period the RF amplifier is switched off and therefore has an output lower than the diodes threshold. The cross diodes on the left in Figure 2.6 are therefore open and isolate the RF amplifier from the rest of the circuit reducing the inevitable noise that would have come from the amplifier itself. Because also the NMR signal is much lower than the diodes threshold, also the diodes at the right of Figure 2.6 (the one to protect the preamplifier from

overloading) are open; therefore the signal goes in the preamplifier and the spectrometer and not to ground.

The quarter wavelength solution is very simple and reliable, however, because the wavelength goes as the reciprocal of the frequency. For very low frequencies the cable necessary becomes really very long and, because of that is preferable to using very high quality thick cable, which is also bulky. In addition, since every cable is intrinsically lossy, it would be preferable to find another solution.

### 2.2.2 Pulse sequence and slice selection

The most useful and robust application of this magnet is the profiling of water in curing concrete. For this purpose the pulse sequence in use before the work presented in this thesis was a  $90x(-\tau-90y)_n$ . The reason for using only  $90^\circ$  pulses instead of a common CPMG was dictated by the fact that the pulses, if applied while a gradient is present, act as slice selective, exciting thickness of sample that is proportional to the bandwidth of the pulse. This is a valuable fact which is used in MRI applications. Longer pulses have a shorter bandwidth and therefore excite a smaller quantity of sample. To maintain the amount of sample constant for all the pulses, therefore, it is required to have constant pulse lengths. This is the reason for using only 90 degree pulses instead of a traditional  $90(-\tau-180)_n$  CPMG at the expense of signal lost.

Discussion on the pulse length is extended if the “fixed coil mode” is used (that is the one adopted). In this case, it must be considered that the distance between the targeted volume and the coil varies. This means that the pulse that is a 90 degree one while exciting the shallower slices does not rotate the magnetisation of the deeper slices of the same angle. A solution to cope with this could be to increase the pulse length as the slice is deeper, incurring again in the different slice thickness already discussed. The alternative of changing the pulse amplitude (instead of the length) with depth is a better solution to keep the rotation angle the same. Being the power of the amplifier limited and already set at its maximum, this would mean to decrease the power for the shallower slice (and increase the length for all the depths), not being possible to further increase it during the detection of the deeper one, wasting power and dramatically losing resolution. For these reasons none of the alternatives were adopted, but the fixed pulse length and amplitude one, although being aware that the flip angle will not be constant with the depth, it was in fact adopted.

### 2.2.3 Signal processing

To determine the density of the spin for each slice (and therefore the amplitude of the profile for the depth) each echo of the CPMG is multiplied with a Gaussian shaped function to eliminate part of the noise. The multiplication in the time domain acts as a convolution in the frequency domain, and therefore as a smoothing on the frequency domain. This is a filter in signal processing terms.

To cope with the issue of non constant sensitivity (and flip angle) over the depth range due to the fact that we will operate the system in the fixed coil mode, one possibility is to measure a sample that is known to be homogeneous (in our case a rubber block will be used). Its profile should be, of course, flat, but it will not be due only to the non constant sensitivity. The profile can then be fitted with an appropriate (arbitrary empirical) function  $fit_{pr}(d)$  of the depth. This, being a function only of the sensitivity, can be considered as the “sensitivity function”. The correction function can then be easily calculated as  $1/fit_{pr}(d)$  and be applied to all the other unknown raw profiles via simple multiplication.

### 2.2.4 Other equipment

A 2 kW RF amplifier (TOMCO model BT 02000) has been used for both the laboratory and the site experiments.

The preamplifier used was a custom modified Doty Scientific LN-2L (5-500 MHz bandwidth 4  $\mu$ s recovery time)[141].

On site the power was generated by a Honda (EU 20i) 2 kW inverter portable petrol power generator capable of a constant power output of 1.6 kW and a peak power of 2.0 kW. A careful comparison has not been made due to its non fundamental utility and for the fact that is not straightforward using both the generator in the lab or the main outside it. The RF noise coming from the generator, that was one of the main concerns while planning the outside experiments, has been found to be absolutely negligible, and possibly even lower than the noise coming from the university main power supply. The necessity of using a generator came from the fact that the UK safety regulations on the construction sites limit the voltage of the power supply to 110 V. All our equipment, instead, run at 240 V. Because we were actually using 240 V on a construction site, a risk assessment had to be prepared and approved by the site manager. The solution was to introduce an exclusion zone made with some mobile fencing; in this way the “high” power supply was completely isolated from the activities of the builders and therefore accepted.

## 2.3 Improvements to the system

In this section the improvements to the system achieved during the three years will be presented.

### 2.3.1 Software and new spectrometer

The effect of having different pulse length has been discussed when explaining the reasons of using only 90 degree pulses. It is possible to also use other flip angles, but these must be obtained changing the amplitude of the pulses and not their length. Not all the spectrometers (as the older one that was in use on the Surface GARField before the work explained in this thesis) have this capability of amplitude modulation, and therefore the solution of using only 90 degree pulses.

The purchase and installation of a new KEA (produced from Magritek) spectrometer allowed achieving amplitude modulation and therefore to move to an ordinary CPMG pulse sequence. The 90 and 180 degree pulses of different amplitude instead of different length should always excite the same slice because of the same bandwidth, however, there are fringes outside the sensitive slice for both  $B_0$  and  $B_1$  where there are spins that undergo a much more complex dynamic than the one described by the simple CPMG (that is true only for the spins exactly on resonance for both  $B_0$  and  $B_1$  fields and for which the two are perpendicular). Spins that do not fulfil the conditions above can be detected anyway, causing the signal measured not to be anymore a full CPMG decaying with characteristic time  $T_2$  but with characteristic relaxation time that is a complex mixture of  $T_1$ ,  $T_2$  and, if the intensity of the averaged  $B_1$  field is much greater than the local dipolar magnetic field (this happens in case of rapid repeated RF pulses), also  $T_{1\rho}$ .

The new Kea spectrometer allowed also to make the equipment lighter and smaller. In addition, the new software allowed completely new capabilities as the automation of the motor controller. This spectrometer is supplied with the Prospa data analysis software and an acquisition extension specifically produced for the Kea spectrometer.

A serial interface built in the software allowed interacting directly with the motor controller within the acquisition macro.

A very useful feature of the new software is the pulse programming macro that allows easy modification and creation of new pulse sequences using simple commands.

The macro written for the acquisition acquires a CPMG every slice, moving the motor of the predefined distance between each slice. At the end of the experiment the motor return to the

zero position and if the number of profiles required is higher than one it starts all over again with a new name.

To monitor the noise for each slice, after the acquisition of the CPMG an FID without exciting pulse is acquired as a representative of the random external noise. Because the random noise cancels out increasing the number of scans, this experiment is performed for only one scan. The limitation is that this noise measurement is representative of only ~17 ms every slice acquired (~12 minutes).

To be able to perform the analysis of the profiles as soon as they are acquired (and also during the acquisition obtaining partial profiles) the analysis software has been first developed in Matlab and then re-written in the Prospa language.

### 2.3.2 Lumped element $\lambda/4$

As an alternative to the bulky, heavy  $\lambda/4$  cable a more “compact” lumped element  $\lambda/4$  has been considered, built and tested. This component consists in a circuit that simulates the real  $\lambda/4$  and can be enclosed in a small box. The reasons for preferring such a solution instead of the quarter wavelength have already been discussed, and are: compactness of the instrument, elimination of a long, lossy and possibly source of noise cable that at the operating frequency is almost 20 m long!

#### 2.3.2.1 Scheme and theory and building

The electric scheme of the lumped element  $\lambda/4$  used is shown in Figure 2.7:

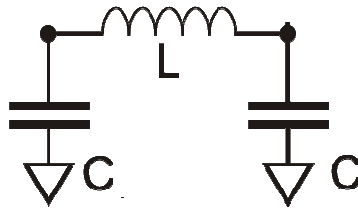


Figure 2.7 Electric scheme of the lumped element  $\lambda/4$

When  $\omega^2 LC = 1$  the lumped element  $\lambda/4$  circuit is at resonance and behaves as a quarter wave line with a characteristic impedance of  $\frac{1}{\omega C}$ . From this can be calculated that for the frequency of interest (2.825 MHz) and for the impedance to match ( $50 \Omega$ ) the required values are  $C = 1127 \text{ pF}$  and  $L = 2.82 \mu\text{H}$ . The value of the  $C$  and  $L$  values as a function of the frequency required is plotted for completeness in Figure 2.8.

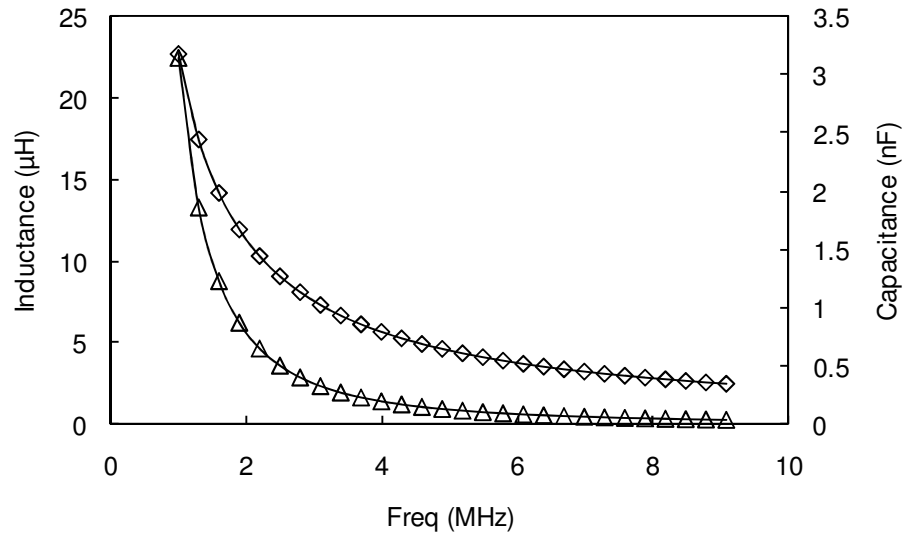


Figure 2.8 Required capacitance (diamonds, right scale) and inductance (triangles, left scale) to build a lumped element  $\lambda/4$  circuit for different resonant frequencies. All values are calculated for  $50\ \Omega$  impedance.

The inductor has been homemade wrapping a thin insulated copper wire around a ferrite core. The number of turns necessary has been determined empirically. In practice the attempt started from an excess of turns and the wire has been unwrapped one or two turns, each time measuring the inductance with a meter until the wanted value was reached. The capacitors used are the same as the one used to tune the main circuit. Figure 2.9 is a picture of the Lumped element  $\lambda/4$  made and tested in this thesis.

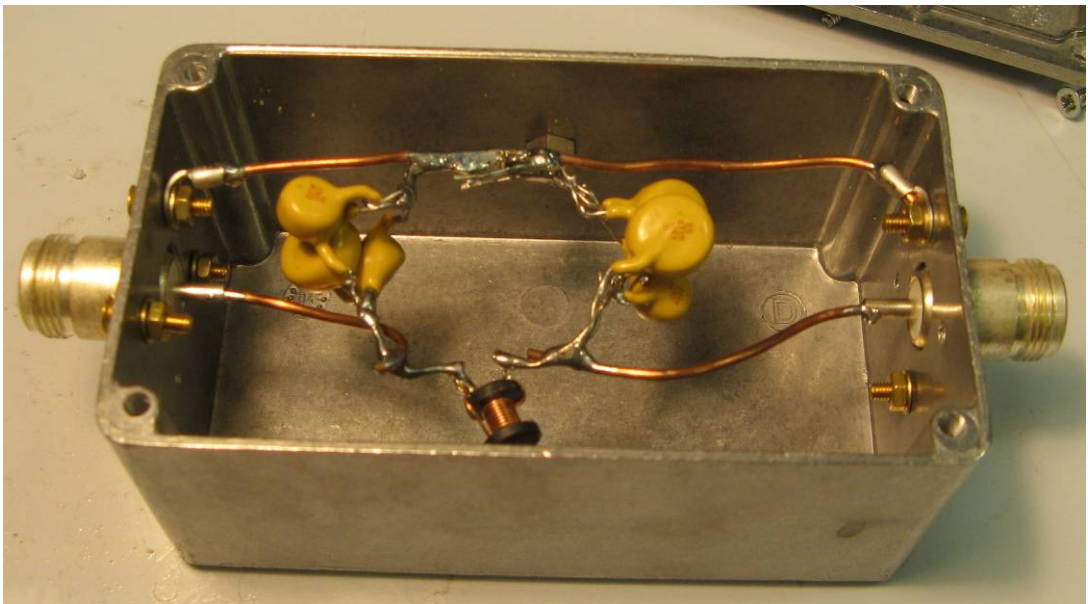


Figure 2.9 Picture of the lumped element  $\lambda/4$  made and tested.

### 2.3.2.2 Tests

#### 2.3.2.2.1 Impedance measurements

To test the functioning of the lumped element  $\lambda/4$ , its impedance as a function of the frequency has been measured and compared with the one of the quarter wavelength cable. Two different cases have been used: one with the component short circuited at the other end, to reproduce the situation during transmission when the cross diodes placed to protect the preamplifier conduct, and the other with component closed on a  $50\ \Omega$  dummy load, to reproduce the situation during acquisition when the cross diodes do not conduct and therefore the cable is effectively closed on the  $50\ \Omega$  resistance of the preamplifier.

All the measurements were performed with a HP 4815A Vector Impedance Meter.

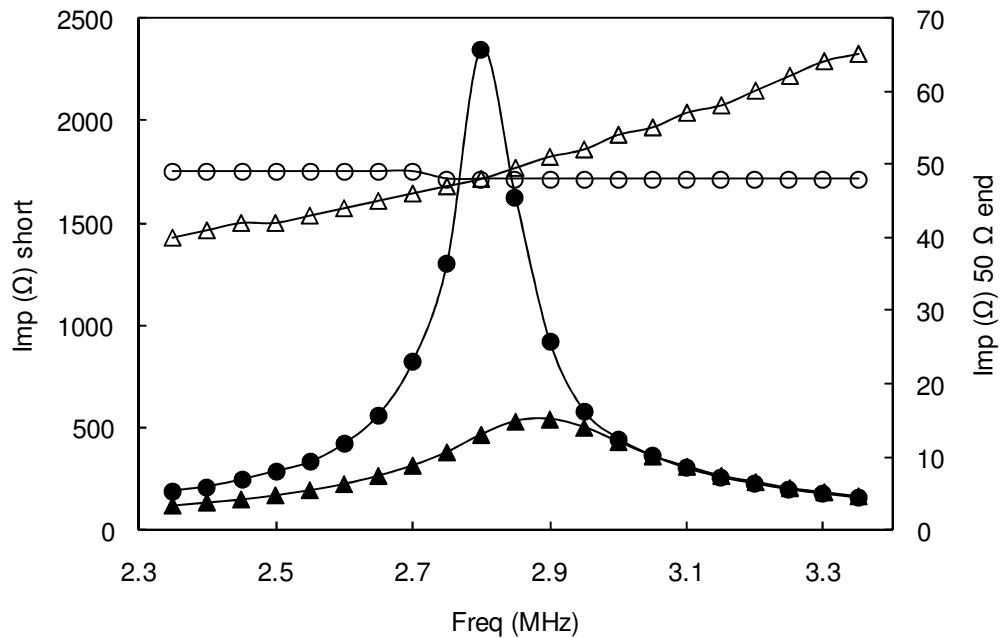


Figure 2.10 Impedances of the lumped element  $\lambda/4$  (triangles) and the quarter wavelength cable (circles) while short circuited at the other end (left scale, full markers) or closed on a  $50\ \Omega$  dummy load (right scale, empty markers). The smoothed lines connecting the markers are a guide for the eye.

The results of the first test performed on the lumped element  $\lambda/4$  built are shown in Figure 2.10. The behaviour while connected to the  $50\ \Omega$  end shows that the lumped element  $\lambda/4$  is slightly more frequency dependent compared to the cable that has a much flatter response. This, although interesting, will probably not affect the system and therefore has not been taken into account or discussed in detail; we only observe that, at the operating frequency,

the impedance is very close to the designed  $50\ \Omega$  (slightly lower but absolutely comparable with the cable one, which is slightly lower than  $50\ \Omega$  as well).

The most interesting behaviour is the one for the short circuited terminal. Here the peak of the impedance versus frequency for the lumped element  $\lambda/4$  (triangles) is at 2.85 MHz, a bit higher compared to the design 2.825 MHz, but within measurement errors. The behaviour is exactly the one expected, with a peak of higher impedance at the design frequency. It is interesting to note that the absolute value of the peak impedance is much higher for the cable than for the lumped element  $\lambda/4$ . This suggests a lower quality for our purposes of the lumped element  $\lambda/4$  versus the more traditional solution, in fact the lower impedance should mean that during the pulses more current flows through the device and discharges through the cross diodes. This should “waste” some of the amplifier power increasing the pulse length.

### 2.3.2.2.2 Pulse length

To check the hypothesis introduced in the previous section concerning the effect of the lumped element  $\lambda/4$  on the pulse length, this has been measured for both solutions plotting the amplitude of the echo following a  $90_x-180_y$  pulse sequence as a function of the pulse length. The two pulses have the same length but different amplitude. The results are presented in Figure 2.11.

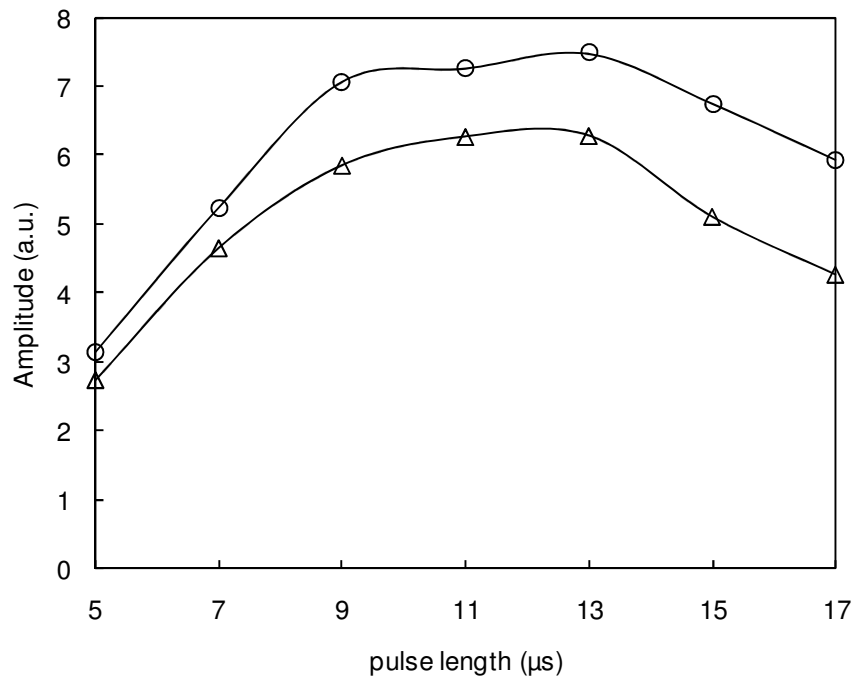


Figure 2.11 Analysis of the pulse length for both the quarter wavelength (circles) and the lumped element  $\lambda/4$  (triangles).

To interpret Figure 2.11 there are two phenomena that influence the amplitude of the signal that must be taken into account. They occur at the same time as the pulse length increases. The first is that, as the pulse length increases, it gets first nearer to a 90 degree pulse and therefore the transverse component of the magnetization increases; after reaching a maximum, the pulse gets nearer a 180 degree and the transverse magnetisation decreases eventually reaching zero again. This fact should give a sine shape at the Figure 2.11. The second is that, as the pulse length increases, its bandwidth decreases and therefore also the thickness of the slice excited and therefore the signal generated. This effect superimposes a  $1/t_p$  (where  $t_p$  is the pulse length) behaviour to the plot.

From Figure 2.11 it can be seen that the pulse length has not varied significantly, there is a slight decrease in total amplitude ( $\sim 15\%$ ) introducing the lumped element  $\lambda/4$  but nothing compared to the dreaded effect that could have been hypothesised looking at the difference in peak amplitude in Figure 2.10.

The first experiment to be performed has been a simple CPMG, with the same parameters used later in the profiles. The results are shown in Figure 2.12.

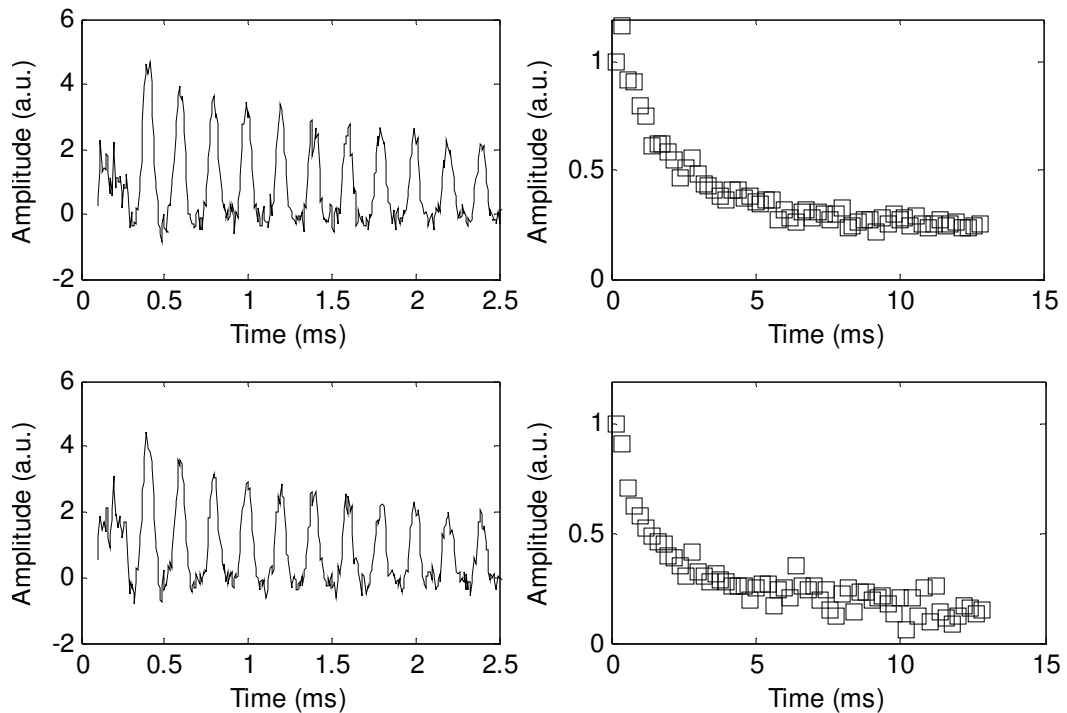


Figure 2.12 CPMG signal performed in exactly the same condition once with the cable (top) and once with the lumped element  $\lambda/4$  (bottom). Data have been phased with the same angle.

From Figure 2.12 it is clear that the introduction of the lumped element  $\lambda/4$  did not affect the result significantly. The amplitude is equal and the echo attenuation data for the lumped element  $\lambda/4$  seems to be showing a slightly higher noise in the tail of the data compared to the cable one.

Important and critical parameter in any kind of NMR equipment (and even more in the low field one) is the dead time. A test has been performed to analyse the difference in this parameter using the cable or the lumped element  $\lambda/4$ .

For this measurement, a CPMG with a shorter echo time has been performed, where all the echoes have been added together.

In this experiment the most relevant parameters were:

Parameter	Value	Units
acqTime	0.13107	$\mu\text{s}$
nrScans	128	
nrPnts	128	
nrEchoes	32	
echoTime	190	$\mu\text{s}$
repTime	333	ms
b1Freq	2.825	MHz

This means that the centre of the echoes were at  $95 \mu\text{s}$  from the pulses, and the beginning of the acquisition at  $31 \mu\text{s}$  from the pulse.

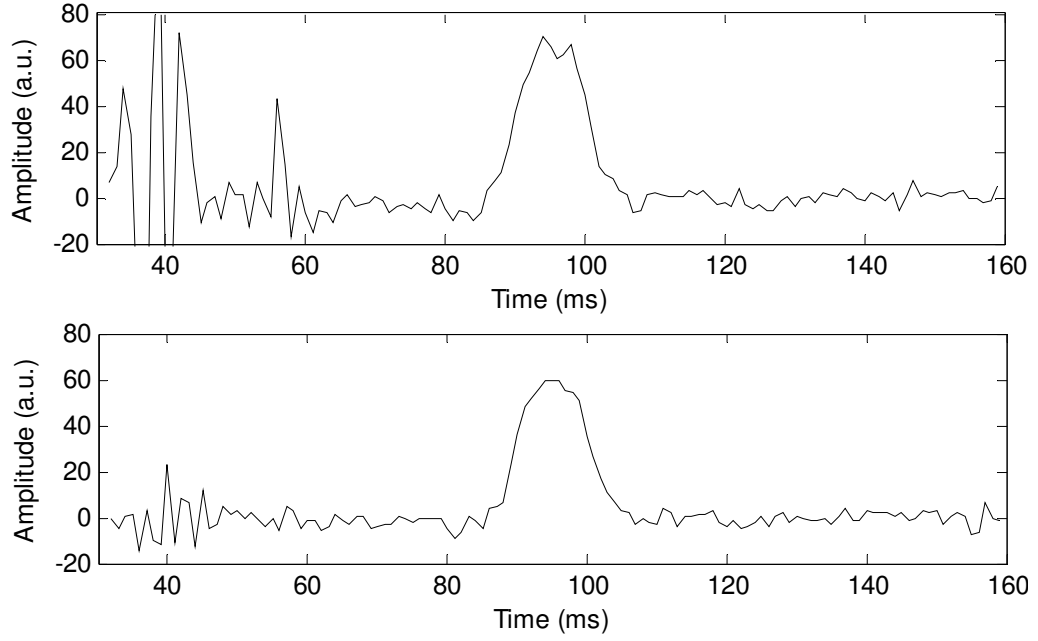


Figure 2.13 The sum of the echoes of the CPMG measured with a short echo time and long acquisition window to visualise the dead time of the system. Top with the cable, bottom with the lumped element. The vertical scale is the same to allow comparison and the data have not been filtered. The time is calculated from the centre of the pulse.

From Figure 2.13 it can be seen that the dead time does not change very significantly between the experiment performed with the cable and the lumped element  $\lambda/4$ , however, the amplitude of the ringing signal is much smaller with the lumped element  $\lambda/4$  than with the cable, while the amplitude of the “real” signal is comparable. This led to the conclusion that the performances using the lumped element  $\lambda/4$  are slightly superior to the one using the cable.

### 2.3.3 Resonant coil

#### 2.3.3.1 Increased thickness of probe

One of the first modifications to the magnet performed during the period of the work presented in this thesis has been the increasing of the thickness of the probe. The empty space between the Printed Circuit Board (PCB) coil and the back plate has been increased from 0.5 to 2 cm to increase the space for the return magnetic field flux. Increasing this distance helped in increasing the strength of the  $B_1$  achievable. This is because, when a conducting plane is placed in the vicinity of a coil an “imaginary induced coil” is created behaving in the opposite way compared to the primary one:

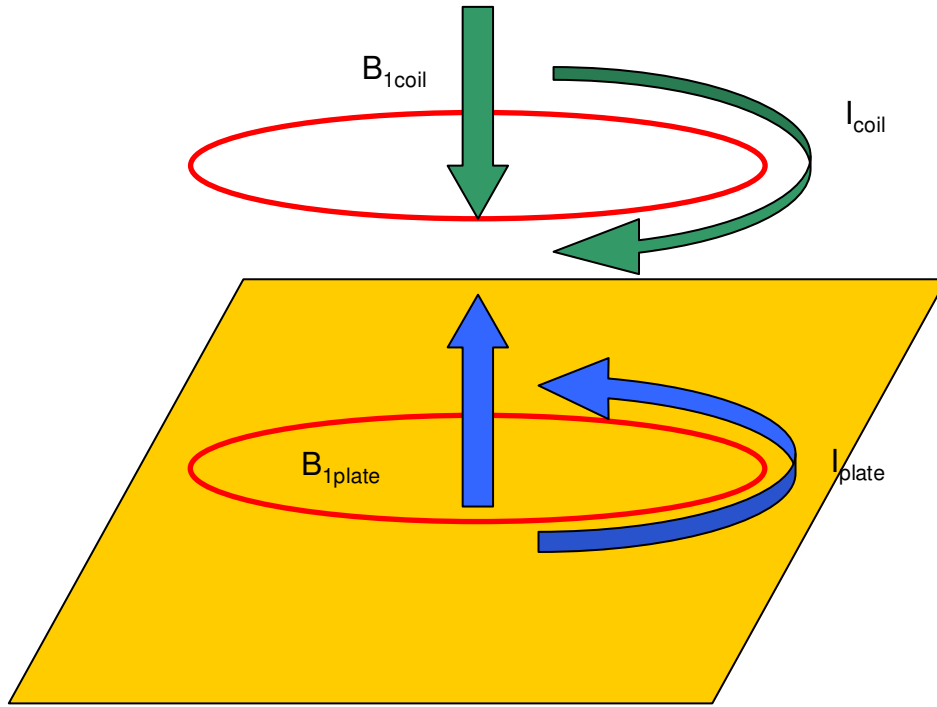


Figure 2.14 Sketch of the imaginary coil created in the back plate by the primary coil

In fact the coil-backplate ensemble behaves as a dipole, where the distance between the two poles is proportional to the strength of its magnitude. If the plate is too close,  $\mathbf{B}_{1\text{plate}}$  field strongly reduces  $\mathbf{B}_{1\text{coil}}$  also in the neighbours of the coil.

The increasing of the coil thickness diminished the possible excursion of the magnet limiting the possible penetration. To overcome this limitation and target a deeper slice in the sample, the frequency has been lowered. The value that has been considered a “good compromise” between sensitivity and depth achievable is 2.825 MHz. This is the frequency that has been kept constant over all the experiments presented.

The overall achievement of this increased thickness has been to reduce the pulse length moving from 10  $\mu\text{s}$  for the 90 degree pulse to 11  $\mu\text{s}$  for the 180 one.

### 2.3.3.2 Analysis of the original S/N

To try to improve the S/N, the first step is, of course, to determine the origin of the noise, especially if it appears to be coherent. To achieve this, a series of tests have been performed. A large dataset of noise (signal of experiments performed without sample) has been acquired.

The pulse sequence used has been the classic CPMG, due to the fact that, that is the one that probably will be the most used. The parameters kept constant throughout all the dataset are:

Parameter	Value	Units
acqTime	0.26214	$\mu$ s
nrScans	256	
bandwidthFile	1.024	MHz
nrPnts	256	
rxPhase	20	Degrees
rxGain	40	dB
acqShift	0	$\mu$ s
nrDummies	0	
nrEchoes	8	
echoTime	400	$\mu$ s
pulseLength	10	$\mu$ s
repTime	500	ms

The 4 variables of the dataset (parameters that have been changed independently through the experiments) are:

Parameter	Values	Units
Magnet to coil distance	30, 20, 10, 0	mm
Frequency	2.9, 3.0, 3.1, 3.13, 3.2, 3.3	MHz
Transmitting power	0, -6, -12, -18, -21, -24	dB
Phase cycle	a. P90	-x, x, -x, x
	P180	-y, y, y, -y
	acq	-x, x, -x, x
	b. P90	-x, x, -x, x, -x, x, -x, x
	P180	-y, y, y, -y, -x, x, x, -x
	acq	-x, x, -x, x, x, -x, x, -x

Because all the parameters have been changed independently the total dataset is composed of 288 traces.

The effect of changing each variable independently will be now carefully examined.

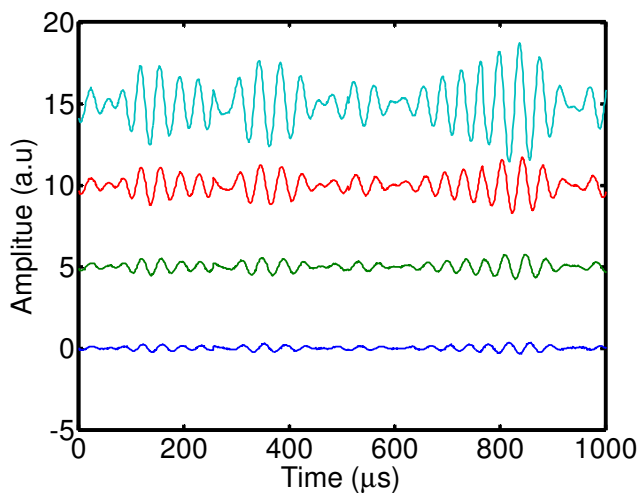


Figure 2.15 Effect of the magnet coil distance. The distance increases from top to bottom (0, 10, 20 and 30 mm).

In Figure 2.15 is shown the effect of the magnet coil distance, all the other parameters are the same for all the traces. It can be seen that the amplitude of the coherent noise increases as the distance decreases.

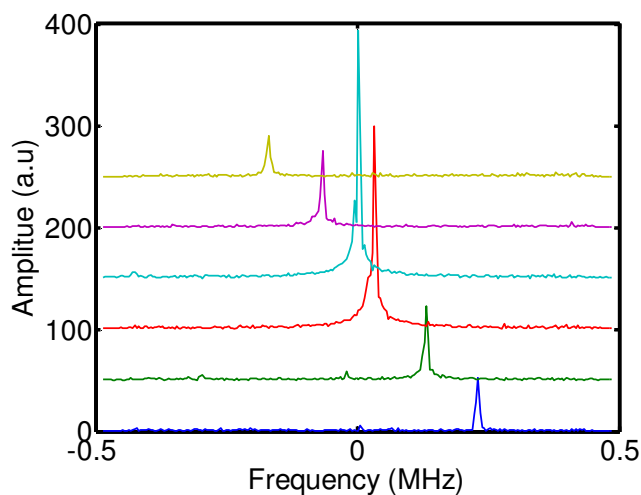


Figure 2.16 Effects of the different spectrometer frequency on the signal measured. This is expressed in the frequency domain to show the frequency shift of the peak. The spectrometer frequency increases from bottom to top.

In Figure 2.16 can be seen that the frequency of the coherent noise is the same whatever the frequency of the exciting RF signal is. The fact that the signal appears to be shifting is because the zero frequency is the demodulated one.

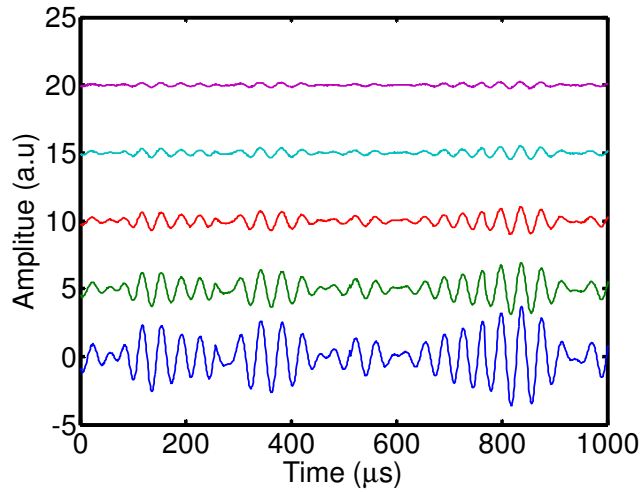


Figure 2.17 Effect of the transmitting power on the amplitude of the noise. The power increases from top to bottom.

In Figure 2.17 can be seen that the noise increases as the transmitting power increases.

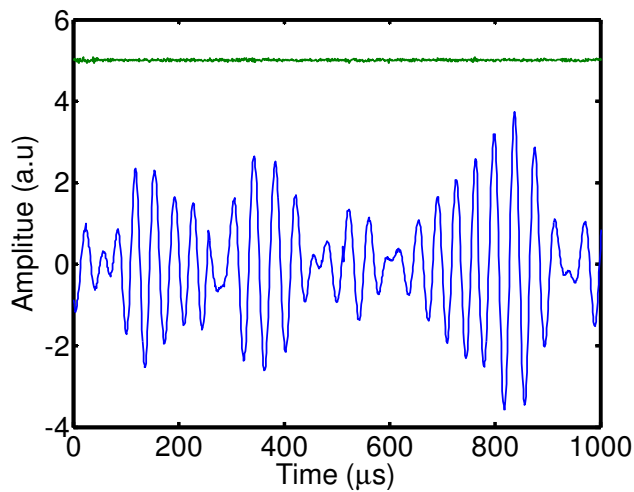


Figure 2.18 The effect of different pulse sequences. The top trace is the 8 step phase cycle, the bottom is the 4 one.

Figure 2.18 shows the effect of different phase cycles; the difference between the 4 step phase cycle and the 8 step is definitely clearly visible.

The conclusion that can be drawn is that the type of noise was coherent and strongly dependent on the experimental parameters, therefore due to some feedback of the instrument and not from external sources.

There are some other observations that can be made concerning the noise: that it increases when the magnet is closer to the coil, it increases when the transmitting power increases, it is at a fixed frequency and it is strongly phase cycle dependent.

All these observations led to the hypothesis that the origin of the coherent noise could have been an acoustic ringing, driven by the pulses. In fact while the coil is energised, it becomes magnetic, and if the fixed magnetic field  $B_0$  is not exactly perpendicular to RF field  $B_1$  (that should be in principle but is never completely true in practice) there are forces due to the interaction of the two magnetic fields. This force is stronger if the distance between the magnets is smaller or if the strength of one magnet is higher (a higher current passing the coil). The coil, as any object, has an intrinsic mechanical characteristic resonance frequency (in this case the mechanical frequency is considered and not electromagnetic frequency); if the frequency of the exciting force is close to the characteristic mechanical resonant frequency of the coil, it will vibrate, but not with a flat response (meaning not at the same frequency of the exciting signal) but at its fixed characteristic frequency. All these characteristics are present in the observed signals.

To solve this kind of problem, one possibility is to try to change the characteristic mechanical resonance frequency of the coil, or, even better, make it much stiffer so the same force causes a much smaller movement. This last approach has been employed.

### 2.3.3.3 Potting

To make the coil stiffer it has been decided to have it potted. This consists of placing a material capable of hardening in the empty spaces between the PCB on which the coil is printed and the metallic back plate. This space (without the back plate) is well visible in Figure 2.5 on page 53.

The back plate has been screwed onto the metallic frame and then the potting compound has been syringed in the empty space through a hole on one side. In this way no empty gap was left.

The potting compound used was the “Blk general purpose epoxy compound” supplied by RS components [142] (code 199-1424). It is supplied in a bag divided by a sector that when removed allows the components to mix and the hardening reaction to start. It remains workable for ~20 minutes and cure at room temperature producing moderate heat. It can be heated to increase the curing speed.

### 2.3.3.4 Analysis of the S/N following potting of the coil

The same experiment performed before the potting has been performed after the procedure. It has been found necessary to slightly change the tuning capacitance to take into account the modified characteristics of the coil, however, the dramatic changes seen in the results cannot be justified totally by this.

In the series of plots in Figure 2.19, the results of the test after the potting are shown; they can be directly compared with the plots from Figure 2.15 to Figure 2.18.

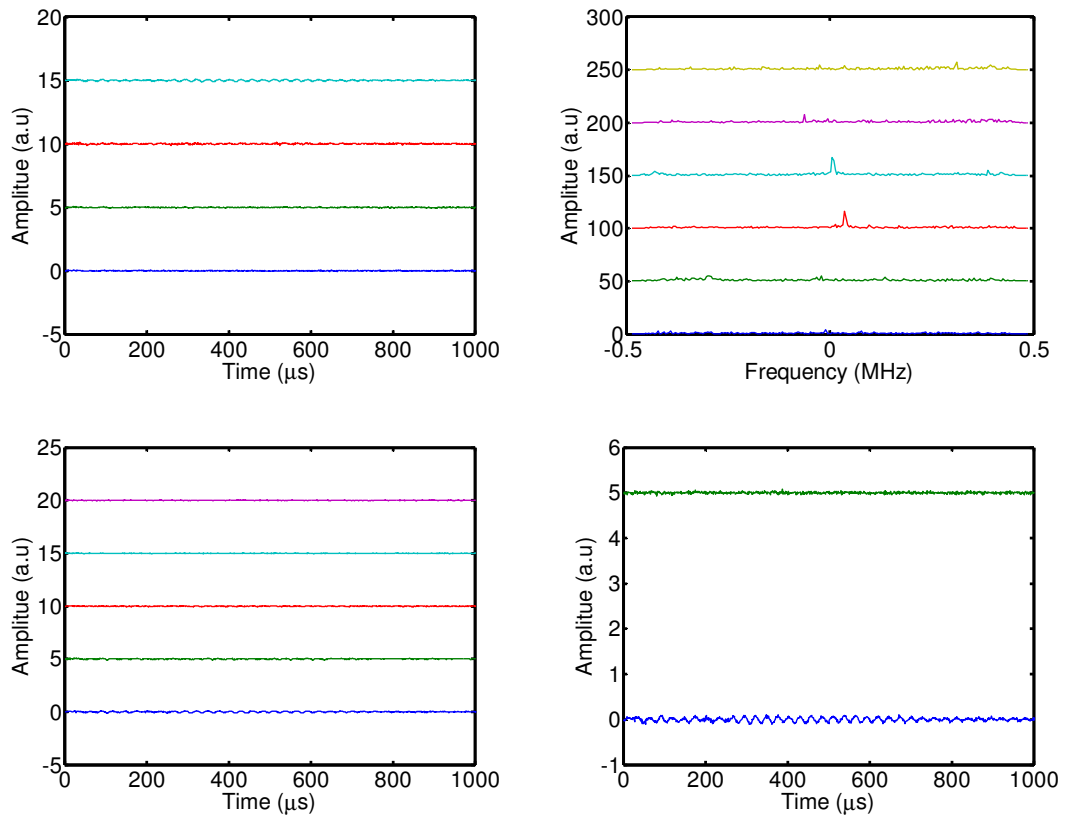


Figure 2.19 The results performed to check the success of the potting procedure. The parameters are the same as the ones used to obtain the data presented in the plots from Figure 2.15 to Figure 2.18. Top left plot is as a function of depth, top right as a function of frequency, bottom left as a function of power and bottom right as a function of phase cycle.

It is immediately noticeable that the amplitudes are decreased enormously, confirming that the source of the high coherent noise was the one hypothesised.

### 2.3.4 Shielding

Another completely different source of noise often comes from the EM field originating from transmission and electric powered tools. As an example a probable source of such noise is the transmissions of the satellite department of the university.

This kind of noise is usually much more difficult to detect and remove because the source is outside the control of the operator and therefore a cause-effect study as the one just described is not possible. The only way of dealing with these random (or not controllable) noises is to shield and earth the instrumentation. This has been found successful in our application. In particular a hole the size of the magnet has been cut in a couple of millimetres thick aluminium sheet. During the measurements the sheet has been placed on the surface before placing the magnet in the hole (Figure 2.20). This solution decreased the typical noise RMS amplitude from  $\sim 50 \mu\text{V}$  to  $\sim 10 \mu\text{V}$

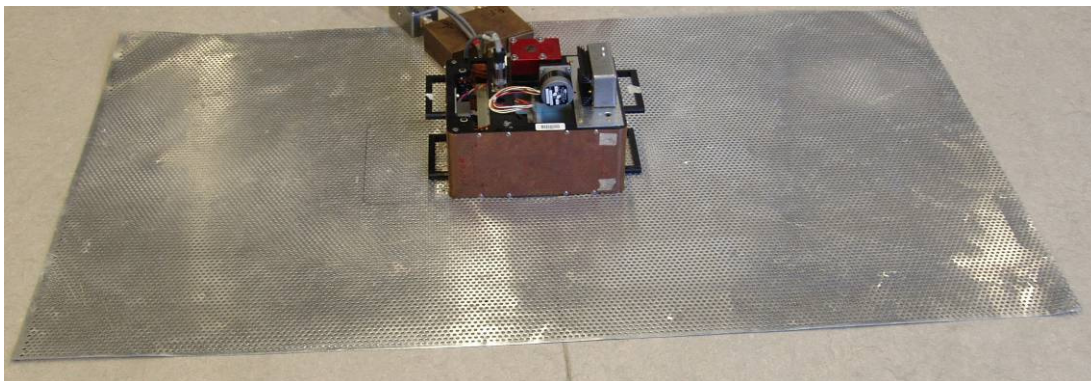


Figure 2.20 The magnet placed in the hole of the aluminium sheet shielding the sample (floor).

Sometimes it has been found very useful also to cover the magnet with a copper cloth. However, other times, especially in the lab, this additional shielding has been found detrimental for the S/N ratio. This is probably due to the fact that very peculiar combinations of noise frequencies or geometries were conveyed in the shielding. The main problem is that, of course, due to the open-side characteristic of the magnet it is not possible to completely shield and isolate it from everything. The empirical approach is not very scientific but must be admitted that sometimes is the only one that is realistically applicable, as happened from time to time in trying to minimise the noise on this magnet. Different combinations of shielding and earthing have been required in different positions within the lab or during the outside experiments. For this reason before each experiment, a few attempts have been required to make to try to minimise the noise changing the combinations.

## 2.4 Test experiments

### 2.4.1 Rubber block for calibration

To allow the calibration with the depth necessary for the reasons explained in paragraph 2.2.3, the profile of a uniform rubber block has been acquired. The result is shown in Figure 2.21.

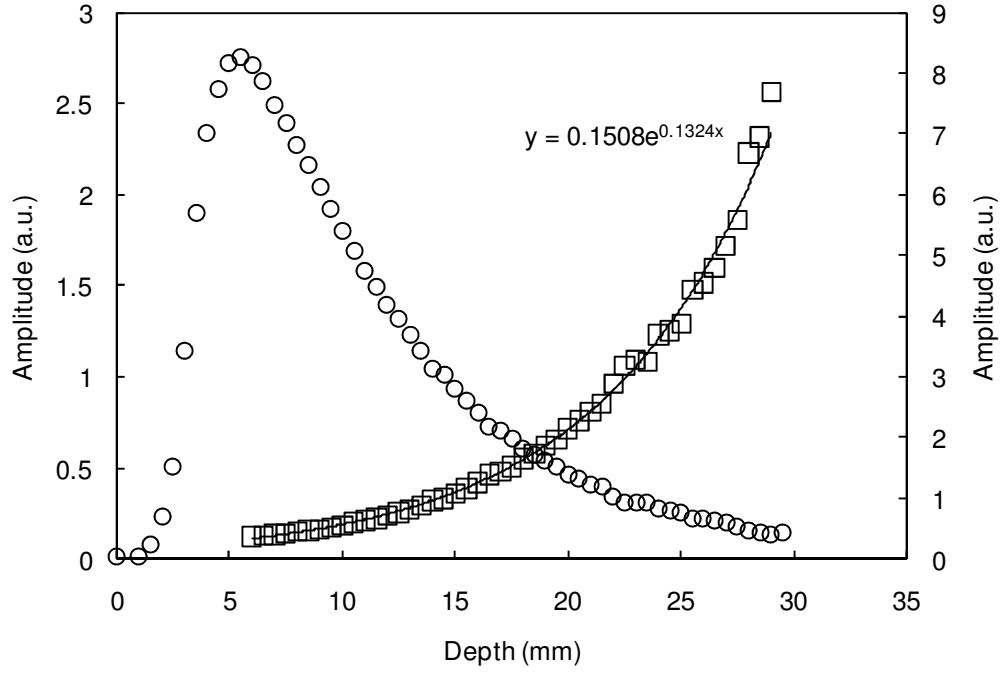


Figure 2.21 Rubber profile (circles) showing the decrease of sensitivity with the depth. Squares show the reciprocal of the profile from the point of maximum (6 mm depth) and its exponential fit. The solid line is the exponential fit. The amplitudes are both arbitrary but with different units.

The exponential behaviour of the fit in Figure 2.21 has been used as correction function. The curve has been renormalized to have value 1 at the first point (6 mm depth) obtaining the equation:

$$corr(d) = \exp(0.1324 \cdot (d - 6)) \quad (2.2)$$

This calibration has been then used to correct all the profiles measured afterwards.

### 2.4.2 Rebars and phantom

To exploit the effect of the steel (and therefore paramagnetic) reinforcing rebars on the signal and estimate how and for which distances or geometries the profiles would have been

affected, a series of tests have been performed. For these tests a phantom specimen consisting of 11 alternate layers of rubber and glass has been built. Each layer was 3 mm thick for a total phantom thickness of 33 mm. The rubber used was the RTV 2005 silicone elastomer (code 448 0163) supplied by RS components [142]. The material has been cast when liquid between two horizontal glass layers kept apart by metallic spacers that were removed upon solidification.

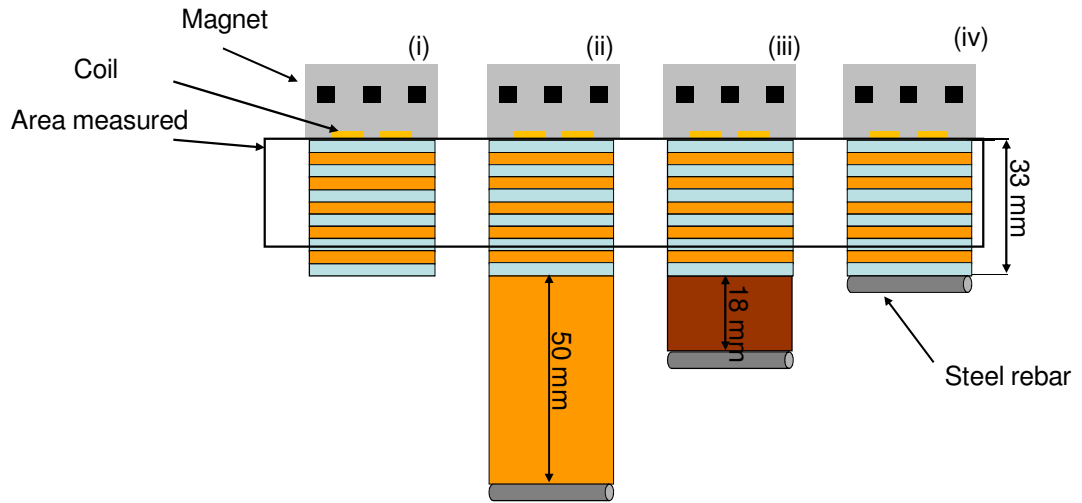


Figure 2.22 The setup of the measurements performed on the 1D phantom to determine the sensitivity of the signal of the Surface GARField into the vicinity of steel rebars. The 4 sections of the picture refer to different setups and therefore different experiments.

In Figure 2.22 the different setups used can be seen; 4 different magnet-bar distances have been used:  $d = \infty$  when the rebar was not in the vicinity of the magnet,  $d = 83$  mm when a 50 mm spacer was placed in between the 33 mm thick phantom and the steel bar,  $d = 51$  mm when a 18 mm spacer was in placed and  $d = 33$  mm when no spacer has been used. Also 2 different orientations of the bar have been analysed: parallel and perpendicular to the main magnetic field  $B_0$ .

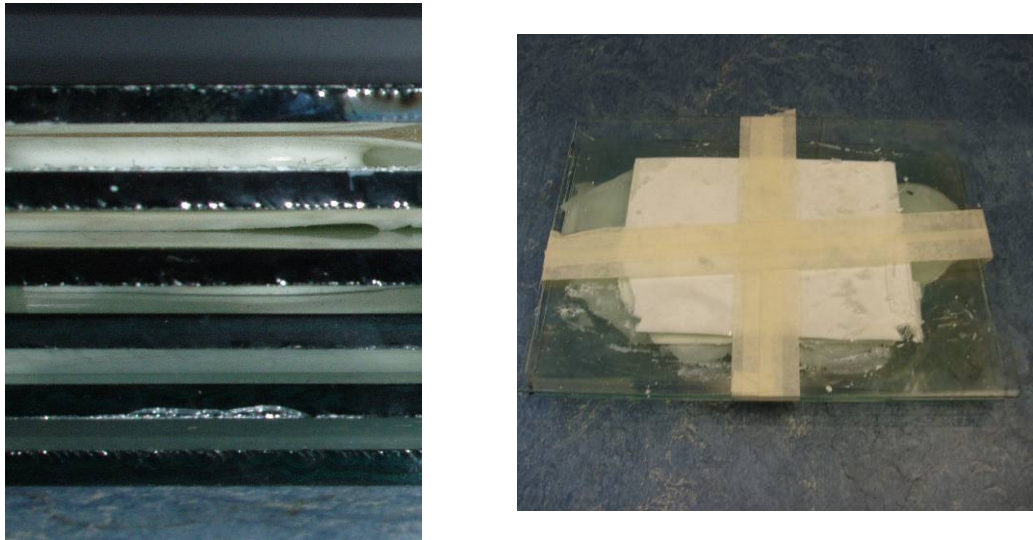


Figure 2.23 Left: lateral view of the phantom, right: top view

The results of the study to determine the effect of the reinforcing rebar are shown in the plots Figure 2.24 to Figure 2.26. Figure 2.24 shows the profile of the phantom without steel rebars, this corresponds to the setup (i) in Figure 2.22.

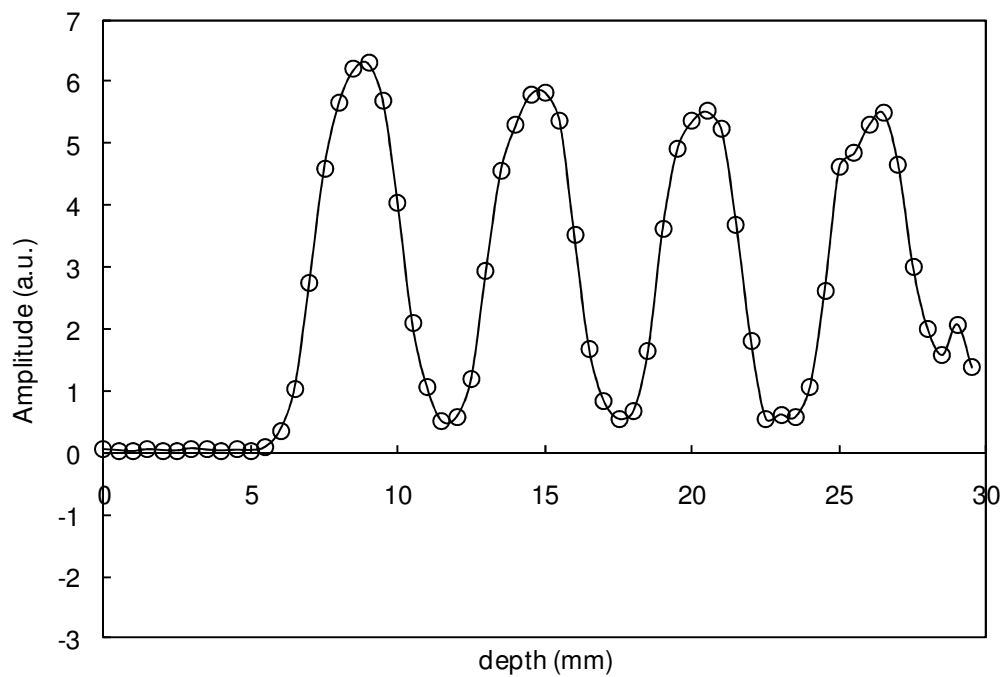


Figure 2.24 Profile of the phantom acquired without rebar; this corresponds to the setup (i) in Figure 2.22. The smoothed line is an aid for the eye.

Figure 2.25 shows the profile acquired without spacer. This refers to the setup shown in section (iv) in Figure 2.22 and bar parallel to  $B_o$ . The difference between this profile and the one acquired without rebar is shown as well in the plot.

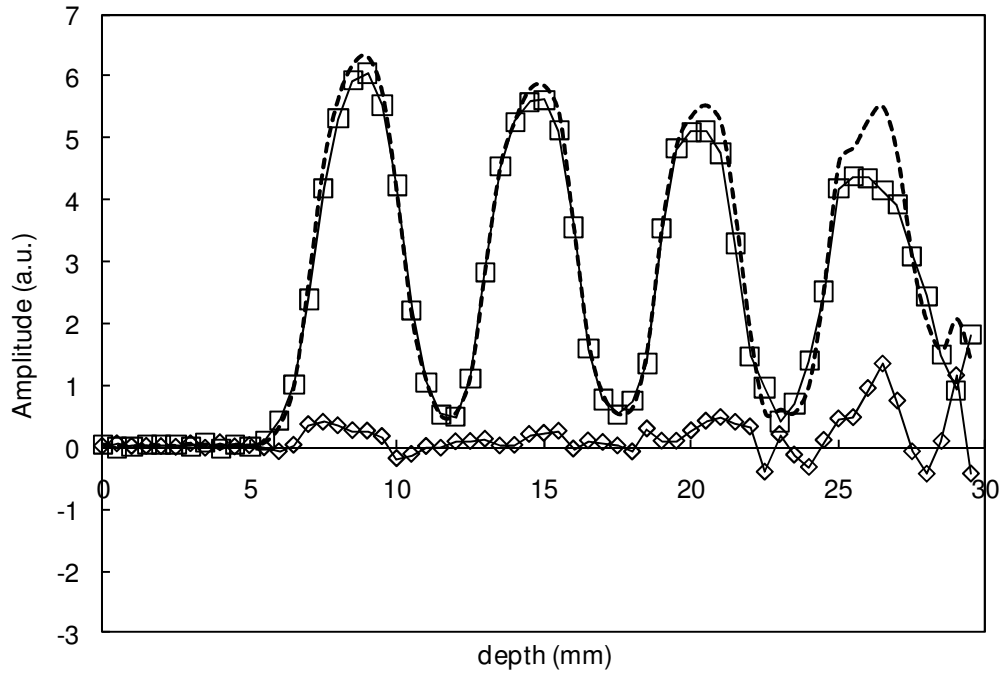


Figure 2.25 Squares are the profile acquired without spacer (setup as in Figure 2.22 (iv)) and bar parallel to  $B_o$ ; the thin solid line is a guide for the eye through the squares. The dotted line is the original profile (the line in Figure 2.24) and the diamonds are the difference between the two.

Figure 2.26 is a plot analogue to the Figure 2.25 but with the rebar perpendicular to the magnetic field instead of parallel. Also here the difference compared with the original profile is shown.

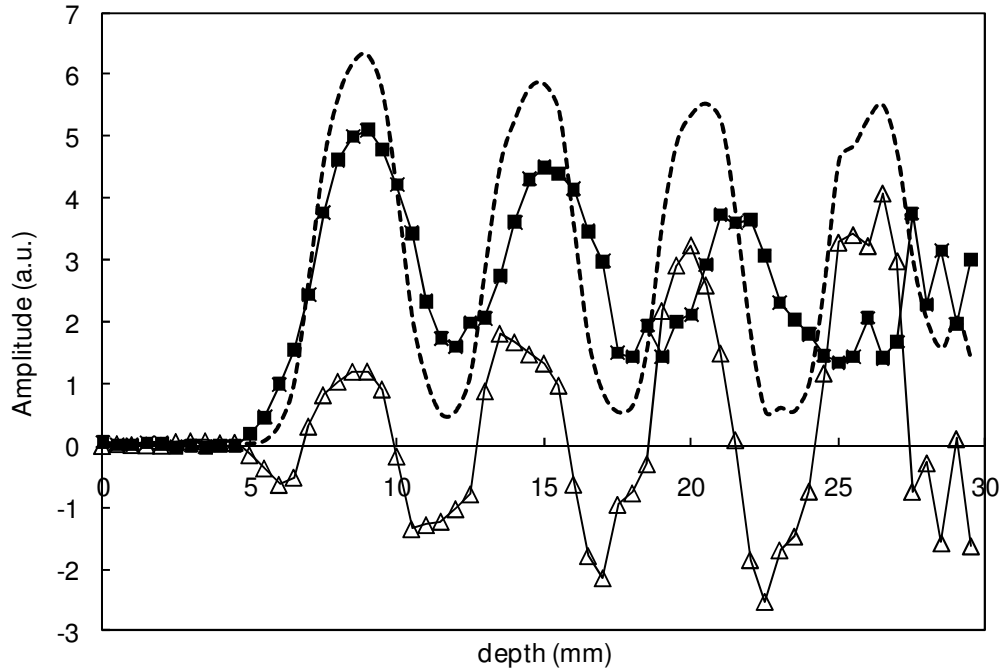


Figure 2.26 Squares are the profile acquired without spacer (setup as in Figure 2.22 (iv)) and bar perpendicular to  $B_0$ ; the thin solid line is a guide for the eye through the squares The dotted line is the original profile (the line in Figure 2.24) and the triangles are the difference between the two.

Whilst discussing the differences, it must be remembered that uncertainties increase with the depth due to the calibration factor that is not a constant with depth.

Because the results for intermediate distances were indistinguishable from the one obtained without steel bar they have not been plotted.

The first conclusion that can be taken is that the orientation of the steel bars under the sample plays a fundamental role. The profiles presented in Figure 2.25 and Figure 2.26 are acquired for the same distance but different orientation. Another conclusion (from the data not shown) is that the results are not affected for distances magnet-steel bars down to 51 mm (because in the setup in Figure 2.22 (i) (ii) and (iii) no difference has been noticed). Is remarkable to consider that at the last distance (section (iii)) the steel bar was “sticking” to the magnet, without however noticeably affecting the readings.

The conclusion is that in a typical operating situation the presence of the steel reinforcing rebars is not a major issue.

### 2.4.3 On-site experiments

The first outside application of the Surface GARField will be presented in this section. The samples measured will be a concrete floor that has been monitored during setting and drying

over 10 days and a thick screed applied to another floor. To obtain a more compact and smooth surface the concrete floor was treated, just after pouring, with a levelling tool (described as an “upside down helicopter”) that makes the bigger aggregates settle slightly leaving the finer aggregates and a richer cement pastes layer on the surface. This surface is roughly 5 mm thick.

For the profiles acquisition the parameters used are:

Parameter	Value	Units
Frequency	2.825	MHz
nrScans	2048	
bandwidthFile	1.024	MHz
nrPnts	32	
nrEchoes	64	
echoTime	150	$\mu\text{s}$
pulseLength	11	$\mu\text{s}$
repTime	333	$\mu\text{s}$

The duration of the experiments is strongly dependent (proportional) on the number of scans and the number of slices acquired; for the experiment shown in this thesis, with 2048 scans and 16 slices, the required time was just over 3 hours.

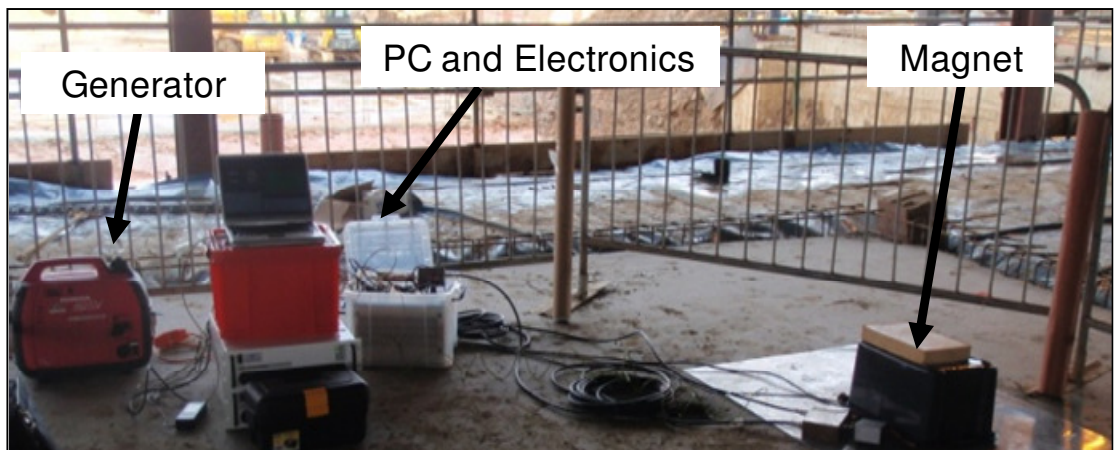


Figure 2.27 The experimental setup for the outside experiments. The spectrometer, motor controller, preamplifier and the most delicate parts of the electronic circuit are enclosed for protection in a plastic box.

The results of the series of measurements made on the concrete floor are summarised in Figure 2.28. The profiles have been acquired at 1, 2, 7 and 10 days from pouring.

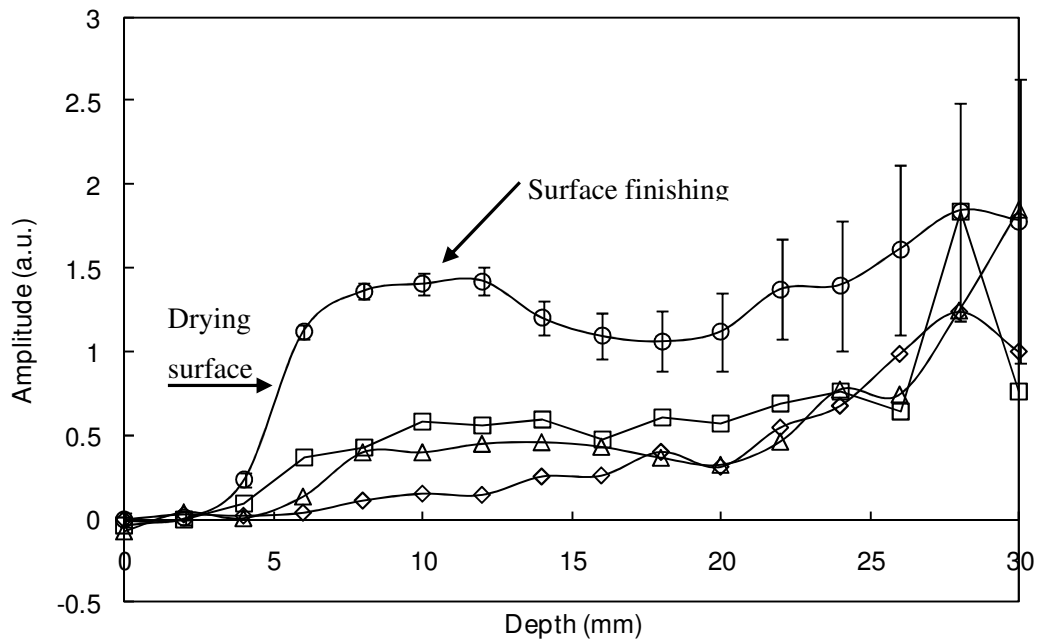


Figure 2.28 The profiles during curing acquired outside the lab on a concrete floor finished with ~5 mm of fine layer. Circles refer to 1 day after casting; squares after 2 days; triangles after 7 and diamonds after 10. The surface finishing is visible at the early stage (1 day). The depth is measured from the furthest position the magnet achieves, the sample surface is therefore at ~3 mm on the scale. The error bars on the first line are obtained multiplying the rms of the raw profile by the correction function.

The profiles in Figure 2.28 demonstrate the applicability of the Surface GARField to structures outside the lab. A good result is the ability to detect the surface finishing and to be able to capture the evolution of the moisture.

The error bars have been calculated estimating the fluctuation of the raw data profiles and then multiplying this number for the calibration factor. For this reason (already mentioned) the uncertainty increases with depth. In the next plots, to keep the plot “cleaner”, the error bar will not be plotted.

Another application has been the monitoring of another surface of a different nature. In this case a thicker (~15 mm) screed applied on the surface of a floor at the accommodation construction site has been monitored. Two locations have been compared one where the screed were freshly laid (laid in the afternoon and measured on the following morning) and another section that was laid two days earlier. The comparison between the two is shown in Figure 2.29.

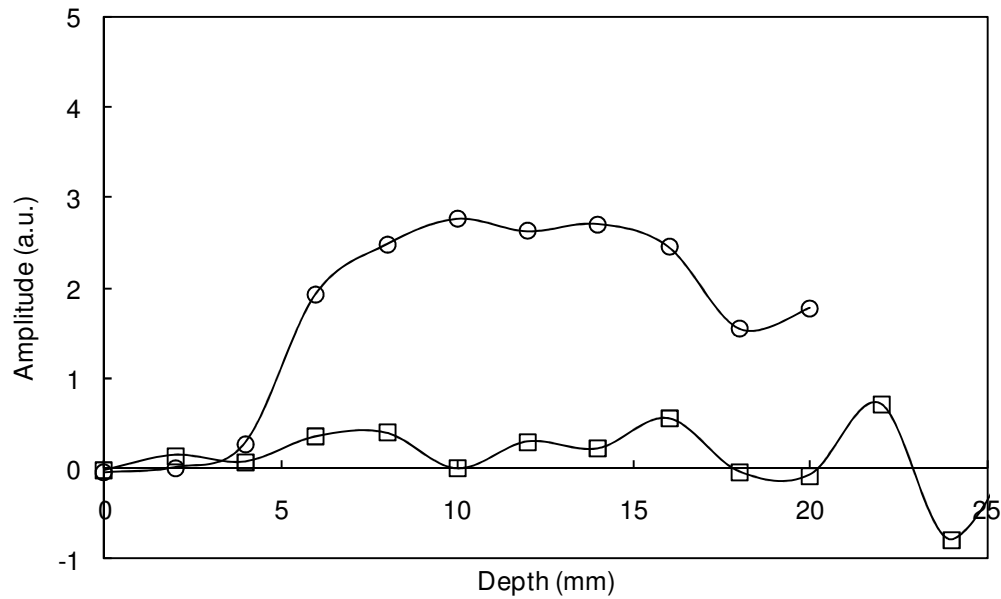


Figure 2.29 Comparison of two stages of drying for a screed laid on a concrete floor. Circles a few hour after laying, squares after 2 days.

Unfortunately, due to time constrictions (we were not allowed to stay on the construction site outside the working hours) this experiment is incomplete, allowing comparison of the two profiles only up to 20 mm depth. It can be immediately seen that the speed of curing for this material is much quicker than the concrete measured in the previously shown experiment, reaching an undetectable level after only two days.

#### 2.4.4 Calibration

An attempt has been tried to calibrate the instrument. The aim was to have an independent measurement to compare the amplitude of the NMR signal with.

It consists of burying some RH sensors in the concrete to monitor the moisture in it. The sensor used are the “Integrated Circuitry Humidity, Lead Pitch SIP” made by Honeywell and supplied by RS. The Manufacturers Part No.is HIH-4000-004 and the RS Stock No.2509176370.

The logging has been done with a National Instrument data logger (NI USB-6008 12-Bit, 10 kS/s Low-Cost Multifunction DAQ) directly supplied by National Instrument.

To achieve spatial resolution a Perspex holder has been built to keep the sensors at the constant distance between them of 2 mm. This holder while still outside the concrete can be seen in Figure 2.30 together with the data logger used. The concrete used has been a slab casted for the purpose and kept in the lab.

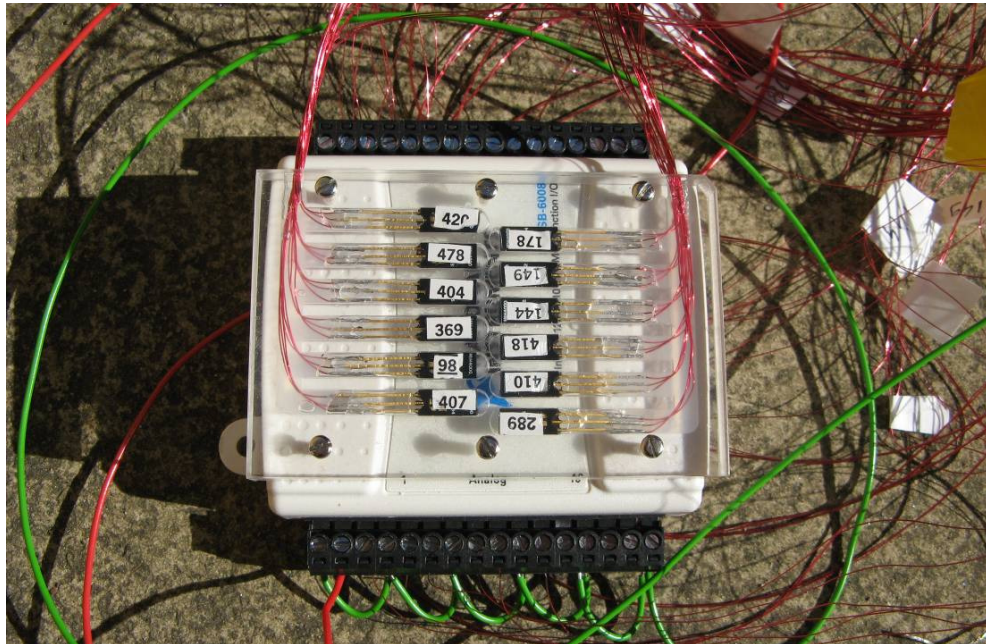


Figure 2.30 The Perspex holder to keep the RH probes at the right depth in the sample and all the wiring. The white box under the holder is the acquisition board used.

In Figure 2.31 the same holder can be seen after being buried into the concrete. Are visible the small holes (0.5 mm) which allow the moisture but not the concrete to reach the sensor.

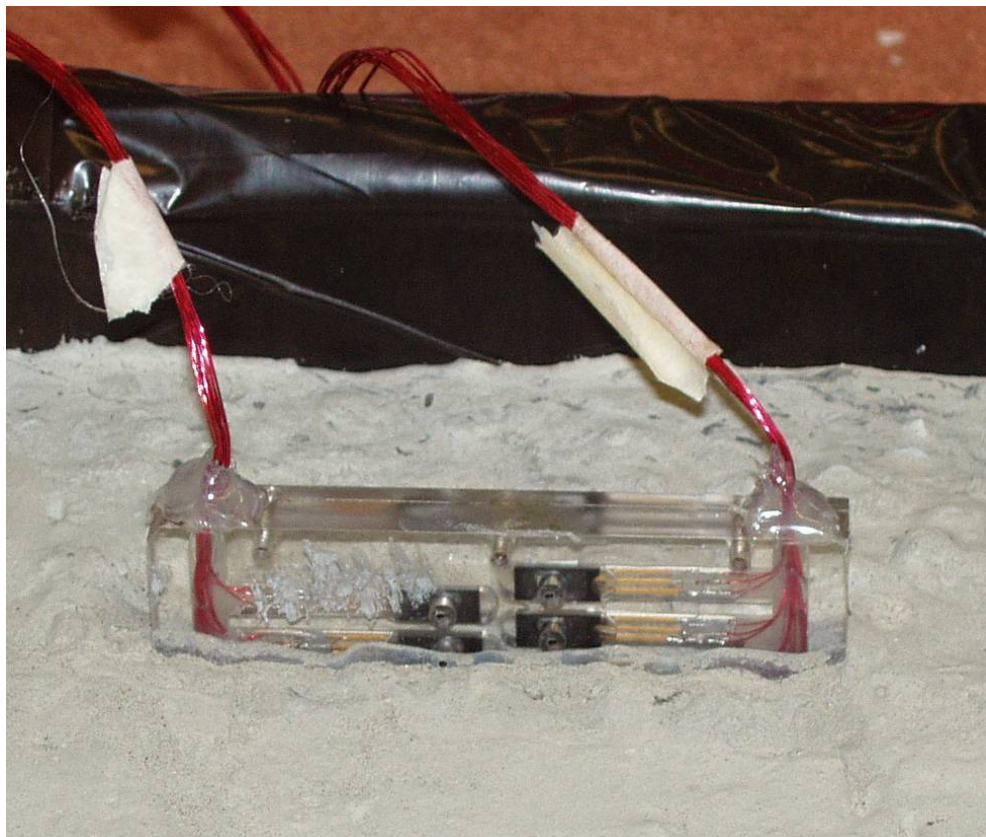


Figure 2.31 The RH sensor embedded in the concrete sample.

The sample have been sealed in a plastic bag just after casting to keep all the moisture in and data acquisition has started just after setting. It has been left on for one week allowing the acquisition of 100 profiles with the typical acquisition parameters used also in the on-site experiment. The vast majority of the NMR signal has been lost in the first couple of days, after which the variation of the signal intensity becomes undetectable. The RH probes, instead, keep giving the same readings after weeks without detecting any decrease of the moisture in the concrete. To check if the RH probes were able to recover or if they were completely damaged from the concrete, the plastic bag has been opened and the concrete left to dry in the open air. The data acquired from the RH during this drying in the open air are presented in Figure 2.32.

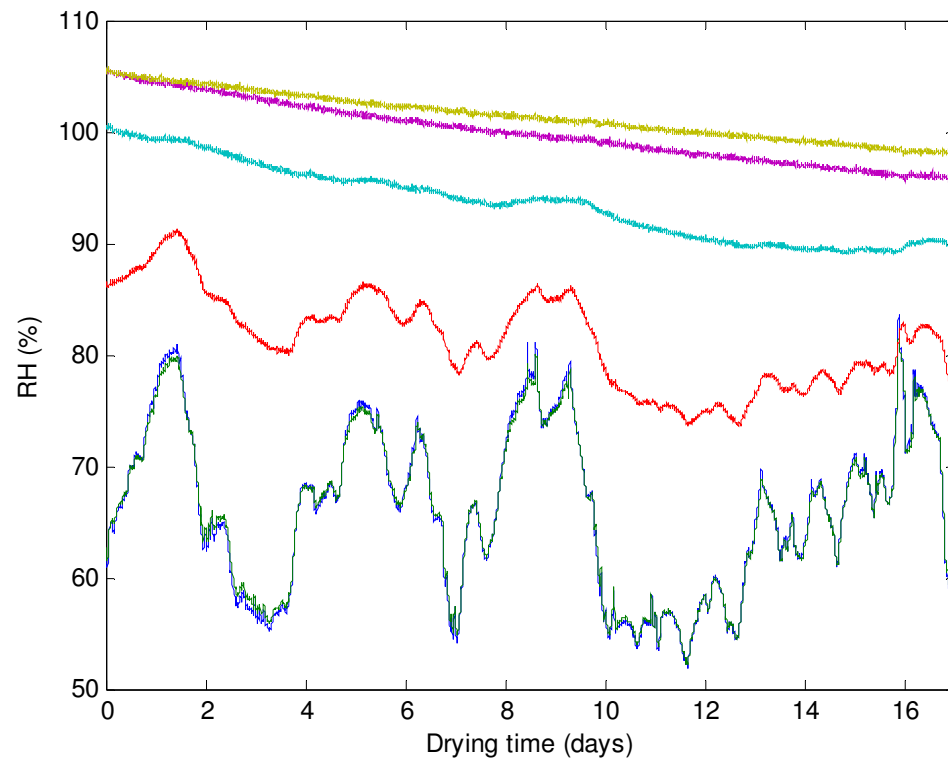


Figure 2.32 Plot of the RH measured as a function of drying time for the uncovered slab. The depth of the sensors increases from bottom to top. The two lower traces refer to the sensor outside the sample that are therefore subject to the room RH variations.

It is clear that the RH sensors saturate at high moisture and are not able to detect changes in the range of moisture content in which the NMR signal can be acquired. In addition, it seems that the calibration is not very reliable at high moisture contents obtaining values higher than 100 % RH.

In Figure 2.32 it can be seen the slow recovery of the sensor deeper in the sample and the room RH fluctuation measured by the sensor not buried (visible in Figure 2.31). The conclusion drawn is that this kind of sensor is not suitable for this very high RH environment.

An alternative can be to use resistivity measurement, this kind of probe are been developed by Raupach et al. [143] at the Institute for Building Materials Research, Aachen University. This technique is not very highly resolved because the path of the current is not well defined; however it is probably the only solution at the moment having the alternative attempt of the RH probes failed.

## **2.5 Conclusions**

Has been shown in this chapter the improvements achieved on the S/N ratio of the Surface GARField and the first application outside the laboratory.

The high coherent noise present has been carefully analysed and has been found to be due to acoustic ringing (mechanical vibrations). This issue has been brilliantly solved by stiffening the coil via potting obtaining a noise decrease of over 90%.

The bulky quarter wavelength cable placed to protect the receiver preamplifier during transmission of the pulses has been replaced with a homemade lumped element  $\lambda/4$ . This has been carefully tested showing comparable (equal) performances in terms of signal detected and pulse length, while the dead time seems slightly reduced.

The first applications of the Surface GARField outside the laboratory confirmed the feasibility of the experiments. Different samples have been characterised showing different curing speeds. The resolution has been demonstrated to be sufficient to detect a  $\sim 5$  mm surface finishing layer on the top of a concrete floor. The power supply, obtained via a 2 kW petrol generator, has been found to be more than sufficient to feed all the equipment (included the 2 kW RF amplifier), stable and possibly “cleaner” from RF interferences than the university main.

The effect of the reinforcing rebars has been investigated showing that the magnet is almost insensitive to steel bars as shallower as  $\sim 5$  cm. The orientation of the bars in respect of the main magnetic field played a strong role, for quantitative analysis sampling over different areas may have to be taken into account.

The attempt of the calibration using RH probes has not been successful, because the range of applicability of the two techniques (NMR and probes) seems not to overlap.

## 3 2-D relaxometry

### 3.1 Introduction

As discussed in 1.4.6, the  $T_2$ - $T_2$  experiment explained in paragraph 1.4.2.2 has been successfully applied on cement in previous work carried out at the University of Surrey within the Nanocem core project 2 and the results were published in [68]. The main outcomes of the work are the ability of detecting and estimating the speed of the exchange between two different magnetisation reservoirs in cement and estimating the pore size of these two reservoirs (see sections 1.4.2.2 and 1.4.6).

Concerns came from the fact that it looks unrealistic to be able to detect an exchange over such a long distance (of the order of microns) between structures of 3 orders of magnitudes smaller (nanometers). In practice, although being a huge step forward in the understanding of pore water dynamics and interactions in cement pastes, that work [68] (as any research work) has left some questions open.

Another question remained open from the work mentioned arises from the fact that the exchange peaks in  $T_2$ - $T_2$  experiments are visible only for young samples (up to circa 4 days). This may tell us something about the evolution of the connectivity of the pore space; however, the reason has not been yet clarified.

In addition to the questions left open by the previous project, discussions with other projects during NANOCEM meetings and presentations the question was raised as to the validity of an alternative explanation where the water seen to exchange was between pores of comparable size ( $r = v/s$ ) but different surface relaxivity  $T_{2,s}$ .

In this hypothesis, the apparently larger pores type could, instead, have a lower density of paramagnetic impurities (mainly  $\text{Fe}^{3+}$ ) than the apparently smaller ones.

### 3.2 Theory

Because the entire pore size analysis in a porous media is based on the equation (1.15), where the characteristic size  $v/s$  appears always multiplied by the surface relaxivity it is very difficult to discriminate between the effects of higher  $v/s$  ratio or a higher relaxivity. Figure 3.1 show a sketch of two materials of different porosity and paramagnetic impurities whose combined effect is to obtain an equal relaxation time.

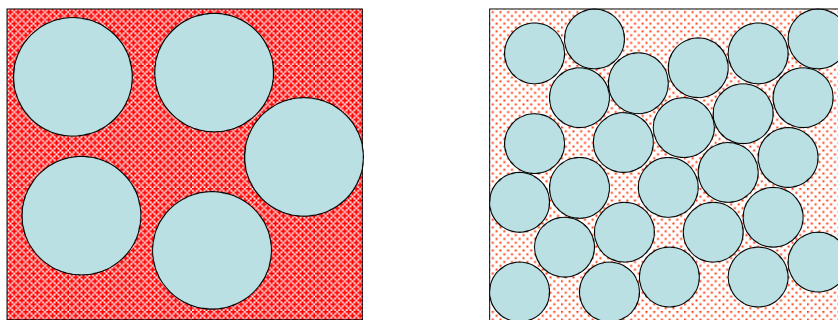


Figure 3.1 sketch of two different materials having the same  $T_{2,s}$ . The left has higher surface relaxivity but also higher V/S ratio.

There are two alternative hypotheses to explain the exchange seen by the  $T_2$ - $T_2$  experiment; the first, suggested in [68] is that the exchange is between the smaller and larger inter crystallites, the other is that the exchange is between intra sheet and inter crystalline water. If the first one is considered, the different sizes could be related to the inner and outer product as suggested again in [68].

The aim of the work described in this chapter is to try to clarify the effect of the Fe in the relaxation time analysis and in particular to determine if the alternative explanation of exchange between two materials with different paramagnetic impurities was realistic or not. The doubt can be summarised in the question “in the  $T_2$ - $T_2$  exchange experiment, are we looking at exchange between pores reservoirs of different pore size, or simply with different  $\text{Fe}^{3+}$  surface concentration?” Trying to pursue this aim the consideration of the different alternative hypothesis has always been kept in mind.

The reason for the different paramagnetic richness environments originated by the fact that cement is highly heterogeneous and is well known that some of the hydrate phases (as the AFm) include quantities of Fe much higher than other. However, small quantities of Fe could also be enclosed in other phases as for example the highly interesting C-S-H which may contain low quantities of Fe impurities.

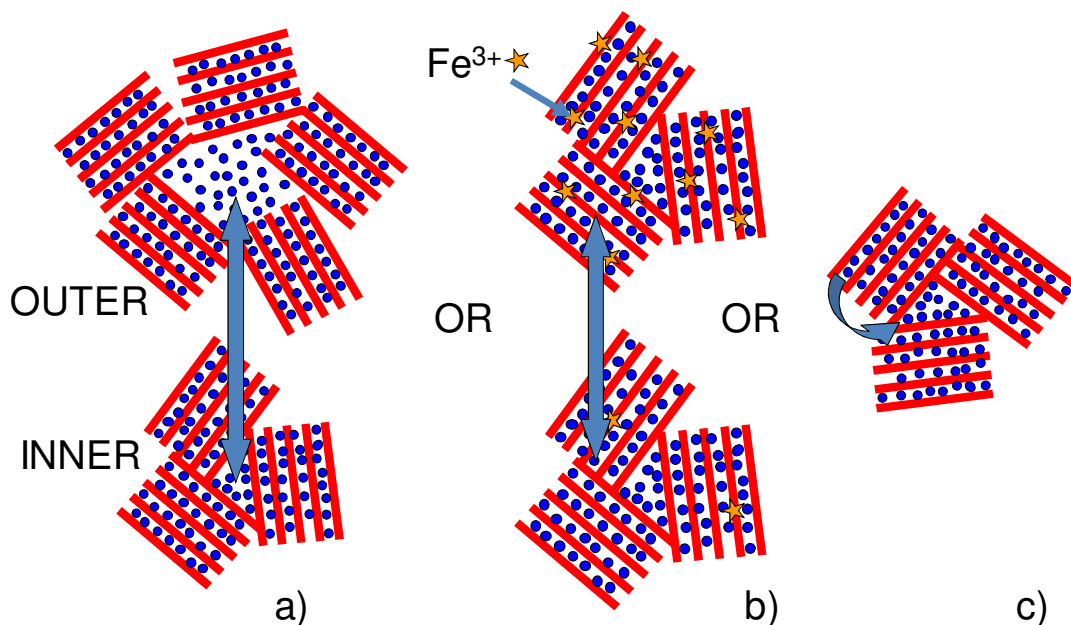


Figure 3.2 Alternative hypothesis to explain the exchange seen in the  $T_2$ - $T_2$  exchange experiment. a) exchange between inner and outer product having different intra sheet porosity; b) exchange between materials with different paramagnetic impurity concentration, c) exchange between inter and intra C-S-H layers.

The idea of tackling this question has been to try to modify the Fe content in the samples. If the different paramagnetic impurities hypothesis was true, few alternative possible results could have been hypothesized. These are described below.

In the case of two reservoirs of equivalent total volume and different relaxation times the spectra can be schematically represented as two peaks of the same amplitude but at different relaxation times (Figure 3.3). The distributions chosen for the examples presented here are Gaussian.

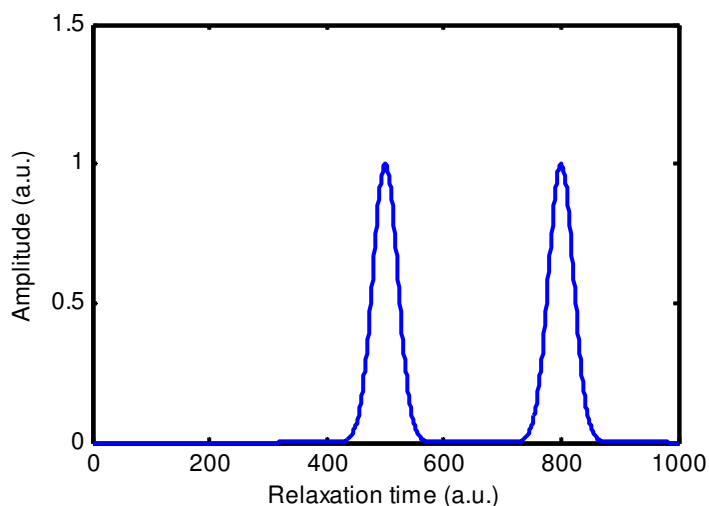


Figure 3.3 schematic relaxation spectra for two magnetisation reservoirs of equal total volume but different relaxation time (representing two materials with the same total porosity and either different pore size or surface relaxivity)

The first possible expected result as the Fe is added is that the material with higher Fe content, and therefore higher relaxivity (shorter relaxation times, and therefore on the left of the plot) “pick up” the additional Fe. This can occur in the hypothesis that the one with lower Fe content was already Fe saturated. In this case, the relative peak moves to even lower values further left. The effect on the spectra is to transform the plot in Figure 3.3 into something similar to the one in Figure 3.4:

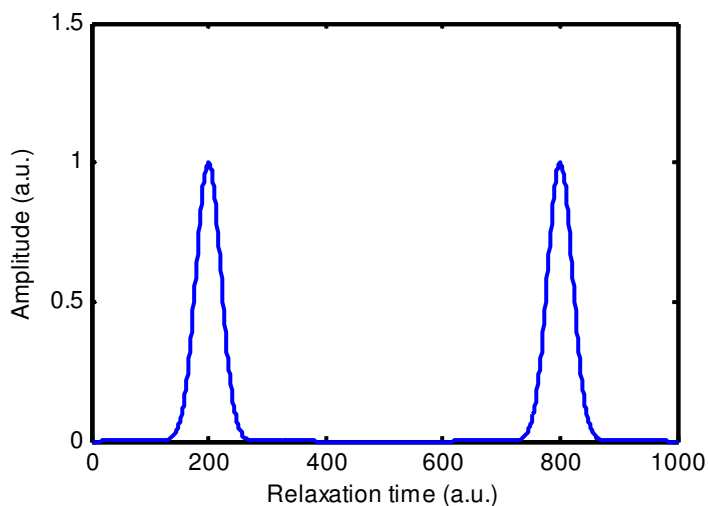


Figure 3.4 How the plot in Figure 3.3 changes if the added iron goes in the short relaxing environment.

An alternative hypothesis is that the Fe concentration of the two materials is a constant and the amount of material the variable as Fe is added. In this case the ratio of the amplitude of

the peaks varies with the Fe addition increasing the amplitude of the short component peak on the left and decreasing the amplitude of the long component one. The visualization of such process is to modify the spectra in Figure 3.3 in the one presented in Figure 3.5

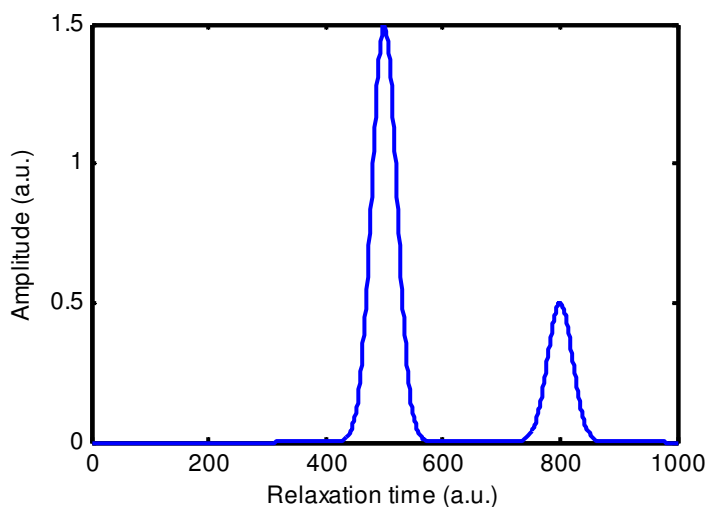


Figure 3.5 How the plot in Figure 3.3 changes if the Fe concentration in the two materials remain the same and the relative amount of the two materials the variable as Fe is added.

Third and last hypothesis is that as Fe is added, it is introduced in both materials, decreasing the relaxation time of both environments; in this case both peaks shift obtaining a relaxation spectrum similar to the one in Figure 3.6.

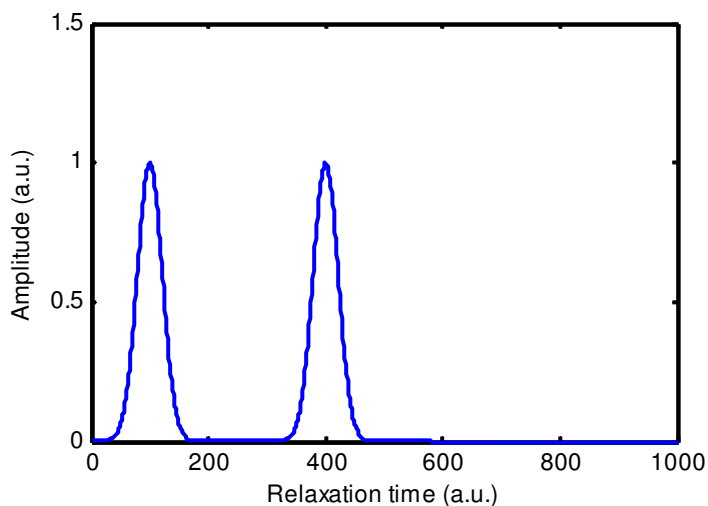


Figure 3.6 How the plot in Figure 3.3 changes if the Fe added goes in both materials.

Another observation, not directly related with this doping experiment, but useful to mention is that, in the case of a situation where the different relaxation times are due to different

paramagnetic impurities and not different pore sizes, the total removal of them bring the peaks together and overlaying.

To achieve the result of having different quantity of Fe in the sample 3 approaches were proposed and have been tried.

The first was to try to “dope” white cement samples; the idea of this came from the fact that commercial cements all have several different characteristics and was apparently not really possible to compare different cements considering them only for their Fe content. They all hydrate in different ways, producing different proportions of materials, and being unsure which signal the  $T_2$ - $T_2$  detects was really impossible to understand what effect was due to the Fe and what to all the other characteristics.

Another possible approach was to try to work with much simpler and better defined materials than ordinary cement. In this way we could have analysed only the interesting part of the phenomenon, “filtering” out other complications. The material proposed has been Alite ( $C_3S$  in the cement chemistry nomenclature). This material hydrates similarly to cement (although has been reported to have a quicker reaction) producing pure C-S-H without other phases such as ferrite and ettringite.

On this idea of using simpler systems, a paste of C-S-H synthesised from analytically pure reagent and therefore totally Fe free, has been analysed.

### **3.3 Experimental materials and methods**

#### **3.3.1 Pulse sequence**

$T_2$ - $T_2$  experiments have been performed at room temperature on a Maran 20 MHz  $^1H$  NMR frequency benchtop spectrometer (Oxford Instruments Molecular Biotools Ltd, Oxon, UK). The data have been acquired following the pulse sequence described in paragraph 1.4.2.2. The echoes were logarithmically spaced over 128 intervals with the first  $\tau$  value equal to 25  $\mu s$  and the last equal to 25 ms. Using these values the first echo occurred at 50  $\mu s$  and the last at  $\sim 1$  s; therefore all the range of  $T_2$  from few tens of  $\mu s$  up to circa 1 s was well explored. The first dimension has been acquired for only the even echoes to decrease the length of the experiment as the odd are not required due to phase evolution errors, In the second dimension, however, all the echoes have been acquired, (although only even echoes are used in the analysis); the acquired dataset size was therefore 128 x 64.

The typical pulse length was 2.3  $\mu s$  for the 90 degree and 4.6  $\mu s$  for the 180 degree one; the dwell time 1  $\mu s$  and 8 points per echo were acquired with a filter width of 200 kHz. The

receiver delay was kept constant to 1 s from the end of the pulse sequence and the typical number of scans was 128; with this accumulation the experiment lasted 2.5 hours for each storage time, but for some sample with lower signal 256 scans have been used doubling the acquisition time.

Full  $T_2$  decay has been achieved in all the experiments; this requirement has been imposed for maximum signal detection,  $T_2$  resolution and for the stability of the 2D Laplace inversion used to analyse the data.

The phase cycle used was (in timing order):

First CPMG 90	x, -x, x, -x, -x, x, -x, x, y, -y, y, -y, -y, y, -y, y
First CPMG 180	y, y, y, y, -y, -y, -y, -y, x, x, x, x, -x, -x, -x, -x
Storage 90	x, -x, -x, x, -x, x, x, -x, y, -y, -y, y, -y, y, y, -y
Second CPMG 90	-x, x, -x, x, x, -x, x, -x, -y, y, -y, y, y, -y, y, -y
Second CPMG 180	y, y, y, y, -y, -y, -y, -y, x, x, x, x, -x, -x, -x, -x
Acquisition	x, -x, -x, x, -x, x, x, -x, y, -y, -y, y, -y, y, y, -y

Different storage delays have been used, however, the fact that during the storage time the magnetisation decays with constant time  $T_1$  puts an upper limit to the applicable values. Typical values used were in the order of 1 to few milliseconds, but, in the case of the C-S-H, also storages up to seconds have been tried.

### 3.3.2 Laplace inversion

The time domain data acquired as described above have been analysed through Laplace inversion using the algorithm proposed by Venkataramanan et al. [66] and implemented in Matlab by Y.Q. Song of Schlumberger Doll Research called Fast Laplace Inversion (FLI) running on a desktop computer. A full 64×128 dataset were analysed within seconds.

Care should be used in determining the limit of applicability of the algorithm. Song [104] extensively examined this mainly in terms of the S/N ratio, the regularisation parameter introduced in paragraph 1.4.5.1, and their relationship. Our approach to have reliable results has been to keep the regularisation parameter  $\alpha$  constant equal to 1 for almost all the experiments and setup the acquisition parameters (e.g. the number of scans) to achieve a S/N ratio equal to ~400. These parameters have been tested and found that the inversion was reliable. In some cases, where the S/N was particularly good, also smaller values of  $\alpha$  have been used to try to detect additional peaks. For the dataset with a considerable lower S/N, instead, an empirical test to check the uncertainties of the amplitudes obtained via inversion

has been occasionally applied. It consists in determining the average amplitude of the noise of the dataset (calculated as the RMS of the last line and last row of the dataset) and adding to the measured dataset an artificial source of white Gaussian noise with amplitude equal to the RMS. The uncertainties in the amplitudes have then been extracted from the scatter of the results obtained from the same dataset but different realisation of random numbers.

### **3.3.3 ESR measurements**

To measure relative amounts of paramagnetic impurities ESR experiments have been performed in the chemistry department of the University of Aberdeen in collaboration with Professor Russell Howe and his group. The instrument used was an electromagnet with Bruker spectrometer and the range of frequency sampled was between 0.05 to 0.55 Tesla.

Because the interest was in the relative amount of paramagnetic impurities contained and not in the absolute amount, a reference sample has not been measured. This kind of measurement has been previously done on a different unhydrated white cement powder by Montheilhet [68]. In his work also other materials and hydrated pastes will be measured.

### **3.3.4 Materials and sample preparation**

The ordinary cement samples have been prepared using the materials supplied by the Ecole Polytechnique Fédérale de Lausanne (EPFL). At the beginning of all the Nanocem projects, a selection of representative materials were chosen and a large amount of each one from the same batch were stored on the site of the consortium coordinator (EPFL). This wise action ensures that every project is working with exactly the same material, independent of the natural and quite broad variability of each production plant. The results coming from different projects are therefore comparable and the analysis performed by one project can be used by all the others. Thanks to this we have full characterisation of all the materials.

According to the Nanocem nomenclature within the projects the cements used in this thesis are the A as white cement and the B and C as greys. The full characterisation performed at the EPFL by Vanessa Kocaba is reported in Table 3.1.

Phases of anhydrous cements (%)	Formula	Cement A	Cement B	Cement C
<b>Alite</b>	$C_3S$	67.1	51.4	62.3
<b>Belite</b>	$C_2S$	23.6	21.1	18.4
<b>Ferrite</b>	$C_4AF$	0.0	10.0	7.1
<b>Aluminate</b>	$C_3A$	3.5	6.5	6.0
<b>Lime</b>	C	0.8	1.6	0.0
<b>Periclase</b>	M	0.2	1.9	0.7
<b>Gypsum</b>	$CaSO_4 \cdot 2H_2O$	0.0	0.3	0.7
<b>Hemihydrate</b>	$CaSO_4 \cdot 0.5H_2O$	0.8	1.9	1.6
<b>Anhydrite</b>	$CaSO_4$	2.9	2.8	2.1
<b>Portlandite</b>	CH	0.5	0.9	0.6
<b>Calcite</b>	$CC$	0.6	1.8	0.5
<b>Quartz</b>	S	0.0	0.0	0.0
<b>Total</b>		100.0	100.0	100.0

Table 3.1 characterisation of the cements used (from [144])

The  $C_3S$  and doped  $C_3S$  samples (that will be tagged with the abbreviations  $C_3S$  and  $C_3SF$  respectively, with F indicating the Fe addition) as well as the synthesised C-S-H have been prepared by members of the André Nonat group at the University of Bourgogne (Dijon, France).

The procedure used to prepare the C-S-H is the one described in [145]. The procedure consists of homogenising a dry mix of  $Ca(OH)_2$  and highly reactive high surface silica gel and then dissolving the mixture in  $CO_2$  free distilled water. The container, that has to be air tight to prevent carbonation, has to be kept agitated to facilitate the reaction for several months.

The two  $C_3S$  samples were laboratory made [146] by burning a stoichiometric mix of  $CaCO_3$  (Prolabo), and silica (Aerosil 380 Degussa) at  $1600^\circ C$ . The mix is successively burnt and ground until the reaction is completed (checked by X-ray diffraction). For the iron enriched sample, a small amount of  $Fe_2O_3$  is introduced with  $Al_2O_3$  and  $MgO$ .

The chemical analysis of the product determined by X-ray fluorescence is given in Table 3.2.

Phase	Percentage
SiO <sub>2</sub>	25.33 %
Al <sub>2</sub> O <sub>3</sub>	0.50 %
Fe <sub>2</sub> O <sub>3</sub>	0.77 %
CaO	73.08 %
MgO	0.08 %

Table 3.2 chemical analysis of the doped C<sub>3</sub>S determined by X-ray fluorescence (from [146])

The X-ray diffraction pattern (recorded by Nonat, not reproduced) shows the coexistence of 2 main phases, triclinic C<sub>3</sub>S and a monoclinic solid solution Ca<sub>54</sub>MgAl<sub>2</sub>Si<sub>16</sub>O<sub>90</sub>. The ratio of these two phases has been determined by full profile analysis by the Rietveld method (59 % C<sub>3</sub>S, 37 % monoclinic alite and 4 % C<sub>2</sub>S).

The C-S-H, which has been received in suspension, has been centrifuged at 2000 rpm for 20 minutes so to obtain a paste of a consistency similar to toothpaste. Unfortunately, it is very difficult, if not impossible to determine the final concentration of the synthesised C-S-H after centrifugation; this is because an undefined amount of material always remained in suspension in the liquid phase.

The doped cement samples have been supplied by Tiziana De Marco and Luca Bottalico of CTG Italcementi and have been produced in the CTG laboratories in Bergamo with the following procedure:

1. The cement powder has been carefully dried.
2. The finely ground (< 315 µm) iron powder has been added. 6 samples have been prepared with the following amounts: 0 % for the reference, then 0.25 % 0.50 % 1 % 2 % and 5 %.
3. The mixture has been dry mixed for 1 hour in a homogeniser laboratory mixer specific for powders
4. The powder has been hand mixed with a water/cement ratio of 0.35 and the samples cured sealed at 20 °C for one week.
5. After curing the samples have been crushed and cooked again at 1400 °C for 30 minutes.

The obtained powders have been subsequently shipped to Surrey and used to prepare pastes samples as if they were be ordinary cement powder.

The preparation procedure described has been suggested because during the cooking at 1400 °C the conditions are similar to the one in the kiln during the production of cement. The phases partially melt and therefore the material should mix really deeply within the phases.

The collaboration with Italcementi also allowed having the characterisations of both the clinker powders before shipping them to the University of Surrey and the cement pastes after the NMR experiments were performed at the University of Surrey. The results of these analyses are shown and discussed in the next sub section.

The mixing procedure was agreed as well with all the other Marie Curie Nanocem projects because previous projects carefully examined the effect of different preparation parameters that were apparently insignificant such as the mixing speed and time or size of the batch and some differences were found (although the reasons of those differences have not been fully investigated and may have originated simply by different amount of energy introduced by the different procedures).

160 grams of cement have been used for each cement mix. The water to cement ratio used has been kept constant to 0.4, and therefore 64 grams of distilled water were used. The mixer used is equipped with a rpm meter and the paddle used to mix is standard (within the Nanocem projects, and supplied by the EPFL) as well the timing of the mixing procedure, that is constituted by 3 intervals

1. 3 minutes mixing at 500 rpm
2. 2 minutes pause during which the absence of sedimentation on the bottom of the container were manually checked
3. Additional 2 minutes of mixing at higher speed (2000 rpm)

For the mixing of the  $C_3S$  and doped  $C_3S$  pastes, as well as for the doped cement samples, the same procedure cannot be adopted due to the limited amount of material used. In this case a manual mixing procedure has been used, keeping however the W/C ratio the same.

All the samples have been cast in a Perspex homemade moulder of cylindrical shape 8 mm in diameter and 20 mm in length and cured under water for various lengths of time. Before measurement the samples were taken from the curing bath, gently dried with tissue paper and placed in a sealed 10 mm NMR tube for measurement. During measurement a piece of wet

paper has been introduced onto the top of the tube (well outside the sensitive area of the coil) to keep the environment inside the tube RH saturated.

### 3.3.4.1 Characterisations of samples performed at CTG Laboratories

All the measurements presented in this section have been originated by the collaboration with CTG Italcementi during the visit to their laboratories in Bergamo.

The samples analyzed were the 0.25 % 0.5 % Fe content for the clinkers (unhydrated cement pastes) and 0 % 0.25 % 0.5 % for the hydrate pastes.

Microscopic observations and diffractometry analysis have been performed on the powders; whereas microscopic observations, calorimetric measurements and porosimetry measurements have been performed on the pastes.

#### Optical and Electronic microscopy

The samples have been analyzed in the following way: the powders have been observed at the metallographic microscope in reflected light to identify the phases distribution (alite, belite and interstitial phase), the pastes, instead, have been observed at the scanning electron microscope to identify the Fe distribution.

The sample preparation consisted in having polished section of both powders and pastes embedded in resin.

Microscopy observations on the powders show that the three clinkers are formed by small alite and belite crystals and in some samples an interstitial phase. Belite shows shape from circular to sub-circular and seems that increasing the amount of Fe in the sample the amount of belite grows and the distribution get worse (Figure 3.7, Figure 3.8 and Figure 3.9).

The interstitial phase is constituted mainly by  $C_3A$  and rare crystals of  $C_4AF$  have been seen in the clinkers (Figure 3.9).

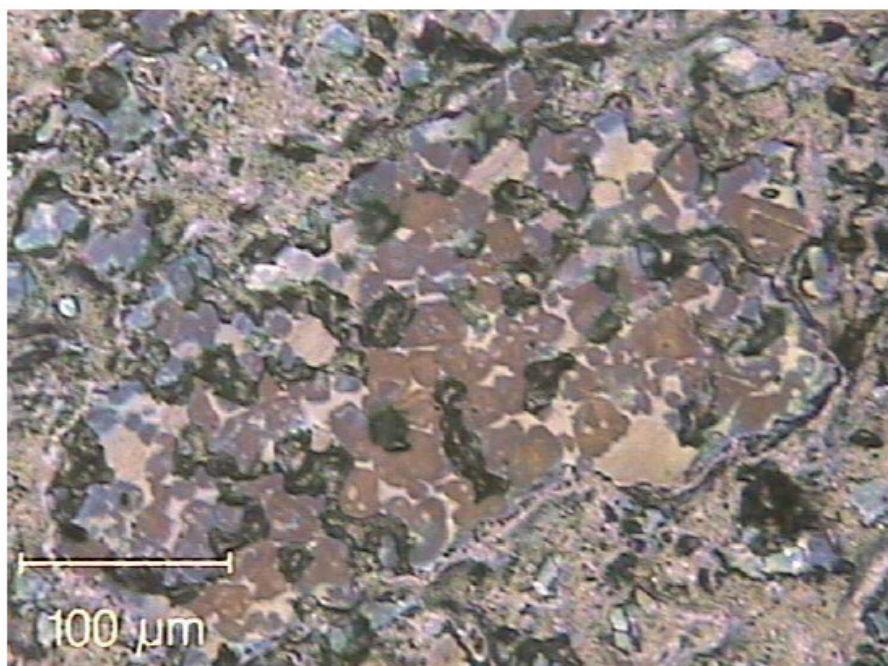


Figure 3.7 Typical belite distribution in the clinker samples. (Data acquired at the CTG Italcementi laboratories).

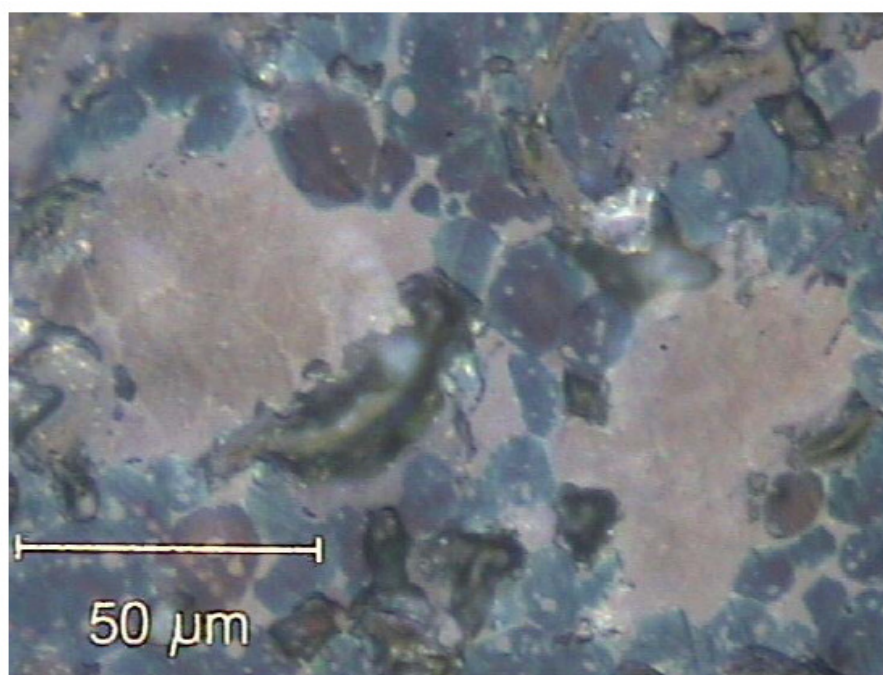


Figure 3.8 Belite "nests" found in all the samples. (Data acquired at the CTG Italcementi laboratories)

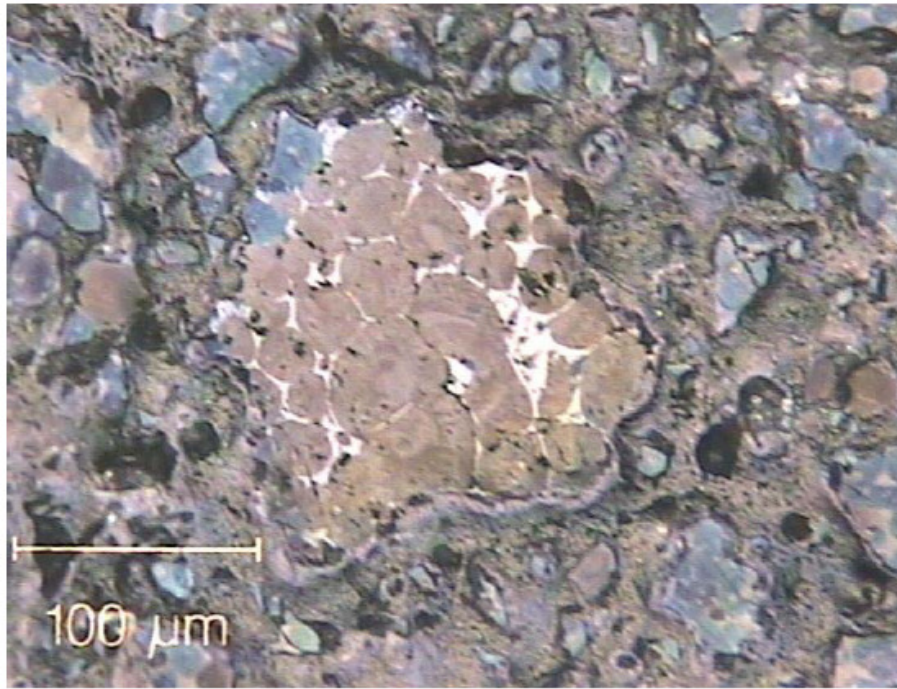


Figure 3.9 belite nests and ferrite (white) in the sample with the highest amount of Fe added.  
(Data acquired at the CTG Italcementi laboratories)

The cement pastes polished section treated with graphite to make them conducting have been observed at the scanning electron microscope via backscattered electrons.

Looking at all the samples, the typical result was several grains of unreacted clinker and a matrix constituted by portlandite and some C-S-H. Figure 3.10 is representative of almost all the different pastes and therefore the other results have been omitted.

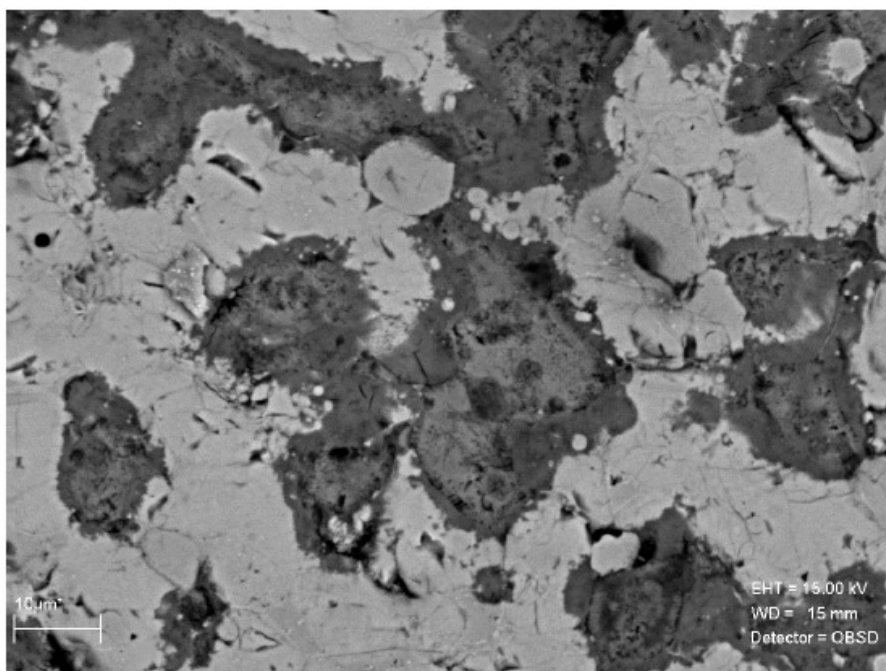


Figure 3.10 unreacted clinker (dark grey) portlandite (white) and C-S-H at the interface. (Data acquired at the CTG Italcementi laboratories)

The X ray spectra measured with the diffractometer show that in all the samples alite( $C_3S$ ), belite( $C_2S$ ) and  $C_3A$  are present.

In all the samples the presence of anhydrite ( $CaSO_4$ ) has been observed. Spatial resolved X ray mapping show that the Fe is concentrated in the  $C_4AF$  present in the unreacted clinker, while in the hydration products a not detectable amount was present.

The results of the thermogravimetric analysis can be summarised in Table 3.3 and Table 3.4.

Variation in %	25-70°C	70-140°C	140-170°C	170-370°C	370-470°C
0% Fe	2.13	4.28	1.38	3.87	4.49
0.25% Fe	1.93	4.61	1.29	3.53	4.54
0.50% Fe	2.13	3.93	1.23	3.33	4.15

Table 3.3 mass losses for each interval of temperature, the loss in the range 170-370 °C is relative to the decomposition of the C-S-H. (Data acquired at the CTG Italcementi laboratories)

Sample	Ca(OH) <sub>2</sub> (%)
0% Fe	18.47
0.25% Fe	18.67
0.50% Fe	17.07

Table 3.4 Percentages of Ca(OH)<sub>2</sub> in the different samples. (Data acquired at the CTG Italcementi laboratories)

Mercury porosimetry measurements have been performed on all the paste samples.

BET measurements, due to their time consuming nature, have been performed only on 2; the two sample of extreme Fe content.

## 3.4 Results

### 3.4.1 $T_2$ - $T_2$ NMR

In this section one typical  $T_2$ - $T_2$  result will be first described in detail. For all the following results, only the relevant characterising feature distinguishing each from the typical one will be described.

#### 3.4.1.1 Typical example, the white cement

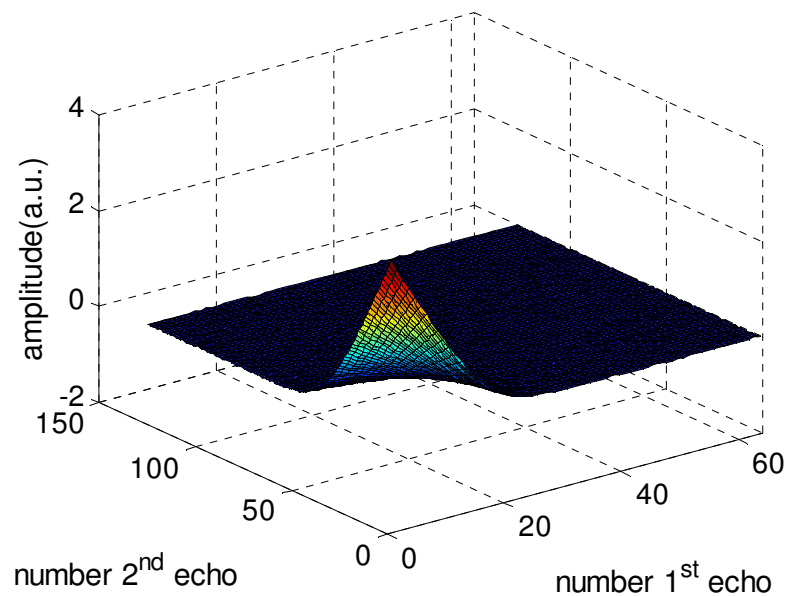


Figure 3.11 Raw dataset acquired, in this specific case the A white cement. It is prepared as described and cured 1 day under water at 20 °C. The exchange time is 3 ms.

In Figure 3.11 the raw dataset is shown. It is a measurement performed on a white cement sample (cement A) prepared following the standard procedure described and cured 1 day under water. The exchange time is 3 ms. The format of the dataset downloaded from the spectrometer is a 2 columns (real-imaginary or x-y components) text file with all data saved in order of acquisition. This has been subdivided into one dataset for each storage time. Then, each dataset has been phase rotated to minimise the imaginary component and recast into a 2D dataset having the number of the echoes in the first and second half of experiment as variables. The representation of the echo distance in the time domain is shown in Figure 3.12. Only the real part (after rotation) is shown in Figure 3.11.

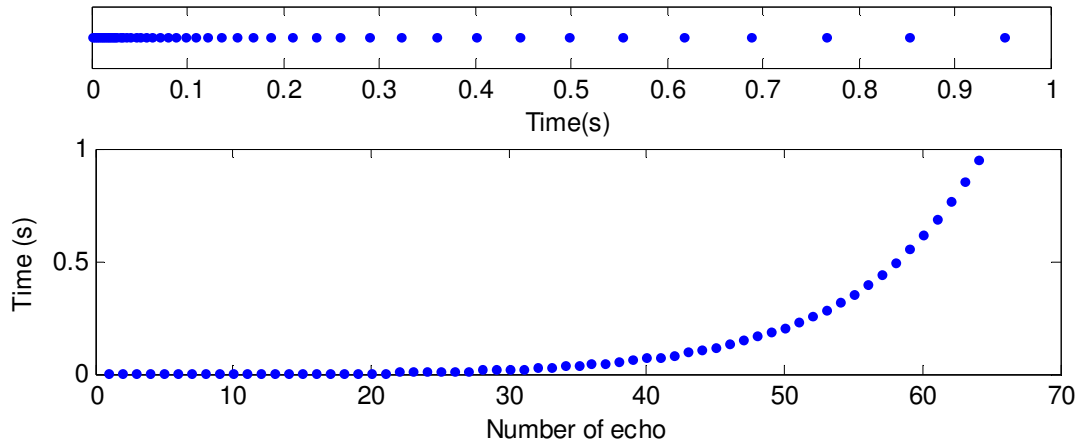


Figure 3.12 Top: representation of the timeline of the different echoes. Bottom the plot of the echo time versus the number of echo.

The signal to noise ratio has been estimated dividing the maximum amplitude by the root mean squared value calculated over the last rows of each dimension. In this particular dataset the value  $S/N = 743$ .

It must be remembered that the echoes are not equally spaced in time, therefore the decay in the real time space is much sharper than what appears in Figure 3.11. Because the differences are not easily noticeable in the raw data they will not be normally shown together with the next results.

In Figure 3.13 the result of the Laplace inversion performed on the dataset in Figure 3.11 is shown. It is typical of the work previously performed on cement [68] and confirms that the procedure of data acquisition and analysis is correct.

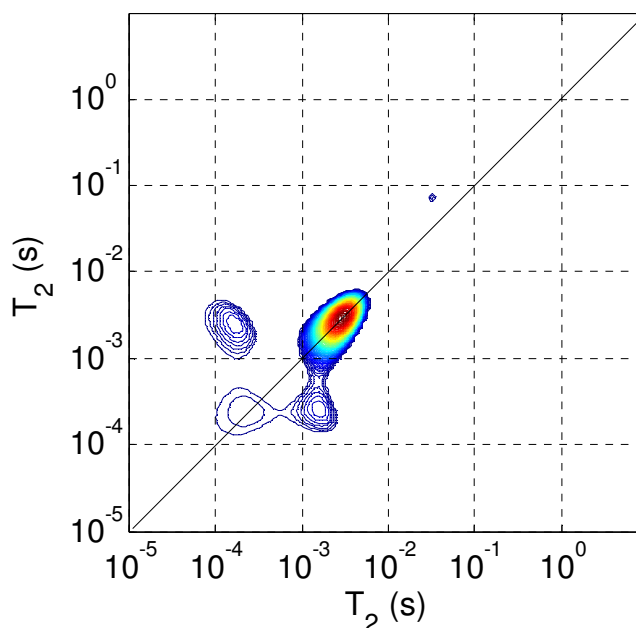


Figure 3.13 2D Laplace inversion of the data shown in Figure 3.11

This dataset does not show any long relaxation components that may be attributed to capillary porosity. This is common in this experiment and compared to some conventional understanding, surprising. The reason may be due to the fact that the coarser porosity measured in young samples by other techniques is actually created by the technique itself or by the sample preparation. Figure 3.13 shows an intense peak centred at circa 2 ms and another much weaker at around 200  $\mu$ s. The exchange peaks are the one outside the diagonal, clear and symmetric. The small peak at values of  $T_2$  circa 0.1 s is an artefact of the inversion. The fastest relaxing components representing the bound protons and therefore expected at few tens of micro seconds is, as usual, not detected.

The results have been found, except in rare and easily detectable cases when the ambient temperature changed dramatically during the acquisition, to be highly reproducible. As confirmation of reproducibility and stability of the equipment in Figure 3.14 is shown the result of a similar experiment as the one just presented, performed months before on a sample prepared and cured in the same way. In this case the signal to noise ratio is a bit lower ( $S/N = 595$ ) but the features observed are in the same position.

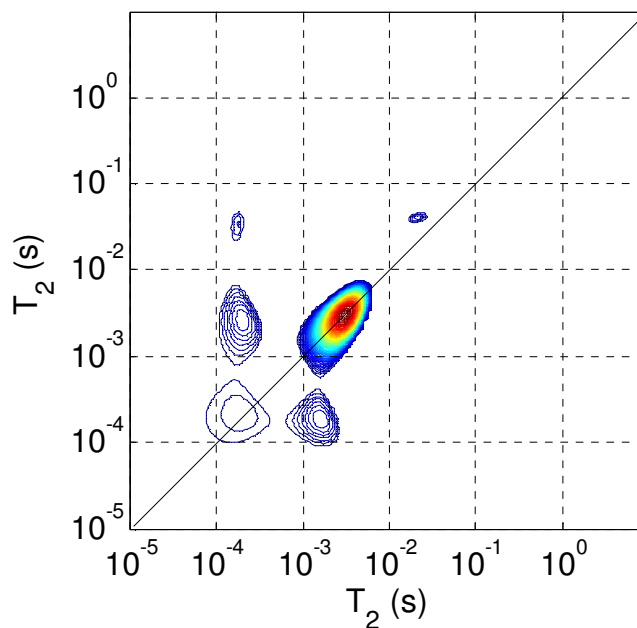


Figure 3.14 Result of an experiment with the same parameters and sample preparation as the one shown in Figure 3.13 but performed months before that confirmed high reproducibility.

### 3.4.1.2 The grey cement

The same experiment performed on a sample prepared and cured in the same way (1 day at 20 °C) but using the grey C cement.

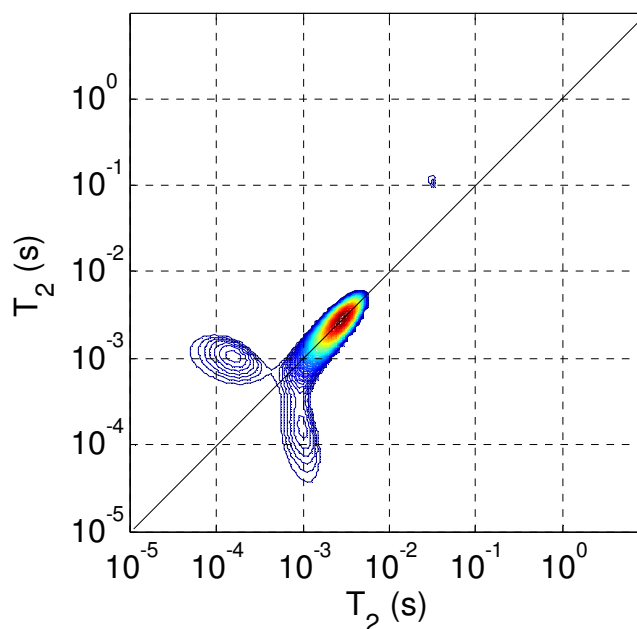


Figure 3.15 Result of an experiment performed on a sample prepared as the one which results are shown in Figure 3.13 (1 day old, cured under water at 20 °C) but using grey cement C

In the 2D LI of the grey cement sample it can be seen that the diagonal long relaxation peak is in the same position compared to the white cement sample. The lower one instead appears to have moved outside the plot (or possibly in the region where the experimental parameters did not allow detection). In this case the signal to noise is still very good but is decreased a bit ( $S/N = 444$ ).

### 3.4.1.3 The doped cement samples

In this section, the  $T_2$ - $T_2$  results of the doped cement samples prepared at CTG Italcementi laboratories following the procedure described in paragraph 3.3.4 and analysed into detail in paragraph 3.3.4.1 will be presented.

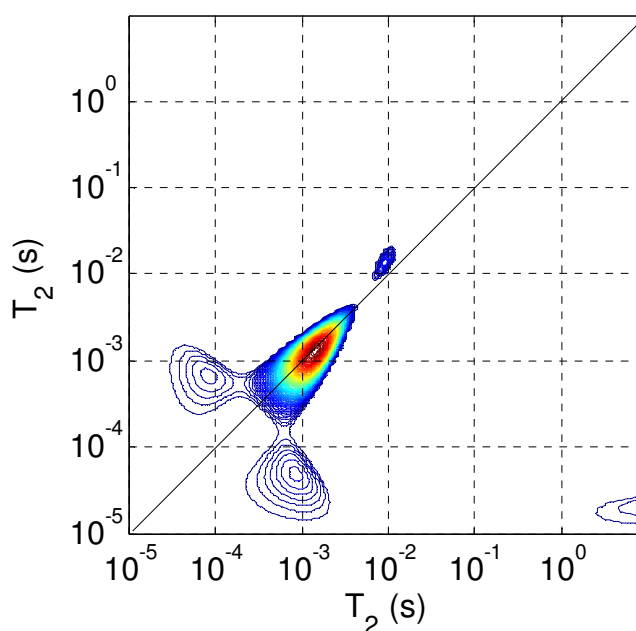


Figure 3.16 2D LI of the reference sample without Fe added (0 %). The S/N of the data is 369.

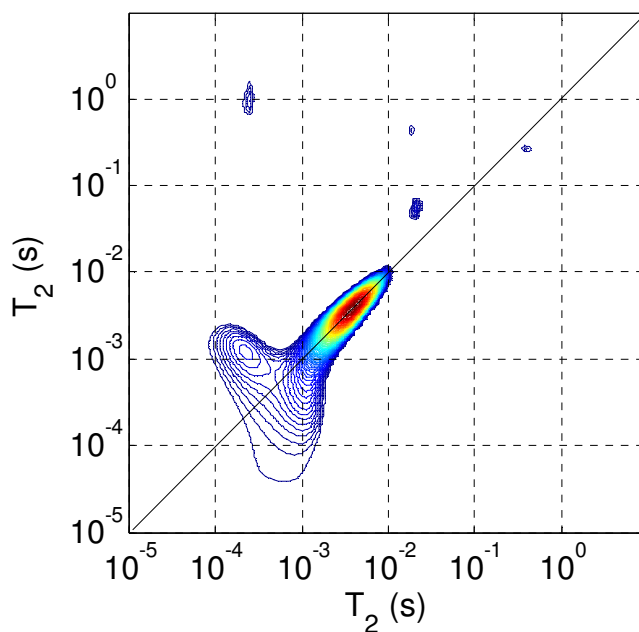


Figure 3.17 2D LI of the sample with 0.25 % Fe added. The S/N of the data is 604.

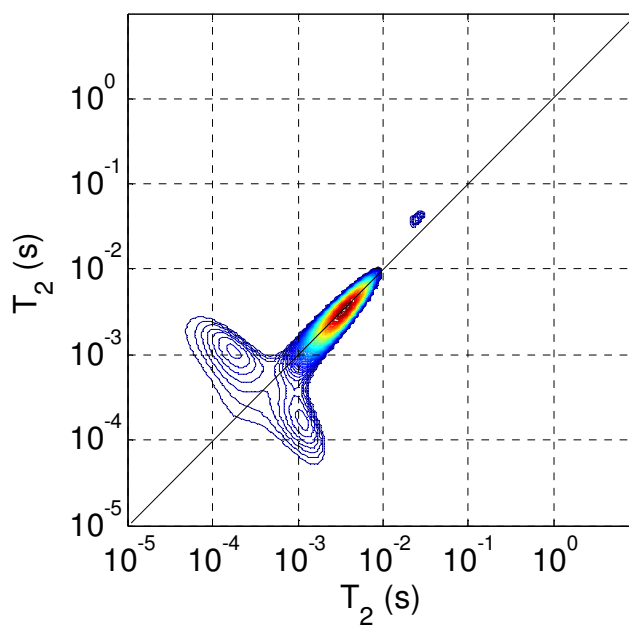


Figure 3.18 2D LI of the sample with 0.5% Fe added. The S/N of the data is 398.

The only difference that can be noticed is that, moving from the reference sample to the sample with 0.25 % Fe added, the long component peak moves to a slightly longer relaxation time, while no differences can be seen between the 0.25 % and 0.5 % samples.

### 3.4.1.4 The C<sub>3</sub>S and doped C<sub>3</sub>S samples

Below are presented the results of the measurements on the C<sub>3</sub>S and the Fe doped C<sub>3</sub>S paste produced by members of André Nonat group at the University of Bourgogne as previously described.

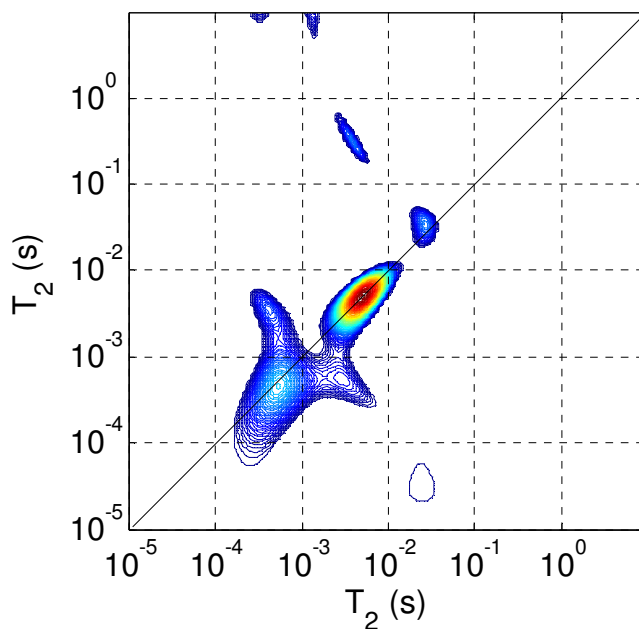


Figure 3.19  $T_2$ - $T_2$  result on a 3 day old C<sub>3</sub>S paste sample cured at 20 °C. The S/N of the data is 827.

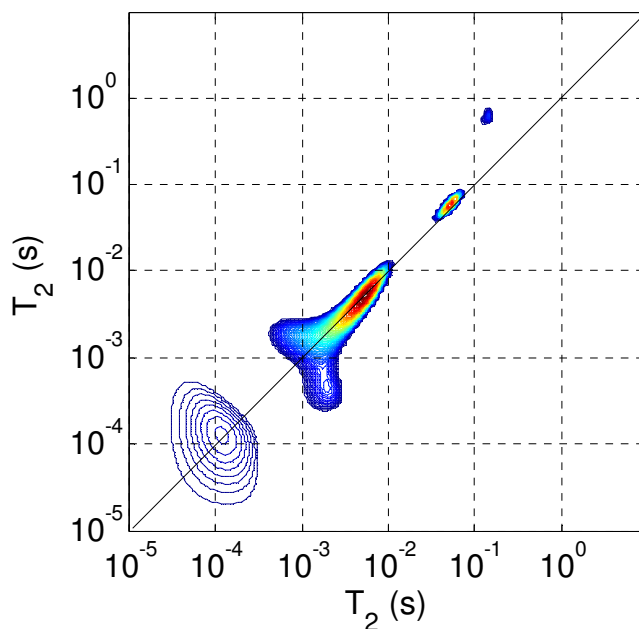


Figure 3.20  $T_2$ - $T_2$  result on a 3 day old Fe doped C<sub>3</sub>S paste sample cured at 20 °C. The S/N of the data is 338 (and therefore the inversion has been checked for stability)

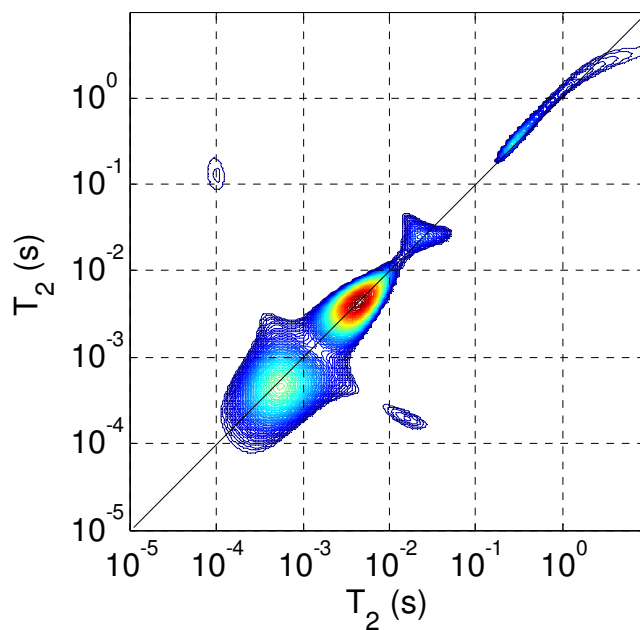


Figure 3.21 As Figure 3.19 ( $C_3S$  no doped) but 7 days old. The S/N is 107

Due to the low signal to noise in this dataset, the test previously explained with the addition of white noise has been performed. The different results are shown in Figure 3.22:

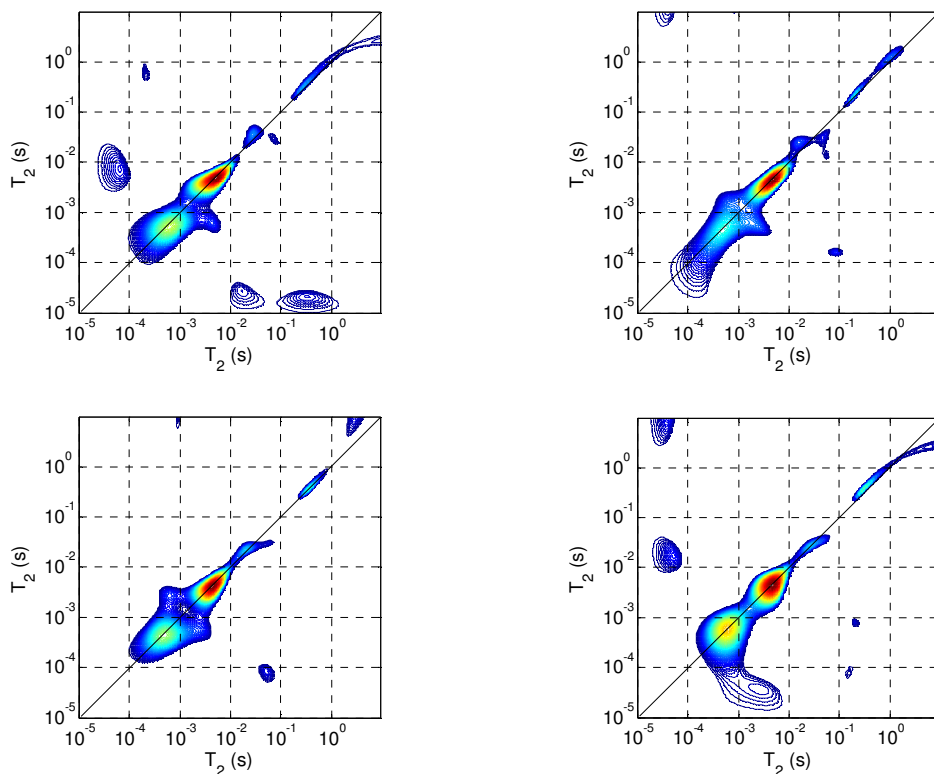


Figure 3.22 The same dataset presented in Figure 3.21 but analysed adding four different realisations of random noise as explained in the method paragraph.

The results differ visibly from each other, especially for the narrow “spikes” around the plot, however the main peaks are the same. The dataset can be analysed with a larger value of the regularisation parameter. This has been done and is shown in Figure 3.23.

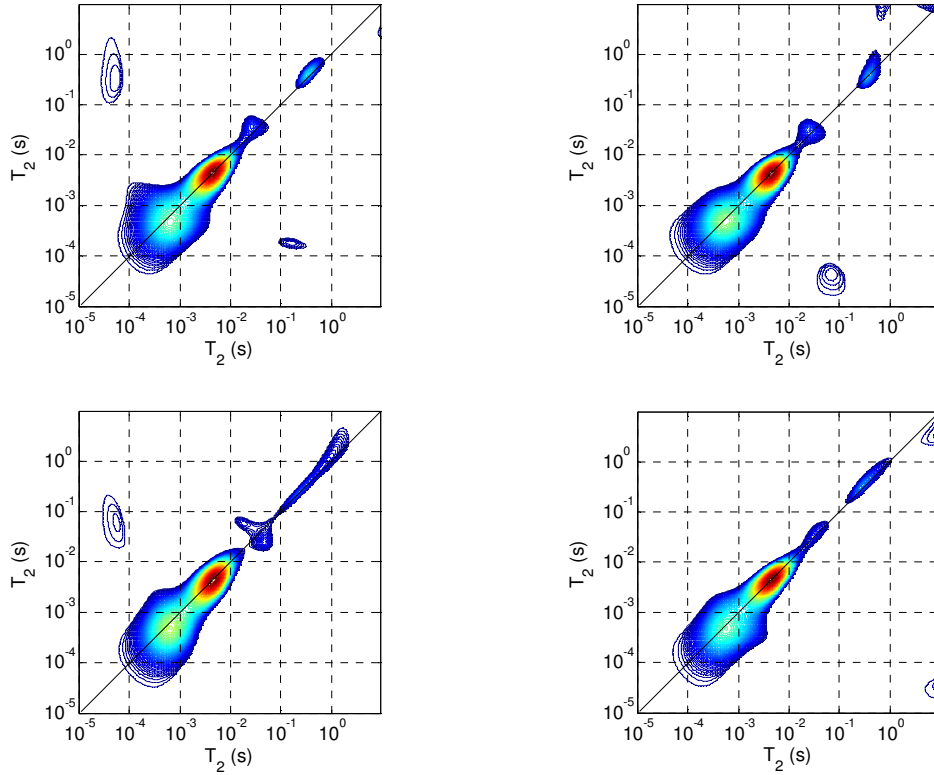


Figure 3.23 The same dataset presented in Figure 3.21 but analysed adding four different realisations of random noise as explained in the method paragraph and changing the regularisation parameter from 1 to 10.

In Figure 3.23 it can be seen that the results are more stable but any hint of cross peaks has disappeared. Probably thanks to the simple structure of the spectra, the first analysis with  $\alpha = 1$  has been revealed to be fairly stable.

The result for the doped sample 7 days old is presented in Figure 3.24, while the results for the samples at 10 days are shown in Figure 3.19 and Figure 3.20 for the not doped and doped samples respectively.

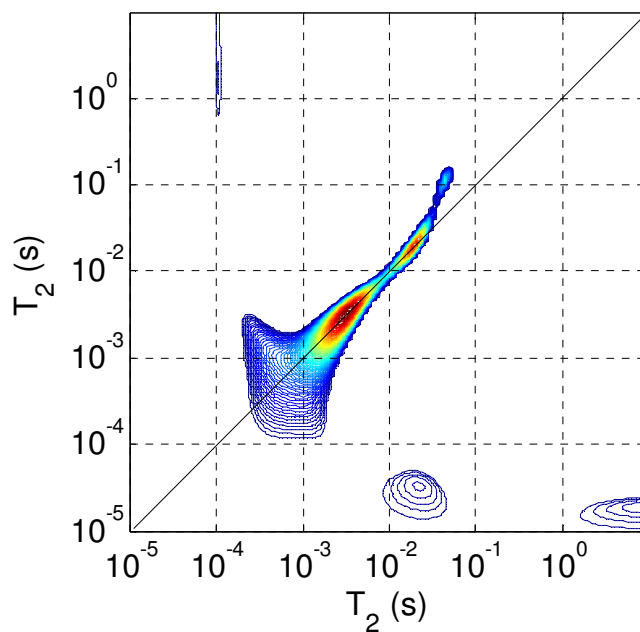


Figure 3.24 As Figure 3.20 (doped  $C_3S$ ) but 7 days old, the S/N is 212.

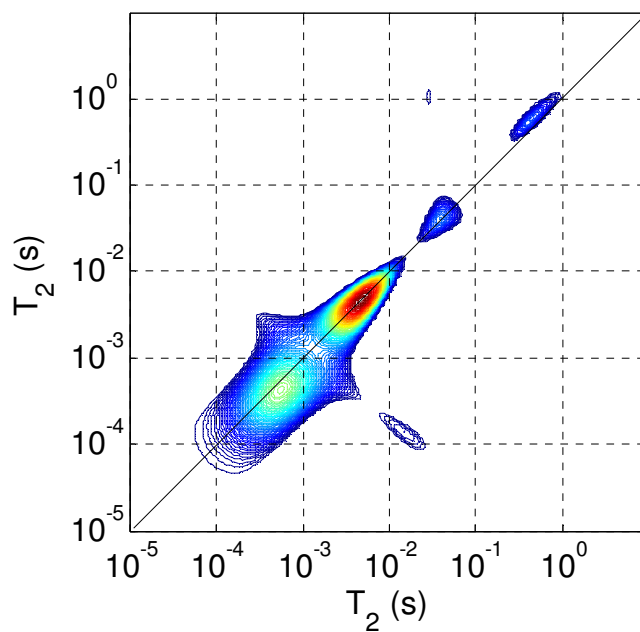


Figure 3.25 As Figure 3.19 ( $C_3S$  no doped) but 10 days old (S/N 251)

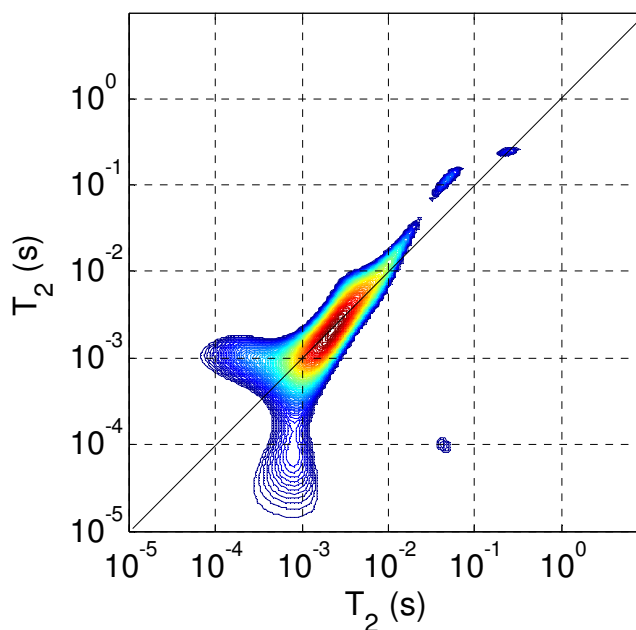


Figure 3.26 As Figure 3.20 (doped  $C_3S$ ) but 10 days old and double the number of scans  $S/N = 196$  also in this case the stability has been checked.

Also these last two datasets, due to their relatively low  $S/N$ , have been checked for stability with a positive outcome. In Figure 3.25 two peaks are visible on the diagonal (although without clear exchange peaks). In Figure 3.26 there is a peak visible elongated on the diagonal and two features fairly symmetric outside the diagonal that may be a hint of exchange peaks, however no short relaxing peak is observed.

#### 3.4.1.5 Synthesised C-S-H

A typical result of the measurements on the synthesised C-S-H is presented in Figure 3.27. The regularisation parameter used is  $\alpha = 1$ .

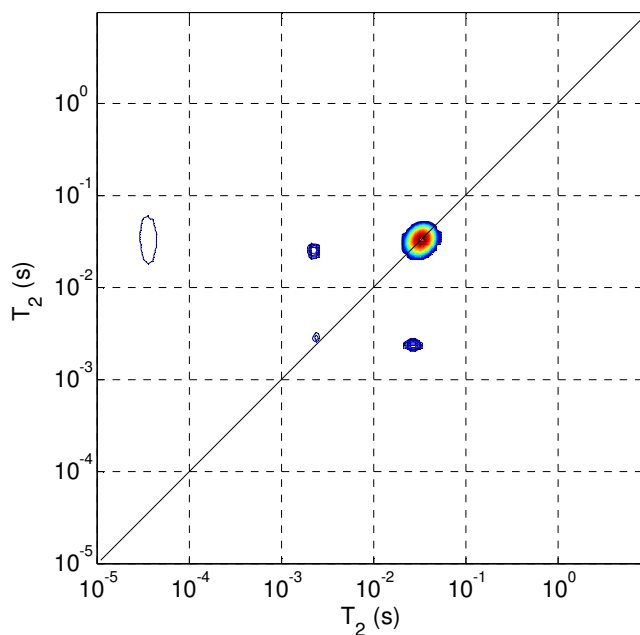


Figure 3.27  $T_2$ - $T_2$  result of the experiment performed on the synthesised C-S-H, with exchange time 7 ms, the S/N of the data is 2378

In the plot a strong diagonal peak at  $T_2$  value of  $\sim 20$  ms and a much weaker one at  $\sim 2$  ms are visible. The two exchange peaks outside the diagonal are clear and well visible. A very weak artefact peak is visible on the left edge of the plot. Because the S/N in this experiment was so high, the analysis has been performed for a much lower value of  $\alpha$  (0.01) to examine if there was more structure in the spectra that could have been resolved.

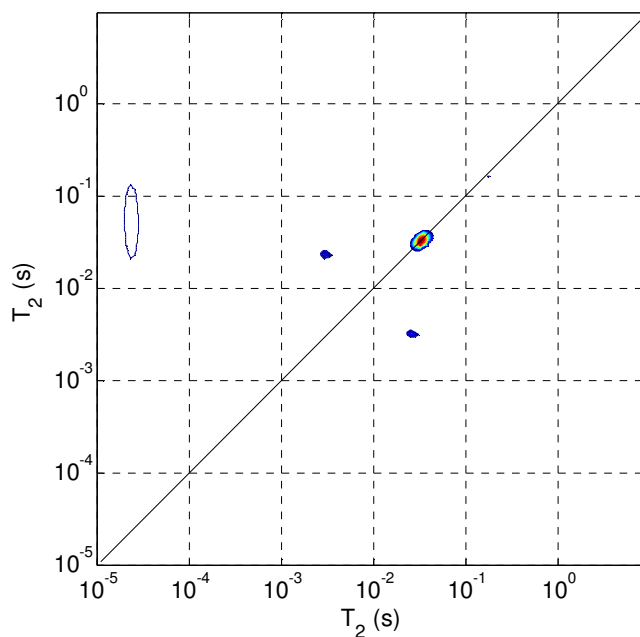


Figure 3.28 The same dataset presented in Figure 3.27 but analysed with a smaller value of the regularisation parameter ( $\alpha = 0.01$ ).

In Figure 3.28 it is possible to notice a much sharper distribution, in fact the long relaxing peak cover a smaller area, as well as the two exchange peaks, the fast relaxing peak, instead, has disappeared. No additional structure is visible.

The same dataset has been analysed also for a bigger value of the regularisation parameter ( $\alpha = 10$ ). The result is shown in Figure 3.29.

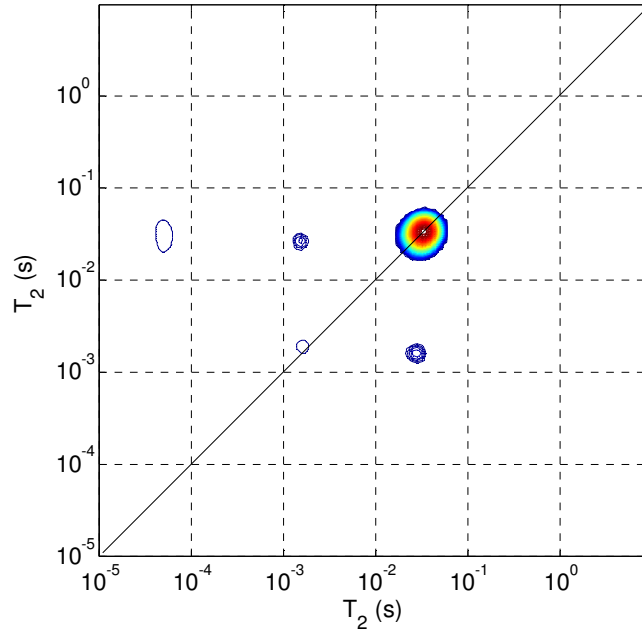
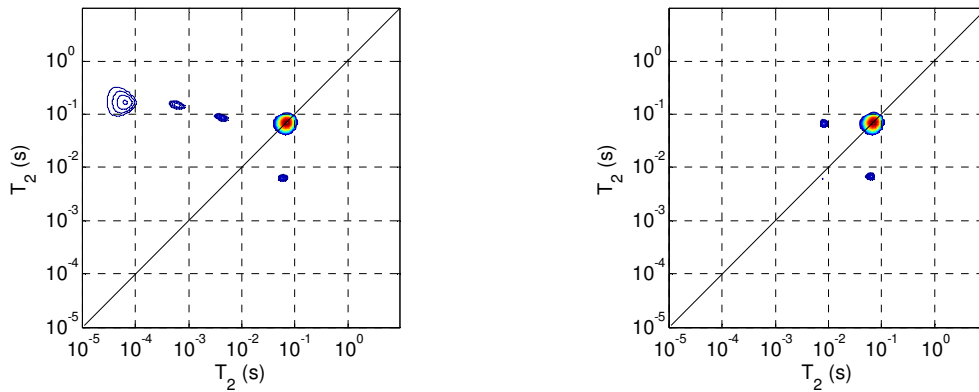


Figure 3.29 The same dataset presented in Figure 3.27 but analysed with a bigger value of the regularisation parameter ( $\alpha = 10$ ).

In Figure 3.29 all the peaks are more visible, covering a bigger area in the 2D plot, also the fast relaxing peak is well visible. In this case the visibility is increased at expenses of resolution, that however seemed to be useless due to the absence of further details in the dataset.

The experiments on C-S-H, thanks to the much higher S/N, have been attempted for a broad range of exchange times (between 1 and 20 ms). The series is presented in Figure 3.30.



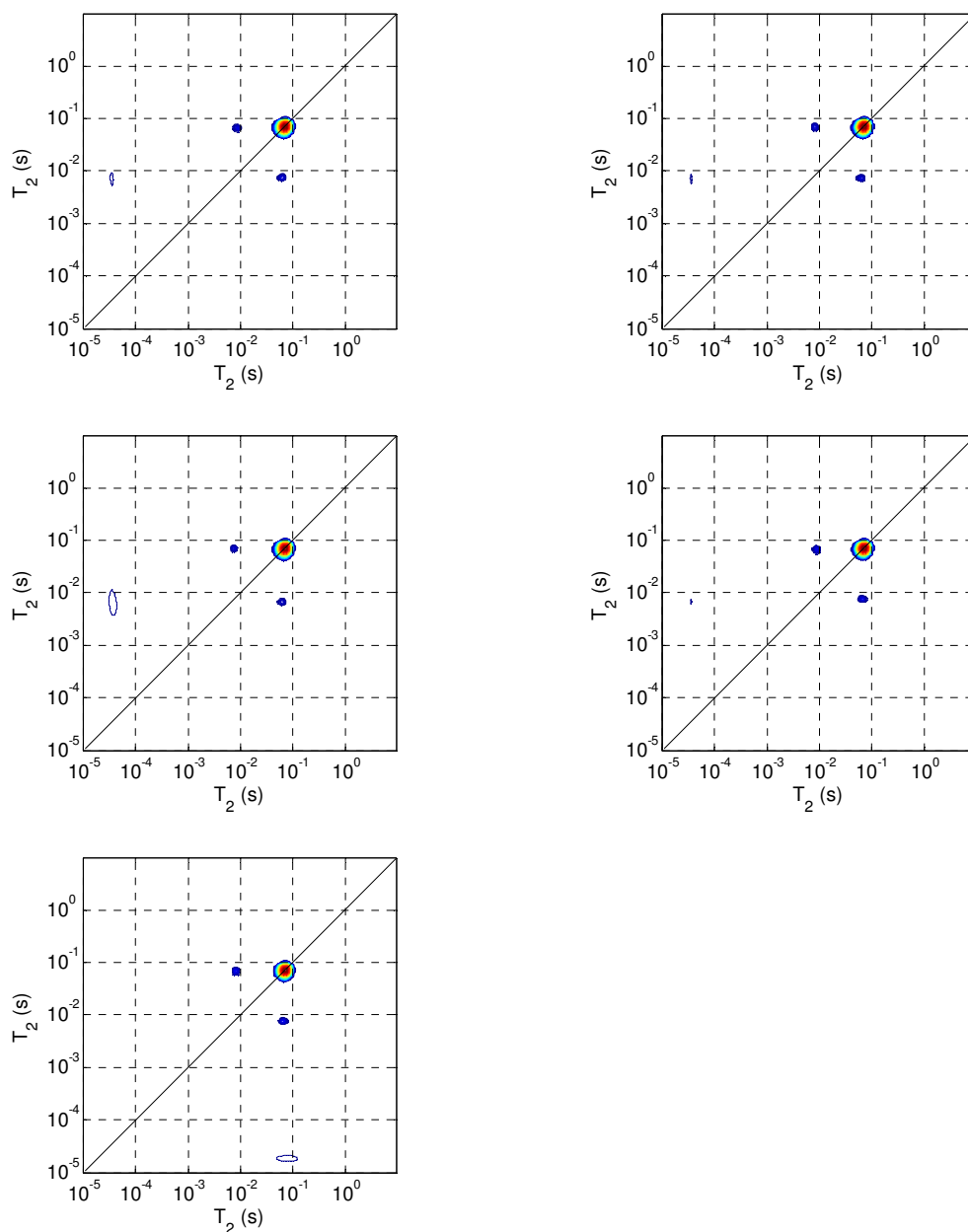


Figure 3.30 From left to right and from top to bottom, series of  $T_2$ - $T_2$  experiments on C-S-H with increasing storage time the values used are 1, 2, 3, 5, 8, 10 and 20 ms. The S/N ratio was  $\sim 2000$  for all the results.

All the plots look very similar (if not identical), showing a very weak dependence with the exchange time. The bottom peak on the diagonal is almost always missing.

An experiment on another batch of synthesised C-S-H has been performed; in this case the storage time used spanned values up to 2 seconds. The results are presented in Figure 3.31.

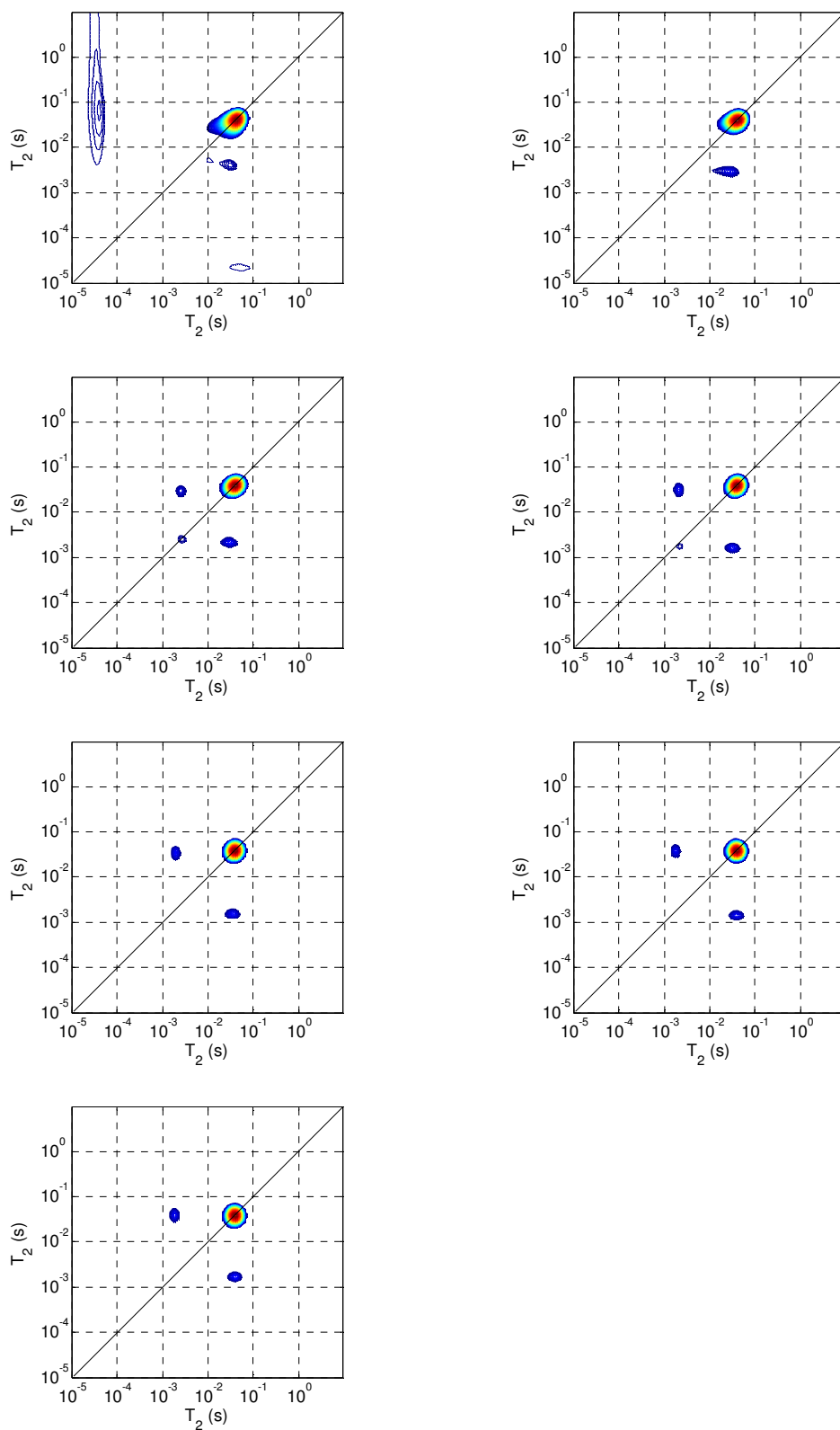


Figure 3.31 From left to right and from top to bottom, series of  $T_2$ - $T_2$  experiments on C-S-H with increasing storage time the values used are 0.01, 0.1, 1, 10 100 1000 and 2000 ms. The signal to noise ratio was greater than 400 for all the results.

In Figure 3.31 it is visible that the very short exchange time (below  $\sim 1$  ms) introduces a conspicuous noise in the data, this is also confirmed looking at the raw data (not shown). All the other plots (for exchange times from 1 ms to 2 s) look very similar, with the only trend visible that the short relaxing peak disappears. At this very long storage time the cross peaks are still visible. The long component peak is in a slightly different position but this may have originated from a different compaction (see discussion).

An analysis of the behaviour of the amplitudes of the cross peaks as the exchange time increases have been performed. To obtain this, the ratio between the cross peaks and the total peak amplitude has been plotted versus the exchange time. The results are shown in Figure 3.32.

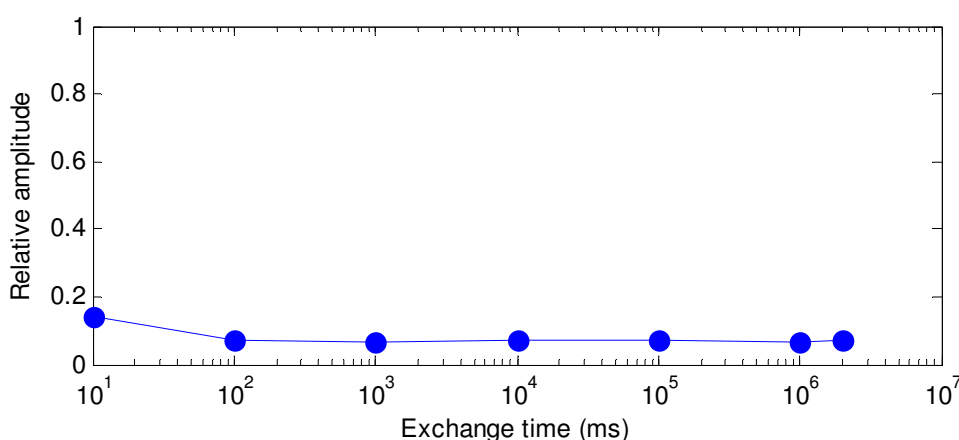


Figure 3.32 Relative amplitude of the cross peaks compared to the total as a function of the exchange time. This is extracted from the data presented in Figure 3.31.

Figure 3.32 confirm what was already qualitatively noticed in Figure 3.31 that the ratio between the cross and diagonal peaks does not change significantly over all the exchange time analysed. The amplitudes have been checked with the addition of noise technique and the error bars fall within the markers.

#### 3.4.1.6 ESR results

On the  $C_3S$ , doped  $C_3S$  and C-S-H EPR measurements have been taken to estimate the total amount of paramagnetic impurities in the materials. The results are shown below. The measurements have been taken for fixed mass of sample; the samples ending with U refer to un-hydrated samples (i.e. cement powders), the one ending with a number refer to the number of days of hydration (at  $20^\circ\text{C}$ ). Only 14 days old samples shown here.

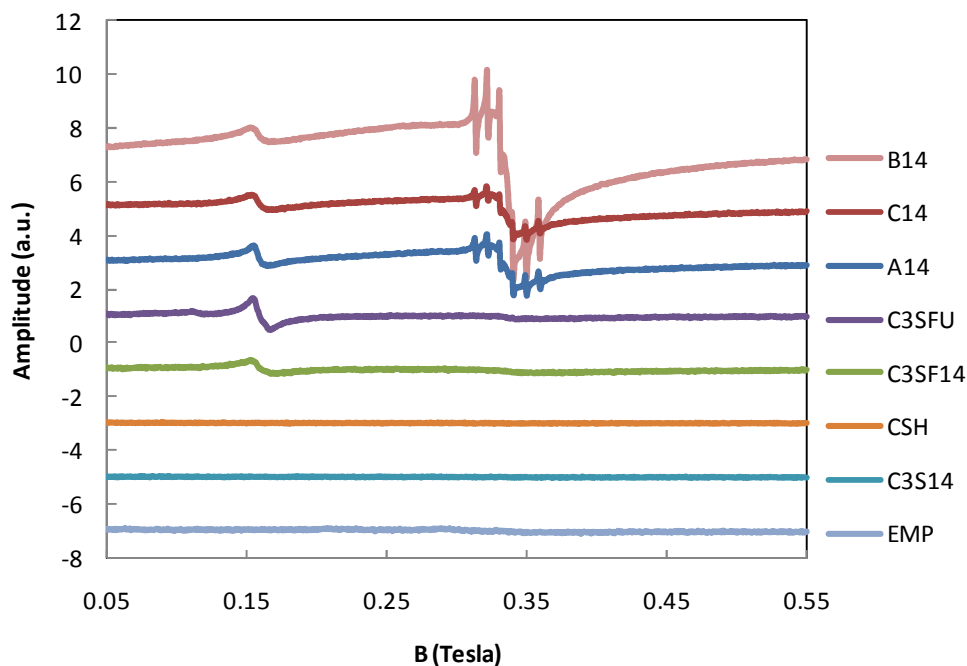


Figure 3.33 ESR results shown in differential mode of experiments performed on: white cement A (A14), grey cement C (C14) (both hydrated 14 days); doped C3S hydrated 14 days (C3SF14) and un-hydrated (C3SFU), C3S hydrated 14 days (C3S14); C-S-H (CSH) and empty probe (EMP). The plots are stacked at a spacing of 2 a.u. for clarity.

In Figure 3.33 the signal arising from two Fe environments (the broad lines centred at around 0.15 and 0.34 T) can be seen. Another feature visible is the characteristic multiplet of the Magnesium (6 lines centred at around 0.34 T) that superimposes onto one of the Fe ones.

### 3.5 Analysis and discussion

#### 3.5.1 ESR measurements

The ESR measurements have been analysed assuming the presence of two environments, the discrimination of the Mg signal from the Fe one has not been considered. The double integration, considering the boundary of the two lines at  $\sim 0.22$  T gave the results shown in Figure 3.34.

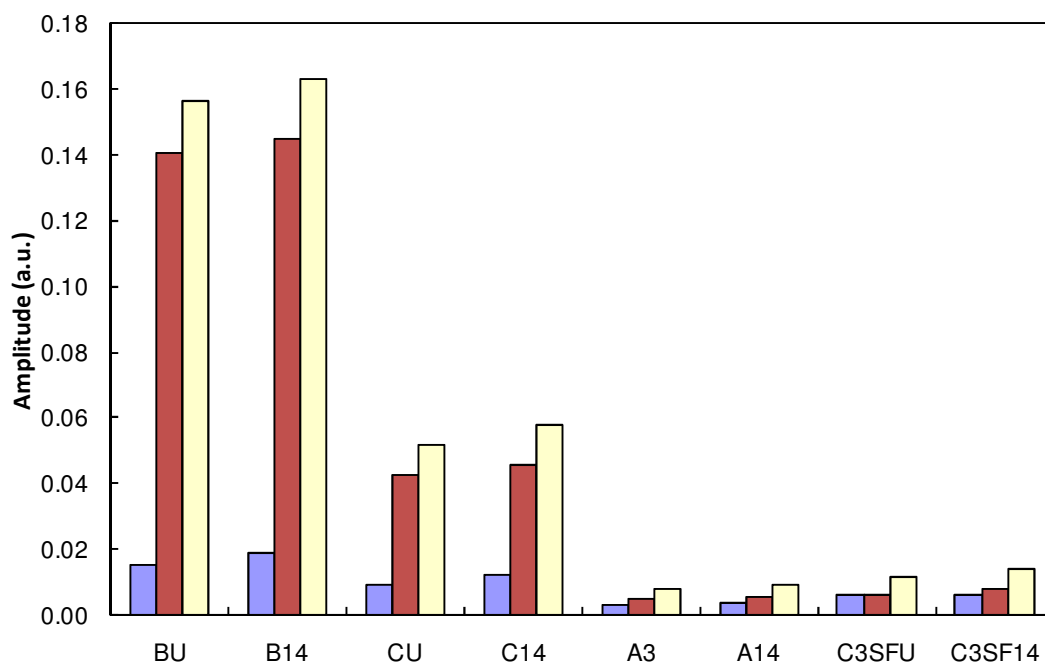


Figure 3.34 Integrated amplitude of the ESR peaks; 1<sup>st</sup> 2<sup>nd</sup> and total from left to right. The sample with a U in the name refer to unhydrated samples. C<sub>3</sub>S and C-S-H are not present because the signal was absolutely comparable to the empty probe and therefore below the detection limit. The signal of the empty probe has been subtracted before integration.

From the separation of the peaks, we can see that the environment in which the Fe is does not seem to change with hydration. In fact the two couples of samples BU-B14 and CU-C14 show the same amplitudes before and after hydration. This supported the hypothesis that the iron did not go into the hydrates. Careful comparisons have been made between the amplitudes of the two peaks and the amount of different phases in the clinker (Table 3.1), however no relationship has been found, suggesting that the two environments may be distributed between the different phases. The C-S-H and the C<sub>3</sub>S has been confirmed to be Fe free

### 3.5.2 White and grey cements

The differences in the  $T_2$ - $T_2$  results between the white and grey cement are significant but not dramatic. The long component peak is at exactly the same position, while the short one appears at even lower values. The S/N ratio decreases a bit, probably due to faster relaxation with characteristic time  $T_1$  during the exchange period.

### 3.5.3 The doped cement samples

This attempt has been really time and resources consuming, but the differences in the  $T_2$ - $T_2$  relaxation spectra are not evident and do not show any meaningful pattern or behaviour. The fact that moving from the reference sample to the one with the smallest addition of Fe the larger peak moved visibly to longer values of relaxation times has been considered as hint that the material was not behaving as expected and therefore questions on the reliability of the sample preparation procedure arise.

From the analysis performed at CTG Italcementi laboratories arises the situation that the microscopy observation on the clinker powders, due to the tiny size of the grains it has been impossible to describe the phase distribution inside the clinker carefully. However, a suggestion of highly inhomogeneous distribution, especially moving from low to high Fe amounts emerged. In the cement pastes, the microscopic observations showed a high amount of unreacted clinker and portlandite, with only minor quantities of C-S-H. Fe were detected only in the unreacted products but not in the hydrates. The fact that in all the samples the presence of anhydrite ( $\text{CaSO}_4$ ) has been observed, suggest that the cooking temperature was too low or the time too short to allow a complete combination of the sulphur in the clinker phases. Thermogravimetric measurements confirmed the presence of a high amount of portlandite in all the samples.

Mercury porosimetry showed that the porosity centred at about 20 nm radius in the 0 % sample moved on higher values and spread on a bigger interval increasing the Fe content.

From the BET analysis (Page 17), instead, the two samples analysed show an almost equal BET specific surface, and apparently have no micro-pores (< 2.5 nm diameter). The hydration peak is, for both samples, around 2-3 nm and the porosity detected by this technique seems not affected by the different Fe amounts.

All this analysis confirmed the supposition of unreliable samples, showing that the procedures were not able to produce a highly enough uniform material that would have been comparable to ordinary cement. The production in laboratory probably did not reach the temperature required for total homogenisation, decarbonation and combination of the sulphur in the clinker phases.

### 3.5.4 $\text{C}_3\text{S}$ and doped $\text{C}_3\text{S}$

These experiments were much more successful than the previous set. In all the experiments it can be seen that between the not doped material and the doped one, the long relaxing peak

always appears in a pretty constant position, while the short relaxing one moves to lower values in the doped sample.

A very important observation is that exchange is clearly visible also in the non doped  $C_3S$  that has been confirmed to be completely Fe free. This is the first confirmation that the exchange seen in  $T_2$ - $T_2$  experiments cannot be explained only as exchange between regions with different paramagnetic impurities surface density but the two pore size hypothesis is the one that has to be taken into account.

Although it has not been carefully measured, the exchange time observed is of the same order of magnitude as the one in cement. All the measurements showing cross peaks are for 3 ms exchange, the value that more clearly shows exchange also in cement pastes.

### 3.5.5 Synthesised C-S-H

These experiments gave additional valuable information on the nature of the exchange seen in cement.

These experiments, although showing peaks at much longer  $T_2$  times (roughly one order of magnitude longer) definitely and very clearly show exchange. The considerable shift to longer relaxation times can be explained in two ways, and probably a combination of these two effects is the most realistic hypothesis. The complete deficiency of Fe in the C-S-H is the first, however this cannot fully justify the effect because in  $C_3S$  pastes, that hydrate to produce pure C-S-H as well, do not show equal shift. The second reason is that the synthesised C-S-H has been prepared in suspension and therefore the particles are realistically much more coarsely packed than the one found in a hydrated paste. It is probably possible to imagine the synthesis of the C-S-H as a hydration at a very high W/C ratio, giving for a sort of Power model, a much higher porosity. It has not been possible to successfully measure the exchange rate in C-S-H because the cross peaks are already at their maximum after just 1 ms exchange rate (that is close to instrumentation limits), however, this can suggest a lower limit. The surprising fact is that the cross peaks remain visible for values of exchange time much longer, and do not show a hint of collapsing behaviour up to 2 seconds. The  $T_1$  relaxation for the sample is circa 1.2 seconds, demonstrating that experiments with exchange time longer than  $T_1$  are feasible.

A very important consideration is that in this synthesised material, of course, there is no existence of outer or inner product C-S-H. This is for the simple reason that there are no cement grains at all. The measurement of an exchange time comparable to the cement one, thought to be an exchange between inner and outer product, was at first sight surprising. However, this is, together with the answer of the “Fe versus size question” the most useful

and interesting result of the work shown in this chapter. It is in contrast with the previous idea but gives a clue to an alternative explanation to the most discussed point in the previous belief.

The exchange seen, because it is characteristic of the C-S-H itself and not of the cement grain structure, is a much more “universal” and “fundamental” characteristic of the nature of cementitious materials than thought before.

Considering the scheme in Figure 3.2, showing a pictorial representation of the original hypotheses to explain the exchange seen in cement, we can conclude that the one that seems correct is the bottom one, reproduced in Figure 3.35 for convenience.

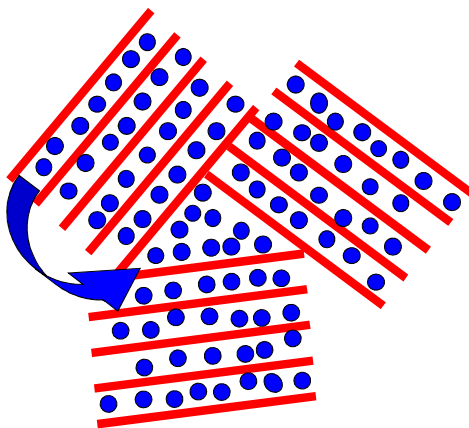


Figure 3.35 The most probable hypothesis of exchange arising from the work presented.

### 3.6 Conclusions

The experiments did not clarify completely where the water seen to exchange in the  $T_2$ - $T_2$  is moving to and from. This is reasonable considering that the structure of the amorphous C-S-H is not fully resolved itself (only the crystalline phases have well defined structures and compositions). However the hypothesis of exchange between an iron rich and an iron deficient region has been discarded. It has also been found that the previous explanation that the exchange was between inner and outer product is very likely to be wrong. The exchange with characteristic time of the order of milliseconds has been measured also in synthesised C-S-H, where the cement grain is absent and therefore the ideas of inner and outer products collapse as well.

An alternative explanation could be found in addressing the exchange between water within the layers of the C-S-H and the bigger porosity found in between the C-S-H “bricks” or “globules” whatever these terms mean.

## 4 Solid echo and drying model

### 4.1 Introduction

As already discussed and stressed, the interpretation of the  $T_2$ - $T_2$  experiments did not fully clarify the microstructure of cement. This fact, together with the complexity of the model and the necessity of a calibration dependent on several parameters (some of which are estimated with a fairly high uncertainty) caused some scepticism (especially in the cement community) on the validity of this technique and its practical utility in the understanding of cement nanostructure. The reason is that the uncertainty on the parameters is reflected in the uncertainty of the sizes determined with this technique, leading to a doubtful addressing of the magnetisation reservoir to determined microstructures.

In chapter 3 an alternative hypothesis raised of exchange between Fe rich and Fe deficient regions (where  $T_{2,s}$  rather than  $S/V$  is the key variable) has been discussed (and discounted). In this chapter we will try to make progres in the interpretation of the pore sizes of the two different reservoirs.

The aim of the work presented in this chapter is to find and present a different approach to probe and calculate the size of the same pores with a totally independent and hopefully calibration independent (or at least less calibration sensitive) method.

The difficulty in detecting and attributing the different relaxation time components to the different water reservoirs in cement is in part a matter of definition. It is also in part a consequence of the experimental apparatus or method employed: not all spectrometers or all measurement protocols can detect all components. Notwithstanding these differences, it is valuable to consider carefully the water reservoirs within the cement to which each component belongs. The widely accepted assignment is as follows. The shortest lived component reported has a  $T_2$  relaxation time of the order of 10  $\mu\text{s}$ . It is assigned to chemically combined water most obviously within micro-crystalline phases such as Portlandite (Calcium hydroxide,  $\text{Ca(OH)}_2$  or, in cement chemistry notation CH); it is not detected by the  $T_2$ - $T_2$  experiments due to the fact that the first echo is at 50  $\mu\text{s}$  that corresponds at  $\sim 5 T_2$ . The longer relaxation time components are generally assigned to gel and capillary pore water. The next two components have relaxation times of the order of 80-120  $\mu\text{s}$  and 500  $\mu\text{s}$  to 2 ms respectively [113,147]. Separately resolved, these may therefore be assigned to “gel-pore” and “micro-capillary” water respectively. Any longer component is generally assigned to water in micro-cracks and to water adsorbed on the

sample surface. Assignment of remaining water within the inter-layer sheets of the calcium silicate hydrate (C-S-H) gel is less clear. It is sometimes considered that this has similar NMR properties to the chemically combined water; sometimes it is considered as gel pore water. This debate mirrors debates in the wider cements literature as to the characteristics of gel water and to a wider debate concerning the detailed morphology of the microstructure of C-S-H.

The relative amplitude of each  $T_2$  relaxation component is directly proportional to the fraction of water, or, more strictly  $^1\text{H}$ , in that reservoir. While both the amplitudes and relaxation times may be modified by the presence of exchange, according to this simple model, the amplitude of the relaxation components reflects the relative amount of  $^1\text{H}$ , and hence water, in each of the different environments of cement.

The idea developed in this chapter is to carefully examine the amplitude of the different  $T_2$  relaxation time components in cement pastes as evaporable water is slowly removed. By this method we seek to assign more carefully especially the shorter different relaxation time components to water in different environments. A by-product of the study has been the realisation that the NMR measurement leads to an alternate assessment of the gel pore size based not on the absolute value of the more mobile component *relaxation time*  $T_2$  through equation (1.12)  $T_2 = \frac{v}{s\rho}$ , but rather on the *amplitude* of the seen “CH” component as a function of moisture content.

The amplitude of the shortest relaxation time fraction has been explored using a solid echo experiment combined with a FID analysis. The solid echo experiment in particular can be quantitatively analysed for signal amplitude as opposed to decay time or line shape. By this means the chemically combined fraction of the signal has been measured as a function of sample moisture content during careful, and ultimately destructive, drying starting with a few minutes a few degrees above ambient and ending at temperatures in excess of 380 °C for several hours. Experiments on  $\text{Ca(OH)}_2$  have also been performed considering that its proton should have been representative of the bound fraction in cement. The key new result which enables us to progress understanding is that, during the early stages of drying during which easily evaporable water is lost, the fraction of adsorbed water increases. Analysis of the signal amplitude data permits us to make an estimate of the micro capillary size that is in accord with that arising from an analysis of the relaxation time data. The analysis also sheds some light on the means of drying of these pores.

## 4.2 *Materials and methods*

The cement used in these experiments is the same cement A described in the paragraph 3.3.4 “Materials and sample preparation” for the experiments already described (Table 3.1 at Page 92). The preparation followed the same standard mixing and casting procedure. The only difference was the age of the samples. Because the interest was in having the maximum amount of C-S-H in the sample and because a criticism of the  $T_2$ - $T_2$  experiment was also the fact that it is not really representative of an old sample (more than ~4-5 days) we used samples of the age of two weeks and 1 month.

For these experiments, samples were dried with tissue paper (just to remove the excess of water from the surface) and have been crushed to obtained powder. The drying has been done in a vacuum oven up to 200 °C and in another oven (without vacuum) for temperature in excess of 200 °C and up to 380 °C.

A first set of experiments has been performed measuring the solid echo signal amplitudes for a limited (23) number of drying stages. A second set has been performed with a much higher number of drying steps (37) to obtain a much more detailed curve of NMR intensities as a function of relative mass of the sample. In this second experiment, the total slow drying process took ~3 months.

$\text{Ca(OH)}_2$  was supplied by Sigma Aldrich and has been studied in parallel experiments. The total detailed curve for cement has been obtained up to 380 °C while solid echo NMR experiments for  $\text{Ca(OH)}_2$  have been carried out for some steps of drying only from room temperature up to 200 °C.

Considerable care was taken to prevent contamination of samples by re-adsorption of atmospheric water subsequent to the drying treatments and during measurements. All measurements were taken at room temperature leaving the sample to cool down from the high drying temperature before inserting it in the magnet.

### 4.2.1 NMR measurements

#### 4.2.1.1 Solid Echo

A “Maran” NMR spectrometer (20 MHz) has been used for all solid echo experiments. The pulse sequence is the one presented in paragraph 1.4.1.2 (equation (1.20)) and its scheme is re shown with detailed timing in Figure 4.1.

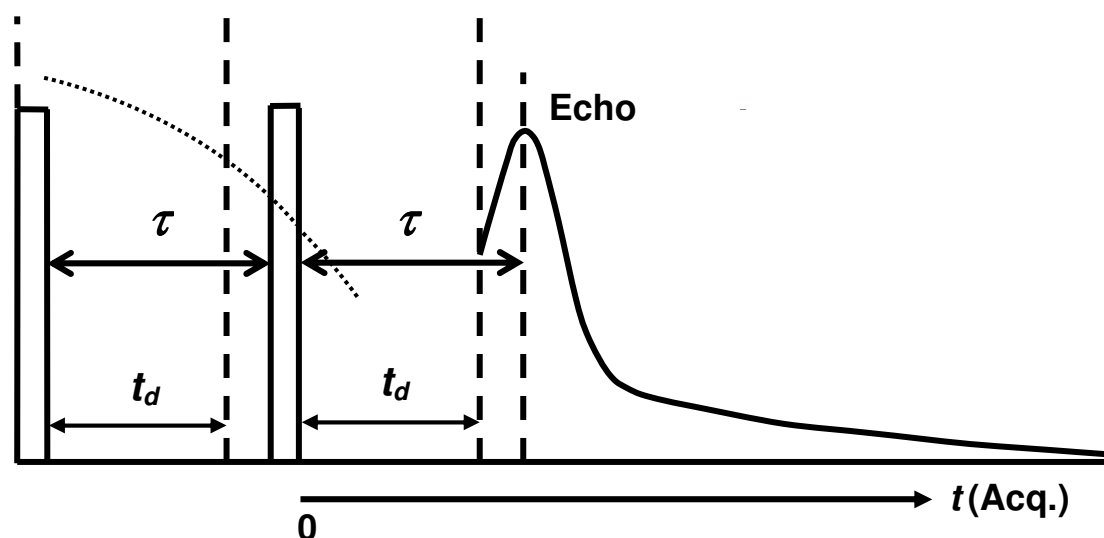


Figure 4.1 Scheme of the  $90_x\text{-}\tau\text{-}90_y$  pulse sequence with timing used and sketch of the typical signal obtained for a sample containing both mobile and solid protons.

Values  $\tau$  have been varied from 10 to 45 ms in 8 equal steps.

The spectrometer receiver filter width was 1 MHz, the dead time circa 10  $\mu$ s. In all cases a small residual NMR signal emanating from the NMR probe was subtracted from measured data. The number of accumulation was varied from 512 to 2048.

### 4.3 Data analysis

Following the magnetisation with the vector model, we can visualise that the first pulse rotates the total magnetisation from equilibrium (and therefore both mobile and bound populations of spins) along the y axes in the NMR rotating frame. During the interval  $\tau$ , the magnetisation due to the mobile fraction of spins precesses at the Larmor frequency in the laboratory frame, and therefore is static along the y axis in the rotating frame. For this component, the second pulse is “invisible” and does not change its magnetisation. The signal that arises from the mobile fraction of the water is therefore a Free Induction Decay with origin at the first pulse.

For the bound component, for which the dipole-dipole interactions are not averaged to zero by fast isotropic motion, the spin dynamics is different. This also rotates at the Larmor frequency  $\pm$  local frequency, but the local frequency is much greater and complex. Powles and Strange [48] showed that the  $90_x\text{-}\tau\text{-}90_y$  sequence refocuses pairs of isolated spin 1/2 nuclei coupled by dipole-dipole interactions at time delay  $t = \tau$  from the second pulse giving an echo. The refocusing is total for isolated pairs but not for interacting pairs with a maximum estimated error in the order of  $3/2(\tau/T_2)^4$  that can be regarded as a measure of the

deviation of the echo decay from the true Bloch decay for the coupled spins that occurred just after the first pulse. The reasons for the decay of the echo are complex and their analysis is outside the scope of this thesis. This gives an explanation of the  $\tau$  dependence of the echo amplitude and is an expression of the incoherent part of the spin-spin interactions. The decay due to the dipole-dipole interaction is not exponential and can be roughly modelled as a Gaussian echo. The equation of the decay, in the reference with  $t = 0$  at the second pulse is therefore:

$$I(t, \tau) = I_m(\tau) \exp\left(-\frac{(t + \tau)}{T_2}\right) + I_s(\tau) \exp\left(-\left(\frac{t - \tau}{\sigma}\right)^2\right) \quad (4.1)$$

where  $I_m$  and  $I_s$  are the mobile and solid intensities respectively,  $\sigma$  is the Gaussian width (approximate solid  $T_2$ ) and  $t$  is the time from the second pulse. Experimentally, the requirement to have good refocusing is to have a value of  $\tau$  smaller than  $T_2$ . When bound protons are considered, this relaxation time is of the order of few  $\mu s$ , therefore it is not easy to fulfil the condition of good refocusing. A way of dealing with this is to acquire the echo amplitude for several values of  $\tau$  and then extrapolate the amplitude to  $\tau = 0$

The solid echo signal has been analysed interpreting it as the superposition of the signal arising from the bound water fraction plus the one coming from the mobile one.

The equation used to fit the data is the (4.1).

$I(t, \tau)$  is the function fitted to the time domain data acquired. This means that for each value of  $\tau$  one value of  $I_m$  and one of  $I_s$  values are obtained. These values have then been plotted versus their variable  $\tau$  and then fitted to extrapolate the amplitudes at  $\tau = 0$ . The functions used to fit the dependence are exponentials. In the early stages of this experiment other functions have been tested, as, for example, a Gaussian, however, it has been found empirically that the exponential fit has always been by far the best one and therefore has been used to analyse all the datasets.

Of course, as any extrapolation, this technique introduces additional uncertainties.

## 4.4 Theory

The much simplified model of cement microstructure that we consider is of a material composed of tetrahedral silica layers interspersed by layers of water and calcium ions forming sheets of nano-crystalline C-S-H. For clarity we refer to this water as *intra*-C-S-H gel water. The C-S-H sheets are randomly stacked into crystallites with water in the *inter*-C-S-H

crystallite gel pores. Water in both intra and inter C-S-H gel may be considered as being confined to planar pores. We include within this description of C-S-H other comparably (from the viewpoint of water) structured phases such as AFm and Ettringite. In addition there are solid phases such as Portlandite, CH where the water is bound.

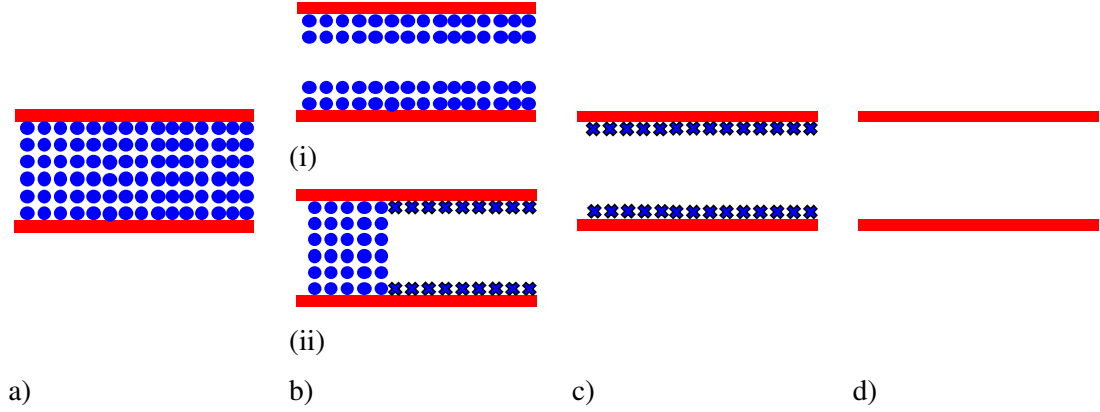


Figure 4.2 A schematic picture of a planar pore as in the model presented. Circles represent mobile water molecules, crosses adsorbed ones. a) Pores completely filled; all the water appears as mobile. b) Two possible modes of emptying a pore showing mobile and adsorbed water; there are two environments, the liquid component is decreased compared to a), the remaining monolayer is restricted and appears as solid; the bound component is therefore increased. c) A pore with surface adsorbed water only. d) An empty pore.

Consider a planar pore as suggested by Figure 4.2 a). In this pore, the water molecules associated with the surface are in rapid exchange with those in the bulk of the pore. Hence they are characterised as mobile and the NMR signal has a long relaxation time. Figure 4.2 d) shows the pore completely dried, with no water remaining. There will be no signal. Figure 4.2 c) shows an intermediate stage of drying where all the readily evaporable water has been removed and the remaining water is adsorbed to the surface. The water is relatively immobile and so has a short relaxation time. Figure 4.2 b) (i) and Figure 4.2 b) (ii) illustrate two alternate drying scenarios leading to Figure 4.2 c). In Figure 4.2 b) (i), water is removed uniformly across the pore. The pore surface to volume ratio of the remaining water is increasing so that  $T_2$  is decreasing. However, the  $T_2$  distribution remains unimodal. This is not observed experimentally and therefore this scenario is discarded. The scenario of Figure 4.2 b) (ii) arises if capillary forces are significant. Here there is a clear demarcation of the  $T_2$  distribution corresponding to a component with the original value Figure 4.2 a) but decreasing amplitude, and a second short component with increasing amplitude Figure 4.2 c). This is the scenario observed experimentally.

Suppose that, for as a prepared sample, the total specific area of inter-C-S-H gel water measured in water molecules squared per unit volume of C-S-H is  $M$  and that a typical inter-C-S-H gel pore is  $(p+2)$  water molecules thick. The inclusion of the additional two water

layers above  $p$  will become apparent. The model is insufficiently precise to warrant distinction between water molecules adsorbed to pore surfaces and surface hydroxyls. Suppose further that the signal intensity per unit volume of water molecules is 1. Then the signal intensity due to the inter gel pore water is  $M(p+2)$ . A similar argument can be composed for the intra-C-S-H gel water save here we have a specific area of  $N$  molecules per unit volume and write the water layer thickness as  $(q+q')$  molecules. The reason for writing  $q'$  rather than 2 is that is, at this stage, unclear whether as well as surface adsorbed water, water molecules associated with Ca ions in the later stage of drying should be considered as immobile. Hence the signal intensity due to the inter-C-S-H gel pore water is  $N(q+q')$ . Finally, we assume that the signal intensity due to the CH is  $Lr$  where  $L$  and  $r$  are an effective CH surface area per unit volume of C-S-H and CH thickness respectively.

The total initial signal intensity is normalised to 1. Hence

$$M \cdot (p+2) + N \cdot (q+q') + Lr = 1 \quad (4.2)$$

The pore water is in fast exchange with the surface adsorbed water and hence appears as mobile. The CH water is bound and solid like. Thus, the initial intensities for the mobile ( $I_m$ ) and solid ( $I_s$ ) fractions are

$$I_m = 1 - I_s = M \cdot (p+2) + N \cdot (q+q') = 1 - Lr \quad (4.3)$$

Consider now that the pores are dried according to the schematic Figure 4.2 b (ii). Evaporable water is removed from a fraction  $(1-s)$  and  $(1-s')$  of the specific area of the inter- and intra- C-S-H gel water respectively, leaving an upper and lower surface mono layer in the former case and a total  $q'$  molecules per unit area in the latter (Figure 4.3).



Figure 4.3 Definition of the variables  $p$ ,  $q$ ,  $s$  and  $s'$  of the model

Once the evaporable water is removed, the remaining water that was in fast exchange is immobilised and joins the “solid” fraction. Hence, during drying

$$I_m = M \cdot (p + 2) \cdot s + N \cdot (q + q') \cdot s' \quad (4.4)$$

and

$$I_s = 2M \cdot (1 - s) + q'N \cdot (1 - s') + Lr \quad (4.5)$$

The normalised mass of water remaining during drying is:

$$\rho = 1 - Mp \cdot (1 - s) - Nq \cdot (1 - s') \quad (4.6)$$

Experimental evidence to be presented suggests that the drying is characterised by three distinct stages. It is assumed that the first stage corresponds to removal of evaporable water from the inter-C-S-H gel pores only. Hence, during the first stage,  $s' = 1$ , leading from (4.4) and (4.6) to

$$I_{m1} = a_1 \rho + b_1 \quad (4.7)$$

$$\text{where } a_1 = 1 + \frac{2}{p} \text{ and } b_1 = M \cdot (p + 2) - \frac{2}{p} + N \cdot (q + q') - 1.$$

Equation (4.7) characterises the mobile signal intensity as function of mass during early drying. The relationship is linear, with gradient  $a_1 = 1 + \frac{2}{p}$  and intercept

$$b_1 = M \cdot (p + 2) - \frac{2}{p} + N \cdot (q + q') - 1.$$

The second stage is assumed to correspond to the removal of evaporable water from the intra-C-S-H layers. During this stage,  $s = 0$  and  $s' < 1$ . Thus

$$I_{m2} = a_2 \rho + b_2 \quad (4.8)$$

Hence, using the same notation as above, for the 2<sup>nd</sup> stage of drying to  $a_2 = 1 + \frac{q'}{q}$  and

$$b_2 = Mp + \frac{q'}{q} \cdot (Mp - 1) + N \cdot (q + q') - 1$$

The model parameters  $p$ ,  $q$  and  $M$  and  $N$  can be calculated from equation (4.7) and (4.8) as:

$$p = \frac{2}{a_1 - 1} \quad (4.9)$$

$$q = \frac{q'}{a_2 - 1} \quad (4.10)$$

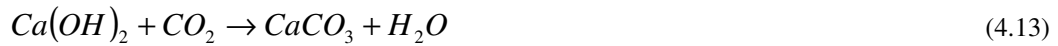
$$M = \frac{\frac{2}{p} - \frac{q'}{q} + b_1 - b_2}{2 - p \frac{q'}{q}} \quad (4.11)$$

$$N = \frac{\frac{q'}{q} - Mp \cdot \left(1 + \frac{q'}{q}\right) + b_2 + 1}{q + q'} \quad (4.12)$$

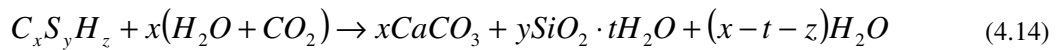
The product  $Lr$  is available from the solid signal intensity at time zero although nothing can be said about the  $L$  and  $r$  separately, that is the shape of the CH crystals.

The final stage of the drying, which only occurs with more extreme heating, is removal assumed to be due to removal of the “solid” water. It is broken down into several processes. First, the removal of intra-C-S-H water associated with the calcium ions, secondly removal of surface adsorbed water both from inter and intra C-S-H gel pores and thirdly, water lost due to breakdown of CH into C+H; that is  $\text{Ca}(\text{OH})_2$  into  $\text{CaO}$  and water.

A further process that is not “drying”, but which materially affects the results, is carbonation of the C-S-H and CH. Carbonation involves the ingress of  $\text{CO}_2$  such that



and



The ingress of  $\text{CO}_2$  causes an increase in mass. Hence the rate of mass loss decelerates compared to the rate of signal loss.

During the “normal” drying the total signal loss rate per unit mass loss rate is unity in terms of water molecules.

This mean 2  $^1\text{H}$  are lost for each 18 amu (1 water molecule has two protons and weighs 18 atomic mass units). If in the “drying + carbonation” the slope become  $k$ , this means that there are  $2k$  H lost every 18 amu lost, or equivalently, 2  $^1\text{H}$  lost every  $18/\text{k}$  amu lost.

We notice now that every  $\text{H}_2\text{O}$  lost decreases the  $^1\text{H}$  count by 2 and the mass by 16 amu and every  $\text{CO}_2$  uptake increases the mass by 44 amu leaving the  $^1\text{H}$  count unchanged. This can be more easily clarified visualising the changes graphically using a  $^1\text{H}$  versus amu plane (Figure 4.4).

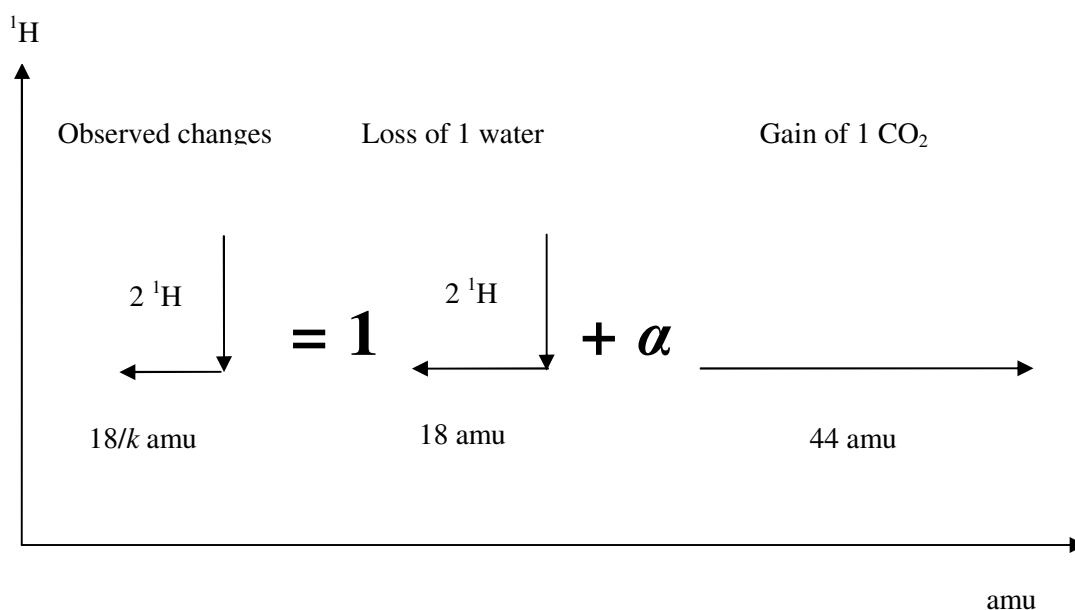


Figure 4.4 Graphical representation of the movements in the  $^1\text{H}$ -amu plane. Left, the required movement to fit the data; centre, the movements due to the loss of 1 water, right, the one due to the gain of 1  $\text{CO}_2$ . The required movement is divided as the sum of 1 water loss and  $\alpha$   $\text{CO}_2$  gained

To achieve 2  $^1\text{H}$  lost and  $18/\text{k}$  amu lost we can assume that we are losing one  $\text{H}_2\text{O}$  that takes fully into account for the  $^1\text{H}$  count, and then that we gain a number  $\alpha$  of  $\text{CO}_2$  molecules to take into account for the right mass change.

The number  $\alpha$  can be calculated considering that must be true that

$$\frac{18}{k} = 18 - 44\alpha \quad (4.15)$$

and therefore

$$\alpha = \frac{18}{44} \cdot \left(1 - \frac{1}{k}\right) \quad (4.16)$$

This means that the observed slope is reproduced if  $\alpha$  CO<sub>2</sub> are bound in the sample for each H<sub>2</sub>O evaporated.

In this way any slope  $k > 1$  can be justified. Of course a slope  $k < 1$  would require, to be justified, a loss of CO<sub>2</sub> that is definitely not realistic for temperatures lower than a few hundred °C.

## 4.5 Results

To ensure that the experimental setup was suitable to detect the bound protons present in CH and other comparable environments in cement, we performed the solid echo experiment on dried calcium hydroxide. The result is shown in Figure 4.5. This shows a solid echo signal measured from dried and powdered reagent grade Ca(OH)<sub>2</sub>.

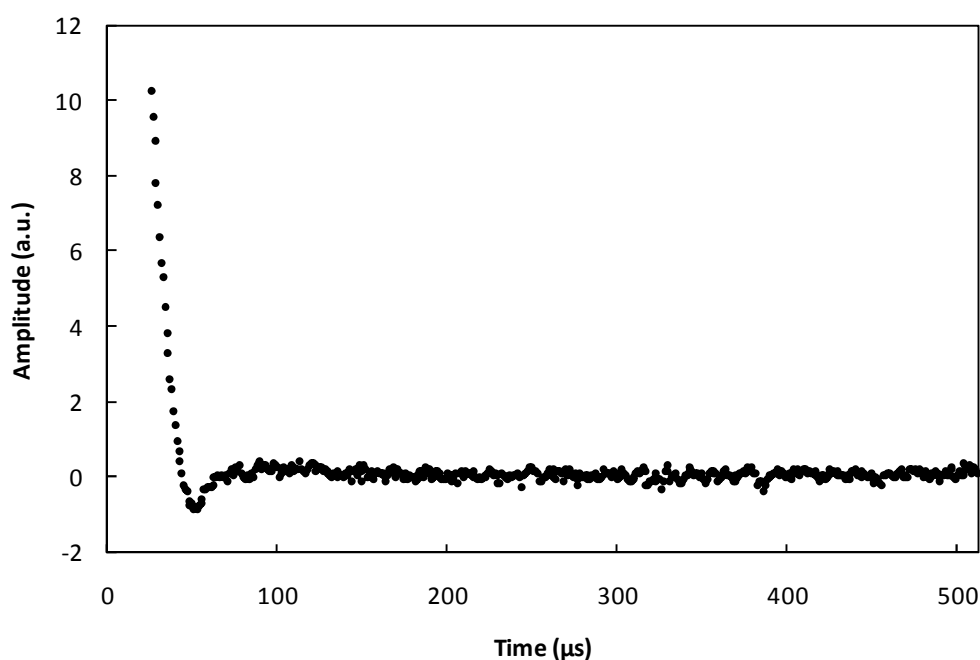


Figure 4.5 An exemplar solid echo signal ( $\tau = 20 \mu\text{s}$ ) recorded from a dry Ca(OH)<sub>2</sub> sample. The oscillation visible is typical of a Pake doublet.

In this measurement,  $\tau = 20 \mu\text{s}$ . The echo is seen to decay rapidly and to be followed by the small negative oscillation typical of the Pake doublet. Because Pake doublets are a well known feature of systems comprising rigid pairs of dipolar coupled spin 1/2 nuclei such as

hydrogen protons in  $\text{Ca(OH)}_2$ , we are confident that we are detecting the protons in such an environment, validating our approach. The Fourier transform of the data in Figure 4.5 is presented in Figure 4.6; also here are well visible the two symmetric feature typical of the Pake doublet.

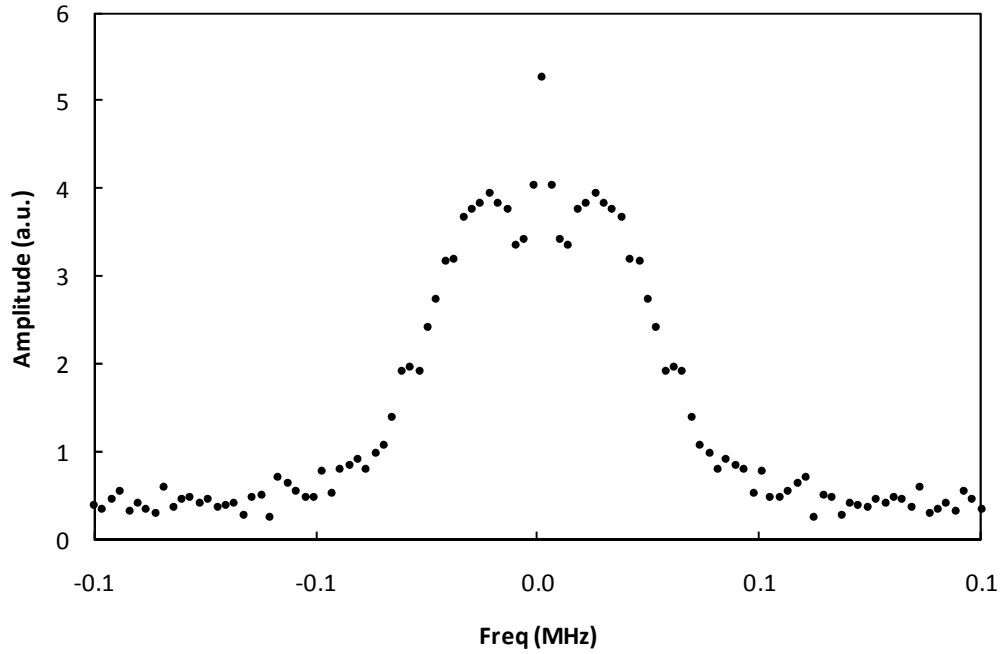


Figure 4.6 Fourier transform of the data shown in Figure 4.5. Are well visible the two symmetric peaks typical off the Pake doublet. The central peak at zero frequency is probably an artefact of the Fourier transform.

Figure 4.7 shows an exemplar echo signal as recorded from a cement paste sample.

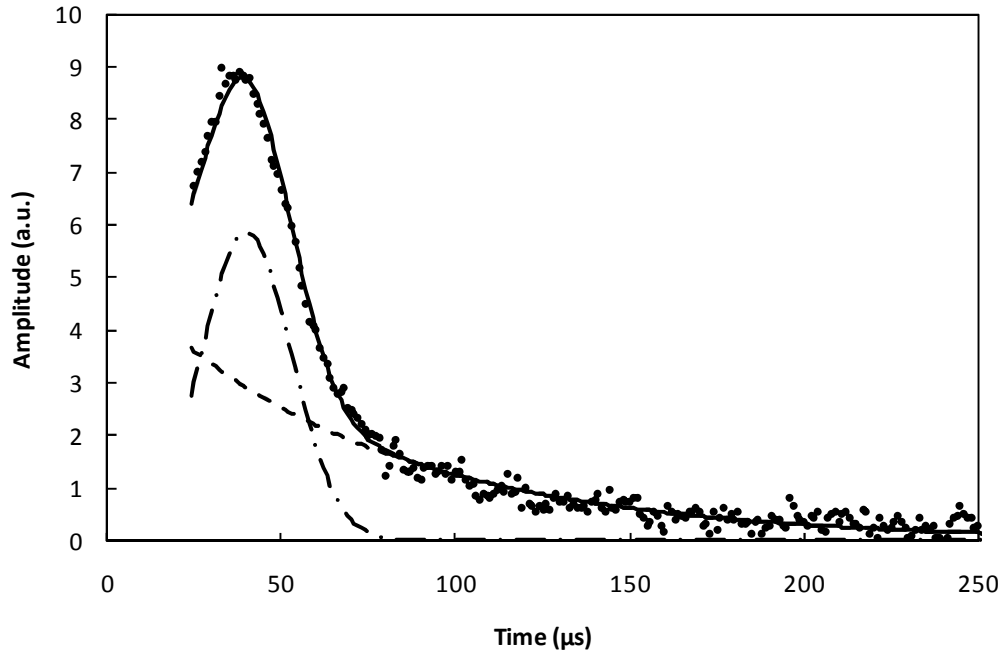


Figure 4.7 An exemplar solid echo signal ( $\tau = 40 \mu\text{s}$ ) recorded from white cement paste after drying to 0.8 the initial mass. The dot-dash and dashed lines show the Gaussian and free induction decay signals fit to the data as from the two components of equation (4.1). The Gaussian is centred on  $t = \tau$ , while the decay is extrapolated back to  $t = -\tau$  (not shown). The solid line is the combined total fit as equation (4.1).

The sample of this example has been dried progressively at temperatures up to  $120^\circ\text{C}$  and at this stage has attained a fractional mass compared to the start of 0.8 so that most of the evaporable water has been lost. The pulse gap  $\tau$  is  $40 \mu\text{s}$ , which is relatively long, so the solid echo is already significantly attenuated. Hence, the signal to noise ratio of this measurement is relatively low at 15. It is therefore close to a “worst case” data set from the viewpoint of data analysis. Nonetheless, the signal can be well fit to an exponential decay and a Gaussian according to equation (4.1). The relaxation time fit parameters are  $\sigma = 18.3 \pm 0.5 \mu\text{s}$  and  $T_2^* = 71 \pm 3 \mu\text{s}$  for the bound and mobile components respectively. The corresponding signal amplitudes are  $5.8 \pm 0.2$  and  $9 \pm 1$  respectively. Looking at the amplitudes of the fits in the plot, it may seem that the amplitudes are very different and not comparable as described, however, what must be taken into account is that the amplitude of the exponential is considered at its zero time that is  $\tau$  before the second pulse and therefore at  $t = -\tau$  on the axes.

In the stack plot Figure 4.8 the time domain data for different  $\tau$  values are shown. The  $\tau$  used are (bottom to top) 15, 20, 25, 30, 35, 40, 45  $\mu\text{s}$ . As the pulse gap increases the shape of the echo is more evident and its top becomes visible. At the same time the signal decreases for both echo and exponential components.

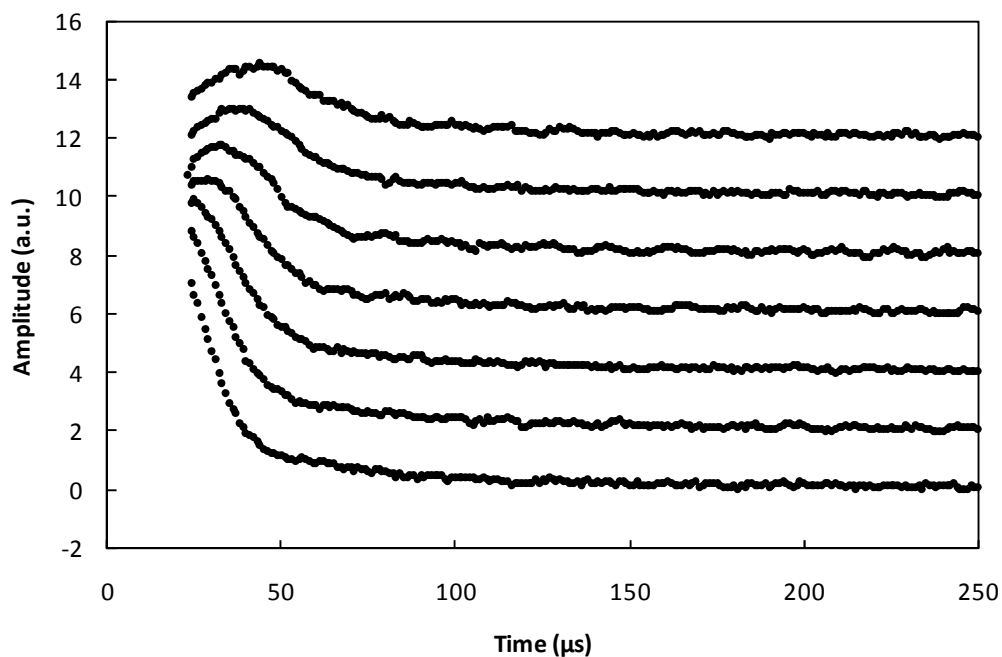


Figure 4.8 Stack plot of the time domain data for different  $\tau$  values. The  $\tau$  used are (bottom to top) 15, 20, 25, 30, 35, 40, 45  $\mu\text{s}$ . As the pulse gap increases the shape of the echo is more evident and its maximum become visible. At the same time the signal decreases for both echo and exponential components.

Figure 4.9 shows the pulse gap dependence of the echo and FID decay fit amplitudes for the cement sample at the same drying conditions as in Figure 4.7. It is seen that the bound signal amplitude is a strong function of the pulse gap whereas the mobile signal amplitude is a much weaker function. Both amplitudes have been fitted to a single component exponential decay curve as a function of the pulse gap and back extrapolated to zero time in order to gain the best estimate of the bound and mobile hydrogen fractions. In this example the amplitudes at zero time are 48.3 (bound) and 8.2 (mobile).

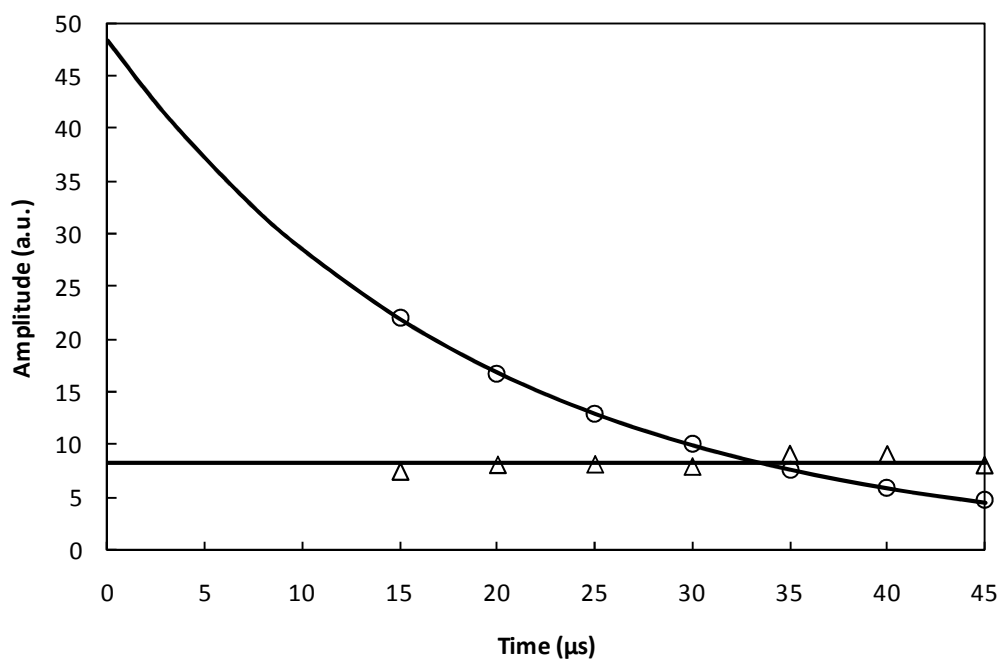


Figure 4.9 The  $\tau$  dependence of the solid echo (circles) and mobile exponential component (triangles) signal intensity for white cement paste after drying to 0.8 the initial mass. The solid lines are exponential fits to the data.

Figure 4.10 shows the amplitude of the bound and liquid signals and their combined total as a function of the sample mass. All signal amplitudes have been normalised to the initial total (solid + mobile) amplitude and are therefore fractions. The arrows above the plot shows the maximum drying temperature used to reach the corresponding sample masses. This is indicative only of the temperature required since, to a limited extent, the same mass can be achieved by a longer drying period at lower temperature or, conversely, shorter period at higher temperature than actually used.

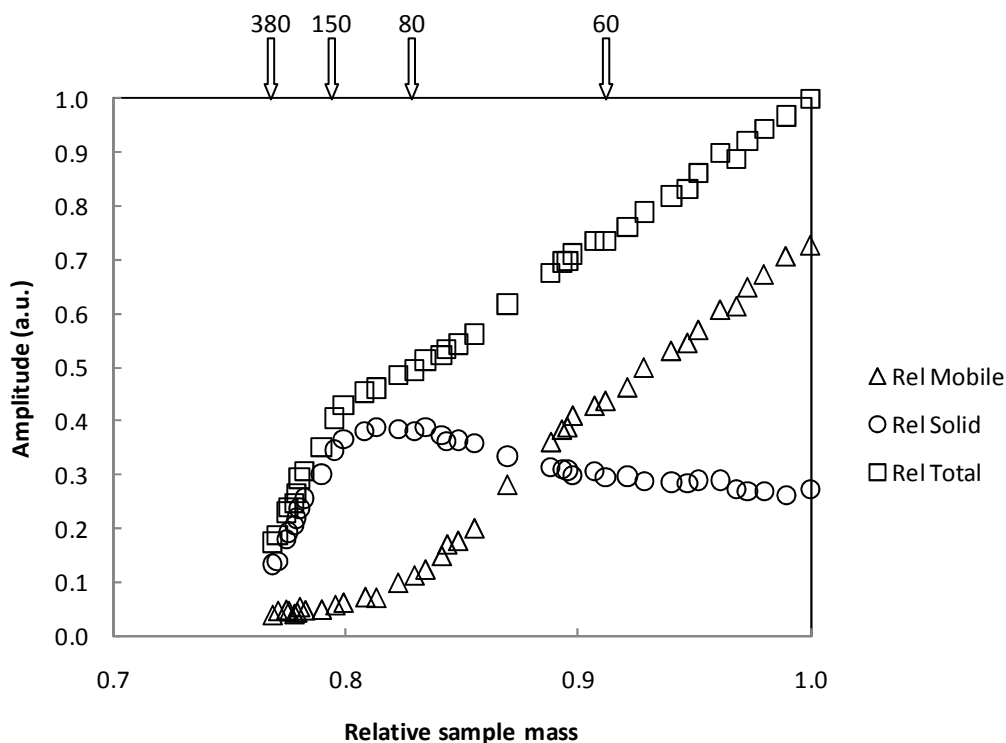


Figure 4.10 The total NMR signal (squares), solid (circles) and mobile (triangles) signal fractions as a function of the actual relative mass of the sample the arrows at the top refer to the maximum drying temperature ( $^{\circ}\text{C}$ ).

It is seen that the sample dries to 77% of the initial mass at the maximum temperature attained.

This experiment has been repeated on samples with different ages (between 2 weeks and several months) and different drying speeds, although not always with the same number of points. The features observed and discussed in the next section have been found to be reproducible. In Figure 4.11 two dataset are plotted together to show this reproducibility.

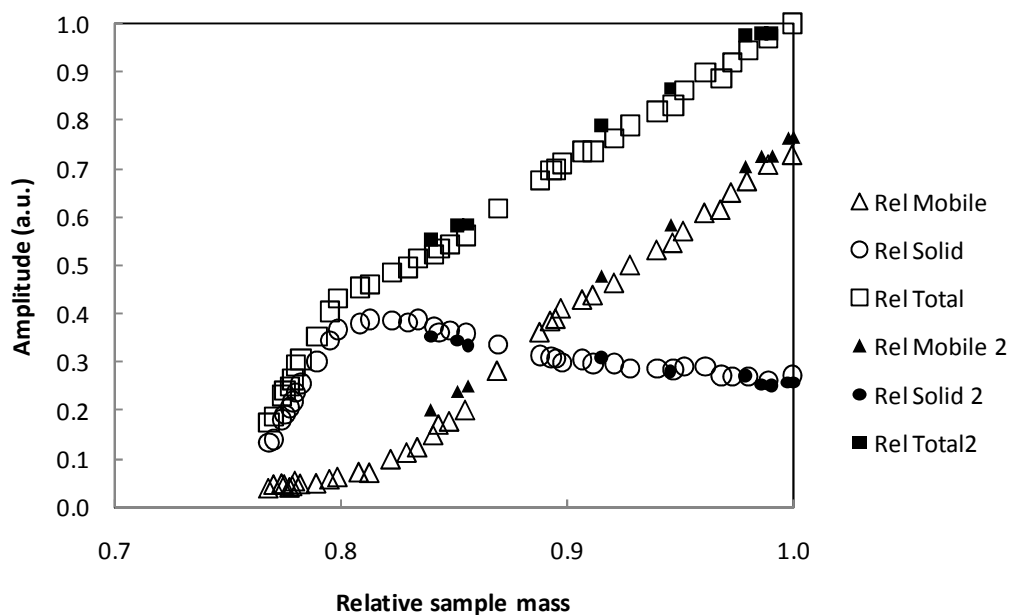


Figure 4.11 Two different dataset (measured on different age samples). The one shown with empty marker is the same shown in Figure 4.10)

## 4.6 Discussion

The reproducibility of the features visible in the Figure 4.10 for different drying processes (faster or slower) and sample age (2 weeks or 2 months) suggest that the different drying speed does not play a role in the determination of the shape of the plot; In addition, for the purposes of this study, the characteristics of the sample do not appear to change within this range of ages.

The primary observation to be made from Figure 4.5 is that we are satisfactorily working in a regime where we can see the broadest line components as evidenced by observation of the Pake doublet for  $\text{Ca}(\text{OH})_2$ . For cements, the signal arising from the solid echo experiment is clearly partitioned into two components reflecting the bound and more mobile water. Interestingly, the same is true for as-received  $\text{Ca}(\text{OH})_2$  which clearly holds a significant fraction of adsorbed water on the crystallites. The Figure 4.5 is for dried material.

In all the solid echo experiments performed we were not able to discriminate between different relaxation components contributing to the FID. This is probably due to the fact the exponential decay is a FID and not a CPMG, therefore the magnet inhomogeneities are not refocused giving a  $T_2^*$  decay instead of the  $T_2$  of the CPMG. The  $T_2^*$  is mainly magnet dependent, therefore “hide” the sample characteristics. However this should not worry us, in fact we always use the amplitude, not the relaxation rate.

The first conclusion to be drawn from Figure 4.10 is that, initially, 27 % of the signal is in the solid fraction and 73% in the mobile. It is suggested that, at this stage, the bound fraction is made up exclusively of signal from the CH: the Portlandite. The cement pores are fully saturated and the pore water hydrogens, if not the water molecules themselves, are in rapid exchange with water and hydroxyls occupying the pore surface. Hence all the C-S-H water appears as mobile.

As water is removed from the sample, so the total signal decreases. The decrease is linear in two distinct regions with different gradients: first in the relative sample mass range 1.0 to 0.8 and then with an accelerated gradient below 0.8. More careful inspection of the bound and mobile fractions in the range 1.0 to 0.8 mass fraction suggests that the first part itself divides into two stages. Hence we refer to three stages of drying: the first and second from 1.0 to 0.8 mass fraction and the third below 0.8.

Linear signal loss with mass is expected as each lost water molecule contributes equal signal: hence the observation of accelerating signal loss below 0.8 mass fraction in stage 3 is a surprise, discussed further below. For the present we confine discussion to the behaviours between 1.0 and 0.8. In this range, it is reasonable to expect that readily evaporable water is lost. One therefore expects the mobile fraction to decrease in parallel with the total. In fact, it decreases more quickly while the bound fraction increases.

To better interpret the data in Figure 4.9, a recalculation can be performed to express the data not as a function of the actual sample mass, but as a function of water content. This can be calculated from the known initial w/c ratio that is equal to 0.4.

$$w_c = \frac{w}{c + w} = 0.286 \quad (4.17)$$

Where  $w_c$  is the relative water content,  $w$  the initial water content and  $c$  the initial cement content. Knowing this we can recalculate a new x axes mapping the 0.714 to 1 range to the 0 to 1 range. The result is shown in Figure 4.12; line  $x = y$  has also be drawn and the reason will be clarified soon.

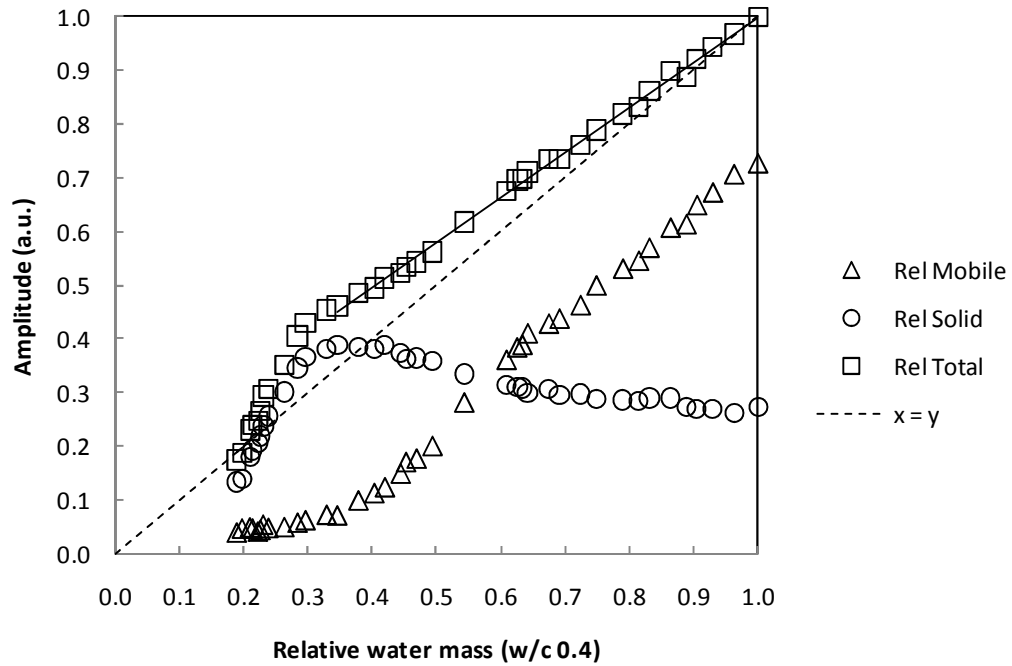


Figure 4.12 The data shown in the Figure 4.10 but with the x axis recalculated to show the water content assuming a w/c ratio of 0.4. The solid line is the linear fit to the total signal. The dotted line is the line  $x = y$ ; does not refer to any type of fit but shows the expected behaviour of the total component of the signal.

Based on this axis, the gradient of the total water signal loss curve is 0.836 (solid line in Figure 4.12). This is close to, but not equal to, the expected value of 1.0 (dotted line in the same plot). The reason is almost certainly due to error in the water fraction calculation. The sample was cured under water, which probably raised the effective water to cement ratio. Equally, the cured sample was crushed in air before use and probably dried slightly. A correction is required for both effects and can be carried out. Looking forward to what follows, we note that applying either or both of them does not substantially affect the quantitative conclusions of this work. The correction adopted first is to change the effective water to cement ratio in order to force the gradient of the best fit line to the total signal loss relative to the calculated water fraction to be equal to 1.0 down to a sample mass fraction of 0.8. The effective water to cement ratio required to achieve this is found to be 0.52. This is reasonable because as the sample is cured under water, it absorbs water during the early stages of the hydration. This is the basis of the axes in which the plot has been re-drawn in Figure 4.13.

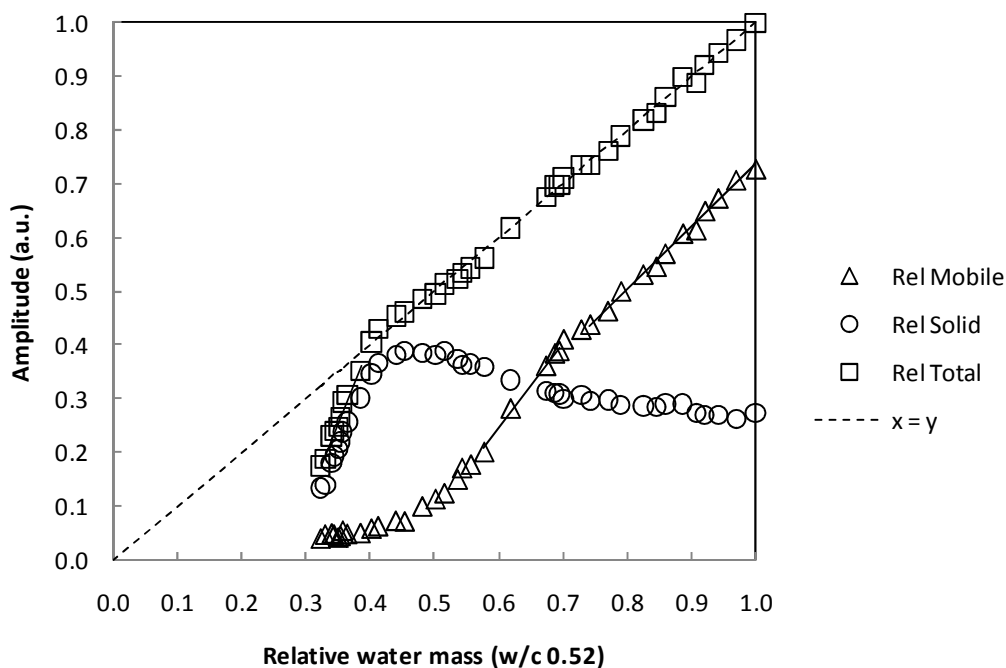


Figure 4.13 The same data as in the previous plots, but calculating the water mass assuming a  $w/c = 0.52$ , this is the required to achieve a slope 1 for the total signal in the first two stages of drying. The linear fits to the liquid component in the first and second stage and the total component in the third stage are also presented (solid lines). The dotted line is the  $x = y$  one.

Unless otherwise explicitly stated, all further discussion refers to this last representation.

The mobile fraction decreases linearly between water fractions 1.0 and circa 0.75. We refer to this as the first stage of drying. Below 0.75, the mobile fraction starts to decrease at a slightly faster rate before plateauing out close to zero. This is the second stage. The bound fraction increases in sympathy while the mobile signal remains before decreasing sharply towards zero in the final third stage of drying as previously noted.

There are therefore two clear stages of loss of evaporable water. We seek to apply the model embodied by equations (4.2) to (4.12). To that end, we have fitted the mobile water loss to a straight line function first in the range 1.0 to 0.74 (stage 1) and then again in the range 0.69 to 0.57 (stage 2). Figure 4.13 shows the best fit lines. In stage 1, the gradient and intercept are 1.16 and -0.424 while in stage 2 they are 1.60 and -0.717. Direct application of the model, and assuming  $q' = 2$  representing a mono-layer of adsorbed hydrogen in the sheet pores yields pore thicknesses of  $(p+2) = 14.6$  water molecules and  $(q+2) = 5.3$  water molecules for the two pore types respectively.

It is reasonably assumed that the first pores to dry are the inter crystallite gel pores and that these therefore have a nominal width of 4.1 nm on the basis of 0.28 nm per water molecule.

Equally, it is reasonable to assume that the second stage involves water loss from the intra-crystalline sheet pores in which case these have a width of 1.5 nm. These results, which are based on the *amplitudes* of the NMR signal are in fairly good agreement with previous estimates of these sizes [68],  $6 \pm 2$  nm and  $1 \pm 0.3$  nm respectively which were based on the NMR relaxation *times*. Both methods assume fast exchange of hydrogen between pore surface and bulk sites. The latter however, requires considerable reliance on careful calibration of the pore surface relaxivity and detailed model dependence that is not inherent to the new estimates.

The current analysis goes further than the previous analysis based on relaxation times in so much as the relative specific surface area of the two pore types can also be evaluated. The intercepts of the fit lines in Figure 4.13 can be used in conjunction with equations (4.11) and (4.12) to yield  $M = 0.027$  and  $N = 0.065$  both in arbitrary signal intensity units. The ratio,  $N/M$  is the ratio of the specific area of sheet to inter crystalline gel pores respectively. This ratio is 2.4. As a guide, if it is assumed that gel pores arise from the arbitrary stacking of crystallites of a few sheet layers each, then they will likely have a comparable area. Hence one may conclude that the crystallites are on average 2 to 3 sheets thick.

Also, one can calculate the ratio of the sheet to gel porosity as  $N(q+2):M(p+2)$ . This is found to be equal to 0.88, implying that the sheet porosity is 0.47 of the total. However, if the porosity is based on the evaporable water fraction only, then the volume ratio is  $Nq:Mp = 0.63$  so that the sheet porosity is 38%.

Calculations according the Powers-Brownyard model reported in reference [7] suggest that circa one third of the porosity is interlayer space although there is difficulty in precisely defining the two within this model.

These calculations have been based upon a calculated effective water to cement ratio of 0.52. The alternative correction factor is to add a constant to the sample mass to reflect water loss during crushing, again to force the gradient of the total signal loss to unity. The necessary correction factor required is -29.9% of the water content at  $w/c = 0.4$ . This is negative suggesting that the sample gained water from the air during crushing. This is unrealistic, reflecting the fact that the actual water content at the start of crushing was likely to be much greater. Notwithstanding, the fit parameters for this correction yield  $(p+2) = 14.6$  and  $(q+2) = 5.3$ . These are both unchanged reflecting the pore thickness model invariance to these corrections. The pore specific areas are more affected:  $M = 0.011$  and  $N = 0.084$  giving an areal and volume ratio of 7.6 and 2.8 respectively. The other difficulty with this correction is that the predicted portlandite fraction becomes 39%.

A further enhancement to the fitting is to not only force the gradient of the total signal loss to unity, but also to require the portlandite fraction to be the expected value of 28.8% [144,148]. This is achieved for an effective water to cement ratio of 0.49 and a crushing water mass gain of 6%. In this case  $(p+2) = 14.6$  and  $(q+2) = 5.3$  as before and  $M = 0.024$  and  $N = 0.068$  so that the sheet to gel pore area and volume ratio of 2.9 and 0.51 respectively is in good agreement with the earlier estimate based on water to cement ratio correction only.

Finally, we explore the third stage of drying. Here we find that, after a transition around 120 °C, relative sample mass 0.8 (and therefore related to Figure 4.10) where the bound fraction signal goes through a maximum; we see greatly accelerated loss of total signal with mass. The graph is near linear with a gradient of 3.0 (Figure 4.12). Since signal is lost in direct proportion to water loss in the readily evaporable stages, the only possibilities are that, to a greater or lesser extent, hydrogen, but not oxygen, is being lost or that the sample is also gaining mass in parallel with drying. The temperature range at the start of this region seems too low for the former and we look to carbonation as a mechanism for the latter. Given the molecular mass of water (18) and carbon dioxide (44), we calculate using equation (4.16) that the observed total signal loss with mass is achieved if, for every water molecule leaving the sample, 0.273 CO<sub>2</sub> are gained. Put another way, we gain 1 CO<sub>2</sub> for every 3.66 waters lost. Up to a temperature of 180 °C, where the bound intensity re-attains the initial value, it is reasonable to assume that this is carbonation of the C-S-H. This would be in accord with conventional understanding where carbonation accelerates in partially dried C-S-H [149].

Beyond a temperature of 180 °C the experiment begins to enter a regime where breakdown of the Portlandite is possible into C and H and where carbonation of the C within Portlandite can become significant. Hence the total signal decreases below the initial bound value.

## 4.7 Conclusion

In this chapter the following has been presented: an analysis of the porosity in white cement pastes based upon NMR signal amplitudes as a function of sample mass during controlled drying. The analysis has been interpreted in terms of water loss from two reservoirs of nano-scale planar pores that are suggested to be first the sheet pores of C-S-H and second the inter-crystallite C-S-H gel pores. The best estimates for the intra- and inter- crystallite pores thicknesses are 1.5 and 4.1 nm respectively. The ratio of the specific areas of the two pores types is estimated to be 2.4. The total volume ratio of the pore types is 0.88 whereas the volume of readily evaporable water within them is 0.63, implying that the sheet total (mobile water) porosity is 0.47 (0.38) of the total.

## 5 DQF

### 5.1 Introduction

As briefly mentioned in paragraph 1.4.1.3,  $^1\text{H}$  DQF NMR is sensitive to protons experiencing interactions with anisotropic structures. This is due to the fact that the particular pulse sequence is able to filter out the entire signal originating from water that experiences isotropic motion on the timescale of the NMR experiment.

This technique has been widely applied to biological structures as tendon and cartilages [49,150-153]. Applications in material science have also been reported in literature [154].

Due to the layered structure of the C-S-H, the protons in the intra-layer spacing should experience a strongly anisotropic environment; the water in the inter-layers could have some residual dipolar effect and therefore show in the DQF spectra.

To our knowledge no work has been published up to now on DQF applications on cement.

This work has been partially performed in parallel with the previously described solid echo experiments; in fact the behaviour of the DQF signal has been measured during drying as well (although not for the same high number of steps).

### 5.2 Experiment materials and methods

#### 5.2.1 Sample preparation

The samples used in this experiment have been prepared in the same way as those used for the relaxation and solid echo experiments following the NANOCER guidelines described in the relevant chapter (paragraph 3.3.4 “Materials and sample preparation”). Both white and grey cements have been measured; the composition of which has been already given in Table 3.1 at Page 92. The names (A, B and C) used will match those in the table.

The drying experiment has been performed in the same way as the one with the solid echo, drying in a vacuum oven first and in a traditional one later.

#### 5.2.2 NMR experiments

The experiments have been performed on a 400 MHz CMX Infinity superconducting magnet. The room temperature at which all the measurements have been taken was constant at 22 °C. The pulse sequence used is the one presented in paragraph 1.4.1.3 on page 23. The

90 degree pulse length has been always 11.4  $\mu\text{s}$ , the number of averages has been varied from 128 to 1024 depending on the intensity of the signal per scan.

In parallel with the DQF experiments, the single quantum NMR (FID) signal has been acquired for some samples.

### 5.3 Model

#### 5.3.1 General model

The model that has been formulated takes into account the dipolar interactions between the two protons of a water molecule and a  $\text{Fe}^{3+}$  ion. These are represented in Figure 5.1.

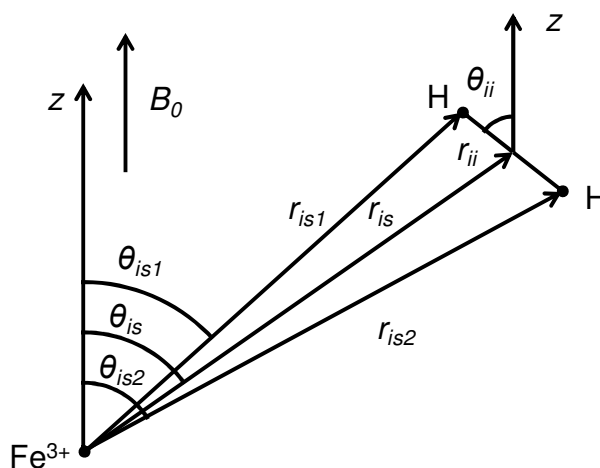


Figure 5.1 Representation of the interactions taken into account in the DQF model proposed

Because only the dipole-dipole interactions have been considered, their strength is a function of the angles between the magnetic field and the vector connecting the two spins considered and the distances only. These are the angles  $\theta_{is1}$ ,  $\theta_{is2}$  and  $\theta_{ii}$  and the distances  $r_{is1}$ ,  $r_{is2}$  and  $r_{ii}$  in Figure 5.1. This is because the Hamiltonian governing the interaction is of the type:

$$H = \frac{C}{r^3} \cdot (1 - 3\cos^2(\theta)) \quad (5.1)$$

To simplify the system a “far field” field approximation has been adopted. This assumes that the angle between the Fe and each of the two protons is the same and that the Fe-proton distance is the same for both protons ( $\theta_{is}$  and  $r_{is}$  in Figure 5.1).

### 5.3.2 Sheet model

The first geometrical model that has been attempted to be solved was the one consisting of a plane containing the Fe particle and water molecules distributed on its surface. The geometry of both protons lying in the plane has been chosen. It is too complex to analyse also other orientation with one proton out of the plane because an extra variable is introduced.

This reduces the symmetry of the system. To describe this system a laboratory frame is defined requiring the Fe to be at the origin and the  $z$  axis to be parallel to the magnetic field. We consider a C-S-H sheet pore to define a plane. The  $y$  axis in the lab is taken as being within the plane without loss of generality. The plane is made unique by requiring the Fe-H<sub>2</sub>O vector to lie in the plane (Figure 5.2). In this way the normal to the plane  $\hat{n}$  has the coordinates (in the lab frame)  $[\sin(\theta), 0, \cos(\theta)]_{\text{lab}}$ .

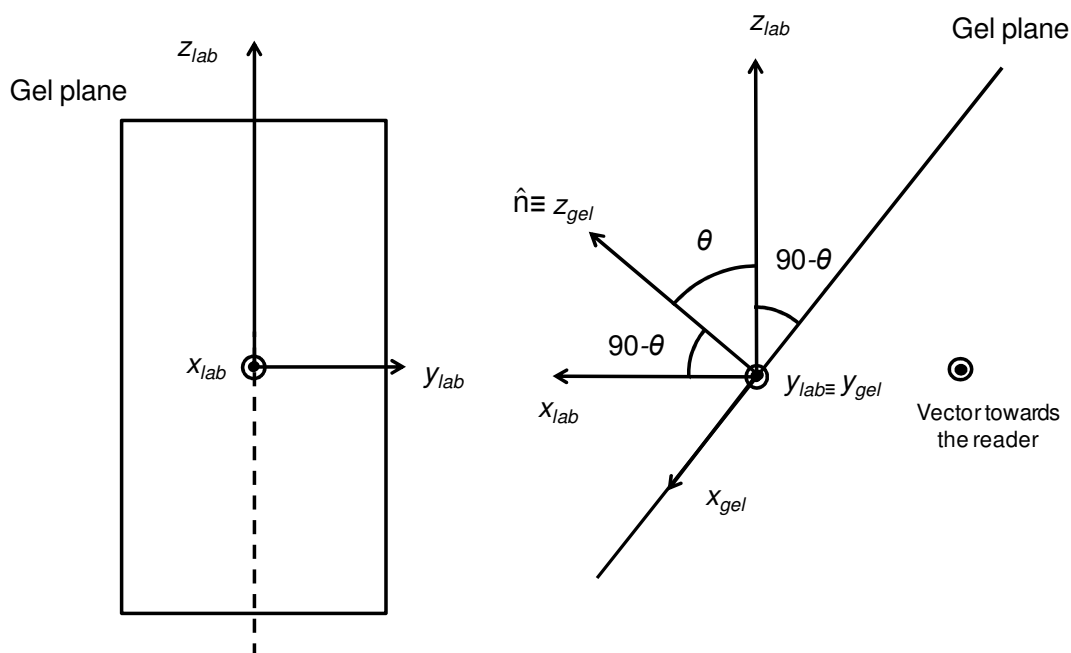


Figure 5.2 Coordinates in the laboratory frame and in the gel plane. Left, view along the  $x_{\text{lab}}$  axis, right along the  $y_{\text{lab}} \equiv y_{\text{gel}}$  axis.

A second coordinate set is defined, the sheet set, having the same origin and same  $y$  axis and  $z$  axis orthogonal to the sheet (Figure 5.2). In the gel frame the vector from the Fe to the water ( $V_{is}$ ) is defined by a single angle  $\alpha$ , which is the angle between itself and the  $x_{\text{gel}}$  axis, and the distance  $r_{is}$  (Figure 5.3)

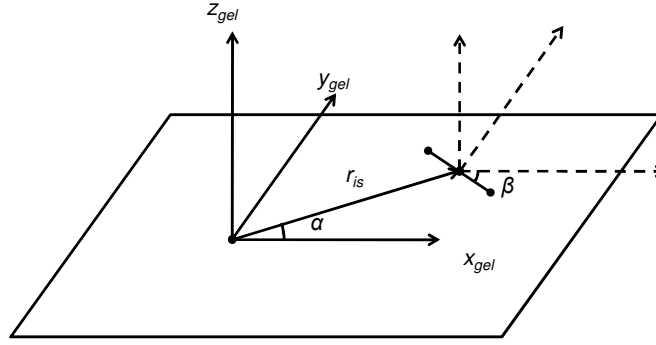


Figure 5.3 Definition of the angles  $\alpha$  and  $\beta$  that describe the relative position of the Fe and protons on the plane.

This is because of the requirement to have it in the plane. The coordinates of this vector are  $r_{is}[\cos(\alpha), \sin(\alpha), 0]_{\text{gel}}$  (Figure 5.3). For the same reason, also the proton-proton vector ( $V_{ii}$ ) is defined by a single angle beta and the  $r_{ii}$  distance (Figure 5.3). Its coordinates will be  $r_{ii}[\cos(\beta), \sin(\beta), 0]_{\text{gel}}$ . To move from the gel frame to the lab frame, due to the particular geometry chosen, we need only a rotation around the  $y_{\text{lab}}$  axes by  $-\theta$ . This can be expressed as:

$$\begin{aligned} V_{is,\text{lab}} &= R_y(-\theta) \cdot V_{is,\text{gel}} \\ V_{ii,\text{lab}} &= R_y(-\theta) \cdot V_{ii,\text{gel}} \end{aligned} \quad (5.2)$$

Where

$$R_y(\theta) = \begin{pmatrix} \cos \theta & 0 & \sin \theta \\ 0 & 1 & 0 \\ -\sin \theta & 0 & \cos \theta \end{pmatrix} \quad (5.3)$$

Therefore

$$V_{ii,lab} = \begin{pmatrix} \cos(\theta)\cos(\beta) \\ \sin(\beta) \\ \sin(\theta)\cos(\beta) \end{pmatrix} \quad (5.4)$$

$$V_{is,lab} = \begin{pmatrix} \cos(\theta)\cos(\alpha) \\ \sin(\alpha) \\ \sin(\theta)\cos(\alpha) \end{pmatrix}$$

Because the interactions are a function of the angle between the vectors and the magnetic field only, we are interested in calculating the angles  $\theta_{ii}$  and  $\theta_{is}$  in the lab reference frame. To be more precise, we are interested in the cosines of those angles, which are the terms that appear in the Hamiltonian.

$$\cos(\theta_{ii,lab}) = V_{ii,gel} \begin{pmatrix} 0 \\ 0 \\ 1 \end{pmatrix} = \sin(\theta)\cos(\beta) \quad (5.5)$$

$$\cos(\theta_{is,lab}) = V_{is,gel} \begin{pmatrix} 0 \\ 0 \\ 1 \end{pmatrix} = \sin(\theta)\cos(\alpha)$$

The signal originating from all the water molecules on a specific plane can in principle be calculated by integrating the FID signals for all the possible values of  $\alpha$  and  $\beta$  (that can be reasonably assumed to be between 0 and  $2\pi$  occurring with uniform probability) and the surface of the plane to take into account for the Fe-water distance. Moreover, an additional integral over the possible orientations of the planes can, in principle, be performed. This last integral needs more attention concerning the probability of occurrence. This is because, for a randomly oriented set of vectors passing through the origin, the distribution of the angle  $\theta$  between the  $z$  axis and the vector considered is not uniform. This can be geometrically visualised considering the length of the circle defined by the intersection of the sphere of unitary radius and the cone defined by the angle  $\theta$  with the  $z$  axis. This length is equal to  $2\pi \sin(\theta)$  and proportional to the probability of occurrence of the direction  $\theta$ . Alternatively, this fact can be interpreted by the fact that to be able to fully describe any of the possible orientation of the planes, an additional angle  $\varphi$  would be necessary. This is to remove the

requirement of taking the lab frame having the  $y$  axis in the plane. The integration over any orientation of the plane would require integration over this last angle as well. However, due to the cylindrical symmetry of the problem, it has uniform probability of occurring, and integration over this last angle can be reduced to the weighting function  $2\pi \sin(\theta)$ .

In the appendix of this thesis is presented the calculation necessary to obtain the FID for the system described for a specific value (and therefore a specific geometrical configuration) of the two interactions considered.

The integral proposed has been found too difficult to calculate analytically and extremely [CPU] time consuming to solve numerically.

### 5.3.3 Powder average

The alternative approach used was the one of performing a full powder average using only two angles; one between the magnetic field and the  $V_{is}$  vector ( $\theta_{is}$ , this will be called alpha in the code) and one between the magnetic field and the  $V_{ii}$  vector ( $\theta_{ii}$ , this will be called theta in the code). Cylindrical symmetry has been assumed for both angles and therefore a probability of occurring proportional to the sine of the angles used.

### 5.3.4 Magnetic interactions

The base used for the calculation is the one constituted from:

$$\begin{aligned}
 |1\rangle &= |\alpha\alpha, m_s\rangle \\
 |2\rangle &= \left| \frac{\alpha\beta + \beta\alpha}{\sqrt{2}}, m_s \right\rangle \\
 |3\rangle &= |\beta\beta, m_s\rangle \\
 |4\rangle &= \left| \frac{\alpha\beta - \beta\alpha}{\sqrt{2}}, m_s \right\rangle
 \end{aligned} \tag{5.6}$$

Where  $\alpha$  and  $\beta$  refers to spin up and down respectively and  $m_s$  can assume the values  $-5/2$ ,  $-3/2$ ,  $-1/2$ ,  $1/2$ ,  $3/2$ ,  $5/2$  and represent the spin of the  $\text{Fe}^{3+}$  particle. The total dimension of the basis state is therefore 24 and the density, rotation and evolution matrices 24·24. Because the Hamiltonians used are the truncated; one for proton-proton interaction (for like spins) and one truncated and in the weak coupling approximation (for unlike spins) for the proton-electron interaction, the states for different  $m_s$  do not interact. The calculation can (and has been) therefore performed for each value of  $m_s$  separately and then the results summed together. This is equivalent to limit the work on the 4·4 block matrices on the

Diagram illustrating the addition of angular momentum for two spin-1/2 particles. The vertical axis represents the total spin states  $|1\rangle$ ,  $|2\rangle$ , and  $|3\rangle$ . The horizontal axis represents the total magnetic quantum number  $m_s$ , with values ranging from  $-5/2$  to  $5/2$ . The diagram shows the possible total spin states resulting from the combination of two spin-1/2 particles, forming a triangular pattern of boxes representing the states.

The states shown are:

- $m_s = -5/2$
- $m_s = -3/2$
- $m_s = -1/2$
- $m_s = +1/2$
- $m_s = 3/2$
- $m_s = 5/2$

The Hamiltonian used for the proton-proton ( $I$ - $I$ ) interaction is the one in its truncated form [42]:

$$H_{II} = \frac{\mu_0}{4\pi} \frac{\gamma_i^2 \hbar^2}{r^3} \left( \frac{1 - 3 \cos^2 \theta}{2} \right) \left[ 3 I_z^1 \cdot I_z^2 - I^1 \cdot I^2 \right]$$

For the proton-Fe<sup>3+</sup> (*I-S*) interaction, instead, the one in the weak coupling approximation will be used:

$$H_{ii}^{tr,wc} = \frac{\mu_0}{4\pi} \frac{\gamma_i \gamma_s \hbar^2}{r^3} (1 - 3 \cos^2 \theta) [I_z \cdot S_z] \quad \left( \frac{\mu_0}{4\pi} \frac{\gamma_i \gamma_s \hbar^2}{r^3} \ll |\omega_i - \omega_s| \right)$$

In these approximations, the dipole-dipole Hamiltonians are diagonal and the calculation much simpler.

The calculations to obtain the DQF signal of such a system are described in detail in the appendix of this thesis. Only the results obtained will be presented here. The DQF spectrum for Calcium Hydroxide has also been calculated. This has been done simply varying the proton-proton distance from the characteristic one for water, which is equal to  $1.6 \text{ \AA}$ , to the one for the material that is equal to  $2.186 \text{ \AA}$  and putting  $r_{is}=\infty$ .

In Figure 5.4 the powder averaged spectra for calcium hydroxide obtained for different creation times are shown. The proton-proton distance used in this example is  $2.186 \cdot 10^{-10} \text{ m}$  that is the value reported in literature for  $\text{Ca(OH)}_2$  [155]. As in all the experiments, the evolution time is  $10 \text{ \mu s}$ . The wiggles that appear increasing the creation time are visible. The optimum creation time to obtain maximum signal intensity for the  $\text{Ca(OH)}_2$  simulated spectra has been found to be  $30 \text{ \mu s}$ , while for the  $\text{H}_2\text{O}$   $11.4 \text{ \mu s}$ . This is in accord with the theoretical analytical values.

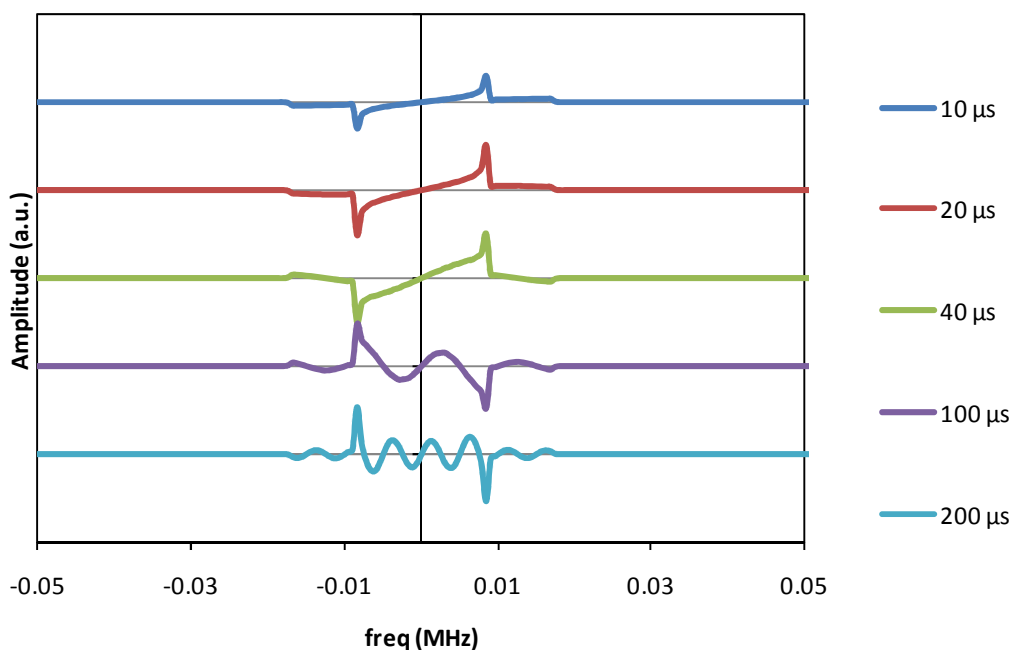


Figure 5.4 Stack plot of spectra calculated using the theory in appendix for different creation times. The proton-proton distance is  $2.186 \cdot 10^{-10} \text{ m}$  and the powder average done on 2500 steps of  $\theta_{ii}$  between 0 and  $\pi$ . The  $\text{Fe}^{3+}$  is far from the protons.

The effect of the different proton-proton distance is presented in Figure 5.5. Also for these simulated spectra the effect of the  $\text{Fe}^{3+}$  is still not introduced. The fact that the splitting (distance between the positive and negative peaks) scale with the proton-proton distance can be noticed.

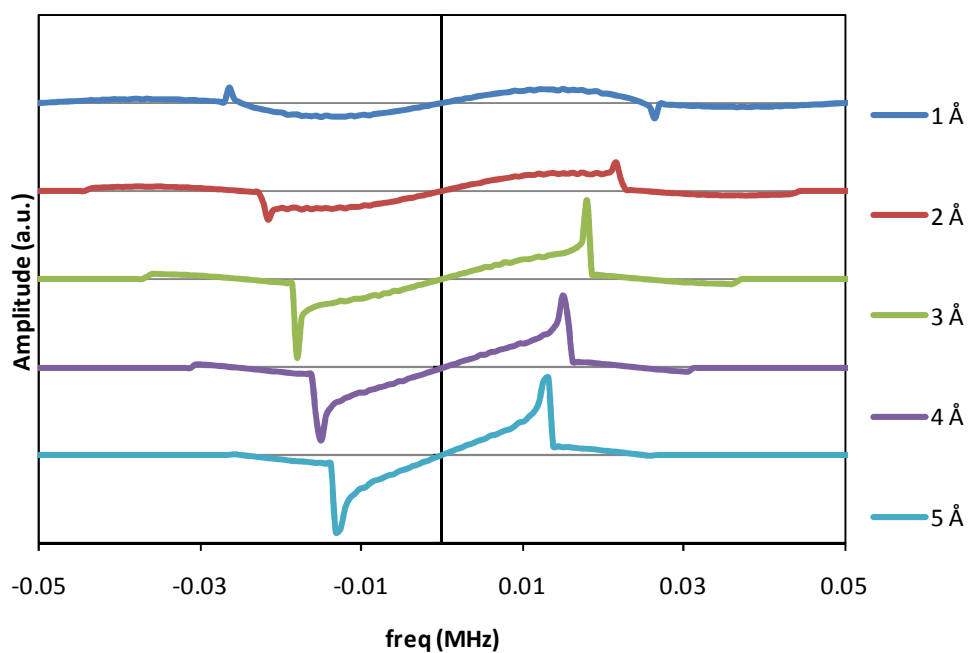


Figure 5.5 Effect of different proton-proton distance. All the DQF spectra are calculated for a creation time of 20  $\mu\text{s}$  and 2500 step for the  $\theta_{ii}$  powder average.

The introduction of the influence of the  $\text{Fe}^{3+}$  brings much more complexity in the spectra simulated. In Figure 5.6 the effect is shown for one particular set of angles (both  $\theta_{ii}$  and  $\theta_{is}$  equal to  $\pi/2$ ).

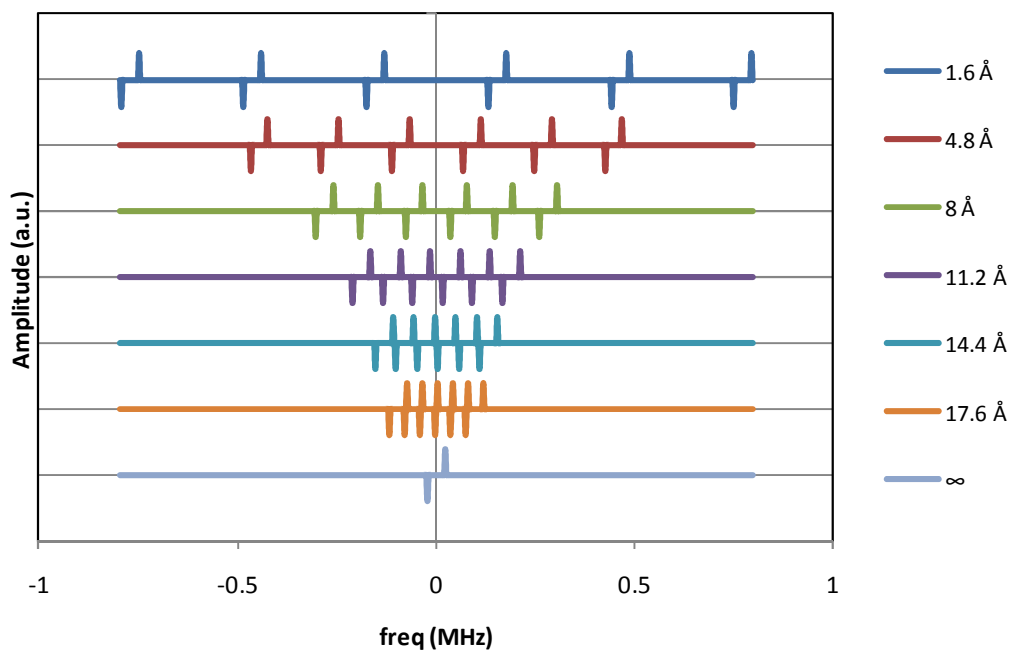


Figure 5.6 The effect of the  $\text{Fe}^{3+}$ -Water distance. The proton-proton distance ( $r_{ii}$ ) is 1.6 Å (as in water) and the  $\text{Fe}^{3+}$ -water distance increases (in units of  $r_{ii}$ , 1 to 5) from top to bottom. The last plot is for water far from the  $\text{Fe}^{3+}$ . The simulation has been performed using creation time of 55  $\mu\text{s}$ , and one specific set of angle (both equal to  $\pi/2$ ).

It is visible how the spreading of frequencies becomes huge as the distance between the  $\text{Fe}^{3+}$  and the water tends to 0. In this case, the powder average must be performed also for the  $\text{Fe}^{3+}$ -water angle and there is an additional variable that is the  $\text{Fe}^{3+}$ -water distance. The effect of the distance  $\text{Fe}^{3+}$ -water for the powder average is presented in Figure 5.7. In this case, to limit the simulation time, the spectra is truncated at  $\pm 0.15$  MHz, so that only the inner multiplets are seen at small distances.

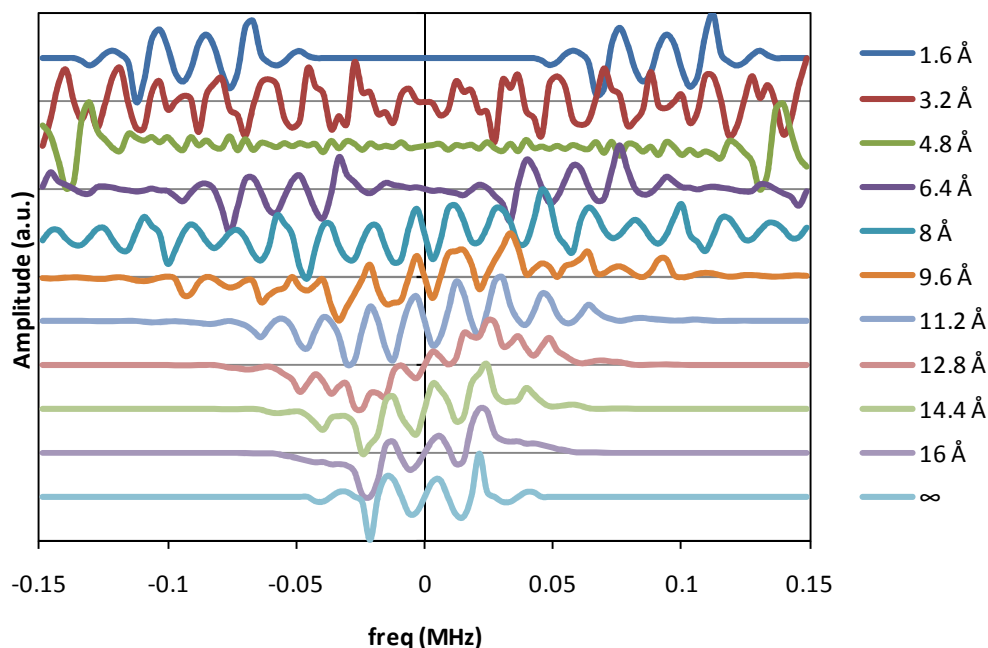


Figure 5.7 The effect of the  $\text{Fe}^{3+}$ -water distance on the powder averaged spectra. The proton-proton distance ( $r_{ii}$ ) is 1.6 Å (as in water) and the  $\text{Fe}^{3+}$ -water distance increases (in units of  $r_{ii}$ ) from top to bottom. The simulation has been performed using creation time of 55  $\mu\text{s}$ , 500 values of angle for the two powder average and 100 points in the spectra.

As the  $\text{Fe}^{3+}$ -water distance increases the shape of the spectra converge to the one for long distance as the one presented in Figure 5.4 for long creation time. The different splitting is due to the different proton-proton distance, in fact, the spectra in Figure 5.7 have been calculated for a proton-proton distance ( $r_{ii}$ ) of 1.6 Å (as in water). The creation time used is 55  $\mu\text{s}$  (as the one adopted in the experiments that will be presented). 500 values for both powder averages and 100 points in the spectra have been used.

The behaviour of the spectra shape as a function of the  $\text{Fe}^{3+}$ -water distance has been presented. Realistically, the observed spectrum is the superposition of spectra for different  $\text{Fe}^{3+}$ -water distance. The simple geometrical model that has been used to calculate the averaged spectra consists in a  $\text{Fe}^{3+}$  ion sitting at the centre of a sphere and several water molecules water uniformly distributed in half of the sphere. The fact that it is not a complete sphere arises because is considered that the  $\text{Fe}^{3+}$  has to sit on the surface of the pore and cannot be at the centre of it.

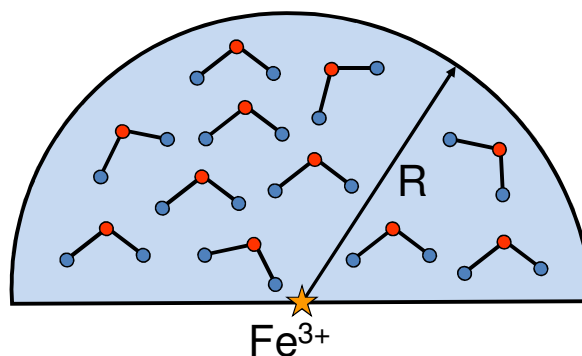


Figure 5.8 Sketch of the simple geometries adopted.

The calculation performed now consists of finding the average spectra for all the water molecules in the space considered. Mathematically this translates (remembering that we consider only half of the sphere) in the finding:

$$\frac{\int_{R_{\min}}^R I(r) \cdot N(r) dr}{\int_{R_{\min}}^R N(r) dr} \quad (5.7)$$

where

$$N(r) = \frac{2}{3} \pi (r^3) \quad (5.8)$$

that is basically saying that the number of water molecules at a determined radius is proportional to the surface of the half sphere having that radius.

In practice, to allow numerical calculation, this has been discretised. The half sphere has been subdivided into shells with boundaries in the middle of each subsequent distance at which the spectra has been calculated. The volume of the shells has been used to weigh the average spectra. The results are shown in Figure 5.9. The thickness of the shells is one proton-proton distance in water and the creation time used 55  $\mu$ s; 500 values for the powder averages and 100 points in the spectra.

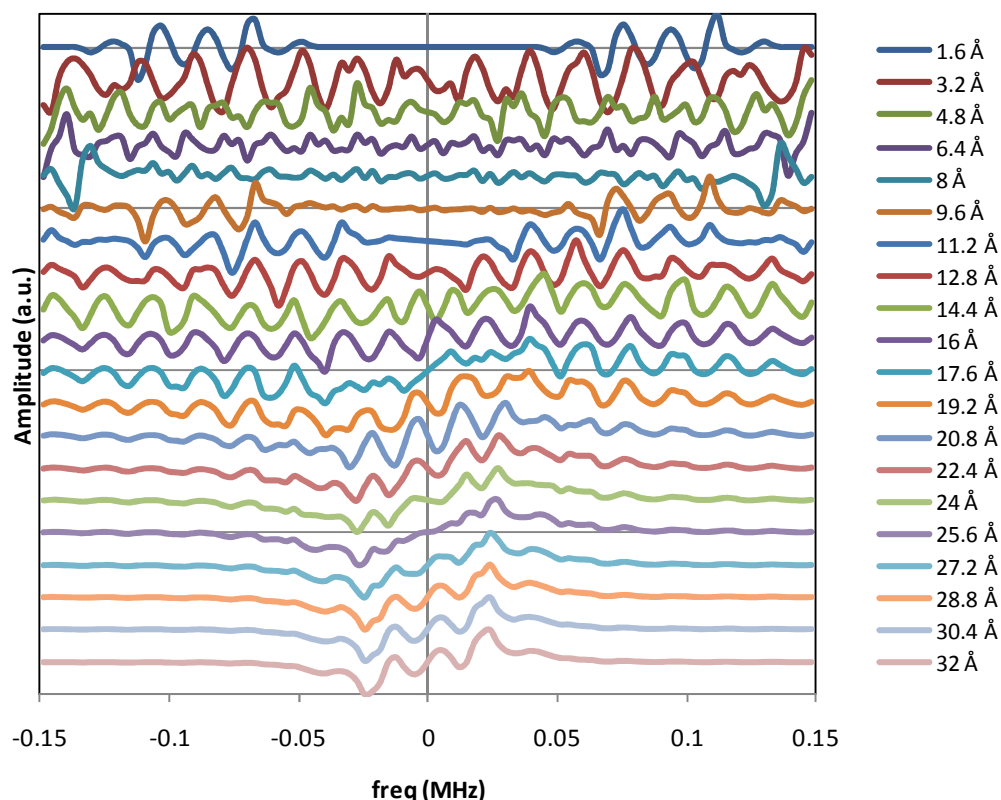


Figure 5.9 Sum of the spectra over the half sphere. The proton-proton distance ( $r_{ii}$ ) is 1.6 Å (as in water) and the  $\text{Fe}^{3+}$ -water distance increases (in steps of  $r_{ii}$ ) from top to bottom. The simulation has been performed using creation time of 55  $\mu\text{s}$ , 500 values of angles for the two powder averages and 100 points in the spectra.

The presence of a “cut off” radius can have two physical explanations: the first is that there are some structures of that characteristic length scale; the other is related to the inter-distance between the  $\text{Fe}^{3+}$ . If the  $\text{Fe}^{3+}$  are uniformly distributed at a distance  $d$  between them, any water molecule will be at a maximum distance  $d/2$  from one  $\text{Fe}^{3+}$ , independently from the size of the structures.

The stability of the numerical simulation has been checked comparing the results for different numbers of values of angles for the powder averages and in the number of points in the spectra. In Table 5.2 are presented the combinations used and in Figure 5.10 the relative spectra. Although the small details are different and are lost for the smaller number of points, the broad features are the same in all the spectra. Considering the short  $T_2$  (and therefore strong broadening) of cement data, the higher number of points used for the spectra (500, 200 and possibly 100) are probably unrealistic and show details that are not detectable experimentally.

	A	B	C	D	E	F	G	H	I
Angles for H-H	30	70	100	200	500	500	500	500	500
Points in spectra	30	70	100	200	500	30	70	100	200

Table 5.2 Combination of the number of value of angles used for the two powder averages and number of points in the spectra.

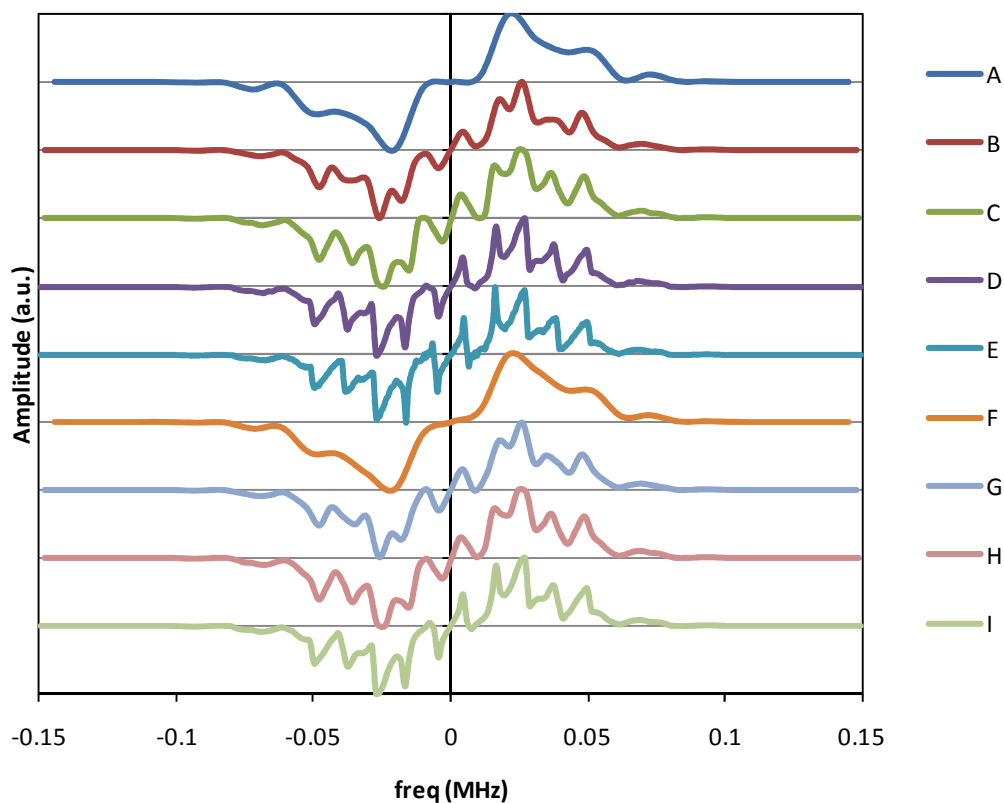


Figure 5.10 Test performed to determine the stability and convergence of the simulation. The parameters are presented in Table 5.2. The top plot refers to the left column in the table and the bottom one to the right column.

## 5.4 Results

The first result presented shows the dynamics of the building up of the DQF integral intensity with hydration, this increase is accompanied by a similar decrease of the single quantum signal (Figure 5.11); in this plot the value of the integral of the magnitude of the signal is considered. The sample is the white cement A mixed with a w/c ratio of 0.4 and hydrated in the magnet at a room temperature of circa 20-22 °C.

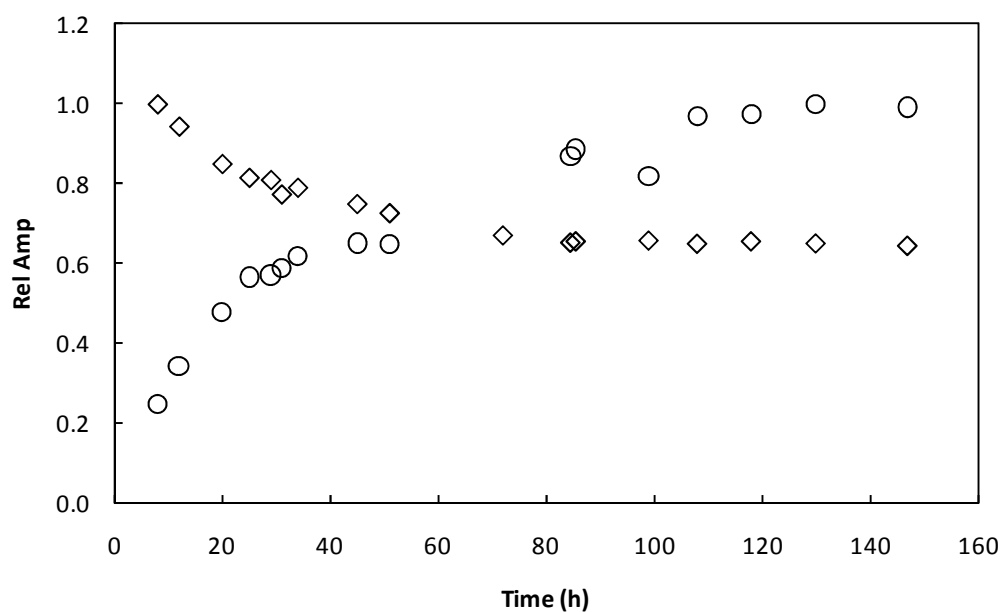


Figure 5.11 Increase of the double quantum filtered signal (circles) and decrease of the single quantum one over a period of circa one week. The data are renormalized to the maximum signal achieved for the DQF; and to the initial signal for the single quantum. The total amplitudes (or their ratio) are therefore not comparable.

The behaviour of the total DQF signal during drying is presented in Figure 5.12 and is compared to the behaviour of the Solid Echo signal already discussed in detail in the chapter 4.

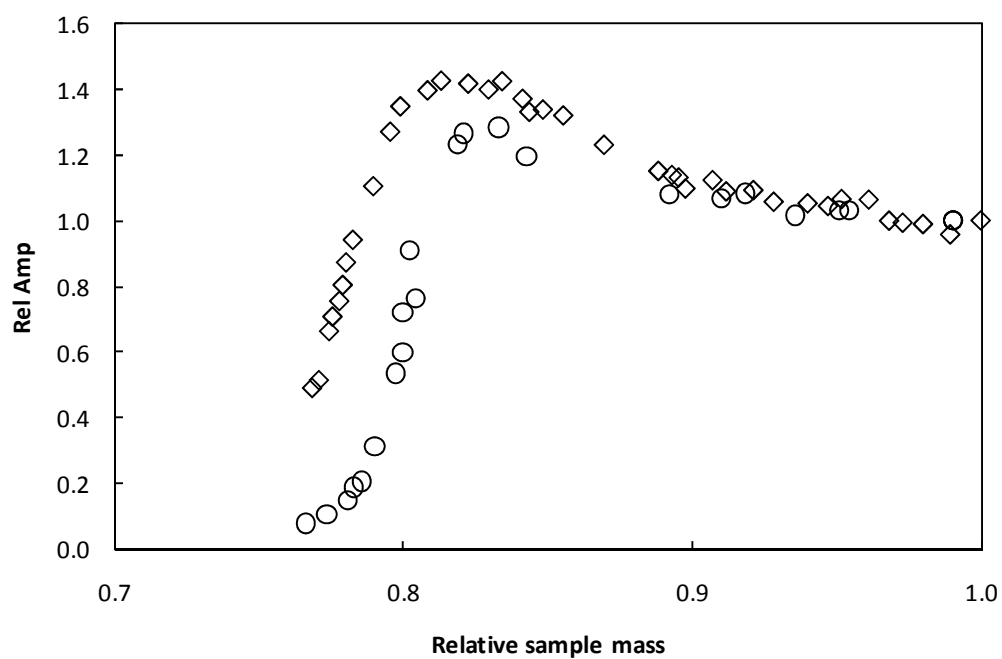


Figure 5.12 Comparison of the behaviour of the DQF (circles) and bound component of the solid echo experiment (diamonds) as function of relative sample mass.

The sample is the white cement A mixed at the standard w/c ratio of 0.4 and hydrated for 1 month at 20 °C. The two behaviours are qualitatively comparable with an early increase in signal and a sharp decrease at later drying stages, however, the maximum relative value is different and the position of the steep slope on the plot is not quite at the same relative sample mass value.

The following results will focus on the shape of the spectra instead of only the total integral. The results of the experiments performed on the three cements are presented in Figure 5.13. The w/c ratio of the samples is 0.4 and the hydration occurred at 20 °C for 14 days. The signals are normalised per unit mass of sample. It is visible that the relative amount of the broad components increases in the order A, C, B; this is also the order of increasing amount of Fe in the samples. The total signal instead decreases in the same order, significantly between the cement A and C and much less (almost imperceptibly) between the C and B. This last effect could be, in principle, due also to detuning of the coil by paramagnetic impurities in the sample.

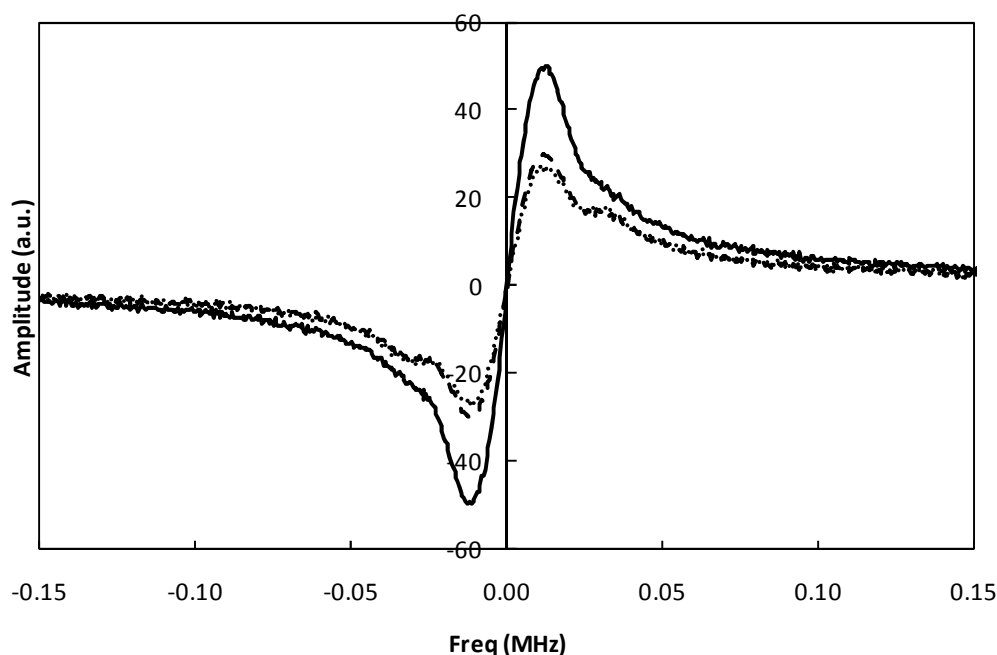


Figure 5.13 Comparison of different kinds of cements: solid line, the white cement A; dashes, the grey cement C; and dots the grey cement B. All spectra are normalised per unit mass of sample. It can be seen that relative amount of the broad line feature increases in the order presented in this caption (A, C, B) that is also the order of increasing Fe content. The total signal is significantly more in the A cement than in the C and B. The w/c ratio is 0.4 and the sample has been cured 14 days at 20 °C. The spectra have been symmetrised as explained in the next paragraph.

## 5.5 Analysis and discussion

### 5.5.1 DQF signal integral amplitude

The first observation we can make looking at the data just presented is the simple but fundamental one that there is a DQF signal coming from hydrated cement pastes and that this increases with curing time in parallel with the decrease of the ordinary single quantum NMR signal. This confirms that the DQF signal actually arises from water that becomes trapped in structures building up during the hydration of cement.

The behaviour of the signal amplitude as a function of the mass during drying is similar, showing an increase of the signal first to decrease sharply later. The main difference that can be seen below 0.9 in relative mass (Figure 5.12) is that the DQF signal increases at later stages (higher drying temperatures) than the bound fraction of the solid echo and that the signal decreases more sharply and to lower final values. However, the temperatures used were at the limit of the oven and the drying time has not been carefully measured (the mass loss was instead the variable considered). In addition, the total initial mass of water in the samples was affected by the same uncertainties discussed for the solid echo experiment. Careful analysis of the amplitudes of the total signal as a function of drying has not been performed for this dataset also because probably many more points (as in the solid echo experiment) would be necessary. The attention has instead been directed more onto the interpretation of the spectra shape, the two components visible in figure Figure 5.1 and the  $\text{Fe}^{3+}$  influence.

### 5.5.2 Analytic fitting

For all the following spectra, and for the ones presented in Figure 5.13, they have all been forced to be anti symmetric applying the transformation

$$I'(f) = \frac{I(f) - I(-f)}{2} \quad (5.9)$$

where  $I$  is the amplitude of the spectra before symmetrisation and  $I'$  after it.

The spectra of the DQF pulse sequence for a single pair of protons is a pair of antisymmetric lines. The suggestion of two environments leads to the first attempt of fitting the data with the sum of two pairs of antisymmetric Lorentzian lines. This fit did not give good results, clearly showing the fact that broader features were present. The fitting procedure, to try to accommodate for the much broader component “pushed together” the pair of lines giving

unrealistically small splitting and badly determined parameters. This effect is presented in Figure 5.14

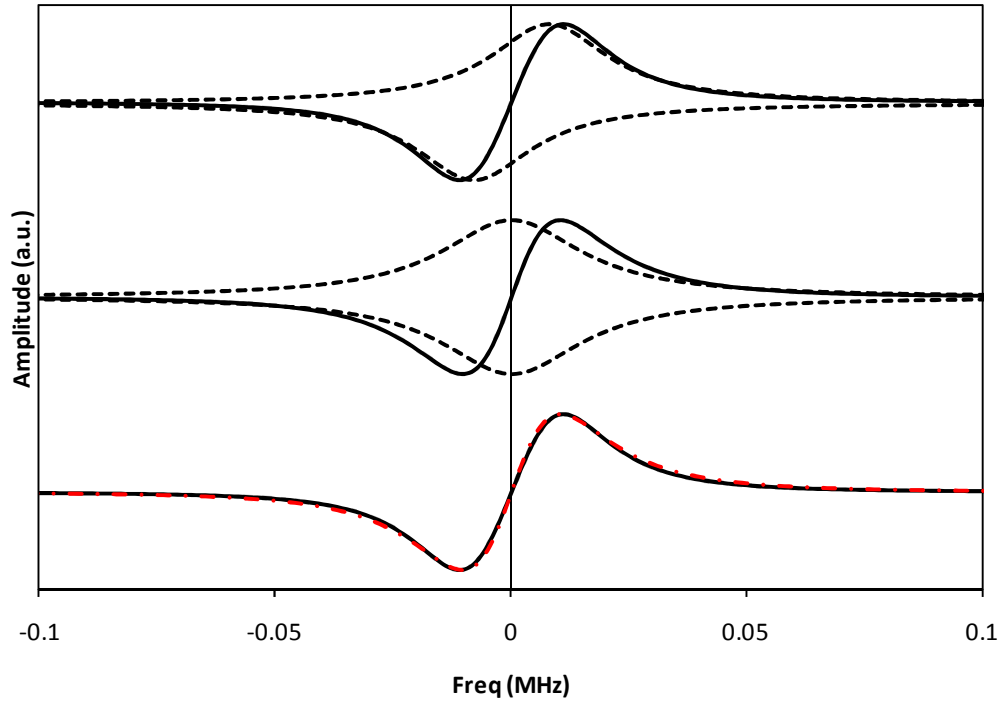


Figure 5.14 Reason of the bad determination of the splitting. Dashed lines are the positive and negative components and solid line is the sum. Each of the series is normalised to itself to emphasise the shapes. The top plot is calculated with a splitting of 0.015 MHz and a width of 0.008 MHz. Middle plot is the same for width and splitting of 0.0018 MHz and  $8 \cdot 10^{-10}$  MHz respectively. Bottom plot is the two summed signals. The difference is almost not appreciable.

### 5.5.3 Analytic-simulated fitting

The following attempt has been to fit the data with a combination of one Lorentzian with fixed width and splitting and one of the simulated spectra presented in Figure 5.9.

$$I = A_L \left[ \frac{1}{1 + \left( \frac{x-d}{w} \right)^2} - \frac{1}{1 + \left( \frac{x+d}{w} \right)^2} \right] + A_S S_{simu}(R). \quad (5.10)$$

Where  $d$  and  $w$  are the splitting and width of the Lorentzian respectively;  $A_L$  and  $A_S$  the amplitudes of the Lorentzian and simulated component and  $S_{simu}$  the simulated spectra that is a function of the cut off distance  $R$  (radius of the disc or sphere) considered. The free

parameters during each fitting were  $A_L$  and  $A_S$  only, but the fit has been performed using different values of  $R$  each time. The parameters for the Lorentzian have been extracted fitting the central part (within 22 kHz) of the experimental spectra in Figure 5.13. The values for the splitting obtained were (within experimental errors) the same for all the three cements and equal to  $0.0087 \pm 0.0002$  MHz. This is the value used to calculate the first part of equation (5.10). This value of splitting is in good agreement with the theoretical splitting calculated for the  $\text{Ca}(\text{OH})_2$  proton-proton distance and the most probable geometrical configuration (proton-proton vector perpendicular to the magnetic field). This calculated value is 0.0084 MHz. The width obtained for the cement B ( $0.0165 \pm 0.0005$  MHz) was slightly bigger than the one obtained for A and C ( $0.01525 \pm 0.00025$  MHz). The analysis has been performed using these values, however the results were indistinguishable from the one obtained using a common value of 0.0155 MHz. The results presented here refer to this second option of equal width for all the three cements. The reason of approximating the  $\text{Ca}(\text{OH})_2$  line shape with a pair of Lorentzian is based on the fact that a strong broadening (to be discussed later) is probably affecting the data.

The fit expressed by equation (5.10) has been repeated using as simulated spectra each one of the spectra shown in Figure 5.9. To be able to sum the spectra point by point the experimental spectra have been resized to have the same number of points as the calculated one. For each cut off distance the RMS difference between the experimental and simulated spectra has been minimised varying only the two amplitudes  $A_L$  and  $A_S$ . The value of  $R$  (cut off distance) for which the RMS was minimum has been taken as the most probable.

The fit has been performed with either 30 or 70 points in the spectra. The first series of this two fits (the one for 30 points) is presented in Figure 5.15. The best fits are shown together with the plots of the RMS values as a function of the cut off distance. The simulated spectra used are the one averaged over the disc.

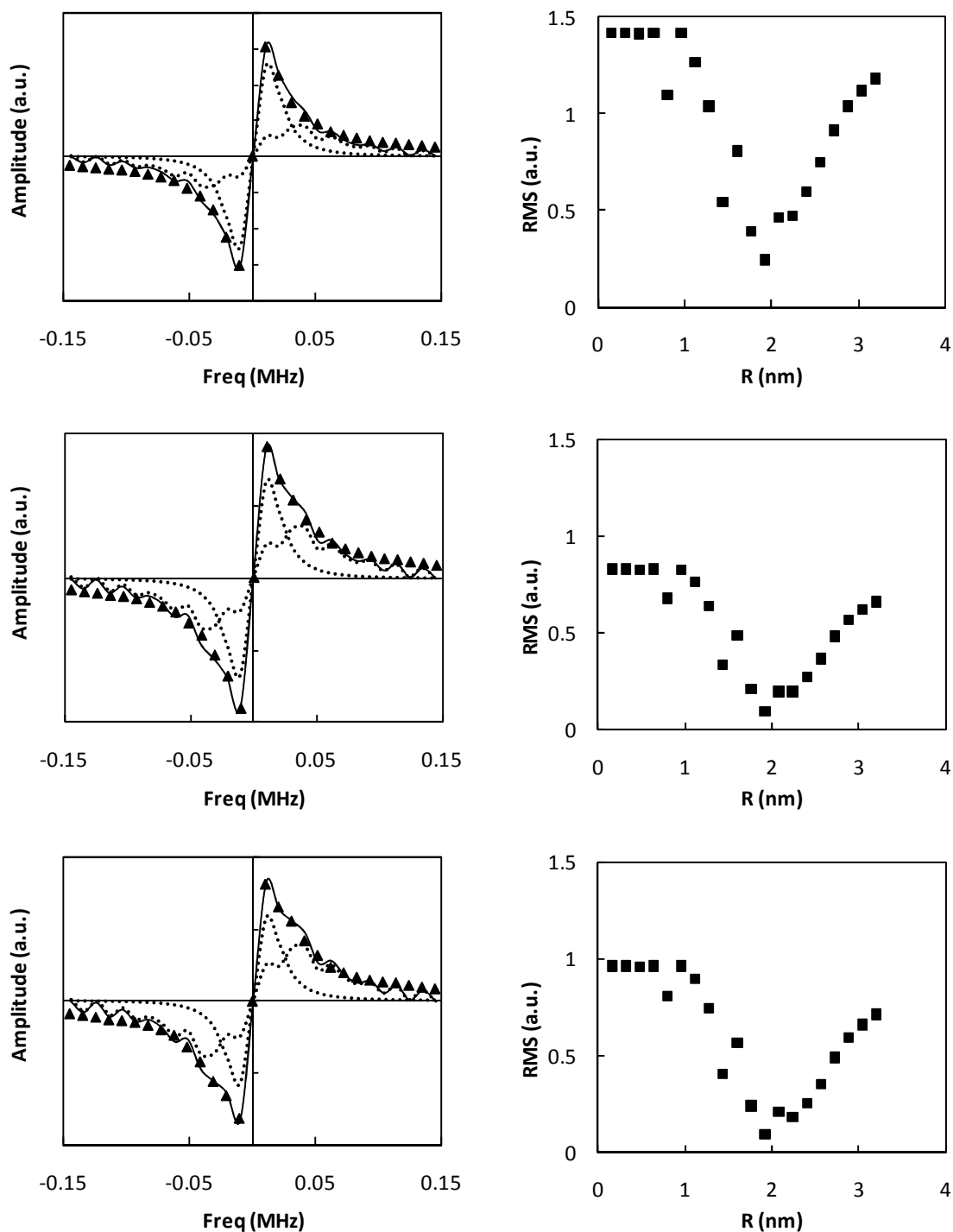


Figure 5.15 Left column: fit performed on the three different cements (top to bottom A, C and B) using 30 points in the spectra. The triangles are the experimental result, the dotted lines, the Lorentzian and simulated components and the solid line the total fit. Right the RMS as a function of the cut off radius. The spectra on the left are the one for the distance that minimise RMS (1.92 nm).

The analogous of Figure 5.15, but for the fits performed for 70, steps is presented in Figure 5.16

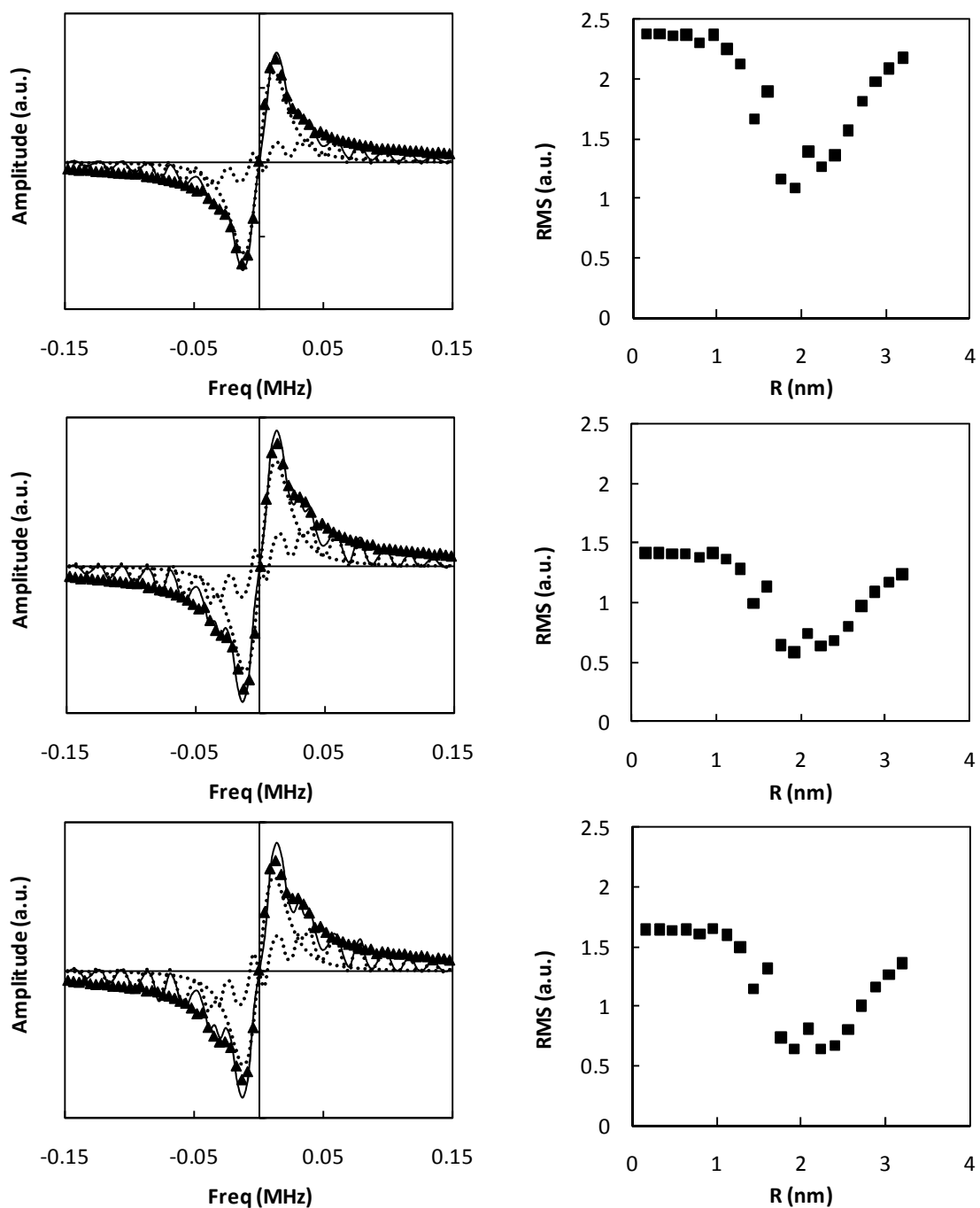


Figure 5.16 Left column: fit performed on the three different cements (top to bottom A, C and B) using 70 points in the spectra. The triangles are the experimental result, the dotted lines the Lorentzian and simulated components and the solid line the total fit. Right the RMS as a function of the cut off radius. The spectra on the left are the ones for the distance of 1.92 nm.

For both the 30 points fit and the 70 points one, the optimum cut off distance was circa 2 nm.

The values of the amplitudes obtained for the two components are presented in Figure 5.17.

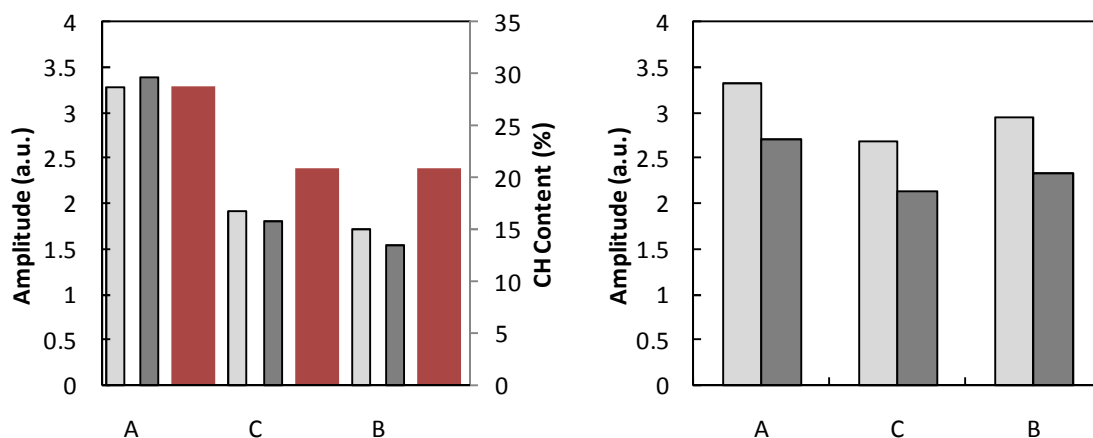


Figure 5.17 Amplitudes of the two components obtained from the fits in Figure 5.15 and Figure 5.16. Left plot is for the narrow component, the right for the wide one. Light grey refers to the 70 points fits, dark to the 30 points one. In the left plot the thicker bars refer to the Calcium hydroxide content in the three cements from independent measurements.

The left plot in Figure 5.17 refers to the narrow component (Lorentzian) while the right plot refers to the broad (simulated). Light grey refers to the 70 points fits, dark to the 30 points one. For the narrow component, the amplitudes can be compared reliably both between the different cements and between the two different number of points used, this because the Lorentzian is a well defined function and is normalised. For the broad component, the comparison between the two different numbers of points is less robust; this is because in the simulated spectra, changing the number of points, not only the resolution changes but the small features of the shape as well. However, the comparison between the different cements is justified for both components. It can be seen that, for the two different number of points used, although the quality of the fit is different, the amplitudes obtained are comparable. The narrow component in cement A is circa twice than in cements B and C. This pattern correlates with the Calcium hydroxide content in the three cements from independent measurements [144,148].

The fit performed for 70 points in the spectra shows some wiggles that are not observed experimentally. This could be due to the fact that the creation time in the simulation was actually longer than the experimental one and has been shown that increasing the creation time introduces wiggles in the spectra (Figure 5.4). This hypothesis is not unrealistic because the experimental creation time is measured from the middle of the RF pulses. These pulses are not short compared with the creation time ( $P_{90} = \sim 10 \mu\text{s}$ ,  $P_{190} = \sim 20 \mu\text{s}$  and  $t_c = 55 \mu\text{s}$ ) while the pulses in the simulation are instantaneous. The fit performed for 30 points in the spectra smoothes these wiggles keeping the total behaviour. This suggests another possible reason for the differences in the “wiggles features” between simulated and measured spectra. The experimental spectrum is already very broad due to the very short  $T_2$  in cement,

additionally the fact that a significant part of the FID is lost in the dead time may worsen this problem. The theory predicts that the signal should start from 0 at  $t = 0$ , this has never been observed in the experimental datasets. This loss of signal may also be the cause of the fact that the experimental spectra are not symmetric. The artificial symmetrisation of the spectra (Equation (5.9)), although helping in the fitting, may have worsened the dead time problem even more, introducing additional broadening effects. This broadening may have eventually led to an artificially low cut off distance.

Another analysis of the dead time effect can be performed in term of the missing part of the signal. The expected signal (apart from an amplitude factor) is expected to have a time dependence of the type  $\sin(at)$ . Because of the dead time, the signal actually measured is

actually  $FID_{\text{exp}} = \sin(at) \cdot \left[1 - r\left(\frac{t}{2t_{\text{dead}}}\right)\right]$  where  $t_{\text{dead}}$  is the dead time and  $r$  the

rectangular function. The multiplication in the time domain is a convolution in the frequency domain, therefore, is possible to write:

$$FT[FID_{\text{exp}}] = i \frac{\delta\left(f + \frac{a}{2\pi}\right) - \delta\left(f - \frac{a}{2\pi}\right)}{2} * [\delta(f) - 2t_{\text{dead}} \cdot \text{sinc}(2t_{\text{dead}} \cdot f)]. \quad (5.11)$$

and performing the convolution we obtain:

$$FT[FID_{\text{exp}}] = i \left[ \frac{\delta\left(f + \frac{a}{2\pi}\right) - \delta\left(f - \frac{a}{2\pi}\right)}{2} - 2t_{\text{dead}} \left[ \text{sinc}\left(2t_{\text{dead}} \cdot \left(f + \frac{a}{2\pi}\right)\right) - \text{sinc}\left(2t_{\text{dead}} \cdot \left(f - \frac{a}{2\pi}\right)\right) \right] \right]. \quad (5.12)$$

Because the sinc function has zeros for values of its argument equal to  $\pm 1$ , the equation (5.12) shows that there is a broadening effect due to the dead time of the order of  $\frac{1}{2t_{\text{dead}}}$ .

This may look nonsense because it implies that the broadening is maximum as the dead time decreases, however, it must be considered that the amplitude of the broad component is proportional to  $2t_{\text{dead}}$ , therefore, as the dead time decrease the broadness increases but the amplitude decreases. For the typical dead time of the experiment presented (10  $\mu\text{s}$ ) a broadening effect up to 50 kHz can be expected. This effect is represented in Figure 5.18.

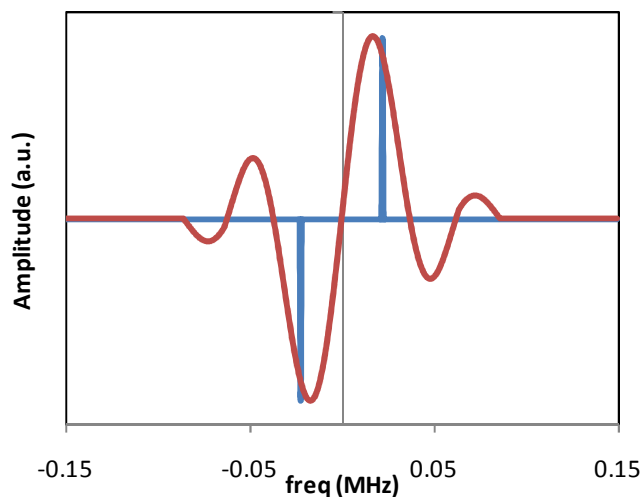


Figure 5.18 Effect of the dead time on the broadening of the spectra. Original “delta spectra” for one particular set of angles and broadened with the effect of  $10\ \mu\text{s}$  dead time. The amplitudes are normalised to facilitate the comparison.

#### 5.5.4 Average splitting

An alternative analysis of the data can be performed on the basis of the calculated theoretical splitting (measured as the second moment of the spectra) as a function of the  $\text{Fe}^{3+}$ -water distance. This is reported in Figure 5.19. This calculation has been performed on all the lines and therefore, as opposite of the spectra in Figure 5.7 is free from truncation effects.

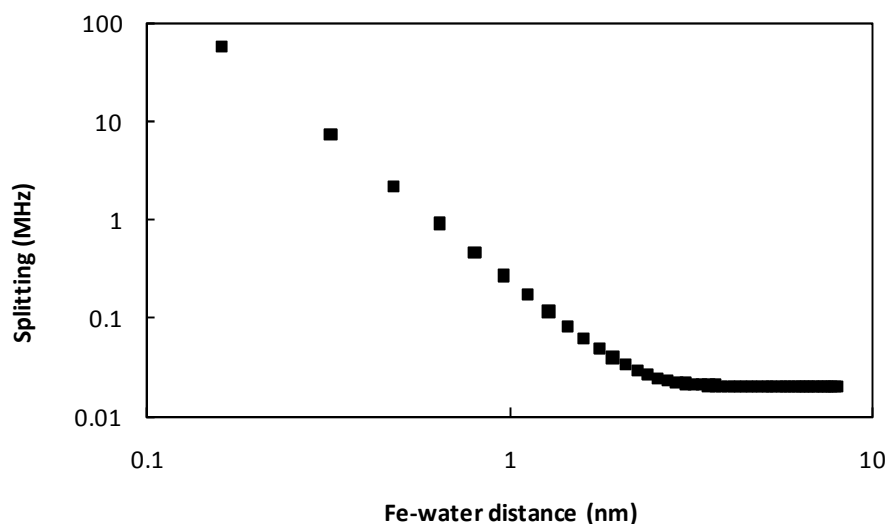


Figure 5.19 The behaviour of the splitting (calculated as the second moment of the magnitude of the spectra) as a function of the  $\text{Fe}^{3+}$ -water distance.

The behaviour of the Splitting as a function of the  $\text{Fe}^{3+}$ -water can be successfully fitted with a function of the type  $S(r_{is}) = \frac{a}{r_{is}^3} + c$  where  $c$  is the characteristic splitting of the water far from the  $\text{Fe}^{3+}$  (20 kHz) and  $a = 2.432 \cdot 10^{-28} \text{ m}^3$ . Having an analytic function of the splitting as a function of the  $\text{Fe}^{3+}$ -water distance, the integral expressed by equations (5.7) can be performed not on the spectra to find an average spectrum but on the splitting themselves. Two different weighting functions have been used in this second attempt. The first was the same as for the first one, based on the volume of spherical shells, the second, going back to the idea of C-S-H layers, based on the surface of concentric rings.

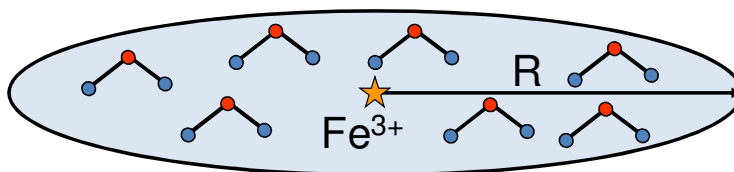


Figure 5.20 Sketch of the simple geometries adopted.

A minimum approach distance must be assumed otherwise, of course, the integral diverges. This parameter will be taken equal to 0.3 nm in accord with [68]. The resulting splitting as a function of the cut off distance is plotted in Figure 5.21.

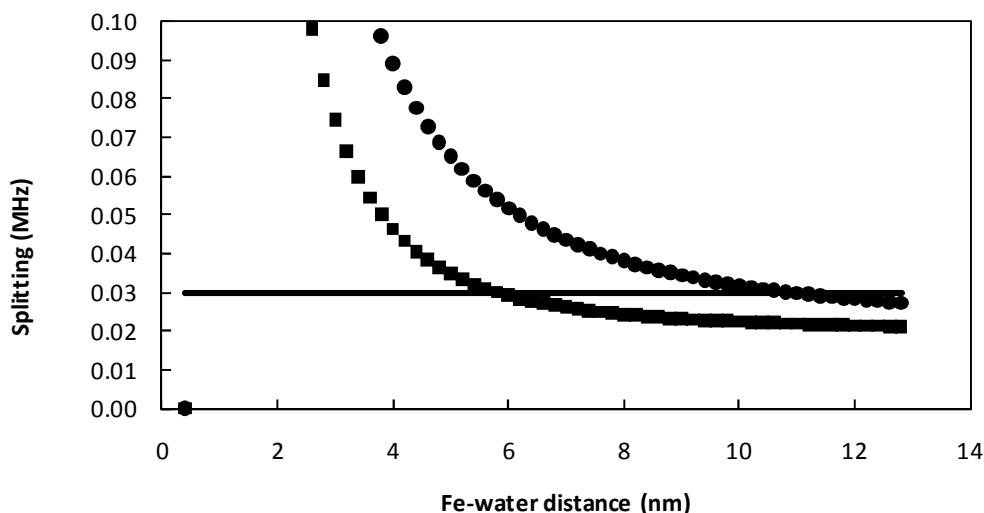


Figure 5.21 Splitting averaged over the disc (circles) and half sphere (squares). The horizontal line at 0.03 MHz represents the observed splitting of the shoulder on the experimental spectra.

From Figure 5.13 the position of the shoulder can be estimated to be at circa 30 kHz. This leads to an average  $\text{Fe}^{3+}$ -water distance of 6 and 12.5 nm for the 3D and 2D model respectively. If the minimum approach is decreased to 0.2 nm, the cut off distances obtained become 6.3 and 15.5 nm for the 3D and 2D model respectively, while, if increased to 0.4 nm they become 5.9 and 10.9 nm. These numbers are much bigger than the one obtained from the fitting previously presented, strengthening the hypothesis that the artificial broadening may have been a significant issue. The  $\text{Fe}^{3+}$ - $\text{Fe}^{3+}$  inter distance obtained is different but not too far from the estimation in [55,68] of 20 nm.

There is a fundamental difference in having planar or spherical pores when considering the DQF signal of moving molecules. In the first case, with respect to the second, when the water does a 2D walk on the surface, the orientation between the proton-proton vector and the magnetic field  $B_0$  can take a much more limited range of angle. Only the extreme case of plane parallel to  $B_0$  allows all the orientations between the proton-proton vector and  $B_0$  to occur. When the water performs a random walk on the surface of a sphere, the spherical symmetry itself makes all the possible orientation to occur with same probability. This isotropic tumbling leads to the fact that the DQF signal goes to zero for such kind of motion but not for the 2D one on the planar pore.

## 5.6 Conclusions

In this chapter the analysis of the DQF signal of cement has been presented; it has been found that the behaviour of the amplitude of the DQF signal during drying is qualitatively similar to the one of the solid component in the solid echo experiment. This suggests that the water detected is the same, allowing comparing results originating from different experiments.

The analysis of the spectra has been quite difficult, the first simple attempts having failed. The DQF signal cannot be fitted satisfactorily with either one or two pairs of antisymmetric Lorentzian lines. A successful fit has been obtained by adding a pair of antisymmetric Lorentzian lines and a simulated spectrum obtained as the weighted average of spectra calculated for different  $\text{Fe}^{3+}$ -water distance. This originates from a simple geometrical model of half a sphere with a  $\text{Fe}^{3+}$  sitting at the centre and water distributed on its surface. The radius of the sphere that gave the best fit may give either an estimation of the structure in which the water is enclosed or, equivalently, an estimation of the  $\text{Fe}^{3+}$ - $\text{Fe}^{3+}$  distance. The two are in principle indistinguishable. The best estimate of this distance has been found to be circa 2 nm. The fact that the cut off distance is basically the same on all the cement samples (despite the different overall  $\text{Fe}^{3+}$  density) may suggest that is a basic characteristic of a

common phase. The amplitude of the narrow component has been found to be in fairly good agreement with the CH content from independent measurements.

An alternative approach of integrating the splitting instead of the spectra has also been presented. This led to much bigger values for the cut off distance (6 and 11 nm respectively for the 3D and 2D model) suggesting that the results of the preceding fitting may have been biased by an artificial exaggerated broadness of the spectra due to the lack of signal at short times and the forced symmetrisation. The  $\text{Fe}^{3+}$ - $\text{Fe}^{3+}$  inter distance obtained with this second method are not too far from previous estimations [55,68].

Although much more simplistic, this second approach is probably also much less affected by the broadening and subsequent fitting issues discussed. For this reason, the 2D model with splitting average is probably the most appropriated in this case.

It is probably worth spending more time discussing the issue of the sizes obtained from the DQF work. The  $T_2$ - $T_2$  work [68] presented a model based on the random walk of the water molecules on the surface of the pore. The main characteristic times were 1.3 nm for the single step ( $r_{step}$ ) and 13  $\mu\text{s}$  for the surface residency time. This leads to 10000 steps per residency time ( $n$ ). Assuming step length of 1.6 Å and a random walk, the radius of the surface explored during the residency time can be calculated as  $R = \sqrt{n} \cdot r_{step}$ . This leads to  $R = 16$  nm. This measure is close to the one obtained for the 2D model in the DQF work. It must be acknowledged that the model considered is quite different, in one the motion is considered, while the other assumes a static distribution. However, the discussed restriction of the angles between the proton-proton vector and the magnetic field during the motion over a disc may cause this limitation to be much less relevant than what may appear.

Extensive discussion is ongoing in the cement community on the size and shape of the C-S-H particles. A fair agreement is present on a clear distinction in structure between the inner and outer C-S-H particles. The inner generally have a very fine particulate morphology, while the outer ones have a very different morphology depending on the chemical composition: at high Ca/Si ratio the structure is more fibrillar, whereas at low Ca/Si ratio a foil or sheet morphology prevails. The particles in inner product cement appear to be globular and accordingly [20] around 3 to 8 nm in diameter. Outer product particles appear instead to be long and thin, citing the same reference, measuring 3 nm by some tens of nm. This wide distribution of sizes does not help in discriminating between our approaches; however the sizes are of the same order of magnitude.

## 6 Conclusions and future work

In this thesis several applications of NMR techniques on cementitious materials have been presented. The achievements will be summarised in this chapter together with some questions that remain open and some suggestions for future work. There have been two main complementary paths but mainly disconnected in practice that have been followed during this thesis. The relaxation analysis and DQF work focused on the understanding of the state of the water in cement at the nanoscale is the first. This water is the basic element of virtually all the phenomena occurring in cementitious materials, from hydration that can be considered the “birth” of any concrete structure to the degradation and eventually the “death” of any structure. The second path has been aimed at the development and improvement of the portable Surface GARField magnet to be able to eventually export the NMR techniques presently used in the laboratories outside on built structures.

### ***6.1 Conclusions of relaxation analysis and DQF work***

The “Fe question”, that suggested the possibility that the exchange seen in the  $T_2$ - $T_2$  experiment could have been between environments with different paramagnetic impurities content has been answered in favour of the more interesting original hypothesis of exchange between different pore sizes. This validated the  $T_2$ - $T_2$  technique and probably helped it to be more trusted by the still sceptical cement community. A “by product” of the long series of attempt to achieve this conclusion is the fact that exchange at a comparable rate has been seen both in cement and synthesised C-S-H. This suggested, together with the other set of experiments, a new model to explain the exchange between different pore sizes. The previous hypothesis of long range exchange between inner and outer products has been revisited suggesting that the  $T_2$ - $T_2$  experiment detects a shorter range exchange between intra and inter C-S-H layer water. Water in these two environments has been monitored during drying using solid echo experiments that allows separating bound and liquid components. The analysis of the rates at which the amplitudes of solid and liquid signals change during drying allowed proposing a model of planar pores and a technique to estimate their thicknesses. These measures have been found to be 1.5 and 4.1 nm for the intra- and inter-crystallite pores respectively. Also the total volume ratio of the pore types has been estimated as 0.88 whereas the volume of readily evaporable water within them is 0.63, implying that the sheet total (mobile water) porosity is 0.47 (0.38) of the total. These results are in good agreement with the previous estimates coming from relaxation time analysis and  $T_2$ - $T_2$  experiments. The value of this agreement is very significant since the two techniques

are completely independent: one based on time measurements and the other on amplitudes measurements.

The DQF work has been a completely new and successful way of detecting water in cement pastes that was never reported in literature before. The application to this material has been found much more challenging than the applications to biological samples or polymers reported in literature due to the very short relaxation time and broad spectra characteristic of cement. A detailed calculation of the theoretical DQF spectrum and the effect of paramagnetic impurities on it has been successfully performed. The shape of this simulated spectrum has been used to fit the experimental data together with a pair of antisymmetric Lorentzian lines representing the CH fraction. The amplitude of the Lorentzian has been found to be in agreement with the CH content in cements. The simulated spectrum that better fitted the experimental data was the one calculated over half a sphere of radius circa 2 nm. This length may relate to a characteristic length of the structures in cement or possibly to an average  $\text{Fe}^{3+}$ - $\text{Fe}^{3+}$  inter distance, however, the fact that it is the same for all the cements independently from the overall  $\text{Fe}^{3+}$  density suggests it is related to a common phase with constant  $\text{Fe}^{3+}$  density. The alternative approach of averaging the splitting instead of the spectra gave significantly bigger value for the cut off distances (6 and 11 nm for the 3D and 2D models respectively). This difference suggests that the lack of signal due to the dead time and the forced symmetrisation of the spectra may have played a significant role in artificially broadening the experimental spectra.

## ***6.2 Conclusion of the work on the portable magnet***

Demonstration of the feasibility of the experiments performed outside the laboratory has been achieved solving all the practical and technical issues found. The magnet is now fully portable and has been successfully running from a portable power generator. This is required firstly, to be independent of power supplies on the construction site, but also imposed by the safety legislation on construction sites that prohibit the use of 220 V power supply. The signal to noise ratio of the device has been greatly increased following a series of improvements on the shielding, earthing and hardware. A positive result of these modifications is also the achieved lightening and improved portability due to the substitution of the original long and bulky quarter wavelength cable with a much lighter and smaller lumped element. These improvements allow acquiring the first profiles on site using this magnet. Results of monitoring of drying of two floors casted with different materials have been presented. The speed of drying of the two has been found very different. The one in

concrete gave signal up to 10 days after casting, while the one covered with screed did not give any signal after only 2 days from casting, showing a much faster reaction.

The effect of the steel reinforcing rebars in the vicinity of the magnet has been analysed using a phantom. It has been verified that the results are not significantly affected for distances magnet-steel bars down to 51 mm, therefore that for the typical depth of the reinforcing rebars should not be a major issue.

The attempt of calibrating the NMR signal with the actual moisture in concrete using RH probes has not been successful. The reason is probably because the ranges of operation of the two methods do not overlap.

### ***6.3 Future work on DQF***

The fitting of the DQF spectra to obtain the dipolar splitting has been revealed to be very hard and uncertain. One of the main (if not the main) reason is probably due to the fact that a significant part of the FID is obscured by the dead time of the spectrometer. One solution for this could be to change the pulse sequence to allow detection of an echo instead of an FID. This will probably require very careful thought about the required phase cycle to filter out any single quantum coherence and is a work that is already planned in the group. Other improvements could come in using a different device. The 20 MHz benchtop magnet used for the solid echo experiments has a typical  $P_{90}$  of 2.5  $\mu\text{s}$ . This is circa 1/4 of the pulse length of the CMX-400 used for this DQF study. Using this different device the “short pulse approximation” would be more realistic. Shorter pulses may also make the introduction of an “additional dimension” possible and examine the spectra as a function of the creation time in a more reliable way. Having seen that the spectra is strongly creation time dependent, the introduction of this additional variable should lead to much better defined splitting measurements. The disadvantage in moving from 400 to 20 MHz is the obvious loss in signal to noise, which in cement is already very low.

Furthermore, the introduction of the spectral motion function of the water molecules would be very interesting, although this will almost certainly introduce extreme complexity and difficulties in studying the system.

### ***6.4 Future work on the portable magnet***

The magnet is now operative outside the lab that was the main objective for the period of this thesis. The next stage of the validation will have to be probably a systematic testing on different materials and locations. The calibration versus moisture content, that has been

revealed to be impossible using moisture probes, could be attempted with other methods like resistivity devices [143]. The attempt with RH devices presented in this thesis was due to the fact that resistivity measurements are not very well spatially resolved; however, they may be the only feasible solution.

## 7 Appendix

### 7.1 Quantum mechanics calculation

In this appendix the calculation of the DQF signal will be performed. To the best of our knowledge this detailed calculation has never been reported for the particular system presented. Also the Matlab code used to simulate the spectra is enclosed at the end of this appendix.

The system considered is the one constituted by a water molecule (and therefore two protons, spin 1/2) and an iron ion ( $\text{Fe}^{3+}$  spin 3/2). The interactions taken into account in the calculation will be the Zeeman splitting and the dipole-dipole interaction, however the calculation will be, until the last substitution, pulse sequence dependent more than Hamiltonian dependent.

The basis used will be:

$$\begin{aligned}
 &|\alpha\alpha, m_s\rangle \\
 &\left| \frac{\alpha\beta + \beta\alpha}{\sqrt{2}}, m_s \right\rangle \\
 &|\beta\beta, m_s\rangle \\
 &\left| \frac{\alpha\beta - \beta\alpha}{\sqrt{2}}, m_s \right\rangle
 \end{aligned} \tag{7.1}$$

The last one does not carry magnetisation and therefore will not be considered throughout the whole calculation. The basis considered will be the one consisting of the first three combinations where  $\alpha$  represents spin up and  $\beta$  spin down.

The calculation will be performed assuming one specific value for  $m_s$  (where  $m_s$  is the spin of the Fe spin and can assume the values -5/2, -3/2, -1/2, 1/2, 3/2, 5/2) and then the result will be the sum for all the values. The letter  $I$  will be used to represent the protons and  $S$  the Fe spin

The Hamiltonians for dipole-dipole interaction are taken from [42], and for the  $I$ - $I$  interaction the truncated form will be used:

$$H_{II} = \frac{\mu_0}{4\pi} \frac{\gamma_i^2 \hbar^2}{r^3} \left( \frac{1 - 3 \cos^2 \theta}{2} \right) [3I_z^1 \cdot I_z^2 - I^1 \cdot I^2] \quad (7.2)$$

For the proton  $I$ - $S$  interaction, the one in the weak coupling approximation will be used:

$$H_d^{tr,wc} = \frac{\mu_0}{4\pi} \frac{\gamma_i \gamma_s \hbar^2}{r^3} (1 - 3 \cos^2 \theta) [I_z \cdot S_z] \quad \left( \frac{\mu_0}{4\pi} \frac{\gamma_i \gamma_s \hbar^2}{r^3} \ll |\omega_i - \omega_s| \right) \quad (7.3)$$

In these approximations, the dipole-dipole Hamiltonians are diagonal and time independent in the basis presented and equal to:

$$H_{II} = \begin{pmatrix} C_{ii}/2 & 0 & 0 \\ 0 & -C_{ii} & 0 \\ 0 & 0 & C_{ii}/2 \end{pmatrix} \quad \left( C_{ii} = \frac{\mu_0}{4\pi} \frac{\gamma_i \gamma_i \hbar^2}{r_{ii}^3} \frac{1}{2} (1 - 3 \cos^2(\theta_{ii})) \right) \quad (7.4)$$

for the  $I$ - $I$  interaction and

$$H_{IS} = \begin{pmatrix} C_{is} \cdot m_s & 0 & 0 \\ 0 & 0 & 0 \\ 0 & 0 & -C_{is} \cdot m_s \end{pmatrix} \quad \left( C_{is} = \frac{\mu_0}{4\pi} \frac{\gamma_i \gamma_s \hbar^2}{r_{is}^3} \frac{1}{2} (1 - 3 \cos^2(\theta_{is})) \right) \quad (7.5)$$

for the  $I$ - $S$  interaction, where the angle  $\theta_{ii}$  is the angle between the proton-proton vector and the main magnetic field,  $\theta_{is}$  is the angle between the Fe-water vector and the magnetic field,  $r_{ii}$  and  $r_{is}$  are the distances between the two protons and the water molecule and the Fe ion.  $\gamma_i$  and  $\gamma_s$  are the gyromagnetic ratio of the proton and electron respectively,  $\mu_0$  the permittivity of the vacuum and  $\hbar$  the Planck constant divided by  $2\pi$ .

Because the Hamiltonian is diagonal, the evolution operator is also diagonal and defined as

$$Evo(t) = \exp^{-iHt} \quad (7.6)$$

To simplify the writing, the elements of the total Hamiltonian (Zeeman interaction included) will be referred to as:

$$H = \begin{pmatrix} H_1 & 0 & 0 \\ 0 & H_2 & 0 \\ 0 & 0 & H_3 \end{pmatrix} \quad (7.7)$$

These elements can be written as:

$$H_1 = \frac{C_{ii}}{2} + 2C_{is}m_s + \frac{C_{Zi}}{2} + m_s C_{Zs} \quad (7.8)$$

Where  $C_{ii}$  and  $C_{is}$  are the ones defined above and  $C_{Zi}$  and  $C_{Zs}$  are the Larmor frequencies for the proton and electron respectively. Using the same notation:

$$H_2 = -C_{ii} + m_s C_{Zs} \quad (7.9)$$

$$H_3 = \frac{C_{ii}}{2} - 2C_{is}m_s - \frac{C_{Zi}}{2} + m_s C_{Zs} \quad (7.10)$$

The initial density matrix will be, considering only the deviatory part from the equilibrium, represented as:

$$\rho_0 = \begin{pmatrix} 1 & 0 & 0 \\ 0 & 0 & 0 \\ 0 & 0 & -1 \end{pmatrix} \quad (7.11)$$

The spin momentum operators can be represented by the matrices:

$$I_x = \begin{pmatrix} 0 & 1/\sqrt{2} & 0 \\ 1/\sqrt{2} & 0 & 1/\sqrt{2} \\ 0 & 1/\sqrt{2} & 0 \end{pmatrix} \quad (7.12)$$

And

$$I_y = \begin{pmatrix} 0 & -i/\sqrt{2} & 0 \\ i/\sqrt{2} & 0 & -1/\sqrt{2} \\ 0 & i/\sqrt{2} & 0 \end{pmatrix} \quad (7.13)$$

While the rotation matrices, calculated for an angle  $\theta$  as

$$R_{\theta x} = \exp^{i\theta I_x} \quad (7.14)$$

(and analogue for y)

$$R_{90x} = \begin{pmatrix} 1/2 & i/\sqrt{2} & -1/2 \\ i/\sqrt{2} & 0 & i/\sqrt{2} \\ -1/2 & i/\sqrt{2} & 1/2 \end{pmatrix} \quad (7.15)$$

$$R_{-90x} = \begin{pmatrix} 1/2 & -i/\sqrt{2} & -1/2 \\ -i/\sqrt{2} & 0 & -i/\sqrt{2} \\ -1/2 & -i/\sqrt{2} & 1/2 \end{pmatrix} \quad (7.16)$$

$$R_{90y} = \begin{pmatrix} 1/2 & 1/\sqrt{2} & 1/2 \\ -1/\sqrt{2} & 0 & 1/\sqrt{2} \\ 1/2 & -1/\sqrt{2} & 1/2 \end{pmatrix} \quad (7.17)$$

$$R_{-90y} = \begin{pmatrix} 1/2 & -1/\sqrt{2} & 1/2 \\ 1/\sqrt{2} & 0 & -1/\sqrt{2} \\ 1/2 & 1/\sqrt{2} & 1/2 \end{pmatrix} \quad (7.18)$$

The 180 x degree pulse (the only used) is

$$R_{180x} = \begin{pmatrix} 0 & 0 & 1 \\ 0 & -1 & 0 \\ 1 & 0 & 0 \end{pmatrix} \quad (7.19)$$

With all these definitions the magnetisation at the end of the pulse sequence can be calculated. The compact notation of the calculus performed is, for the first scan, consisting of  $P_{90x}-t_c/2-P_{180x}-t_c/2-P_{90x}-P_{90x}$  is:

$$\begin{aligned} \rho_{final,1} &= R_{-90x} R_{-90x} Evo\left(-\frac{t_c}{2}\right) R_{-180x} Evo\left(-\frac{t_c}{2}\right) R_{-90x} \\ \rho_0 R_{90x} Evo\left(\frac{t_c}{2}\right) R_{180x} Evo\left(\frac{t_c}{2}\right) R_{90x} R_{90x} \end{aligned} \quad (7.20)$$

While for the second scan, for which the pulse sequence used is represented by  $P_{90x}-t_c/2-P_{180x}-t_c/2-P_{90x}-P_{90y}$  is:

$$\begin{aligned} \rho_{final,2} &= R_{-90y} R_{-90x} Evo\left(-\frac{t_c}{2}\right) R_{-180x} Evo\left(-\frac{t_c}{2}\right) R_{-90x} \\ \rho_0 R_{90x} Evo\left(\frac{t_c}{2}\right) R_{180x} Evo\left(\frac{t_c}{2}\right) R_{90x} R_{90y} \end{aligned} \quad (7.21)$$

Here the evolution time between the last two 90 degree pulses has been considered short enough that no dynamics occur during this period. The total magnetisation, using the complex notation where the real part is the x channel and the imaginary is the y channel can be written, for the first scan as:

$$M_1 = trace(I_x \rho_{final,1}) + itrace(I_y \rho_{final,1}) \quad (7.22)$$

and for the second scan as

$$M_2 = trace(I_x \rho_{final,2}) + itrace(I_y \rho_{final,2}) \quad (7.23)$$

The two analytic expressions, with the substitution  $\Delta = (H_3 + H_1 - 2H_2)t_c/2$  become respectively:

$$M_1 = -\sin(-\Delta + (H_2 - H_3)t) + \sin(\Delta + (H_2 - H_1)t) + i(\cos(\Delta + (H_2 - H_3)t) + \cos(-\Delta + (H_2 - H_1)t)) = \text{Re}_1 + i \text{Im}_1 \quad (7.24)$$

and

$$M_2 = -\cos(\Delta + (H_2 - H_3)t) - \cos(\Delta + (H_2 - H_1)t) + i(-\sin(\Delta + (H_2 - H_3)t) + \sin(\Delta + (H_2 - H_1)t)) = \text{Re}_2 + i \text{Im}_2 \quad (7.25)$$

Because the acquisition phase for the first scan is  $x$  and for the second scan  $-y$ , the total summed magnetisation will be

$$M_{tot} = M_1 + iM_2 = (\text{Re}_1 - \text{Im}_2) + i(\text{Im}_1 + \text{Re}_2) \quad (7.26)$$

The analytic expression for this is:

$$M_{tot} = 2\sin(\Delta) \left[ \cos((H_2 - H_3)t) - \cos((H_2 - H_1)t) + i[\sin((H_2 - H_1)t) + \sin((H_2 - H_3)t)] \right] \quad (7.27)$$

and changing some signs

$$M_{tot} = 2\sin(\Delta) \left[ \cos((H_2 - H_3)t) - \cos((H_1 - H_2)t) + i[-\sin((H_1 - H_2)t) + \sin((H_2 - H_3)t)] \right] \quad (7.28)$$

that can be also conveniently re-written as:

$$M_{tot} = 2\sin(\Delta) (e^{i(H_2 - H_3)t} - e^{i(H_1 - H_2)t}) \quad (7.29)$$

This, apart from the amplitude factor at the front, is expression of the sum of two rotating magnetisation. Examining the two frequencies, calculating  $H_2 - H_3$  and  $H_1 - H_2$  we can see that:

$$H_2 - H_3 = 2C_{is}m_s - \frac{3}{2}C_{ii} - \frac{1}{2}C_{Zi} \quad (7.30)$$

and

$$H_1 - H_2 = 2C_{is}m_s + \frac{3}{2}C_{ii} + \frac{1}{2}C_{Zi} \quad (7.31)$$

Therefore the (7.29) can be also written, isolating the Larmor frequency dependence, in terms of  $C_{ii}$ ,  $C_{is}$  and  $C_{Zi}$  as:

$$M_{tot} = 2 \sin(\Delta) e^{C_{Zi}} \left( e^{i \left( 2C_{is}m_s + \frac{3}{2}C_{ii} \right) t} - e^{i \left( 2C_{is}m_s - \frac{3}{2}C_{ii} \right) t} \right) \quad (7.32)$$

This is valid for each of the values of  $m_s$ , therefore the total magnetisation observed will be the sum of the previous (7.32) for all the possible values of  $m_s = -5/2, -3/2, ..., 3/2, 5/2$ . This can be expressed mathematically (without, for the moment, considering the other dependencies) as:

$$M_{all m_s} = \sum_{m_s} M_{tot}(m_s) \quad (7.33)$$

This will still be dependent on the  $C_{ii}$ ,  $C_{is}$  and  $C_{Zi}$  parameters; the latter represent the Larmor frequency for the protons, and therefore is a constant with the magnet employed and of not much interest. The other two are more delicate to treat; in fact they are dependent on the geometrical orientation of the spins between them and with the magnetic field via the angles  $\theta_{ii}$  and  $\theta_{is}$  and the distances  $r_{ii}$  and  $r_{is}$  defined above via the relationships in (7.4) and (7.5).

The amplitude factor at the front can be better understood examining the value of  $\Delta$  in terms of the parameter  $C_{ii}$  that can be written as:

$$\Delta = 3C_{ii} \frac{t_c}{2} \quad (7.34)$$

The (7.32) becomes then:

$$M_{tot} = 2 \sin \left( 3C_{ii} \frac{t_c}{2} \right) e^{C_{Zi}} e^{i2C_{is}m_s t} \left( e^{\frac{i3}{2}C_{ii}t} - e^{-\frac{i3}{2}C_{ii}t} \right) \quad (7.35)$$

When the magnetisation for the two opposite  $m_s$  values are added this leads to:

$$M_{tot} = 2 \sin\left(3C_{ii} \frac{t_c}{2}\right) e^{C_{zi}} 2 \cos(2C_{is} m_s t) 2i \sin\left(\frac{3}{2} C_{ii} t\right) \quad (7.36)$$

that is an odd imaginary function and has therefore a real spectra.

## 7.2 Matlab code

The one that follows is the Matlab code used to simulate all the spectra used in the DQF chapter.

```
%% calculate
home
clear
close all

alpha_v=linspace(0,pi,500);      %Array of angles for the powder
average of Fe
theta_v=linspace(0,pi,500);      %Array of angles for the powder
average of H-H

u0=4*pi*1e-7;
yi=2*pi*42.576e6;
ys=1.760859e11;
hbar=6.626e-34/(2*pi);
rii=1.6e-10;                      %for water
%rii=2.186e-10;                  %theoric for Ca(OH)2
%rii=1.58e-10                   %as in original Pake for gypsum, should give
peaks at 21KHz... OK
ris_a=rii*[1:1:15];              %Array for the different Fe-H2O distances

tc=55;                            %creation time

freq=zeros(size(ris_a,2),size(theta_v,2)*size(alpha_v,2)*6*2);
%array of all the frequencies
amp=zeros(size(ris_a,2),size(theta_v,2)*size(alpha_v,2)*6*2);
%array of all the amplitudes

for asa=1:size(ris_a,2);          %loop over the Fe-H2O distances
    incre=1;
    ris=ris_a(asa);
    Cii=1/2*u0*yi^2*hbar/(4*pi*rii^3)*1e-6;          %in units of
%omega, must be so otherwise problems with amplitudes
    Cis=u0*yi*ys*hbar/(4*pi*ris^3)*1e-6;             %in units of
%omega
    for a_count=1:1:size(alpha_v,2);
        alpha=alpha_v(a_count);
        Cis_eff=Cis*(1-3*(cos(alpha))^2);
        for t_count=1:size(theta_v,2);
            theta=theta_v(t_count);
            Cii_eff=Cii*(1-3*(cos(theta))^2);
            msc=(-5/2:1:5/2);
            ff_p=(3/2*Cii_eff+2*Cis_eff*msc)/2/pi;      %from here
all in units of frequency
            amp_p=2*sin(3*Cii_eff*tc/2)*sin(theta)*sin(alpha);
```

---

```

        ff_n=(-3/2*Cii_eff+2*Cis_eff*msc)/2/pi;
        freq(asa,incre:incre+11)=[ff_p ff_n];
        amp(asa,incre:incre+11)=[amp_p amp_p amp_p amp_p amp_p
amp_p -amp_p -amp_p -amp_p -amp_p -amp_p -amp_p];
        incre=incre+12;
    end
end

end

%% analyse
close all
home
amp_sum=0;
clear edges
clear amp_sum
bins_n=30; %number of points in the spectra (actually
points=bins_n-1)

edges=linspace(-.15,.15,bins_n);
ax_freq_summed=edges(1:end-1)+(edges(2)-edges(1))/2;
'binning values'
for asa=1:size(ris_a,2); %loop over the Fe-H2O distances
    for bb=1:size(edges,2)-1; %loop over the bins

amp_sum(asa,bb)=sum(amp(asa,and(freq(asa,:)>edges(bb),freq(asa,:)<edges(bb+1)))));
    end
    spl(asa)=sqrt(var(freq(asa,:),abs(amp(asa,:))));
end

for_excell_freq=ax_freq_summed.';
for_excell_amp_sum=amp_sum.';

figure %this is to plot the figure of the spectra NOT
averaged over the disc or sphere
subplot(2,1,1) %normalised for each distance
for aa=asa:-1:1

plot(ax_freq_summed,2*aa+amp_sum(aa,:)/max(amp_sum(aa,:));%,'.')
    hold on
end
xlim([min(edges) max(edges)]);
title(['not averaged R normalised rii = ' num2str(rii) ' ; '
num2str(size(theta_v,2)) ' theta ; ' num2str(size(alpha_v,2)) '
alpha ; tc=' num2str(tc) ' ; ' num2str(bins_n) ' points'])
legend(num2str(flipud(ris_a)))

subplot(2,1,2) %NOT normalised for each distance
for aa=asa:-1:1
    plot(ax_freq_summed,max(max(amp_sum))*aa+amp_sum(aa,:);%,'.')
    hold on
end
xlim([min(edges) max(edges)]);
title(['not averaged R NOT normalised rii = ' num2str(rii) ' ; '
num2str(size(theta_v,2)) ' theta ; ' num2str(size(alpha_v,2)) '
alpha ; tc=' num2str(tc) ' ; ' num2str(bins_n) ' points'])
legend(num2str(flipud(ris_a)))

```

---

```

clear bound
home

bound(1)=ris_a(1)-((ris_a(2)-ris_a(1))/2); %to calculate the limits
of the rings for integration
bound(size(ris_a,2)+1)=ris_a(end)+((ris_a(end)-ris_a(end-1))/2);
for a=2:size(ris_a,2)
    bound(a)=(ris_a(a)+ris_a(a-1))/2;
end

for a=1:size(bound,2)-1
    N2(a)=pi*(bound(a+1)^2-bound(a)^2); %surface of the rings
    to be used as number of H2O in the ring
    N3(a)=4/3*pi*(bound(a+1)^3-bound(a)^3); %volume of the shell to
    be used as number of H2O in the shell
end
amp_sumR2=zeros(size(bound,2)-1,size(edges,2)-1);
amp_sumR3=zeros(size(bound,2)-1,size(edges,2)-1);

'summing over R'
for bR=1:size(bound,2)-1;
    for cR=1:bR;
        amp_sumR2(bR,:)=amp_sumR2(bR,:)+N2(cR)*amp_sum(cR,:);
        amp_sumR3(bR,:)=amp_sumR3(bR,:)+N3(cR)*amp_sum(cR,:);
    end
end

figure %this is to plot the figure of the spectra averaged over the
disc and half sphere normalised for each cutoff distance

subplot(2,1,1) %for the disc
for aa=size(amp_sumR2,1):-1:1

plot(ax_freq_summed,2*aa+amp_sumR2(aa,:)/max(amp_sumR2(aa,:));%,'.')

    hold on
end
xlim([min(edges) max(edges)]);
title(['over circle normalised rii = ' num2str(rii) ' ; '
num2str(size(theta_v,2)) ' theta ; ' num2str(size(alpha_v,2)) '
alpha ; tc=' num2str(tc) ' ; ' num2str(bins_n) ' points'])
legend(num2str(flipud(ris_a)))
hold off

subplot(2,1,2) %for the sphere
for aa=size(amp_sumR3,1):-1:1

plot(ax_freq_summed,2*aa+amp_sumR3(aa,:)/max(amp_sumR3(aa,:));%,'.')

    hold on
end
xlim([min(ax_freq_summed) max(ax_freq_summed)]);
title(['over half sphere normalised rii = ' num2str(rii) ' ; '
num2str(size(theta_v,2)) ' theta ; ' num2str(size(alpha_v,2)) '
alpha ; tc=' num2str(tc) ' ; ' num2str(bins_n) ' points'])
legend(num2str(flipud(ris_a)))
hold off

```

---

```

figure %this is to plot the figure of the spectra averaged over the
disc and half sphere NOT normalised for each cutoff distance
subplot(2,1,1) %for the disc
for aa=size(amp_sumR2,1):-1:1

plot(ax_freq_summed,max(max(amp_sumR2))*aa+amp_sumR2(aa,:));%,'.')
hold on
end
xlim([min(edges) max(edges)]);
title(['over circle NOT normalised rii = ' num2str(rii) ' ; '
num2str(size(theta_v,2)) ' theta ; ' num2str(size(alpha_v,2)) '
alpha ; tc=' num2str(tc) ' ; ' num2str(bins_n) ' points'])
legend(num2str(flipud(ris_a)))
hold off

subplot(2,1,2) %for the sphere
for aa=size(amp_sumR3,1):-1:1

plot(ax_freq_summed,max(max(amp_sumR3))*aa+amp_sumR3(aa,:));%,'.')
hold on
end

title(['over half sphere NOT normalised rii = ' num2str(rii) ' ; '
num2str(size(theta_v,2)) ' theta ; ' num2str(size(alpha_v,2)) '
alpha ; tc=' num2str(tc) ' ; ' num2str(bins_n) ' points'])
legend(num2str(flipud(ris_a)))
hold off
xlim([min(edges) max(edges)]);

for asa=1:size(ris_a,2);
    spl2D(asa)=sqrt(var(ax_freq_summed,abs(amp_sumR2(asa,:)))); %to
calculate the splitting (as second moment) for the disc as a
function of R cut off, THERE ARE FILTERING EFFECTS!!
    spl3D(asa)=sqrt(var(ax_freq_summed,abs(amp_sumR3(asa,:)))); %to
calculate the splitting (as second moment) for the sphere as a
function of R cut off
end

figure
plot(ris_a,spl2D,'.')
hold on
plot(ris_a,spl3D,'o')
hold off
legend(['2D';'3D']);
title('splitting for the two models')
%xlim([2e-9 1e-8])
%ylim([0.02 0.05])

for_excellR2=amp_sumR2.*1e14;
for_excellR3=amp_sumR3.*1e28;

```

---

## Bibliography

1. NANOCEM. 2009 [cited; Available from: <http://www.nanocem.org/>].
2. [www.cement.ca](http://www.cement.ca). [www.cement.ca](http://www.cement.ca). [cited 04/08/2009].
3. Aïtcin, P.-C., *Cements of yesterday and today: Concrete of tomorrow*. Cement and Concrete Research, 2000. **30**(9): p. 1349-1359.
4. Scrivener, K. *Introduction: basic concepts*. in *NANOCEM RTN, 1st training course*. 2006. Aalborg, Denmark.
5. Kirby, A., *CCCC Kick the habit; A un guide to climate neutrality*. 2008: United Nations, Environment Management Group.
6. Geiker, M. *Basic mechanisms*. in *NANOCEM RTN, 3rd training course*. 2007. Madrid, Spain.
7. Taylor, H.F.W., *Cement chemistry* 2nd ed. 1997: Thomas Telford Publishing.
8. Scrivener, K. *Microstructural development*. in *NANOCEM RTN, 1st training course*. 2006. Aalborg, Denmark.
9. Scrivener, K., *The Microstructure of Concrete*, in *Materials Science of Concrete I*, J. Skalny, Editor.
10. Brouwers, H.J.H., *The work of Powers and Brownnyard revisited: Part 1*. Cement and Concrete Research, 2004. **34**(9): p. 1697-1716.
11. Brouwers, H.J.H., *The work of Powers and Brownnyard revisited: Part 2*. Cement and Concrete Research, 2005. **35**(10): p. 1922-1936.
12. Powers, T.C.a.B., T.L., *Studies of the Physical Properties of Hardened Portland Cement Paste*. Journal of the American Concrete Institute, 1946 to 1947. **2-8**.
13. Geiker, M. *Porosity development*. in *NANOCEM RTN, 1st training course*. 2006. Aalborg, Denmark.
14. Hansen, T.H., *Physical structure of hardened cement paste. A classical approach*. Materials and structures, 1986. **19**(144): p. 423-436.

15. Jennings, H.M., *A model for the microstructure of calcium silicate hydrate in cement paste*. Cement and Concrete Research, 2000. **30**(1): p. 101-116.
16. Tennis, P.D. and Jennings, H.M., *A model for two types of calcium silicate hydrate in the microstructure of Portland cement pastes*. Cement and Concrete Research, 2000. **30**(6): p. 855-863.
17. Allen, A.J.; Thomas, J.J. and Jennings, H.M., *Composition and density of nanoscale calcium-silicate-hydrate in cement*. Nature Materials, 2007. **6**(4): p. 311-316.
18. Richardson, I.G., *The nature of the hydration products in hardened cement pastes*. Cement and Concrete Composites, 2000. **22**(2): p. 97-113.
19. Richardson, I.G., *Tobermorite/jennite- and tobermorite/calcium hydroxide-based models for the structure of C-S-H: applicability to hardened pastes of tricalcium silicate, [beta]-dicalcium silicate, Portland cement, and blends of Portland cement with blast-furnace slag, metakaolin, or silica fume*. Cement and Concrete Research, 2004. **34**(9): p. 1733-1777.
20. Richardson, I.G., *The calcium silicate hydrates*. Cement and Concrete Research, 2008. **38**(2): p. 137-158.
21. Taylor, H.F.W., *Models for the composition and structure of calcium silicate hydrate (C-S-H) gel in hardened tricalcium silicate pastes and the incorporation of minor and trace-elements into calcium silicate hydrate (C-S-H) gel in hardened cement pastes - discussion*. Cement and Concrete Research, 1993. **23**(4): p. 995-998.
22. Taylor, H.F.W., *Proposed structure for calcium silicate hydrate gel*. Journal of the American Ceramic Society, 1986. **69**(6): p. 464-467.
23. Richardson, I.G. and Groves, G.W., *Models for the composition and structure of calcium silicate hydrate (C S H) gel in hardened tricalcium silicate pastes and the incorporation of minor and trace-elements into calcium silicate hydrate (C S H) gel in hardened cement pastes - reply*. Cement and Concrete Research, 1993. **23**(4): p. 999-1000.
24. Richardson, I.G. and Groves, G.W., *Models for the composition and structure of calcium silicate hydrate (C-S-H) gel in hardened tricalcium silicate pastes*. Cement and Concrete Research, 1992. **22**(6): p. 1001-1010.
25. Nonat, A., *The structure and stoichiometry of C-S-H*. Cement and Concrete Research, 2004. **34**(9): p. 1521-1528.
26. Glasser, F.P.; Lachowski, E.E. and Macphee, D.E., *Compositional model for calcium silicate hydrate (C-S-H) gels, their solubilities, and free-energies of formation*. Journal of the American Ceramic Society, 1987. **70**(7): p. 481-485.

- 
27. Girão, A.V.; Richardson, I.G.; Porteneuve, C.B. and Brydson, R.M.D., *Composition, morphology and nanostructure of C-S-H in white Portland cement pastes hydrated at 55 °C*. Cement and Concrete Research, 2007. **37**(12): p. 1571-1582.
  28. Metha, P.K. and Monteiro, J.M., *Concrete: microstructure, properties, and materials*. 2006.
  29. Brunauer, S.; Emmett, P.H. and Teller, E., *Adsorption of Gases in Multimolecular Layers*. Journal of the American Chemical Society, 1938. **60**(2): p. 309-319.
  30. Parrott, L.J., *Effect of drying history upon the exchange of pore water with methanol and upon subsequent methanol sorption behaviour in hydrated alite paste*. Cement and Concrete Research. **11**(5-6): p. 651-658.
  31. Parrott, L.J.; Hansen, W. and Berger, R.L., *Effect of first drying upon the pore structure of hydrated alite paste*. Cement and Concrete Research, 1980. **10**(5): p. 647-655.
  32. Canut, M., *Personal communication*. 2007.
  33. Geiker, M. *Porosity characterisation*. in *NANOCEM RTN, 2st training course*. 2007. Ljubljana, Slovenia.
  34. Kjeldsen, A.M. and Geiker, M.R., *On the interpretation of low temperature calorimetry data*. Materials and Structures, 2008. **41**(1): p. 213-224.
  35. Aligizaki, K.K., *Pore Structure of Cement-Based Materials: Testing Interpretation and Requirements*. Modern Concrete Technology. 2006.
  36. Good, R.J. and Mikhail, R.S., *The contact angle in mercury intrusion porosimetry*. Powder Technology. **29**(1): p. 53-62.
  37. Gallucci, E. *High resolution microscopies SEM-TEM-AFM*. in *NANOCEM RTN, 2st training course*. 2007. Ljubljana, Slovenia.
  38. Viehland, D.; Li, J.F.; Yuan, L.J. and Xu, Z.K., *Mesostructure of calcium silicate hydrate (C-S-H) gels in Portland cement paste: Short-range ordering, nanocrystallinity, and local compositional order*. Journal of the American Ceramic Society, 1996. **79**(7): p. 1731-&.
  39. Farrar, T.C. and Becker, E.D., *Pulse and Fourier Transform NMR - introduction to Theory and Methods*. 1971: Academic Press.
  40. Callaghan, P.T., *Principles of Nuclear Magnetic Resonance Microscopy*. 1991.
  41. Blumich, B., *Essential NMR for scientist and engineers*, ed. Springer. 2004.

- 
42. Kimmich, R., *NMR Tomography Diffusometry Relaxometry*. 1997: Springer.
  43. Blumich, B., *NMR Imaging of Materials*. Monographs on the physics and chemistry of materials. Vol. 57. 2000: Oxford science publications.
  44. Abragam, A. and Goldman, M., *Nuclear magnetism: order and disorder*. 1982.
  45. Slichter, C.P., *Principles of Magnetic Resonance third Enlarged and Updated Edition*. 1992.
  46. Fukushima, E. and Roeder, S.B.W., *Experimental Pulse NMR: A Nuts and Bolts Approach* 1981.
  47. Ernst, R.R.; Bodenhausen, G. and Wokaun, A., *Principles of Nuclear Magnetic Resonance in One and Two Dimensions*, ed. O.U. press. 2004.
  48. Powles, J.G. and Strange, J.H., *Zero time resolution nuclear magnetic resonance transients in solids*. Proceedings of the Physical Society of London, 1963. **82**(525): p. 6-&.
  49. Tsoref, L.; Shinar, H. and Navon, G., *Observation of a H-1 double quantum filtered signal of water in biological tissues*. Magnetic Resonance in Medicine, 1998. **39**(1): p. 11-17.
  50. Bloembergen, N.; Purcell, E.M. and Pound, R.V., *Relaxation effects in nuclear magnetic resonance absorption*. Physical Review, 1948. **73**(7): p. 679-712.
  51. D'Orazio, F.; Bhattacharja, S.; Halperin, W.P.; Eguchi, K. and Mizusaki, T., *Molecular diffusion and nuclear-magnetic-resonance relaxation of water in unsaturated porous silica glass*. Physical Review B, 1990. **42**(16): p. 9810-9818.
  52. *Methods in the Physics of Porous Media*. Experimental methods in the physical sciences. Vol. 35. 1999.
  53. McDonald, P.J., *Personal communication*. 2009.
  54. Korb, J.P.; Monteilhet, L.; McDonald, P.J. and Mitchell, J., *Microstructure and texture of hydrated cement-based materials: A proton field cycling relaxometry approach*. Cement and Concrete Research, 2007. **37**(3): p. 295-302.
  55. Barberon, F.; Korb, J.P.; Petit, D.; Morin, V. and Bermejo, E., *Probing the Surface Area of a Cement-Based Material by Nuclear Magnetic Relaxation Dispersion*. Physical Review Letters, 2003. **90**(11): p. 116103.
  56. Godefroy, S.; Korb, J.P.; Fleury, M. and Bryant, R.G., *Surface nuclear magnetic relaxation and dynamics of water and oil in macroporous media*. Physical Review E, 2001. **64**(2).

- 
57. McDonald, P.J.; Korb, J.P.; Mitchell, J. and Monteilhet, L., *Surface relaxation and chemical exchange in hydrating cement pastes: A two-dimensional NMR relaxation study*. Physical Review E, 2005. **72**(1).
58. Korb, J.P.; McDonald, P.J.; Monteilhet, L.; Kalinichev, A.G. and Kirkpatrick, R.J., *Comparison of proton field-cycling relaxometry and molecular dynamics simulations for proton-water surface dynamics in cement-based materials*. Cement and Concrete Research, 2007. **37**(3): p. 348-350.
59. McDonald, P.J.; Mitchell, J.; Mulheron, M.; Aptaker, P.S.; Korb, J.P. and Monteilhet, L., *Two-dimensional correlation relaxometry studies of cement pastes performed using a new one-sided NMR magnet*. Cement and Concrete Research, 2007. **37**(3): p. 303-309.
60. Carr, H.Y. and Purcell, E.M., *Effects of Diffusion on Free Precession in Nuclear Magnetic Resonance Experiments*. Physical Review, 1954. **94**(3): p. 630.
61. Meiboom, S. and Gill, D., *Modified Spin-Echo Method for Measuring Nuclear Relaxation Times*. Review of Scientific Instruments, 1958. **29**(8): p. 688-691.
62. Song, Y.-Q.; Cho, H.; Hopper, T.; Pomerantz, A.E. and Sun, P.Z., *Magnetic resonance in porous media: Recent progress*. The Journal of Chemical Physics, 2008. **128**(5): p. 052212-12.
63. Peemoeller, H.; Shenoy, R.K. and Pintar, M.M., *Two-dimensional nmr time evolution correlation spectroscopy in wet lysozyme*. Journal of Magnetic Resonance (1969), 1981. **45**(2): p. 193-204.
64. Song, Y.Q.; Venkataramanan, L. and Bucaw, L., *Determining the resolution of Laplace inversion spectrum*. The Journal of Chemical Physics, 2005. **122**(10): p. 104104.
65. Song, Y.Q.; Venkataramanan, L.; Hürlimann, M.D.; Flaum, M.; Frulla, P. and Straley, C.,  *$T_1$ - $T_2$  Correlation Spectra Obtained Using a Fast Two-Dimensional Laplace Inversion*. Journal of Magnetic Resonance, 2002. **154**(2): p. 261-268.
66. Venkataramanan, L.; Yi-Qiao, S. and Hurlimann, M.D., *Solving Fredholm integrals of the first kind with tensor product structure in 2 and 2.5 dimensions*. Signal Processing, IEEE Transactions on, 2002. **50**(5): p. 1017-1026.
67. Lee, J.H.; Labadie, C.; Springer, C.S. and Harbison, G.S., *Two-dimensional inverse Laplace transform NMR: altered relaxation times allow detection of exchange correlation*. Journal of the American Chemical Society, 1993. **115**(17): p. 7761-7764.
68. Monteilhet, L.; Korb, J.P.; Mitchell, J. and McDonald, P.J., *Observation of exchange of micropore water in cement pastes by two-dimensional  $T_2$ - $T_2$  nuclear magnetic resonance relaxometry*. Physical Review E, 2006. **74**(6).

- 
69. McConnell, H.M., *Reaction rates by nuclear magnetic resonance*. Journal of Chemical Physics, 1958. **28**(3): p. 430-431.
70. Choudhury, R.P. and Schonhoff, M., *Pulsed field gradient NMR study of phenol binding and exchange in dispersions of hollow polyelectrolyte capsules*. The Journal of Chemical Physics, 2007. **127**(23): p. 234702-9.
71. Korb, J.P.; WhaleyHodges, M. and Bryant, R.G., *Translational diffusion of liquids at surfaces of microporous materials: Theoretical analysis of field-cycling magnetic relaxation measurements*. Physical Review E, 1997. **56**(2): p. 1934-1945.
72. Washburn, K.E. and Callaghan, P.T., *Tracking Pore to Pore Exchange Using Relaxation Exchange Spectroscopy*. Physical Review Letters, 2006. **97**(17): p. 175502-4.
73. Mitchell, J.; Griffith, J.D.; Collins, J.H.P.; Sederman, A.J.; Gladden, L.F. and Johns, M.L., *Validation of NMR relaxation exchange time measurements in porous media*. Journal of Chemical Physics, 2007. **127**(23): p. 9.
74. Sen, P.N. and Axelrod, S., *Inhomogeneity in local magnetic field due to susceptibility contrast*. Journal of Applied Physics, 1999. **86**(8): p. 4548-4554.
75. Song, Y.-Q.; Ryu, S. and Sen, P.N., *Determining multiple length scales in rocks*. Nature, 2000. **406**(6792): p. 178-181.
76. Audoly, B.; Sen, P.N.; Ryu, S. and Song, Y.Q., *Correlation functions for inhomogeneous magnetic field in random media with application to a dense random pack of spheres*. Journal of Magnetic Resonance, 2003. **164**(1): p. 154-159.
77. Glover, P. and Mansfield, S.P., *Limits to magnetic resonance microscopy*. Reports on Progress in Physics, 2002. **65**(10): p. 1489-1511.
78. Bohris, A.J.; Goerke, U.; McDonald, P.J.; Mulheron, M.; Newling, B. and Le Page, B., *A broad line NMR and MRI study of water and water transport in Portland cement pastes*. Magnetic Resonance Imaging, 1998. **16**(5-6): p. 455-461.
79. Petrov, O.V. and Furó, I., *NMR cryoporometry: Principles, applications and potential*. Progress in Nuclear Magnetic Resonance Spectroscopy, 2009. **54**(2): p. 97-122.
80. Mitchell, J.; Webber, J.B.W. and Strange, J.H., *Nuclear magnetic resonance cryoporometry*. Physics Reports, 2008. **461**(1): p. 1-36.
81. Mitchell, J.; Stark, S.C. and Strange, J.H., *Probing surface interactions by combining NMR cryoporometry and NMR relaxometry*. Journal of Physics D-Applied Physics, 2005. **38**(12): p. 1950-1958.

- 
82. Rijniers, L.A.; Huinink, H.P.; Pel, L. and Kopinga, K., *Experimental Evidence of Crystallization Pressure inside Porous Media*. Physical Review Letters, 2005. **94**(7): p. 075503.
83. Danieli, E.; Mauler, J.; Perlo, J.; Blümich, B. and Casanova, F., *Mobile sensor for high resolution NMR spectroscopy and imaging*. Journal of Magnetic Resonance, 2009. **198**(1): p. 80-87.
84. Magritek. *Terranova-MRI: Earth's Field MRI teaching system*. 2009 [cited; Available from: <http://www.magritek.com/terranova.html>].
85. Shushakov, O.A., *Groundwater NMR in conductive water*. Geophysics, 1996. **61**(4): p. 998-1006.
86. Robert, L.K., *NMR well logging at Schlumberger*. Concepts in Magnetic Resonance, 2001. **13**(6): p. 396-403.
87. Robert L. Kleinberg, J.A.J., *An introduction to the history of NMR well logging*. Concepts in Magnetic Resonance, 2001. **13**(6): p. 340-342.
88. Jasper, A.J., *Los Alamos NMR well logging project Part 2: Los Alamos NMR Well Logging Project*. 2001. p. 368-378.
89. Jasper, A.J., *Los Alamos NMR well logging project Part 6: New Development*. 2001. p. 409-411.
90. Schlumberger. *MR Scanner*. 2009 [cited; Available from: [http://www.slb.com/media/services/evaluation/petrophysics/nmr/mr\\_scanner.pdf#page=6](http://www.slb.com/media/services/evaluation/petrophysics/nmr/mr_scanner.pdf#page=6)].
91. Blank, A.; Alexandrowicz, G.; Muchnik, L.; Tidhar, G.; Schneiderman, J.; Virmani, R. and Golan, E., *Miniature self-contained intravascular magnetic resonance (IVMI) probe for clinical applications*. Magnetic Resonance in Medicine, 2005. **54**(1): p. 105-112.
92. Eidmann, G.; Savelsberg, R.; Blümmler, P. and Blümich, B., *The NMR MOUSE, a Mobile Universal Surface Explorer*. Journal of Magnetic Resonance, Series A, 1996. **122**(1): p. 104-109.
93. Perlo, J.; Casanova, F. and Blümich, B., *Profiles with microscopic resolution by single-sided NMR*. Journal of Magnetic Resonance, 2005. **176**(1): p. 64-70.
94. Marble, A.E.; Mastikhin, I.V.; Colpitts, B.G. and Balcom, B.J., *A constant gradient unilateral magnet for near-surface MRI profiling*. Journal of Magnetic Resonance, 2006. **183**(2): p. 228-234.

- 
95. Marble, A.E.; Mastikhin, I.V.; Colpitts, B.G. and Balcom, B.J., *An analytical methodology for magnetic field control in unilateral NMR*. Journal of Magnetic Resonance, 2005. **174**(1): p. 78-87.
96. McDonald, P.J.; Aptaker, P.S.; Mitchell, J. and Mulheron, M., *A unilateral NMR magnet for sub-structure analysis in the built environment: The Surface GARField*. Journal of Magnetic Resonance, 2007. **185**(1): p. 1-11.
97. Perlo, J.; Demas, V.; Casanova, F.; Meriles, C.A.; Reimer, J.; Pines, A. and Blumich, B., *High-resolution NMR spectroscopy with a portable single-sided sensor*. Science, 2005. **308**(5726): p. 1279-1279.
98. Perlo, J.; Casanova, F. and Blumich, B., *Ex Situ NMR in Highly Homogeneous Fields:  $^1\text{H}$  Spectroscopy*. Science, 2007. **315**(5815): p. 1110-1112.
99. Manz, B.; Coy, A.; Dykstra, R.; Eccles, C.D.; Hunter, M.W.; Parkinson, B.J. and Callaghan, P.T., *A mobile one-sided NMR sensor with a homogeneous magnetic field: The NMR-MOLE*. Journal of Magnetic Resonance, 2006. **183**(1): p. 25-31.
100. McDowell, A. and Fukushima, E., *Ultracompact NMR:  $^1\text{H}$  Spectroscopy in a Subkilogram Magnet*. Applied Magnetic Resonance, 2008. **35**(1): p. 185-195.
101. Fukushima, E. and Jackson, J.A., *Unilateral magnet having a remote uniform field region for nuclear magnetic resonance (US 6489872)*. 2002.
102. Fukushima, E. and Jackson, J.A., *Unilateral magnet having a remote uniform field region for nuclear magnetic resonance (US 6828892)*. 2004.
103. Song, Y.-Q., *Novel NMR techniques for porous media research*. Magnetic Resonance Imaging, 2003. **21**(3-4): p. 207-211.
104. Song, Y.-Q. and Scheven, U.M., *An NMR technique for rapid measurement of flow*. Journal of Magnetic Resonance, 2005. **172**(1): p. 31-35.
105. Song, Y.-Q., *Novel NMR techniques for porous media research*. Cement and Concrete Research, 2007. **37**(3): p. 325-328.
106. Butler, J.P.; Reeds, J.A. and Dawson, S.V., *Estimating Solutions of First Kind Integral Equations with Nonnegative Constraints and Optimal Smoothing*. 1981, SIAM. p. 381-397.
107. Wang, W.M.; Li, P. and Ye, C.H., *Multi-exponential inversions of nuclear magnetic resonance relaxation signal*. Science in China Series a-Mathematics Physics Astronomy, 2001. **44**(11): p. 1477-1484.
108. Borgia, G.C.; Bortolotti, V.; Brown, R.J.S.; Castaldi, P.; Fantazzini, P. and Soverini, U., *A comparison among different inversion methods for multi-exponential NMR relaxation data*. Magnetic Resonance Imaging, 1994. **12**(2): p. 209-212.

- 
109. Wang, Z.D.; Xiao, L.H. and Liu, T.Y., *A new method for multi-exponential inversion of NMR relaxation measurements*. Science in China Series G-Physics Mechanics & Astronomy, 2004. **47**(3): p. 265-276.
110. Richardson, I.G., *The nature of C-S-H in hardened cements*. Cement and Concrete Research, 1999. **29**(8): p. 1131-1147.
111. Brownstein, K.R. and Tarr, C.E., *Importance of classical diffusion in NMR studies of water in biological cells*. Physical Review A, 1979. **19**(6): p. 2446.
112. Schreiner, L.J.; Mactavish, J.C.; Miljkovi, L.; Pintar, M.M.; Blinc, R.; Lahajnar, G.; Lasic, D.D. and Reeves L. W, *NMR Line Shape-Spin-Lattice Relaxation Correlation Study of Portland Cement Hydration*. 1985. p. 10-16.
113. Greener, J.; Peemoeller, H.; Choi, C.; Holly, H.; Reardon, E.J.; Hansson, C.M. and Pintar, M.M., *Monitoring of Hydration of White Cement Paste with Proton NMR Spin-Spin Relaxation*. 2000. p. 623-627.
114. Lasic, D.D.; Pintar, M.M. and Blinc, R., *Are Proton Nmr Observations Supportive of the Osmotic Model of Cement Hydration*. Philosophical Magazine Letters, 1988. **58**(5): p. 227-232.
115. Korb, J.P.; Godefroy, S. and Fleury, M., *Surface nuclear magnetic relaxation and dynamics of water and oil in granular packings and rocks*. Magnetic Resonance Imaging, 2003. **21**(3-4): p. 193-199.
116. Kalinichev, A.G.; Wang, J.W. and Kirkpatrick, R.J., *Molecular dynamics modeling of the structure, dynamics and energetics of mineral-water interfaces: Application to cement materials*. Cement and Concrete Research, 2007. **37**(3): p. 337-347.
117. Boguszynska, J.; Rachocki, A. and Tritt-Goc, J., *Melting behavior of water confined in nanopores of white cement studied by H-1 NMR cryoporometry: Effect of antifreeze additive and temperature*. Applied Magnetic Resonance, 2005. **29**(4): p. 639-653.
118. Boguszynska, J. and Tritt-Goc, J., *H-1 NMR cryoporometry study of the melting behavior of water in white cement*. Zeitschrift Fur Naturforschung Section a-a Journal of Physical Sciences, 2004. **59**(9): p. 550-558.
119. Boguszynska, J.; Brown, M.C.A.; McDonald, P.J.; Mitchell, J.; Mulheron, M.; Tritt-Goc, J. and Verganelakis, D.A., *Magnetic resonance studies of cement based materials in inhomogeneous magnetic fields*. Cement and Concrete Research, 2005. **35**(10): p. 2033-2040.
120. McDonald, P.J., *Stray field magnetic resonance imaging*. Progress in Nuclear Magnetic Resonance Spectroscopy, 1997. **30**(1-2): p. 69-99.
121. McDonald, P.J. and Newling, B., *Stray field magnetic resonance imaging*. Reports on Progress in Physics, 1998. **61**(11): p. 1441-1493.

122. Emid, S. and Creyghton, J.H.N., *High resolution NMR imaging in solids*. Physica B+C, 1985. **128**(1): p. 81-83.
123. Balcom, B.J.; Macgregor, R.P.; Beyea, S.D.; Green, D.P.; Armstrong, R.L. and Bremner, T.W., *Single-Point Ramped Imaging with  $T_1$  Enhancement (SPRITE)*. Journal of Magnetic Resonance, Series A, 1996. **123**(1): p. 131-134.
124. Link, J.; Kaufmann, J. and Schenker, K., *Water transport in concrete*. Magnetic Resonance Imaging, 1994. **12**(2): p. 203-205.
125. Bohris, A.J.; Newling, B.; McDonald, P.J.; Raoof, A. and Tran, N.L., *A broad-line nuclear magnetic resonance study of water absorption and transport in fibrous cement roofing tiles*. Journal of Materials Science, 1998. **33**(4): p. 859-867.
126. Beyea, S.D.; Balcom, B.J.; Bremner, T.W.; Prado, P.J.; Green, D.P.; Armstrong, R.L. and Grattan-Bellew, P.E., *Magnetic resonance imaging and moisture content profiles of drying concrete*. Cement and Concrete Research, 1998. **28**(3): p. 453-463.
127. Papavassiliou, G.; Milia, F.; Fardis, M.; Rumm, R.; Laganas, E.; Jarh, O.; Sepe, A.; Blinc, R. and Pintar, M.M.,  *$^1H$  Nuclear Magnetic Resonance Imaging of Water Diffusion in Hardened Cement Pastes*. 1993. p. 2109-2111.
128. Tritt-Goc, J.; Koscielski, S. and Pislewski, N., *The hardening of Portland cement observed by  $H$ -1 spin-lattice relaxation and single-point imaging*. Applied Magnetic Resonance, 2000. **18**(1): p. 155-164.
129. Beyea, S.D.; Balcom, B.J.; Bremner, T.W.; Armstrong, R.L. and Grattan-Bellew, P.E., *Detection of Drying-Induced Microcracking in Cementitious Materials with Space-Resolved  $^1H$  Nuclear Magnetic Resonance Relaxometry*. 2003. p. 800-805.
130. Young, J.J.; Szomolanyi, P.; Bremner, T.W. and Balcom, B.J., *Magnetic resonance imaging of crack formation in hydrated cement paste materials*. Cement and Concrete Research, 2004. **34**(8): p. 1459-1466.
131. Fardis, M.; Papavassiliou, G.; Abulnasr, L.; Miljkovic, L.; Rumm, R.J.; Milia, F.; Chaniotakis, E. and Frangoulis, D., *Effect of clay minerals on the hydration of cement An NMR study*. Advanced Cement Based Materials, 1994. **1**(6): p. 243-247.
132. Apih, T.; Lahajnar, G.; Sepe, A.; Blinc, R.; Milia, F.; Cvelbar, R.; Emri, I.; Gusev, B.V. and Titova, L.A., *Proton spin-lattice relaxation study of the hydration of self-stressed expansive cement*. Cement and Concrete Research, 2001. **31**(2): p. 263-269.
133. Tritt-Goc, J.; Pislewski, N.; Koscielski, S. and Milia, F., *The influence of the superplasticizer on the hydration and freezing processes in white cement studied by  $^1H$  spin-lattice relaxation time and single point imaging*. Cement and Concrete Research, 2000. **30**(6): p. 931-936.

- 
134. Black, S.; Lane, D.M.; McDonald, P.J.; Hannant, D.J.; Mulheron, M.; Hunter, G. and Jones, M.R., *The Visualization of the Ingress of Polymer Treatment Coatings into Porous Building-Materials by Stray-Field Magnetic-Resonance-Imaging*. Journal of Materials Science Letters, 1995. **14**(17): p. 1175-1177.
135. Chowdhury, A.; Gillies, A.; McDonald, P.J. and Mulheron, M., *Vapour phase application of hydrophobic coatings to cement-based materials*. Magazine of Concrete Research, 2001. **53**(5): p. 347-352.
136. Sharma, S.; Casanova, F.; Wache, W.; Segre, A. and Blümich, B., *Analysis of historical porous building materials by the NMR-MOUSE®*. Magnetic Resonance Imaging. **21**(3-4): p. 249-255.
137. Marko, A.; Wolter, B. and Arnold, W., *Application of a portable nuclear magnetic resonance surface probe to porous media*. Journal of Magnetic Resonance, 2007. **185**: p. 19-27.
138. Cano-Barrita, P.F.; Marble, A.E.; Balcom, B.J.; García, J.C.; Masthikin, I.V.; Thomas, M.D.A. and Bremner, T.W., *Embedded NMR sensors to monitor evaporable water loss caused by hydration and drying in Portland cement mortar*. Cement and Concrete Research, 2009. **39**(4): p. 324-328.
139. Halbach, K., *Physical and optical properties of rare earth cobalt magnets*. Nuclear Instruments and Methods in Physics Research, 1981. **187**(1): p. 109-117.
140. Wikipedia. [www.wikipedia.org](http://www.wikipedia.org). [cited 16/07/2008]; Available from: [www.wikipedia.org](http://www.wikipedia.org).
141. <http://www.dotynmr.com/PDF/NMR-cat05.pdf>. [cited.
142. [www.rs-components.co.uk](http://www.rs-components.co.uk). [cited 27/07/2009].
143. Raupach, M.; Dauberschmidt, C. and Wolff, L., *Monitoring the moisture distribution in concrete structures*. 2006.
144. Kocaba, V., *Personal Communication*.
145. Hong, S.-Y. and Glasser, F.P., *Alkali binding in cement pastes: Part I. The C-S-H phase*. Cement and Concrete Research, 1999. **29**(12): p. 1893-1903.
146. Nonat, A., *Personal communication*.
147. McDonald, P.J.; Mitchell, J. and Mulheron, M., *Cement Products: Characterisation by NMR and MRI*. 2005.
148. Scrivener, K., *Influence of slag on CH content*. 2009.

- 
149. Parrott, L.J., *A review of carbonation in reinforced concrete*. 1987, Cement and Concrete Association.
  150. Ikoma, K.; Takamiya, H.; Kusaka, Y. and Seo, Y., *H-1 double-quantum filtered MR imaging of joints tissues: Bound water specific imaging of tendons, ligaments and cartilage*. Magnetic Resonance Imaging, 2001. **19**(10): p. 1287-1296.
  151. Tsoref, L.; Shinar, H.; Seo, Y.; Eliav, U. and Navon, G., *Proton double-quantum filtered MRI - A new method for imaging ordered tissues*. Magnetic Resonance in Medicine, 1998. **40**(5): p. 720-726.
  152. Navon, G.; Shinar, H.; Eliav, U. and Seo, Y., *Multiquantum filters and order in tissues*. Nmr in Biomedicine, 2001. **14**(2): p. 112-132.
  153. Asllani, I.; Shankland, E.; Pratum, T. and Kushmerick, M., *Effects of pH and molecular charge on dipolar coupling interactions of solutes in skeletal muscle observed by DQF, 1H NMR spectroscopy*. Journal of Magnetic Resonance, 2003. **163**(1): p. 124-132.
  154. Wiesmath, A.; Filip, C.; Demco, D.E. and Blümich, B., *Double-Quantum-Filtered NMR Signals in Inhomogeneous Magnetic Fields*. Journal of Magnetic Resonance, 2001. **149**(2): p. 258-263.
  155. Vanvelzen, G.D.F. and Wenckebach, W.T., *Nuclear magnetic ordering in Ca(OH)<sub>2</sub>. I. Molecular field approximation*. Journal De Physique, 1990. **51**(13): p. 1445-1461.